Performance evaluation of surgical techniques for treatment of scapholunate instability in a type II wrist

A Thesis submitted to The University of Manchester for the degree of Doctor of Philosophy in the Faculty of Science and Engineering

2020

Roberto Leonardo Diaz

SCHOOL OF NATURAL SCIENCE
DEPARTMENT OF MATERIALS

Contents

List of Figures

List of Tables

Abbreviations

2D two-dimensional. 54

3D three-dimensional. 55

CT Computer tomography. 30, 36, 99

DoF degrees of freedom. 36

FCR flexor carpi radialis (tendon). 47, 48, 49, 185

FE Finite element. 51, 82, 85, 92, 99, 102

FEM Finite element method. 51, 67

MBT modified Brunelli technique. 23, 47, 50, 141

MRI Magnetic resonance imaging. 30, 36, 46, 62, 99

RBSM Rigid body spring modelling. 51, 53

ROM range of motion. 34

RUD radial ulnar deviation. 21

SL scapholunate. 45, 139

SLAM scapholunate axis method. 23, 49

SLIL scapholunate interosseous ligament. 19, 24, 44, 45, 48, 85, 88, 140

TFCC triangular fibrocartilage complex. 29, 53

Abstract

The scapholunate interosseous ligament (SLIL) is the primary stabiliser of the wrist and the most common injured ligament of the joint. The surgical reconstruction uses a portion of a tendon graft or artificial graft to reconnect the bones via transosseous tunnels across the scaphoid and lunate bones; however, there are unresolved issues with regard to which technique restores better the interaction without affecting the normal kinematics.

This thesis aimed to investigate the performance of scapholunate (SL) ligament reconstruction techniques employing a 3D finite element model of a type II wrist that reproduces carpal kinematics. The model was created from computer tomography (CT) data from a human wrist and considered bones, articular cartilages and ligaments. Each carpal bone has 6 degrees of freedom, its motion is only restricted by its interaction to other bones and a complex set of ligaments. The models were validated with data from cadaveric studies. In addition, a comparison of the carpal mechanics of type I and type II wrists was undertaken to elucidate the difference between the two types.

The performance of the techniques was diverse in all the positions. In comparison to the intact ligament case, Corella reconstruction provided superior outcome restoring the dorsal gap, volar gap, and SL angle to within 3.5%, 7.1%, and 8.4% at clenched fist ulnar deviation posture, respectively. MBT performed better at flexion and extension positions, closing the SL gap at dorsal and volar, and reducing the SL angle to within 1.2% without altering significantly the carpal motion. SLAM did well at radial deviation where recovered the SL dorsal gap and reduced to within 6.2% the SL dorsal gap during ulnar deviation.

Considering the full range of motion analysed, SLAM was better able to restore SL gap SL angle and carpal instability following scapholunate injury. SLAM performed well during radial and ulnar deviation because the generated connexion axis favoured the relative rotation between the scaphoid and lunate which is characteristic in a type II wrist column kinematics. In general, Corella restricted the in-plane rotations of the bones in several positions, whereas the MBT also restricted the rotation of the bones in the radial deviation posture which could lead to a loss of range of motion of the hand after surgery.

Declaration

No portion of the work referred to in the thesis has been submitted in support of an application for another degree or qualification of this or any other university or other institute of learning.

Copyright

Acknowledgements

I would like to thank my supervisors Prof Teresa Alonso-Rasgado, Prof Colin Bailey and Mr Sumedh Talwalkar for all the support during my PhD studies, without their guidance and feedback this PhD would not have been achievable. I would also want to thank Dr Keith Davey and Dr Robert Lindsay for their help to accomplish this duty.

All my gratitude to The National Council of Science and Technology of Mexico (CONACyT) and the Mexican Secretariat of Public Education (SEP) for the scholarship and the financial support to complete my doctoral studies.

My sincere thanks to Dr David Jimenez-Cruz which advice was crucial during this research. Special Thanks go to BPaco for his invaluable help, encouragement and all the fun we had in the last four years. Also, I would like to thank my colleagues for the stimulating discussions, support and friendship.

Finally, I would like to thank the people who mean a lot to me, my Mum and Dad, for the love, care, pain and sacrifice you did to make me the person I am. To my sisters Norma, Diana and Maribel for encouraging me in the accomplishment of my goals. I thank my extended family: Elena, Mayra, Arturo, Paty and the kids, I would never be able to pay back the love, affection and support for every decision I made. To Francis for being the oasis of love and tranquillity, and my safe place.

Publications

Journal publications

1. *Performance evaluation of surgical techniques for treatment of scapholunate instability in a type II wrist* Leonardo-Diaz, R., Alonso-Rasgado, T., Jimenez-Cruz, D., Bailey, C.G., & Talwalkar, S. (2019). International Journal for Numerical Methods in Biomedical Engineering®. https://doi.org/10.1002/cnm.3278

Podium presentations

1. *Finite Element Modelling for wrist type II.* R. Leonardo-Diaz, Alonso-Rasgado, T., Bailey, C.G., & Talwalkar, Wrightington Gold Medal Research Day, Wrightington Hospital, United Kingdom 2017.

2. *Modelling of surgical technique for scapholunate instability.* R. Leonardo-Diaz, Alonso-Rasgado, T., Bailey, C.G., & Talwalkar, S. European Orthopaedic Research Society. EORS Meeting 2018, Galway, Ireland 2018.

3. *Performance evaluation of tenodesis techniques for the treatment of scapholunate instability: a Finite Element Analysis.* Wrightington Gold Medal Research Day, Wrightington Hospital, United Kingdom 2019.

Poster presentations

1. *Biomechanical analysis of two types of human wrist.* R. Leonardo-Diaz, Alonso-Rasgado, T., Bailey, C.G., & Talwalkar, S. The University of Manchester. School of Materials Postgraduate Student Conference. Manchester, United Kingdom 2018.

Awards and honours

1. Awarded the *CONACyT-Mexico scholarship for doctoral studies at the University of Manchester*, Mexico City, Mexico 2016.

Chapter 1

Introduction

1.1 Overview

Scapholunate ligament reconstruction is a surgical method for the treatment of scapholunate interosseous ligament (SLIL) dissociation. The SLIL dissociation is the loss of mechanical linkage between the scaphoid and the lunate due to a partial or complete disruption of the ligament caused by an injury that alters carpal instability [1]. The SLIL is the most common injury of the carpal ligaments; about 5% of wrist sprains cases and 13.4% of distal radius fractures are associated with a rupture at the ligament [2]. It can take between 3 to 12 months after the trauma before the disconnection of the lunate and scaphoid can be seen in an x-ray, this is the reason why the SL ligament injury is often misdiagnosed or untreated evolving into a more serious condition such as wrist arthrosis [3].

The SLIL reconstruction aims to reconnect the lunate and the scaphoid by using a tendon graft to reduce and maintain the scapholunate interval. Follow-up studies comparing different surgical methods report mixed outcomes in terms of pain and hand mobility; even when comparing two patients operated under the same technique [4–6]. Although the relative motion between the lunate and scaphoid is affected by the surgery, there are no studies investigating changes in the carpal kinematics and its effect on the reduction of range of motion.

An impartial comparison of the ligament reconstruction performance is impracticable in clinical and cadaveric studies due to the permanent alteration of the bones, cartilages and ligaments. Two different techniques can not be tested on the same subject. An accurate reproduction of the *in-vivo* situation could be achieved by implementing computational models of the human wrist in which all the surgical methods can be tested under the same anatomic condition. However, the development of a computational model able to reproduce carpal kinematics is challenging, due to its multi-body interactions and restrictions. The latest approach in computational biomechanics of the wrist is restricted to static or semi-static problems.

This thesis presents the evaluation of ligament reconstruction techniques based on virtual surgery using the finite element method. In a comprehensive context, this work took into account the lunate bone morphology that influences the carpal kinematics. The investigation also analysed the carpal motion alterations caused by the rupture of the scapholunate ligament and the subsequent ligament reconstructions. The numerical models of the wrist used in this investigation, are the first finite element (FE) models to reproduce accurately full carpal kinematics in a wide range of motion.

1.2 Research background

Scapholunate ligament reconstruction focuses on reduction and maintenance of scapholunate interval to stabilise the wrist joint. The approach of each technique mainly differs if the re-connection is done at the dorsal, volar or medial region of the bones. The configuration of the attachment is important because may limit the motion of the bones thus reduce the range of motion. Carpal kinematics has been proved to be a challenging area of research due to the scarce information available and the difficulty in data acquisition for small motion patterns.

Traditionally, the wrist joint has been treated as a joint with two degrees of freedom that allow four motions: flexion, extension, radial and ulnar deviation. Unlike the other joints in the human body where only two or three bones are interacting (e.g. the hip, knee and elbow), the wrist joint is more complex as ten bones are interacting at the same time to allow the movement. Carpal motion theories have been proposed to describe the relationship between proximal bones, specifically scaphoid, lunate and triquetrum [7, 8].

Two main theories explain the carpal motion: row theory and column theory. In the row theory, the scaphoid, lunate and triquetrum keep their relative distance during radial ulnar deviation (RUD) moving like components of a row that slides over the radius. In the column theory, the scaphoid, lunate and triquetrum move separately like components of different columns. The side columns rotate around a central column (lunate) to allow the same RUD motion. These theories have been demonstrated in clinical studies [8, 9], but the findings are rarely considered in the development of surgical techniques.

The reason why some subjects have different carpal motion patterns was studied recently. In 1990, Viegas *et al* [10] found common variation in wrist anatomy of the lunate bone. Viegas classified into type I wrist when the lunate articulates with the scaphoid, capitate and triquetrum; and into type II wrist when the lunate has an extra facet in the most proximal region that articulates with the hamate. In 2007, Galley *et al* [9] classified one hundred normal wrists into three groups based on the lunate shape and linked the type of lunate with the two main carpal kinematic theories. Type I wrists show a row wrist kinematics while type II wrists show a column wrist kinematics; a third intermediate group lay between the two groups with intermediate mechanics.

The understanding of the carpal kinematics is essential in the design of scapholunate ligament reconstruction techniques. The configuration of the path in which the bones are reconnected may alter the motion pattern after surgery; however, it is seldom mentioned in recent investigations.

1.3 Objectives

The overall aim of this research is to evaluate the performance of scapholunate ligament reconstruction techniques considering anatomic variations of the carpal bones. The fulfilment of this aim demands the achievement of the following tasks:

1. The development of a Finite Element (FE) model of a type II wrist.
2. The investigation of the carpal kinematics of the wrist using finite element models.
3. The examination of the changes on carpal kinematics after the resection of the scapholunate ligament.
4. The investigation of the effect on the carpal kinematics after surgical reconstruction techniques.
5. The evaluation of the performance of scapholunate ligament reconstruction techniques at clenched fist ulnar deviated posture.
6. The evaluation of the performance of three scapholunate ligament reconstruction techniques in the four positions of the hand (flexion, extension, ulnar and radial deviation).

The accomplishment of this investigation will contribute to the field of hand surgery by analysing carpal kinematics and ligament reconstruction techniques. The use of finite element analyses will set a precedent in the use of virtual surgery simulation to predict outcomes of any carpal operation. However, the construction and validation of functional FE models able to reproduce carpal kinematics is a technical challenge to overcome.

This investigation was developed in collaboration with Wrightington Hospital, Lancashire, UK.

1.4 Methodology of the research

Three-dimensional finite element models of a type II wrist were constructed from computed tomography (CT) data of a human wrist. The final assembly includes bones, articular cartilages and ligaments. The models were validated by simulating cadaveric experiments reported in the literature [11, 12] and comparing the results from the model to those published.

The finite element model of the wrist was constructed from computed tomography. The creation of the model started with the segmentation of the images to create single volumetric surfaces for the eight carpal bones, radius, ulna and five metacarpals. The 3D geometries were imported into Abaqus 6.14 ® (Dassault Systemes, RI) to assemble the joint, to create the cartilage structures and incorporate the ligaments. The articular cartilages were constructed by offsetting surfaces where two or more bones interact.

The modelling of ligaments was completed using spring and shell elements located at anatomically correct insertion points. Spring-ligaments were defined to work only in tension; with a non-linear mechanical behaviour based on a force-strain curve. Shell-ligaments were included to simulate the wrapping effect of the intercarpal and radiocarpal ligaments. The mechanical behaviour of the shell elements was defined with the stress-strain relationship and corresponding cross-sectional area based on the stiffness reported in the literature. The material properties for each tissue (bones, cartilage and ligaments) were assigned, and the interactions and boundary conditions were defined on the assembly.

The completed model was validated by replicating experimental work reported in previous cadaveric studies [11, 12]. All the models employed in the investigation were created based on the validated model, including the ligament reconstruction models simulating the virtual surgeries. This study comprises the following cases: intact ligament, scapholunate sectioned ligament, modified Brunelli technique (MBT), scapholunate axis method (SLAM) and Corella. The analysis was

undertaken at the following position: the neutral position, clenched fist ulnar deviated posture, flexion, extension, radial and ulnar deviation.

1.5 Thesis outline

Chapter 2 presents the literature review into four main subjects. First, the anatomy of the human wrist is explained with the purpose of familiarisation with the structures that compose the wrist joint including bones, cartilage and ligaments. Then, the biomechanics is described in terms of the carpal motion theories; following the explanation of the SLIL injury diagnosis and its treatment. Finally, a revision of works using finite element modelling to investigate the human wrist is presented.

Chapter 3 describes in detail the construction of the finite element model for the type II wrist step by step as well as the validation of the model for the different stages of the investigation.

Chapter 4 presents the performance evaluation of three surgical techniques used in the treatment of scapholunate instability in a type II wrist at the clenched fist position. From the intact FE model of a type II wrist, three virtual surgeries were simulated and compared against each other to identify the variations that each technique has in the surgery outcome. The results obtained in this Chapter has been included in a publication in the *International Journal for Numerical Methods in Biomedical Engineering.*

Chapter 5 describes the performance evaluation of the ligament reconstruction techniques in a type II wrist at flexion and extension positions. Ten FE models were used to simulate 5 scenarios at each position, including Intact SLIL ligament, SLIL sectioning, Corella, Modified Brunelli Technique (MBT) and Scapholunate axis Method (SLAM). The ability to restore the SL gap, SL angle and carpal kinematics was assessed in order to identify which technique has the best performance at flexion and extension.

Chapter 6 contains the results of the performance evaluation at radial and ulnar deviation. For each position, 5 FE models were used to simulate: Intact SLIL ligament, SLIL sectioning, Corella, Modified Brunelli Technique (MBT) and Scapholunate axis Method (SLAM). The evaluation was extended to radial and ulnar deviation in order to evaluate the performance of the ligament reconstruction techniques in a wide range of motion of the wrist.

Chapter 7 presents the conclusions of the performance evaluation of the techniques at the clenched fist ulnar deviated position, flexion and extension, and radial and ulnar deviation positions.
This chapter also describes the limitations of the thesis and the potential opportunities for future work.

Chapter 2

Literature Review

This chapter is divided into four sections. Each section presents information about concepts needed to understand clinical terminology, bones morphology and their relationship to the carpal kinematics. The first section explains the anatomy of the carpal bones and carpal ligaments; the second section contains the literature review about the carpal biomechanics, including the carpal motion theories. The third section describes the scapholunate dissociation and current treatment options; the fourth section shows the trends in the use of biomechanical modelling in the study of the human wrist.

2.1 Anatomy of the human wrist

The wrist joint is a biaxial, ellipsoid-type joint that serves as the articulation between the forearm and the hand. The wrist is a complex mechanism that permits a wide range of motion of the hand. The stability of the joint involves the interplay between carpal bones geometry and a sophisticated arrangement of ligaments. The wrist joint comprises fifteen bones: the distal region of the radius and ulna (forearm), eight carpal bones and the proximal bases of the five metacarpals [13] as shown in Figure 2.1.

The motion of the carpal bones depends on the contact force transmission between bones; the stability of the joint relies on the multi-articulation bone surfaces and the constraints given by the complex set of ligaments. Both structures, ligaments

and bones, are delicately balanced and any injury has the potential to disrupt the system affecting the stability of the entire joint [14].

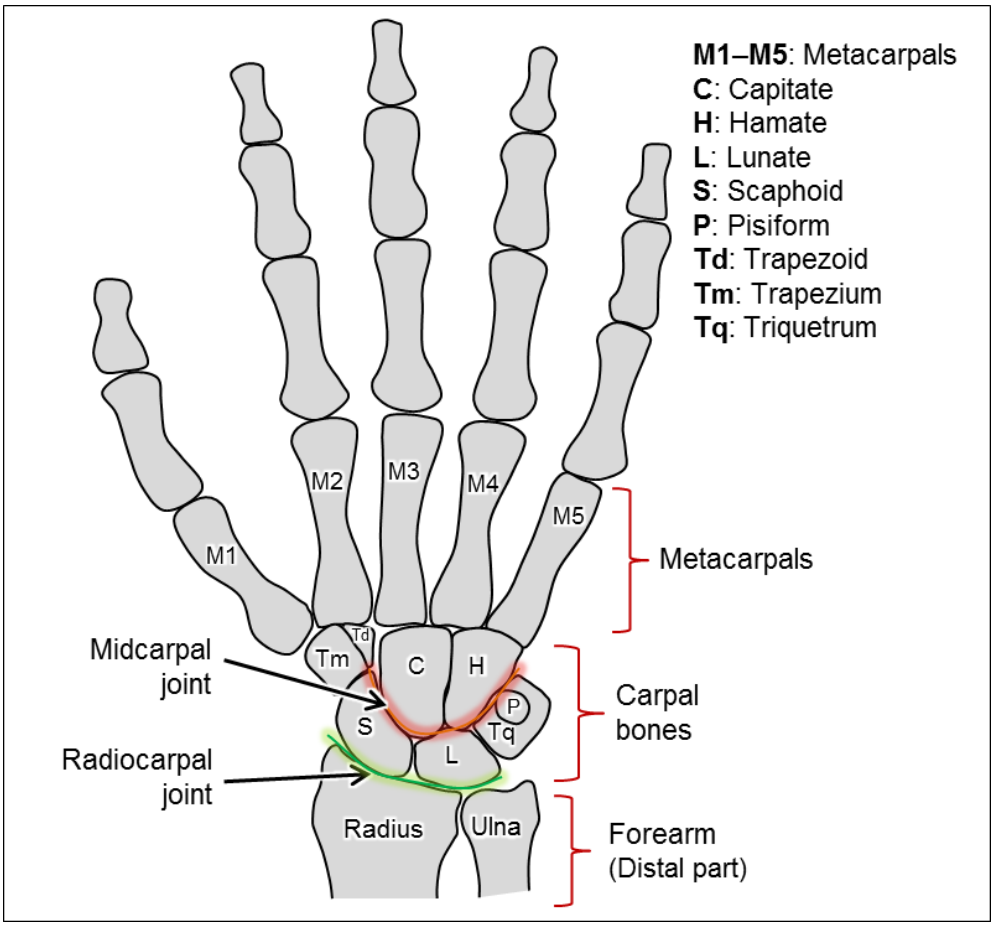

Figure 2.1: Wrist joint. Carpal bones distribution of human wrist; highlighted the midcarpal and radiocarpal joint location.

2.1.1 Bones

The carpal bones are positioned into two rows over the fossa of the radius. The proximal row includes (from radial to ulnar) the scaphoid, lunate, triquetrum, and pisiform; the pisiform is included in the proximal row as it is firmly bound to the triquetrum. The distal row comprises (from radial to ulnar) the trapezium, trapezoid, capitate, and hamate. The metacarpals are named conventionally by a number, beginning with the thumb metacarpal (first metacarpal) and increasing the number towards the little finger metacarpal (fifth metacarpal) [15]. The wrist joint is divided into two joint clinically, the radiocarpal joint between

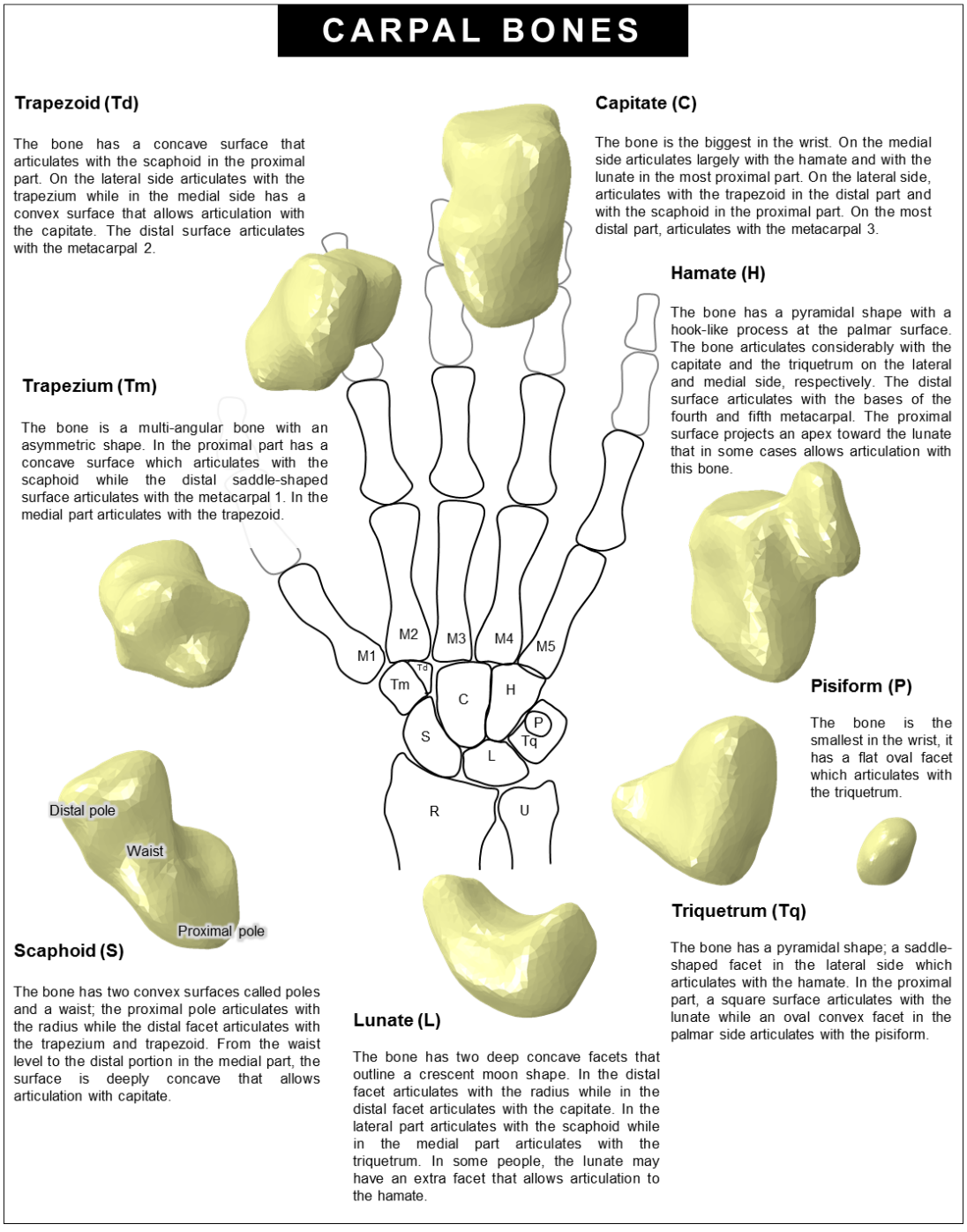

Figure 2.2: Carpal bones description.

the radius and the proximal carpal bones and, the midcarpal joint between the proximal row and the distal row as shown in Figure 2.1.

The carpal bones are irregularly shaped bones with multi-angular surfaces covered with articular cartilage. A brief description of the carpal bones is shown in Figure 2.2. The shape of the carpal bones is critical on the stability of the joint because of their multi-angular faces, protuberances and depressions surfaces work as articular features to the bones and help to the interaction with the surrounding bones.

The distal end of the forearm connects the radius with the carpal bones and it is usually called the radiocarpal joint. The distal surface of the radius may be divided into three concave articular sections: the scaphoid fossa, the lunate fossa and the ulnar notch as shown in 2.3. Over the distal region, the scaphoid and lunate fossae are separated by a ridge which delineates the scaphoid and lunate facets that together form a quadrilateral cross-section over the radius. The extended lateral side of the radius is called the styloid process and limits the movement by impingement during radial deviation [16].

The distal region of the ulna is a semi-spherical bone with a protuberance termed as the ulnar styloid as shown in Figure 2.3. Over the sphere, an oval surface articulates with the ulnar notch of the radius in the downward region and with the triangular fibrocartilage complex (TFCC) in the upper surface. The ulnar styloid is projected from the medial and backside of the bones and serves as the attachment for many ligaments of the wrist. The TFCC is formed by the triangular fibrocartilage disk, the dorsal radioulnar and volar ligaments, the ulnocarpal ligaments, and the tendon sheath of the extensor carpi ulnaris.

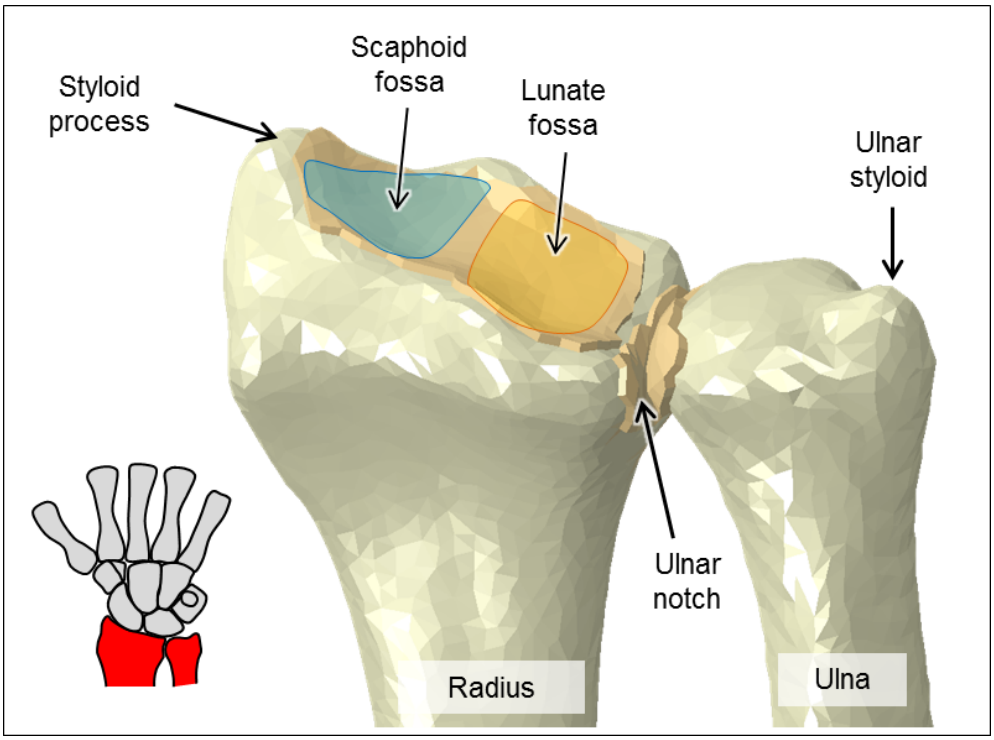

Figure 2.3: Anatomy of the distal region of radius and ulna.

2.1.2 Cartilaginous Tissue

The bones in the wrist are covered with a layer of articular cartilage and surrounded by synovial fluid. The purpose of the cartilage is to distribute loads over a large area; in conjunction with the synovial fluid, allows the bones a smooth glide over their surfaces with minimum friction and wear. Physiologically, articular cartilage is a non-vascular connective tissue, hence has poor potential for healing and regeneration; if damaged, it develops osteoarthritis.

The thickness of the cartilage layer ranges from 1 to $5mm$ and varies along the surfaces of the bone depending on their interaction against each other [17, 18]. Measurement of the cartilage thickness in a cadaver is challenging, not only because it varies from subject to subject but also because the tissue can be damaged during the breaching of the joint. Moore *et al* [17] quantify the thickness of individual carpal bone using μComputer tomography (CT) and Magnetic resonance imaging (MRI) as shown in Figure 2.4.

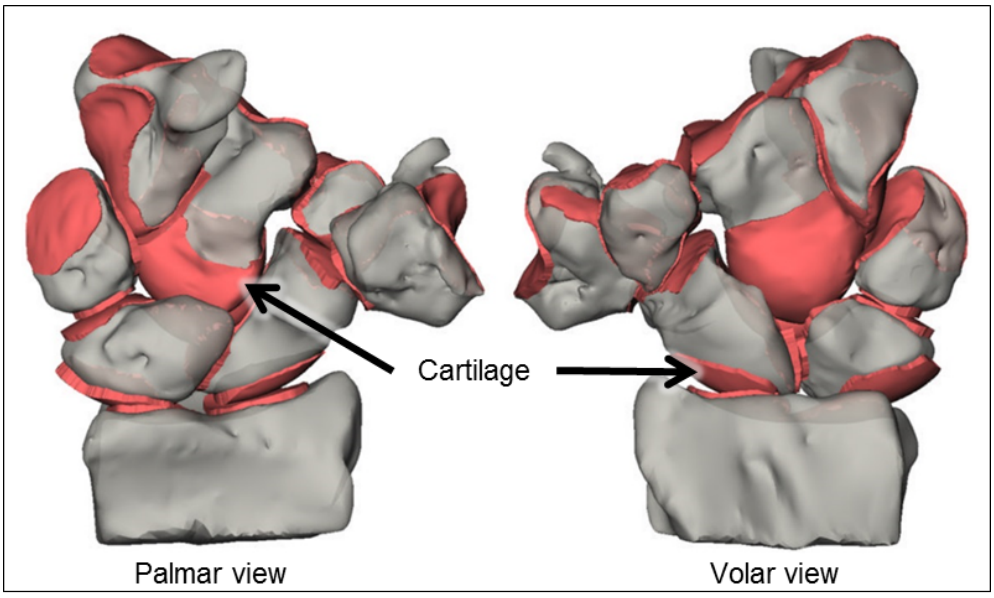

Figure 2.4: Cartilage surfaces (red) generated using μCT. Taken from Moore [17].

2.1.3 Ligaments

The stability of the carpal joint is kept for both geometrical features and a complex set of ligaments. The ligament is a connective tissue that serves to hold bones together; a ligament is composed of dense fibrous bundles of collagenous fibres arranged linearly. The ligaments constrain displacement, guide motion, provide natural alignment between bones, and transfer forces through and across the wrist [19]. Studies on carpal ligaments anatomy, size, insertion points and mechanical properties are available in the literature [20].

Taleisnik *et al* [7] classified the ligaments of the wrist into two groups based on their attachment point location; extrinsic ligaments connect the carpal bones to radius, ulna or metacarpal whereas intrinsic ligaments have origins and insertions within the carpal bones area. The carpal ligaments are named after the bones they connect, naming the bones from the proximal-to-distal and radial-to-ulnar path. Table 2.1 shows the connections between the bones in the wrist; Figure 2.5 shows a graphical representation of the ligaments.

Table 2.1: Ligaments of the human wrist.

Classification	Side	Ligament Name	Connection 1	Connection 2
Extrinsic	**Dorsal**	Dorsal radiocarpal	Radius	Triquetrum and Lunate
		Radial collateral	Radius	Scaphoid
		Ulnar collateral	Ulna	Pisiform, Triquetrum
		Radioulnar	Radius	Ulna
	Volar	Radioscaphocapitate	Radius	Scaphoid and Capitate
		Long radiolunate	Radius	Lunate and Triquetrum
		Short radiolunate	Radius	Lunate
		Radioscapholunate	Radius	Scaphoid and lunate
		Ulnolunate	Ulna	Lunate
		Ulnocapitate	Ulna	Capitate
		Ulnotriquetral	Ulna	Triquetrum
		Radioulnar	Radius	Ulna
Intrinsic	**Dorsal**	Intercarpal	Triquetrum	Scaphoid, trapezoid, trapezium
		Trapeziotrapezoid	Trapezium	Trapezoid
		Capitotrapezoid	Trapezoid	Capitate
		Capitohamate	Capitate	Hamate
		Triquetrohamate	Triquetrum	Hamate
		Lunatecapitate	Lunate	Capitate
		Lunatehamate	Lunate	Hamate
		Scaphocapitate	Scaphoid	Capitate
	Volar	Trapeziotrapezoid	Trapezium	Trapezoid
		Scaphotrapezial	Scaphoid	Trapezium
		Scaphotrapezoidal	Scaphoid	Trapezoid
		Scaphocapitate	Scaphoid	Capitate
		Capitohamate	Capitate	Lunate
		Capitotrapezoid	Capitate	Trapezium
		Triquetrocapitate	Triquetrum	Capitate
		Triquetrohamate	Triquetrum	Hamate
		Lunotriqueral	Lunate	Triquetrum
Interosseossus		Scapholunate	Scaphoid	Lunate
		Lunotriquetral	Lunate	Triquetrum
		Trapeziotrapezoid	Trapezium	Trapezoid
		Capitotrapezoid	Trapezoid	Capitate
		Capitohamate	Capitate	Hamate

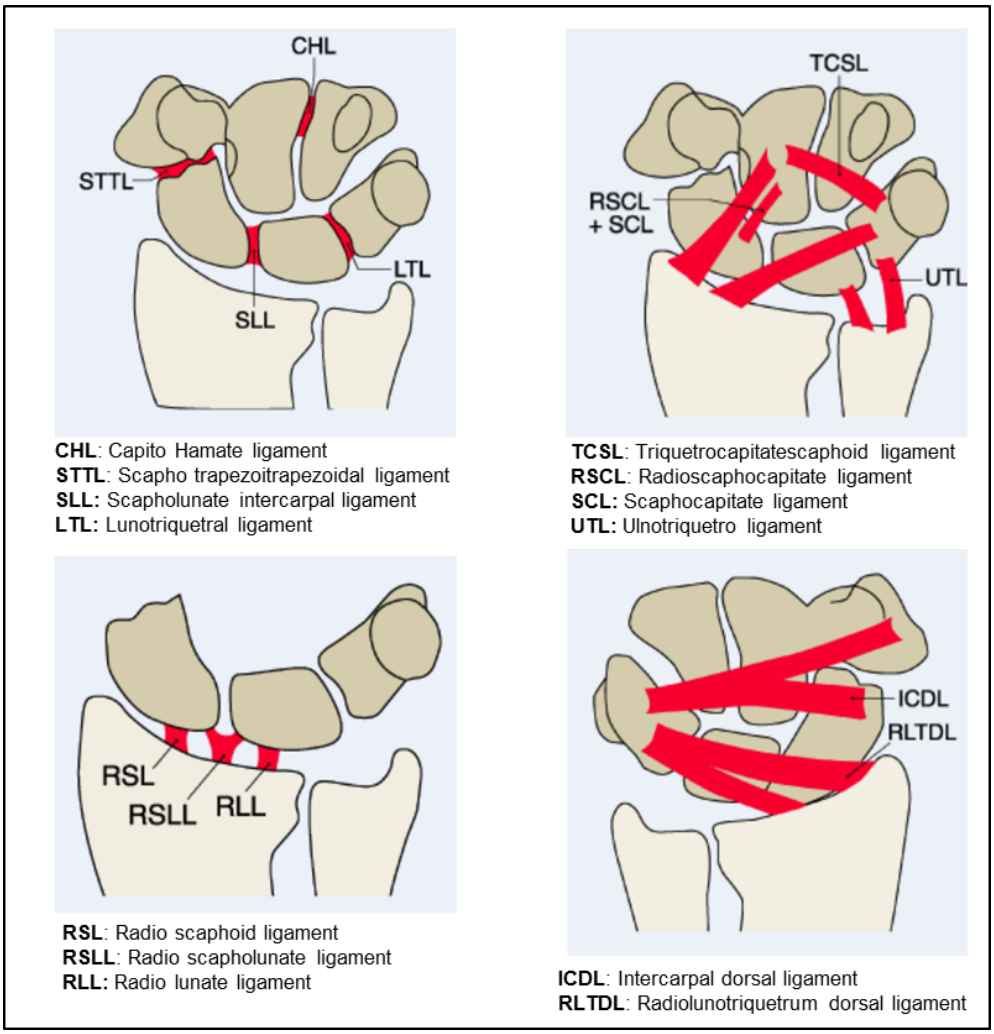

Figure 2.5: Ligament of the wrist.

A typical stress-strain (or load-deformation) curve for a ligament shows a nonlinear behaviour, that can be divided into three regions: *toe, linear, and plastic region* [21]. In the *toe region*, the force applied elongates the ligament fibres to remove the crimps, as the fibres straighten, the curve swings upward; the toe region ends at about $1.5 - 3.0\%$ strain. In the *linear region*, the fibres are stressed in a plastic deformation zone, ending at the *yield point* at about $5.0 - 7.0\%$ strain; the slope of the load-deformation curve in this region represents the stiffness of the ligament, while in the stress-strain curve is a measure of the tissue's modulus of elasticity. In the *plastic region*, after reach the yield point the fibres may damage and the ligament will eventually fail (*failure point*); this occurs at about $12 - 15\%$ strain [22].

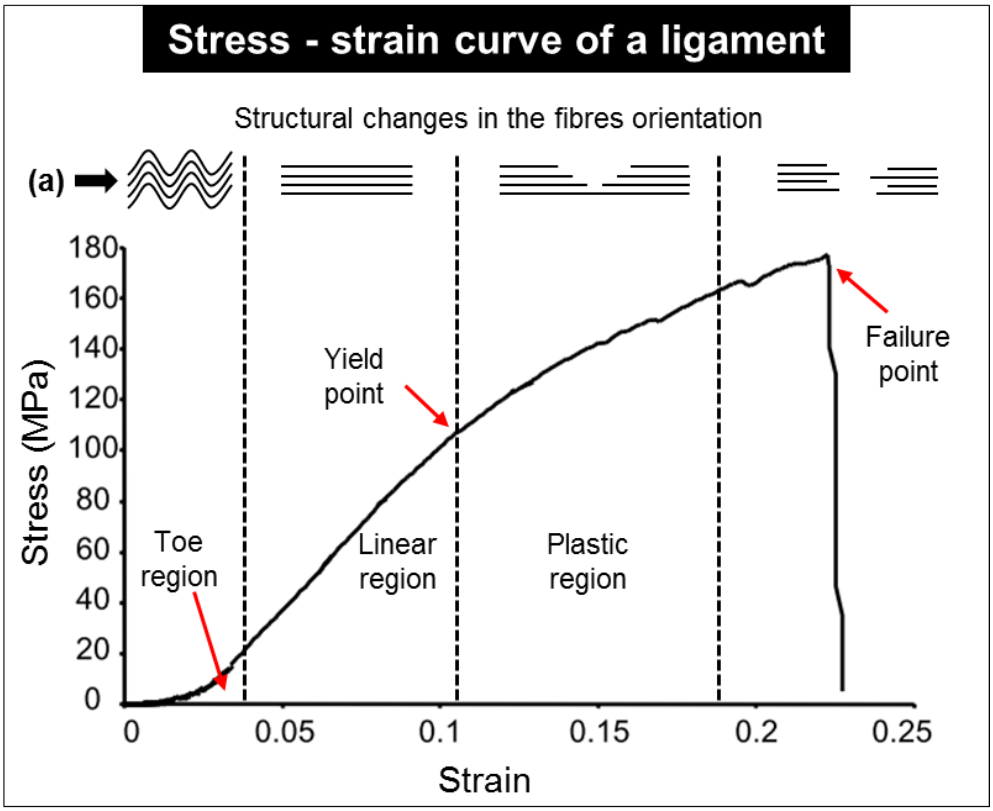

Figure 2.6: Representative stress-strain curve from tensile testing of a rat tail tendon. Modified from Gentleman [23]. (a) Ligament fibres straightening and failure along the different regions of the curve from a crimp pattern at the toe region to the rupture at the failure region.

2.2 Biomechanics

The range of motion (ROM) of the human wrist results from the combination of the movement in two anatomical axes. In one axis occurs flexion and extension, which values range from $60 - 80°$ for flexion and $55 - 75°$ for the extension as shown in Figure 2.7. In other axis occurs the radial and ulnar deviation, which values range from $15 - 25°$ and $30 - 45°$, respectively [24]. Pronation and supination of the hand remain controversial because it is not an independent movement of the wrist, being a forearm motion instead of a pure wrist motion the reason why in this work this plane is not considered as a principal plane of motion of the joint [25].

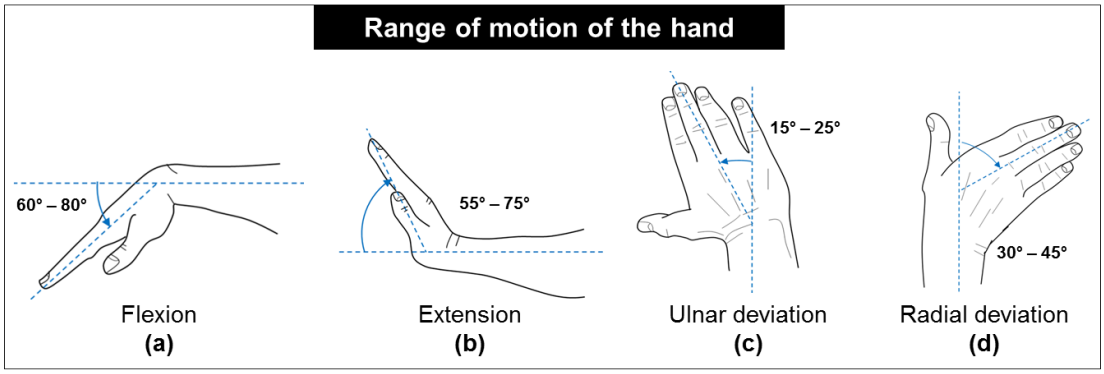

Figure 2.7: Motions of the human wrist and the typical range of motion.

Carpal kinematics is complex to analyse and visualise due to the multi-rotation of the carpal bones in-plane and out-of-plane. Understanding carpal kinematics is essential to identify the effect that a ligament rupture or a surgical procedure has in the normal motion of the bones. Table 2.2 shows the techniques that have been used to discern carpal motion patterns.

The first studies reporting carpal kinematics used plain x-ray images; in this studies, the motion of the bones was assessed by measuring the change in angle or length of the bones in images taken at different positions in flexion, extension, radial or ulnar deviation [25, 26]. The use of x-ray images (two-dimensional projection) limited the observation and explanation of the complex carpal kinematics. Kobayashi *et al* [26] reported that the carpal bones move with six degrees of freedom, and recommended to extend the analysis into a 3D study. To overcome the limitation of a two-dimensional projection, Ferris *et al* [27] used a double x-ray to visualise the carpal motion in two planes at the time: one in the posteroanterior plane (dorsal or volar) and another in the lateral plane; unfortunately, due to the overlapping of the bones in the lateral x-ray image, the border of the carpal bones was not identifiable in that view hence the results were limited again.

With the introduction of three-dimension image acquisition technologies, such as CT and MRI, new studies assessed the motion of the carpal bones *in vivo* [28–34]. Crisco *et al* [28] quantified the carpal kinematics *in vivo* using non-invasive computed tomographic imaging. The technique consisted of a few stages: image acquisition, segmentation of bone structures, contour extraction and registration. The process was repeated in multiple positions to execute a kinematic analysis by tracking the change of position of each bone throughout all the positions. Similar studies in carpal kinematics are available in the literature focusing in particular bones are shown in Table 2.2. The principal advantages of using these techniques include high measurement accuracy and the capability to measure the motion of the bones in different planes at the same time. However, this technique is limited to a quasi-static scenario where multiple positions are required to construct an arc of motion in a frame by frame base.

Recently, probed methods used to track motion in other human joints such as the ankle, knee, shoulder, elbow and hand, has been implemented into the carpal kinematics studies [47, 48]. Fraysse *et al* [47] tracked carpal motion using bone pin-mounted markers and optic registry system. In eight cadaver specimens, markers were inserted and then tracked for the ulna, radius, third metacarpal, scaphoid, lunate, triquetrum and capitate. The study was done during flexion (15°), extension (15°), radial (20°) and ulnar deviation (20°). A 6 degrees of freedom (DoF) robot reproduced the movement of the hand by pulling the metacarpals. The recorded trajectories show clear motion patterns for the radiocarpal and midcarpal joint. The advantage of this method is the reproducibility of the motion and good results accuracy.

In a similar study, Eschweiler *et at* [48] recorded the carpal motion using electromagnetic tracking systems. An electromagnetic tracking sensor was implanted directly into the approximate location of the centroid of the carpal bones in eight cadaver wrists. The specimens were mounted in a customised rig to produce flexion (30°), extension (30°), radial (15°) and ulnar deviation (15°) in passive motion without applied forces. The results reported the motion

Table 2.2: Carpal kinematics studies.

Study	Year	Method	Motions	Number of specimens	Bones involved
Youm [25]	1978	X-ray	Flex (45°), Ext (45°), Radial (20°), Ulnar (20°)	6	Carpal bones
Feipel [35]	1992	CT[1]	Neutral, radial (15°), ulnar (30°)	15	Carpal bones
Jackson [36]	1994	MTD [2]	Neutral, Flex and Ext varies from specimen	2	Scaphoid, lunate, capitate
Kobayashi [26]	1997	X-ray	Neutral, Flex (60°), Ext (60°), Radial (15°), Ulnar (30°)	22	Carpal bones
Wolfe [29]	1997	CT	Neutral, Flex (60°), Ext (60°)	10	Lunate, capitate
Ishikawa [37]	1997	MTD	Neutral, Flex (60°), Ext (30°), Radial (15°), Ulnar (30°)	5	Scaphoid, lunate, third metacarpal
Snel [30]	2000	CT	Neutral, Flex (60°), Ext (60°), Radial (30°), Ulnar (30°)	11	Carpal bones
Wolfe [38]	2000	CT	Neutral, Flex (30°, 60°), Ext (30°, 60°)	20	Scaphoid, lunate, capitate
Ferris [27]	2000	X-ray	Flex (60°), Extension (60°)	34	Lunate, capitate
Moojen [31]	2001	CT	Neutral, Flex (60°), Ext (60°), Radial (20°), Ulnar (20°)	11	Pisiform
Moojen [39]	2002	CT	Neutral, Flex (60°), Ext (60°), Radial (20°), Ulnar (20°)	11	Carpal bones
Moojen [40]	2002	CT	Neutral, Flex (60°), Ext (60°), Radial (20°), Ulnar (20°)	11	Scaphoid
Morimoto [41]	2003	MRI [3]	Neutral, Flex (70°), Ext (70°), Radial (30°), Ulnar (30°)	28	Triquetrum-hamate
Goto [42]	2005	MRI	Neutral, Flex (60°), Ext (60°), Radial (20°), Ulnar (30°)	12	Scaphoid, lunate, capitate
Kaufmann [32]	2005	CT	Radial (20°), Ulnar (30°)	8	Scaphoid, lunate, capitate
Kaufmann [43]	2006	CT	Flex (60°), Ext (60°)	8	Scaphoid, lunate, capitate
Pillaj [44]	2007	MRI	Active grasp	4	Radius, scaphoid, lunate
Moore [33]	2007	CT	Neutral, Flex (60°), Ext (60°), Radial (20°), Ulnar (40°)	30	Carpal bones
Fuomani [45]	2009	4D-RX [4]	Flex (40°), Ext (40°), Radial (15°), Ulnar (30°)	8	Carpal bones
Werner [46]	2011	MTD	Neutral, Flex (50°), Ext (30°), Radial (10°), Ulnar (20°)	37	Scaphoid, lunate
Kamal [34]	2012	CT	Hammering motion	6	Triquetrum-hamate
Fraysse [47]	2014	OTM [5]	Flex (15°), Ext(15°), Radial (20°), Ulnar (20°)	8	Scaphoid, lunate, capitate, triquetrum
Eschweiler [48]	2016	MTD	Flex (30°), Ext (30°), Radial (15°), Ulnar (20°)	8	Carpal bones

[1] CT - Computed Tomography
[2] MTD - Magnetic Tracking Device
[3] MRI - Magnetic Resonance Imaging
[4] 4D-RX - Four-dimensional rotational X-ray
[5] OTM - Optic Tracking Device

pattern of the scaphoid lunate and triquetrum before and after sectioning the scapholunate ligament. Alike as the optical tracking, the advantage of this method is the repeated of the motion and data accuracy; however, the weight of the attached instrumentation could interfere in the natural motion of the carpals.

2.2.1 Wrist motion theories

The challenge to consolidate a general carpal motion theory is to determine the relative contribution of carpal bones to the global wrist motion. Recent studies have demonstrated that the individual carpal motion is complex because the bone moves and rotates in different planes when moving; this limits the deduction of a single theory to describe motion patterns [9, 49, 50]. In general, the spectrum of carpal motions can be described with the two main carpal motion theories: row theory and column theory.

2.2.1.1 Row theory

In the row theory, the carpal kinematics is described as two rows of bones sliding one over other. In this theory, the proximal row comprises the scaphoid, lunate and triquetrum; while the distal row consists of hamate, capitate, trapezium and trapezoid. The bones in the distal row are tightly bound between each other and to the metacarpal which makes them move as a rigid unit [51, 52]. The bones in the proximal row, also known as the "intercalated segment", can move more loosely because of the lack of ligament attachment [53].

In terms of kinematics, each row contributes differently to the global wrist motion. During flexion and extension, the distal row dominates the motion by sliding over the proximal row at the midcarpal joint. During radial and ulnar deviation, the proximal row controls the motion by sliding over the radius at the radiocarpal joint as shown in Figure 2.8.

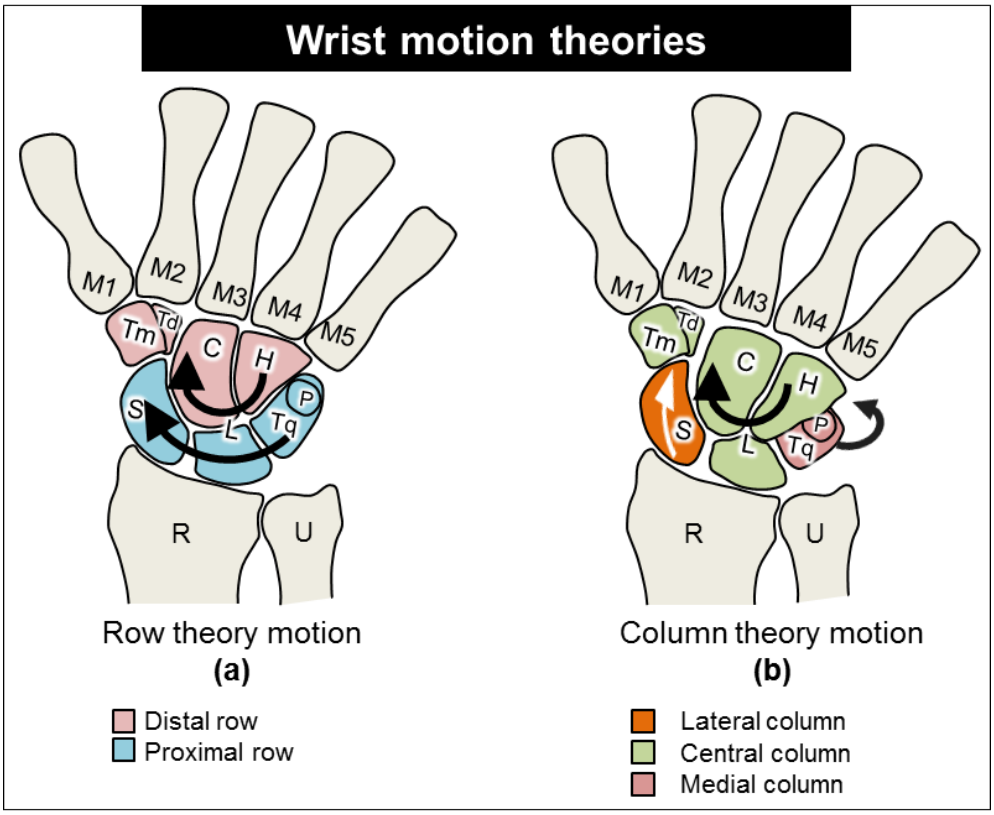

Figure 2.8: Carpal motion theories. a) Row theory b) Column theory

2.2.1.2 Column theory

In the column theory, the carpal kinematics is defined as two side columns rotating around a central column. The central column consists of the lunate, capitate, hamate, trapezium and trapezoid; the lateral column is the scaphoid and the medial column comprises of the triquetrum and pisiform, see Figure 2.8.

In terms of kinematics, the flexion and extension occur in the central column at the midcarpal and radiocarpal joint similar to the row theory. The significant change in kinematics occurs for the radial and ulnar deviation. During radial deviation, the scaphoid flexes (lateral column) to the palmar side to make space to the central column; identical in the opposite direction, the triquetrum moves to the dorsal side sliding over the hamate to make room for the central column during ulnar deviation [54] as shown in Figure 2.8.

To determine which of the theories is correct, Craigen *et al* [49] conducted research calculating the translation ratio of the scaphoid during radioulnar deviation in 52 subjects. The findings lead to the conclusion that there are wrists in which the scaphoid moves in a row pattern and others where the scaphoid behaves as a true column. The general conclusion is that there is a spectrum of motion from clear row type motion to clear column type motion.

Garcia-Elias *et al* [50] evaluated the relationship between the wrist laxity and the scaphoid motion during radioulnar deviation. Similar to Craigen, they calculated a scaphoid kinematic index in 60 subjects. The results confirmed the spectrum of carpal mechanics ranging from row to column. The findings were not conclusive to explain the relationship between the carpal kinematics and the wrist laxity. Galley *et al* [9] were able to relate the lunate bone morphology as a factor to determine kinematic behaviour.

2.2.2 Effect of lunate morphology on carpal kinematics

The lunate bone is positioned in the middle of the carpal bones, its influence on the carpal kinematics has been examined several times. The lunate can be classified into two types based on its shape by distinguishing the presence or absence of a facet at the distal region of the bone. Type I lunate has a single distal facet that interacts with the capitate as shown in Figure 2.9-(a); type II lunate has two distal facets, one articulates with the capitate and the other articulates with the hamate as shown in Figure 2.9-(b) [10].

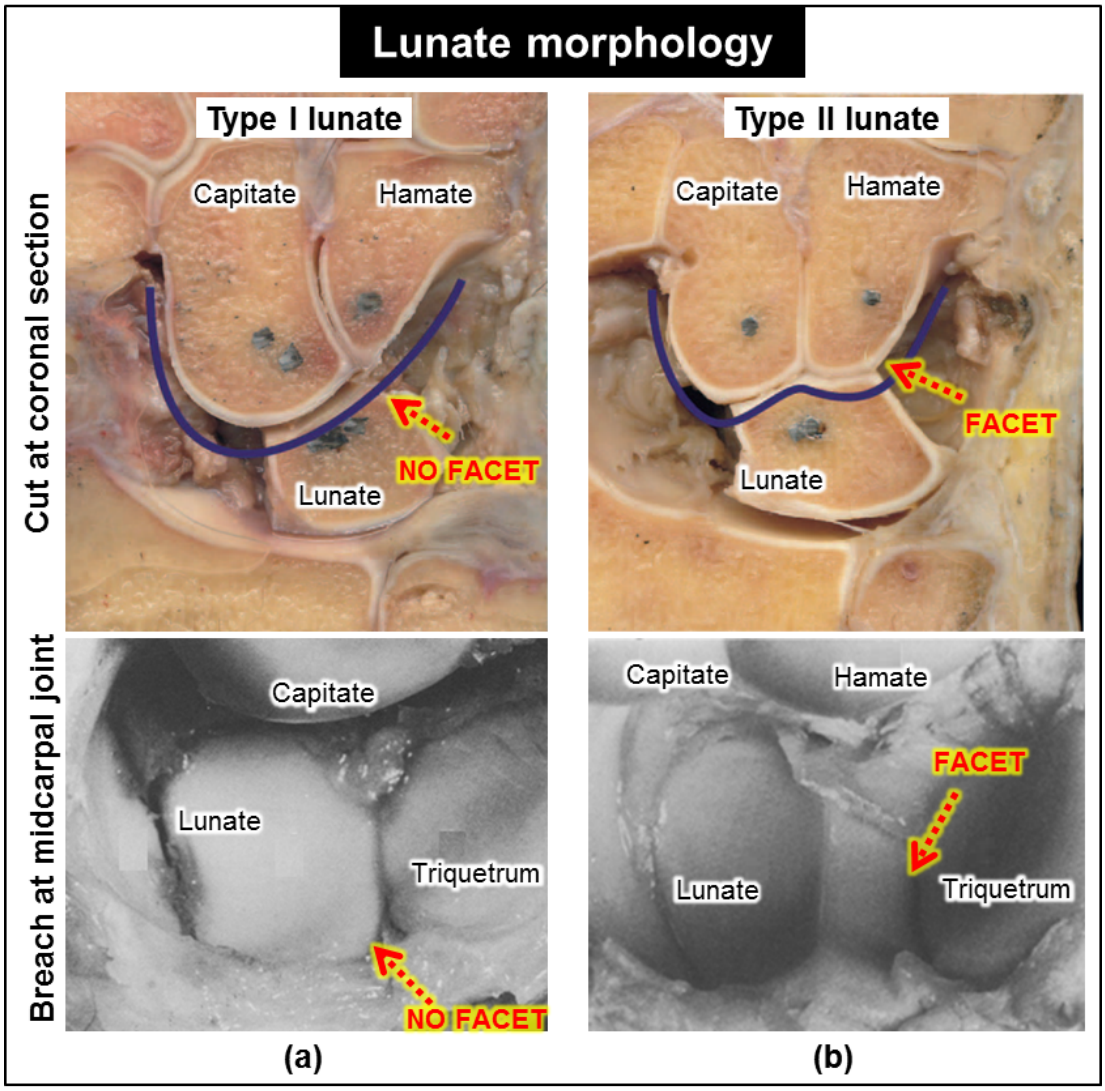

Figure 2.9: Lunate morphology. (a) Type I lunate no articulation between the lunate and hamate, no facet on the lunate (b) Type II lunate, showing the articulation between the lunate and hamate; an extra facet is visible on the lunate. Modified from McLean and Viegas [10, 55]

The size of extra facet in type II lunate is measured on an anteroposterior x-ray as capitate to triquetrum distance (C-T) measured at the most proximal region of the hamate [56]. The width of this facet is used to classify the lunate into type I and type II; however, the value varies among different studies ranging from $\leq 1-2mm$ for a type I lunate and $\geq 3-4mm$ to be considered a type II lunate as shown in Table 2.3.

In terms of the incidence, type II lunate is more frequent among individuals with an incidence ranging from 55% to 80%. Viegas *et al* [10] reported a proportion of 65.5% type II lunate in a study comprising 165 wrists; later, the same research group extended the population to 393 wrists reporting the type II lunate incidence of 73% [57]. In a similar study conducted by Galley *et al* [9], the lunate of 100 subjects was assessed, reporting an incidence of 63% for a type II lunate. Analogously, Kim *et al* [58] and Pang *et al* [59] reported an incidence of 68.6% and 70% for a type II lunate, respectively.

The categorisation into two types of lunate is seldom considered or mentioned in carpal studies and only recently has been included as a variable to associate to kinematics theories and pathologies.

Table 2.3: Incidence of the Lunate

Study	**Year**	**Method**	**Population**	**Type II lunate, incidence (%)**	**C-T distance, (mm)**
Viegas [60]	1990	Cadaver dissection	61	60.7	$2-6$
Viegas [10]	1990	Cadaver dissection	165	65.5	$1-6$
Burgess [61]	1990	Cadaver dissection	28	46.4	NR [2]
Viegas [57]	1993	Cadaver dissection	393	73	$1-6$
Sagerman [56]	1995	Cadaver dissection	81	56.8	$2-6$
Malik [62]	1999	MRI [1]	186	57.5	$1.2-12$
Aufauvre [63]	1999	Plain radiography	100	56	NR [2]
Nakamura [64]	2001	Cadaver dissection	170	71	$1-6$
Haase [65]	2007	Plain radiography	45	53.3	NR [2]
Galley [9]	2007	Flouroscopy	100	63	$4-8.9$
McLean [55]	2009	Cadaver dissection	13	63	$0.7-3.65$
Rhee [66]	2009	Radiograph	58	57	4
McLean [67]	2010	Plain radiography	96	83	4
Kim [58]	2015	Computed tomography	70	68.6	$1.2-4.7$
Pang [59]	2017	Radiograph and MRI	58	70	4

[1] Magnetic resonance imaging

[2] No reported

The lunate type classification has been linked to the carpal kinematics theories. Galley *et al* [9] associated the motion of the scaphoid to the lunate type in a study comprising one-hundred wrist. First, x-ray images were taken to classify the lunate bone into three groups: type I lunate group for the case where the C-T distance was $\leq 2mm$; type II lunate for bones with C-T distance $\geq 4mm$ and the third group for lunate ranging $2.1mm \leq$ C-T distance $\leq 4.0mm$. The incidence of type I, II and the third group was 18%, 19% and 63% respectively. The results showed that type I lunate show statistically greater scaphoid translation during radial deviation, while type II lunate has a greater scaphoid flexion in the same motion. In terms of the carpal kinematics theories, a type I lunate exhibits a row mechanics and a type II lunate a column mechanics. In regards to the mechanics, the results confirmed the finding obtained in previous studies [40, 49, 50, 68] but most important this research was linked to lunate morphology with the carpal kinematic theories.

Further validation regarding the effect of the lunate morphology on the carpal kinematics was corroborated in an *in vivo* study conducted by Bain *et al* [12]. In four wrists for each type of lunate the motion of the proximal carpal bones was tracked using bone pins and optical motion capture systems during flexion (15°), extension (15°), radial deviation (20°) and ulnar deviation (20°), [12]. The results reported distinctive carpal pattern motion for each type of wrist in respect of the relative contribution of the midcarpal and radiocarpal articulation. For a type I wrist, the motion at the radiocarpal joint is grater than a type II wrist during flexion and extension; similar to the row theory. In this study, there was no significant difference in motion between the two types of the wrist during radioulnar deviation. However, according to the results during radioulnar deviation, in the type II wrist, the central column becomes the dominant articulation considering that the capitate shows greater motion compare to the scaphoid and triquetrum; what it is expected in connection to the carpal column theory.

2.3 Scapholunate ligament

The SLIL is a strong ligament that connects the articulating surfaces of the scaphoid and lunate bones except at the distal edges, outlining a C shape as shown in Figure 2.10. Three anatomic regions are observed in the ligament: dorsal proximal and palmar (volar) [69]. The dorsal region is thick, composed of short, transversely oriented collagen fibres; the dorsal region is the strongest being the primary stabiliser resisting forces of up to $260N$. The volar region is thin and composes of obliquely oriented collagen fascicles, this region maintains the stability in terms of rotation stability and can resist forces of up to $118N$ [2, 5]. The proximal region is principally composed of fibrocartilage, with a few superficial longitudinally oriented collagen fibres. In terms of mechanical properties, the proximal region does not provide any significant laxity restraint and can resist forces up to $63N$ [2, 3, 5, 69].

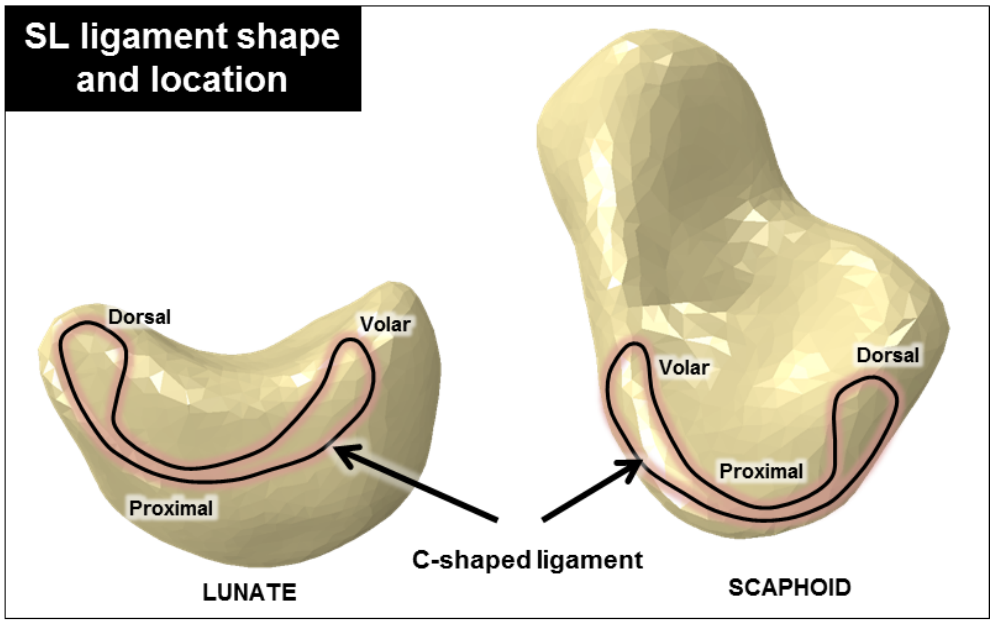

Figure 2.10: The scapholunate ligament.

2.3.1 Ligament injury

The SLIL is the most common injured carpal ligament. The SLIL tear is usually caused by a fall or by a sudden load on the wrist. The severity of the lesion can vary from a mild sprain to complete tear or bone fracture. The injury severity ranges from occult (asymptomatic), dynamic scapholunate dissociation (visible gap), and carpal collapse.

There is no registry reporting exclusively the scapholunate (SL) instability; however, approximately 5% of the cases of wrist sprains are associated with SL tear [3]. SL ligament rupture has been found in 36% of surgeries of distal radius fractures.

2.3.2 Diagnosis and treatment

Carpal instability is the end-result of a wrist ligament injury [1]. The protocol to diagnose SL dissociation consists in identifying malalignment of the bones on a PA and lateral x-ray after a significant wrist trauma. Carpal instability can be classified as static and dynamic. The instability is static when an SL gap $> 3mm$ is presented on neutral, static radiography during the physical examination as shown in Figure 2.11-a. Contrary to the static, in a dynamic instability, the abnormal carpal alignment can not be detected on the X-ray and it is only possible to visualise in stress and load radiographs after thorough physical examination exercises [70] as shown in Figure 2.11-b.

The diagnosis of the SLIL injury can be difficult; frequently, it takes months to years after the wrist trauma before the instability is detected on x-ray at clenched-fist ulnar deviation by detecting an SL gap $> 3mm$ and an SL angle of $> 60°$. To diagnose the instability, the radiological protocol is as follow:

1. On an anteroposterior view, signs of SL dissociation, the normal trapezoidal configuration of the scaphoid, may be lost and it may appear triangular, medical condition known as *"ring sign"*.

2. On the lateral view, a dorsal tilt of the lunate is typically shown: SL angle $> 60°$ and capitolunate angle $> 30°$.

If a malalignment is shown in the radiological evaluation, the severity of the injury should be assessed with an MRI or arthroscopy. Suture repair and pinning of the ligament can be done if the injury is partial and treated within four to six weeks after trauma.

A severe tear of the SL ligament is difficult to re-attach due to the retraction or shortness of the tissue after the injury; additionally, it is unreasonable considering that the ligament experiences large tension and torsion loads which reduce the success rate of end re-attachment. Ligament reconstruction is recommended to address these cases; as well as cases of old injuries with dynamic instability in the absence of arthritis.

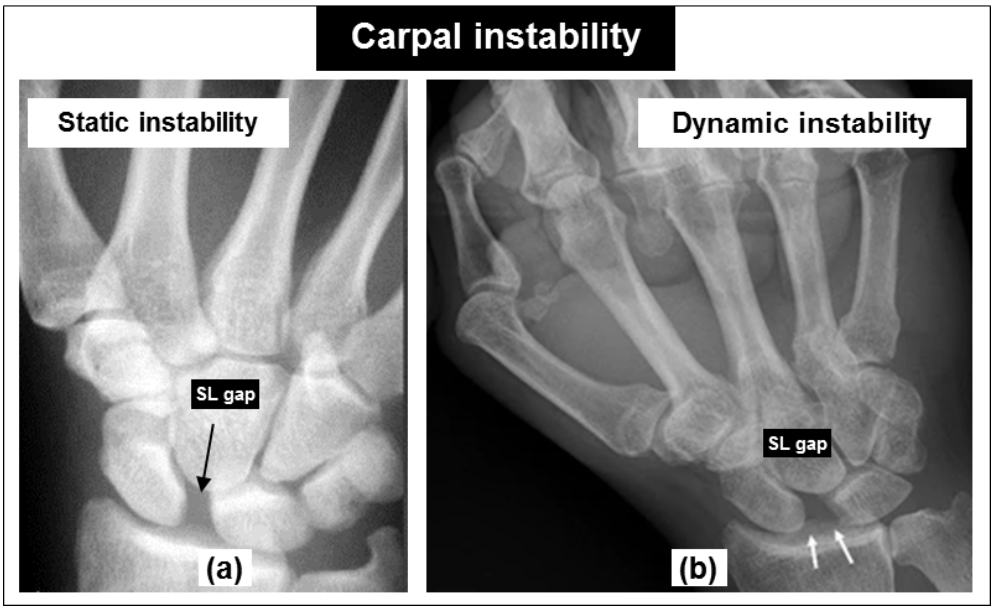

Figure 2.11: Carpal instabilities caused by SL injury. (a) Static scapholunate instability with a complete ligament injury, SL gap $\geq 5mm$. Modified from Moran-Hevia [71]. (b) Clenched pencil view in a dynamic instability with asymmetric widening, SL gap $\geq 8mm$. Modified from Kani [72].

Brunelli *et al* [73] suggested a reconstruction technique to correct the flexion of the scaphoid bone resulted from the lesion of the SL ligament. The technique uses a strip of the flexor carpi radialis (tendon) (FCR) that passes through a transverse hole drilled across the scaphoid and then anchored to the ulnar region of the distal radius as shown in Figure 2.12-a. Talwalkar *et al* [4] suggested a modified Brunelli technique (MBT). The modified technique uses a strip of the FCR that passes through a tunnel drilled from the palmar tuberosity to the dorsal point of insertion of the dorsal SL ligament in the scaphoid. The FCR strip is tightened to ensure that the scaphoid is reduced. After tensioning the FCR strip, the end is suture back on itself and onto the scaphoid using non-absorbable sutures as shown in Figure 2.12-b. Garcia-Elias *et al* [74] suggested the same technique known as *3-ligament tenodesis* or *3LT*. Different to the MBT, the 3LT attaches the FCR strip on the lunate before and after pulled it through the RLT.

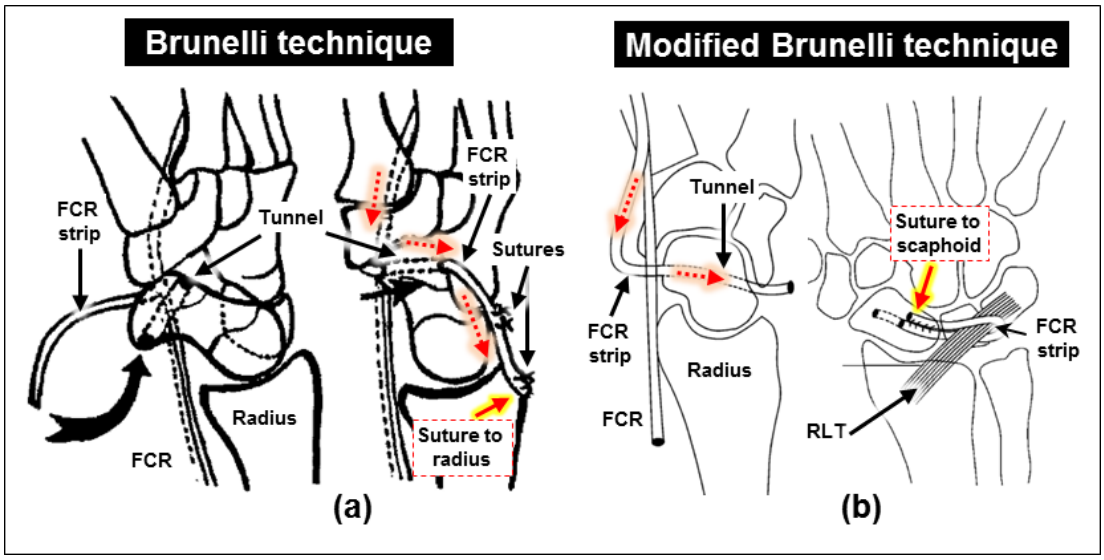

Figure 2.12: Brunelli and modified Brunelli techniques. (a) Brunelli surgical procedure (lateral view), FRC tendon slip is passed through a tunnel made in the distal pole of the scaphoid, the red-dotted line showing the direction of the tendon attachment. Modified from Brunelli [73]. (b) Modified Brunelli technique showing the FCR strip pulled through the distal pole of the scaphoid, then pulled under the radiolunotriquetral (RLT) ligament and sutured to itself. Modified from Talwalkar [4].

Corella *et al* [75] proposed a ligament reconstruction aiming to repair the dorsal and the volar region of the SLIL ligament. The technique consists of drilling a tunnel in both the scaphoid and the lunate. In the scaphoid, the tunnel goes from the palmar (volar) tubercle to the dorsal region at the portion of the scapholunate ligament. In the lunate, the tunnel is performed centred on the lunate, at the level of the dorsal portion of the scapholunate ligament. Once the tunnels are drilled, a portion of the FCR passes sequentially through the scaphoid and the lunate connecting both bones at dorsal and volar sides as shown in Figure 2.13

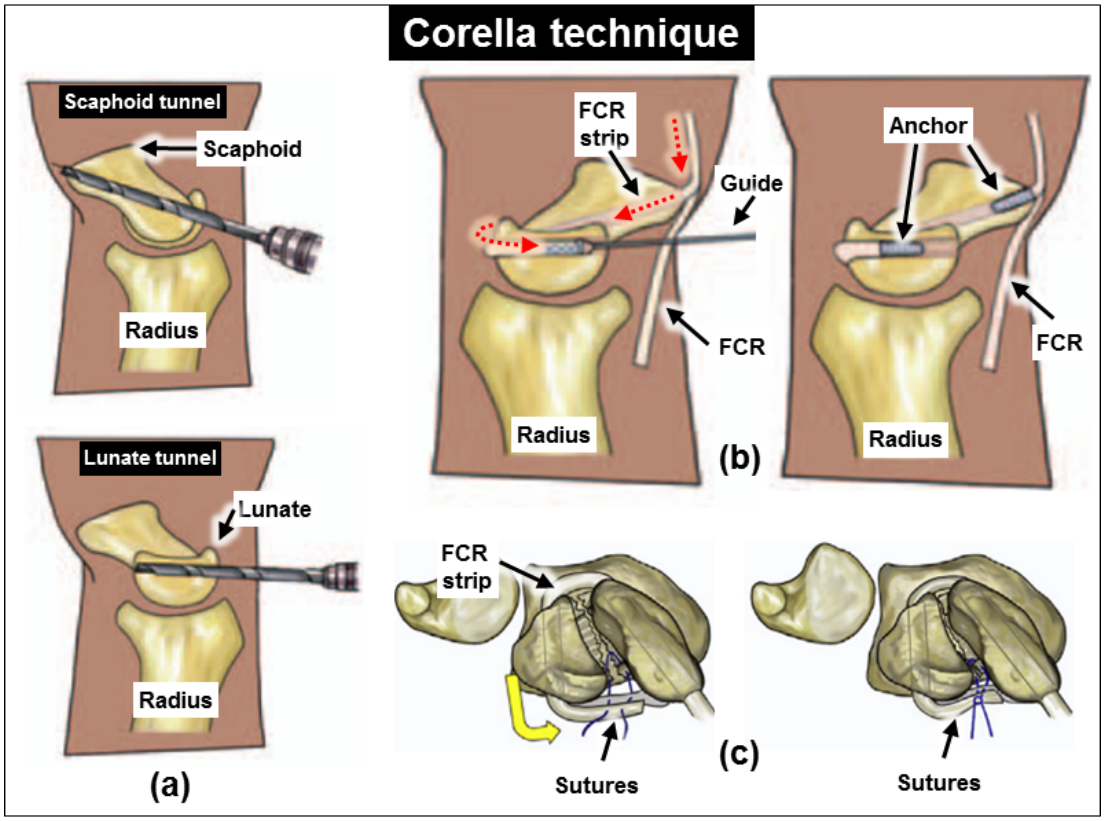

Figure 2.13: Corella reconstruction technique. (a) Drilling on the scaphoid and lunate bones . (b) Tendon strip through the bones, the red-dotted line showing the direction of the tendon attachment, the graft is anchored to the bones with the use of a screw. (c) Volar fixation preventing opening. Modified from Corella [5, 75].

Lee *et al* [6] proposed a different technique for the SLIL reconstruction known as the scapholunate axis method SLAM. This technique corrects the SL gap and SL angle by compressing centrally the lunate and the scaphoid from a lateral approach. The scaphoid and lunate are drilled on the lateral side along the coronal axis. The position of the tunnel is from the mid-lateral side of the scaphoid to the proximal ulnar corner of the lunate; the portion of the FCR is passed sequentially through the scaphoid and the lunate. Figure 2.14 shows the main stages of the procedure.

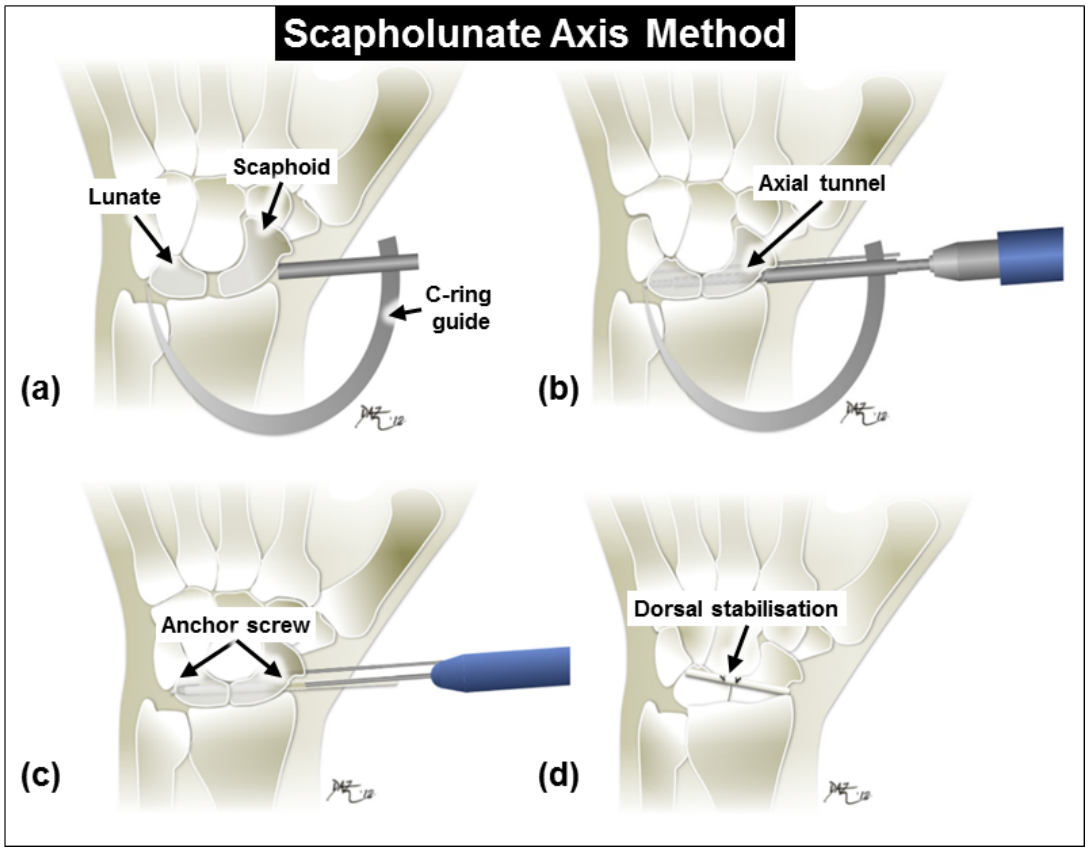

Figure 2.14: Scapholunate axis method (SLAM). (a) Placement of the reduction C-ring guide. (b) Drilling into the lunate and scaphoid in the same axis. (c) Placement of the interference screw into the scaphoid and lunate. (d) Final reconstruction with dorsal stabilisation of the remainder of the graft. Modified from Lee [6].

The outcomes from the application of the reconstruction techniques remain controversial. Post-operative records evaluate the success of the reconstruction by measuring the SL gap and SL angle. Although most of the techniques restore the scapholunate interval, follow-up studies report loss of range of motion and loss of grip strength [1].

Results from MBT report a range of motion reduction by 37% in flexion and 35% in extension compared with the contralateral side [4, 76, 77]. In a 6 months follow-up of the Corella technique in one patient, Corella *et al* [5] reported a reduction in the range of motion by 11% in extension and 22% in flexion after the surgical intervention. Yao *et al* [78] reported the results achieved with the use of the SLAM technique in 13 patients. In average, the mean postoperative wrist flexion and extension was 45 and 56 degrees, respectively.

The approach in which each reconstruction technique tethers the bones directly impacts in the restoration of the range in motion. Modified Brunelli Technique focuses on reconnecting the bones at the dorsal side which may produce an opening at the volar side. The Corella technique reconnects the bones at both dorsal and volar side which may limit the relative rotation between the bones. The SLAM method reconnects the bones at a mid-section between the dorsal and volar side with a dorsal reinforcement which may lead to a stiff articulation.

Abnormal carpal kinematics is deductible after the reconstruction of the ligament, but it has been scarcely investigated. Lee *et al* [6] report that the motion of the scaphoid is restricted after the reconstruction which may progress to fibrous nonunion or arthrosis.

The disparity in the post-surgery results is a consequence of the alteration of the carpal mechanics. For this reason, it is important to extend the evaluation to analyse the carpal mechanics and not only focus on the reduction of the SL gap.

2.4 Numerical modelling approaches in the study of the human wrist

This section includes a review of the application of the Finite element method (FEM) in the study the wrist joint. Similar to the extensively researched hip joint, most of the research on the wrist joint aims to determine the mechanical stress and the load distribution over the radiocarpal joint. Early investigation using FEM started in the mid-1990s in two-dimensional studies [79–81], to progressively become more complex studies in three dimensions, incorporating more instances such as bones and soft tissues. Figure 2.15 shows a timeline of the studies using finite element methods in the study of the human wrist.

The wrist joint is a challenge in biomechanical modelling due to the complexity of the multi interactions and constraints involved during the motion. Garcia-Elias *et al* [50], indicated that a stable joint provides three-dimensional equilibrium under external loading; hence, a reliable model has to be able to reproduce the mechanism that stabilises the joint throughout the whole range of motion. This implies that the model needs to be capable of maintaining the stability of the multi-bone system constrained by the ligaments and also be capable of distributes loads normally.

The technical approach of the finite element modelling depends on the complexity of the system; some joints can be model by a contact force transmission where the bone geometry maintains the joint stable, for example, the hip joint. For more complex joints where the stabilisation depends on ligaments and soft tissue, the best resolution is to include mechanical features simulating that constrain. In the case of Finite element (FE) modelling of the human wrist, the best option to achieve stabilization is the inclusion of spring elements to simulate the effect of the ligaments; this method is known as Rigid body spring modelling (RBSM). In the RBSM, the bones are assumed as rigid bodies interposed by springs simulating constraint ligaments.

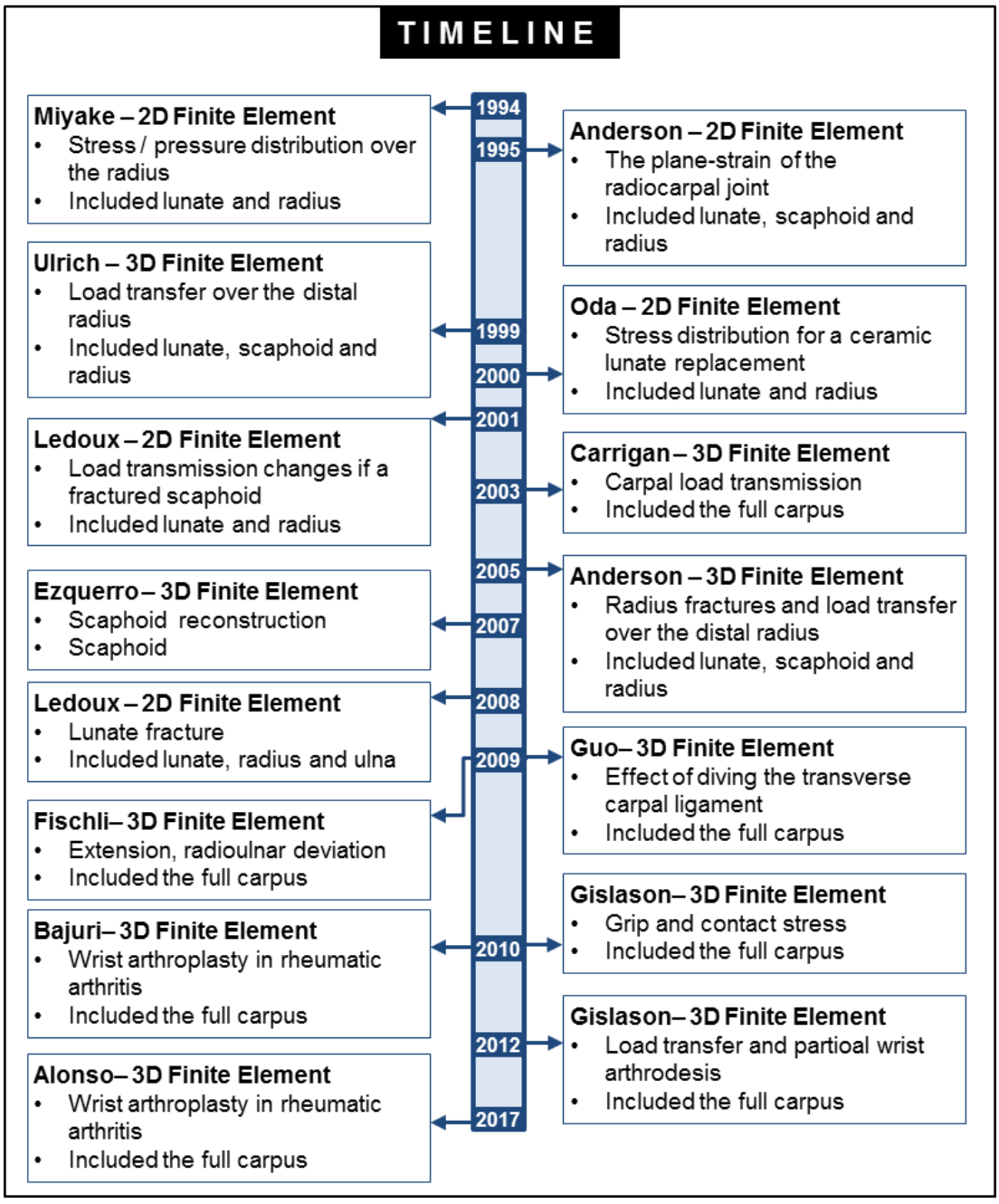

Figure 2.15: Timeline of finite element models on human wrist.

In 1995, Schuind *et al* [80] calculated the force transmission through the wrist using a numerical model based on the RBSM. In the model, the bones were considered as rigid bodies, the cartilages were modelled using compression linear springs, and the ligaments were modelled using tensile linear springs as shown in Figure 2.16. The results showed that 55% of the force was transmitted through the scaphoid/radius while 35% via lunate/radius and 10% over the TFCC on the ulna. Additionally, the carpal contact force distribution obtained using the numerical model (RBSM) at the radio-ulna region was compared to experimental measurements reported by Werner *et al* [82], Trumble *et al* [83] and Blevens *et al* [84] obtaining errors ranging from 9.0% to 12.5%. This was the first mathematical approach for wrist joint modelling.

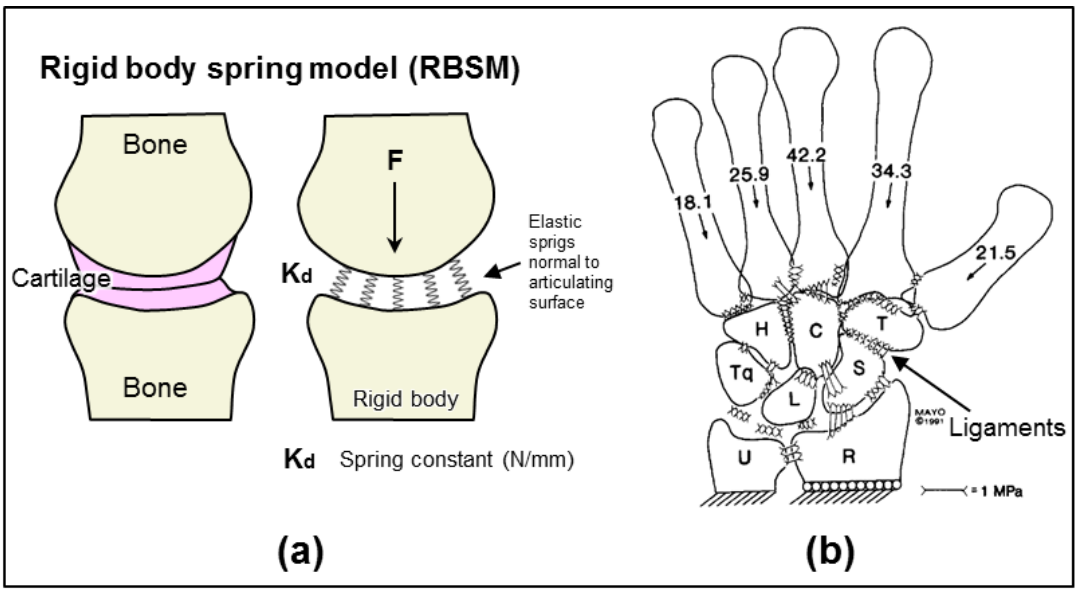

Figure 2.16: Rigid body spring modelling of the human wrist. (a) The general concept of the RBSM, the models are modelled as rigid bodies, cartilage as springs working in compression and ligigaments as springs working in only-tension. (b) Wrist model schematic diagram traced from the AP radiograph. Modified from Schuind [80].

Finite element modelling of the human wrist began with the work of Miyake *et al* [79], Anderson *et al* [81], and Oda *et al* [85] who investigated the stress distribution over the radius in a two-dimensional (2D) analysis. Miyake *et al* [79] evaluated the pressure distribution on a fractured and malunited distal radius. The 2D FE models were constructed from sliced cadaveric samples obtained at the central portion of the lunate/radius regions at sagittal and frontal view using a micro-cutting machine. A load was applied to the radius directed parallel to the lunate as shown in Figure 2.17-a. The computing was done using a general finite element program (MARC, Sun Micro Systems, Inc); the results of stress concentration were compared with values obtained with a pressure-sensitive film. This same research group calculated the stress distribution of a ceramic lunate implant used in the treatment for Kienböck's disease [85] using 2D FE analysis. The model for this second included six carpal bones, radius and ulna as shown in Figure 2.17-b.

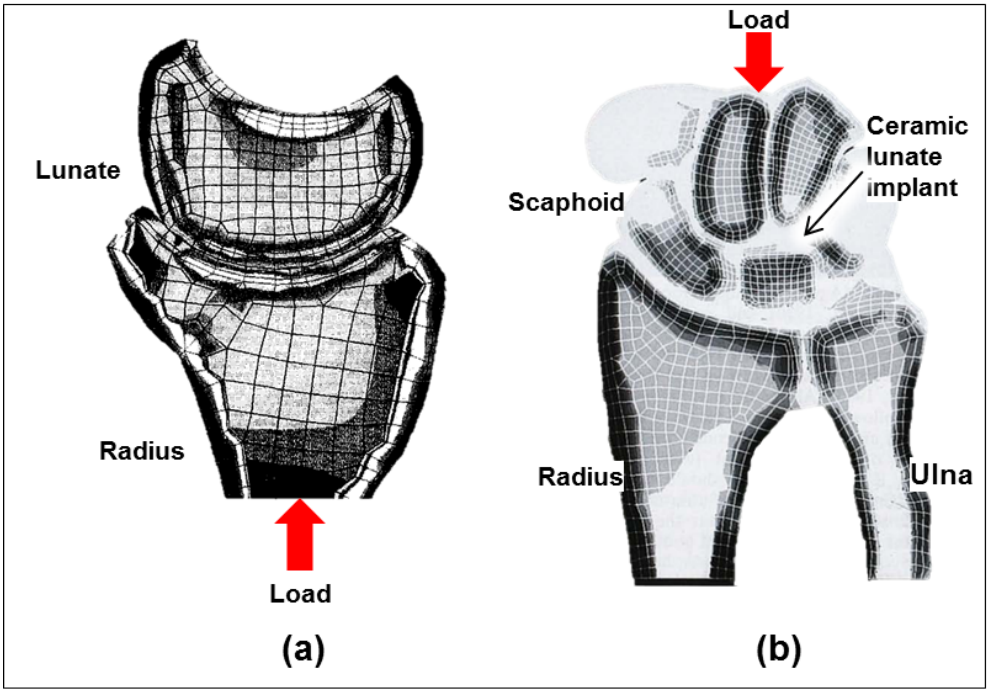

Figure 2.17: FE model of the radiocarpal joint developed by Miyake. (a) 2D FE model of the lunate/radius to calculate stresses on the lunate. Modified from Miyake [79] (b) 2D Finite element model for carpal wrist joint to calculate stresses on a ceramic lunate implant. Modified from Oda [85]

Anderson *et al* [81] investigated the mechanical relationship between the fracture of the distal radius and the onset of osteoarthritis by measuring a plane-strain on a finite element contact model of the radiocarpal joint. The model was constructed based on a scaled anatomic drawing. The radius was fully constrained at the proximal region, the effect of the ulna was modelled by integrating springs fixed to the ground on the lunate region as shown in Figure 2.18. Two loading scenarios were simulated with the model; in both cases, distributed pressures were applied along articular surfaces replicating a cadaveric experiment previously published by Horii *et al* [86]. The results calculated in the FE model were 6% larger in terms of Force transmission, 15% larger in terms of peak contact stress, whereas 64% lower for the ligament forces. The authors highlighted the necessity of developing a three-dimensional (3D) finite elements to obtain more accurate predictions.

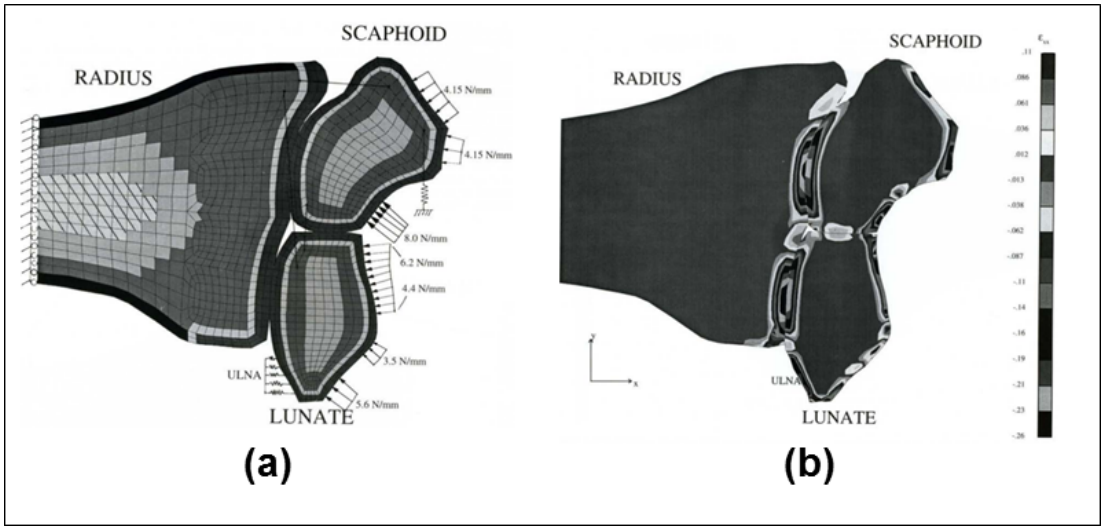

Figure 2.18: Contact-couple FE model of the radiocarpal joint developed by Anderson. (a) Setup of the Finite Element model, (b) Contour plot of axial strain in the articular cartilage layers. Modified from Anderson [81]

Ledoux *et al* published two papers using a 2D finite element model of the wrist. In 2001, this research group modelled the modifications to the mechanical behaviour of the wrist after the fracturing of the scaphoid [87]. The FE model was constructed using enlarged wrist X-ray, it includes the radius and ulna, six carpal bones (lunate, scaphoid, triquetrum, capitate hamate and trapezoid) and five metacarpals constrained by springs to simulate the ligaments as shown in Figure 2.19-(a). The analysis simulated six scenarios, one for the normal wrist and five of the most common scaphoid fractures. The results reported the changes in the pressure values at the radioscaphoid surface.

In 2008, this research group analysed Kienböck's disease [88]. The 2D FE model was a modification of the first model but including only lunate, radius and ulna with the correspondent ligaments as shown in Figure 2.19-(b). In this study, the mechanical properties of the lunate material were changed to determine the propagation of the fracture with the progressive collapse of the proximal lunate. The results reported a change in peak pressure values over the lunate.

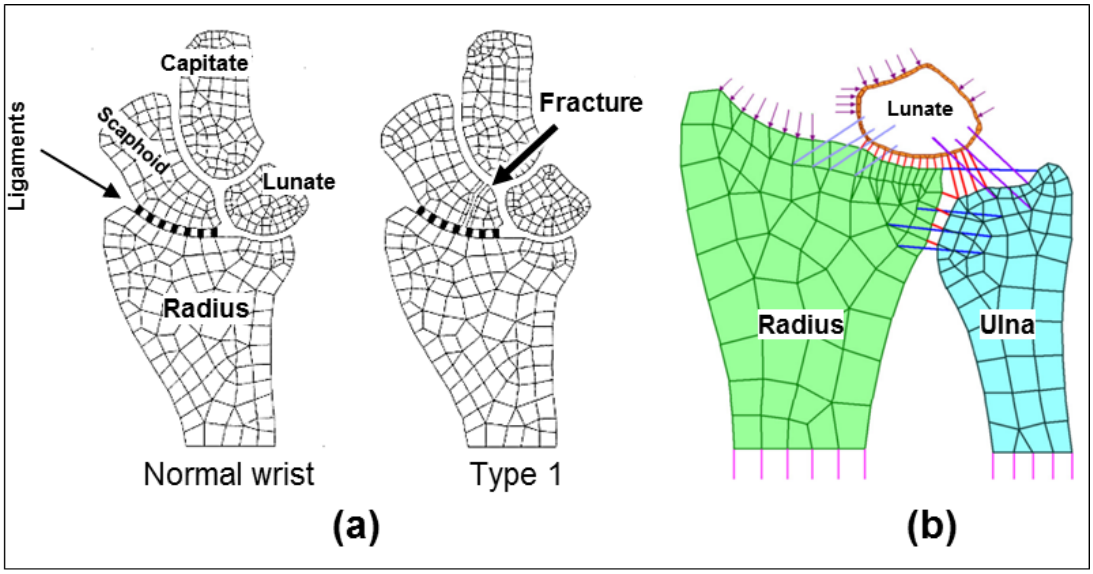

Figure 2.19: 2-D modelisation of the radiocarpal joint developed by Ledoux. (a) Modelling of the scaphoid fracture, (b) Modelling of the Kienböck's disease. Modified from Ledoux [87, 88]

3D FE models of the wrist started with the work of Ulrich *et al* in 1999 [89]. This research group modelled the distal end of the radius, the scaphoid and the lunate based on computed tomography. The FE model included a layer of articular cartilage with a constant thickness of $3mm$; however, the ligaments were not modelled as shown in Figure 2.20. The analysis consisted of the application of two loads on the scaphoid and lunate directed perpendicular to the articular surface of the radius. The loads varied to create four scenarios maintaining a total load of $1000N$ in all cases. The results reported the average strain energy density at eight regions on the radius. A comparison of the load distribution between the cases was included. The model was limited, however, the results helped to understand the Colle's and Chauffeur fractures mechanism.

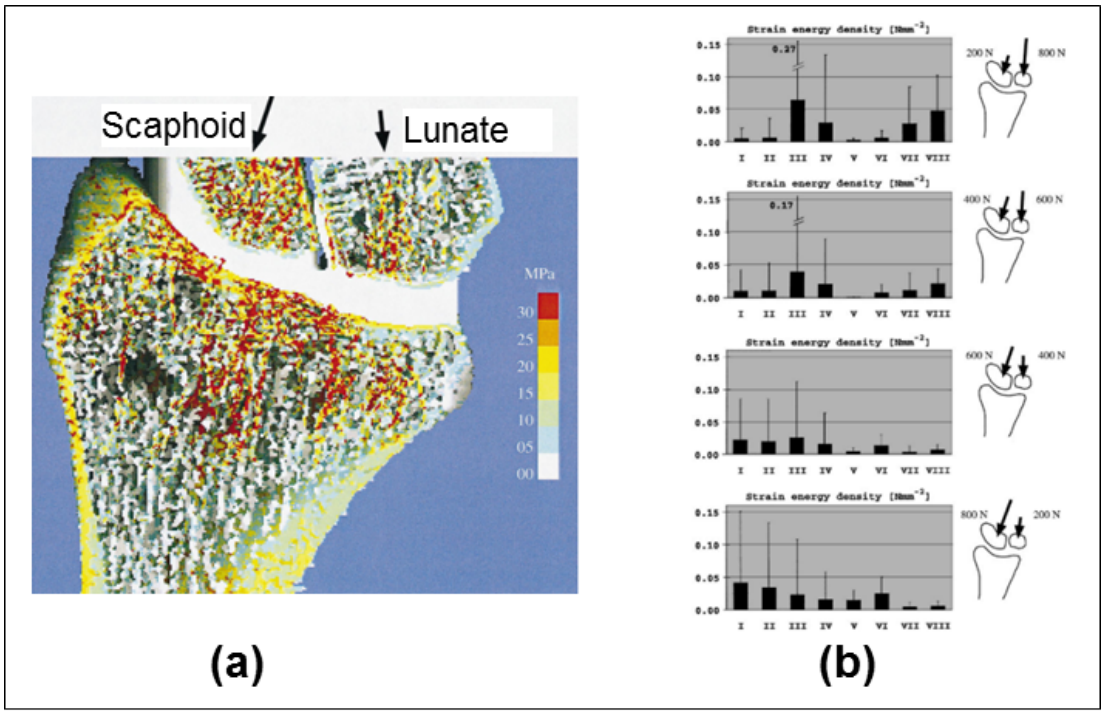

Figure 2.20: 3-D finite element model of radiocarpal joint by Ulrich. (a) 3-D model with load direction indicated. (b) Loading cases and results obtained from the simulation. Modified from Ulrich [89]

Carrigan *et al* [90] used a 3D FE model to inspect the carpal load transmission in a static neutral posture using ANSYS as the numerical solver. The model included bone, cartilage and ligaments, the ligament were model as a single

spring element working in tension-only as shown in Figure 2.21. A $15N$ axial compressive load was applied to the capitate to developed a series of parametric cases where all the carpal bones were constrained to move parallel to the applied load. The results include the contact pressure contours for the radio/scaphoid articulation, the peak values for the contact pressure and the principal compressive stress. The relevance of this study is that it was the first attempt to model the full carpus with a 3D model; however, the carpal bones were constrained to have only one degree of freedom to prevent the collapse of the carpus during the axial loading.

The limitation of taking this approach is the distortion in the obtained results. Restricting the motion of the bones to one degree of freedom forces the contact between the bones along the loading axis. This restriction also ignores the sliding effect of the bones towards other planes of motion. In conclusion, in this scenario, the loading transmission and the contact pressure does not represent the real case.

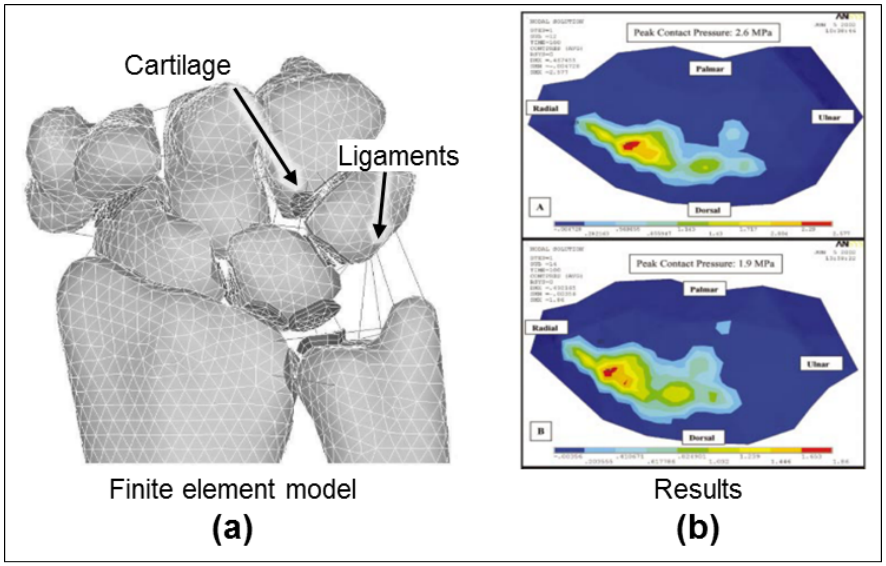

Figure 2.21: Finite element model of the wrist joint by Carrigan. (a) 3-D FE model. (b) Contact pressure contrours for the radioscaphoid articulation shown on the scaphoid cartilage surface. Modified from Carrigan [90]

Anderson *et al* [91] extended their investigation from a 2D model [81] to a 3D model in the analysis of radius fractures and the effect on post-traumatic osteoarthritis. To create the three-dimensional finite element contact model shown in Figure 2.22, a cadaver specimen was sliced sagittally in $0.5mm$ intervals with a microtome; then, each of the 144 tissue slices was photographed and digitised to create parametric bicubic surfaces in a post-processing method. The 3D model includes the cartilage (that can be seen in the photographs) and four ligaments modelled as a linear spring element. The effect of the ulna bone was modelled as an array of compressive spring attached from ground fixed nodes to the lunate. To determined the contact stress distribution over the radius, two loads were applied over the lunate and the scaphoid with a fixed radius. The results showed the maximum contact stress of $4.6MPa$ on the scaphoid fossa. In terms of load transmission, 53% through the scaphoid and 47% through the lunate.

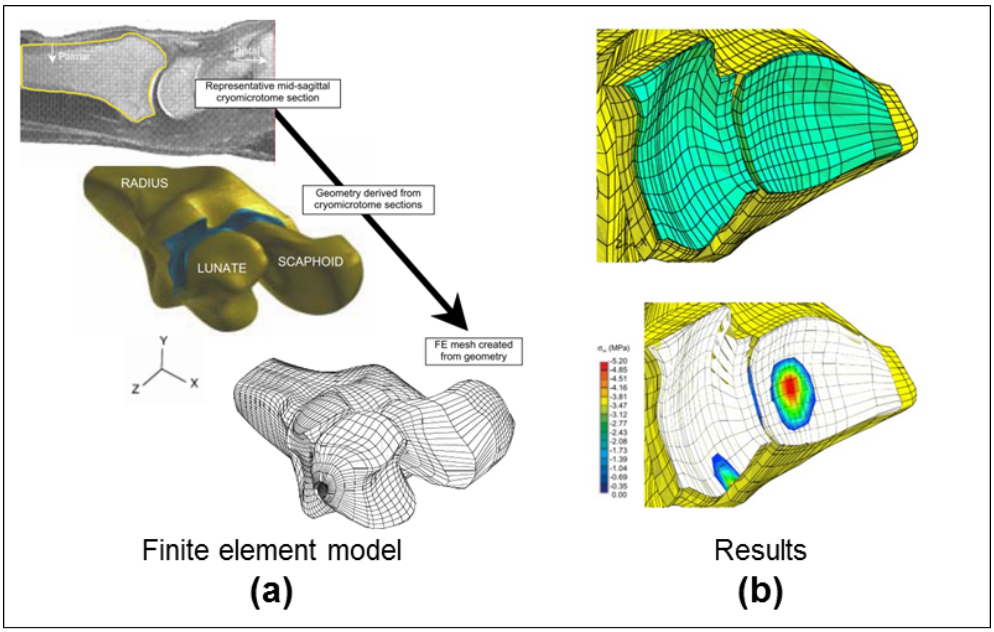

Figure 2.22: 3D FE model of the radiocarpal joint developed by Anderson. (a) Creation of the Finite Element model, (b) Contour plot of contact stress distribution on the radius. Modified from Anderson [91]

In 2009, Fischli *et al* [92] developed a 3D FE model of the full wrist from a CT scan to simulate three motions of the hand. The FE model is shown in Figure 2.23-(a). CT scans were taken in three positions: extension (57°), ulnar (45°) and radial deviation (15°); to achieve and maintain the position during the scan, a traction force was applied on five ligaments in the cadaveric samples. The articular cartilages were modelled as two surfaces offset from the bones (no solid cartilage), which were smoothed to allow free gliding. The ligaments were modelled using non-linear, tension-only spring elements, a single spring for each ligament. To simulate the positions in the FE model, a set of forces were applied to the bones following the lines of action of the ligaments. The results included the bones orientation at the end of each position, showing the overlapping between surfaces predicted by the FE models and the surfaces obtained from the CT images as shown in Figure 2.23-(b).

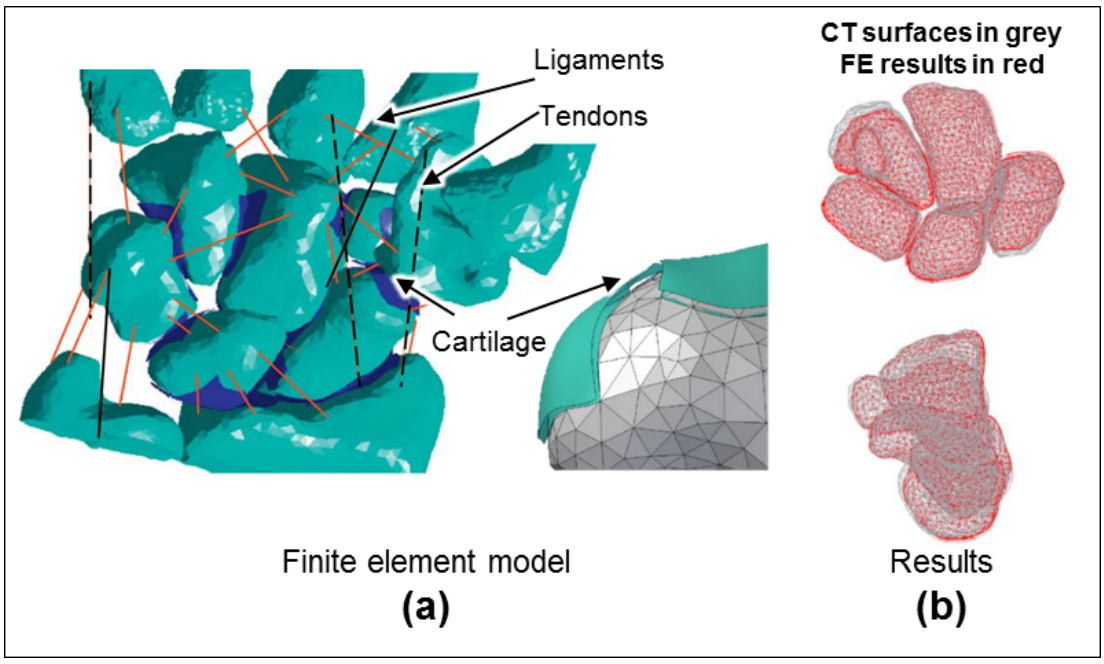

Figure 2.23: Rigid body spring model developed by Fischli. (a) FE model, note the offset surfaces that represents the cartilage layer. (b) Contour surfaces of the bone overlaid from CT scan and FE simulations. Modified from Fischli [92].

Guo *et al* [93] created a 3D model of the full wrist including the transverse carpal ligament as shown in Figure 2.24. The model was built from CT images, the major ligaments were modelled using non-linear, tension-only spring elements; the transverse carpal ligament (TCL) was modelled as a surface with a $1.5mm$ thickness connecting the scaphoid, trapezium, hamate and pisiform. The cartilage layers were built by offsetting the bones surfaces by $1.0mm$. The simulation consisted in applying a load of $100N$ on the second and third metacarpals ($50N$ each) to simulate the grasping of the hand in the neutral position in two scenarios; one with the intact TCL and a second without the TCL. The results reported the contact areas, contact stresses and force transmission between the radius and the proximal row and the axial displacement of the bones after removing the TCL.

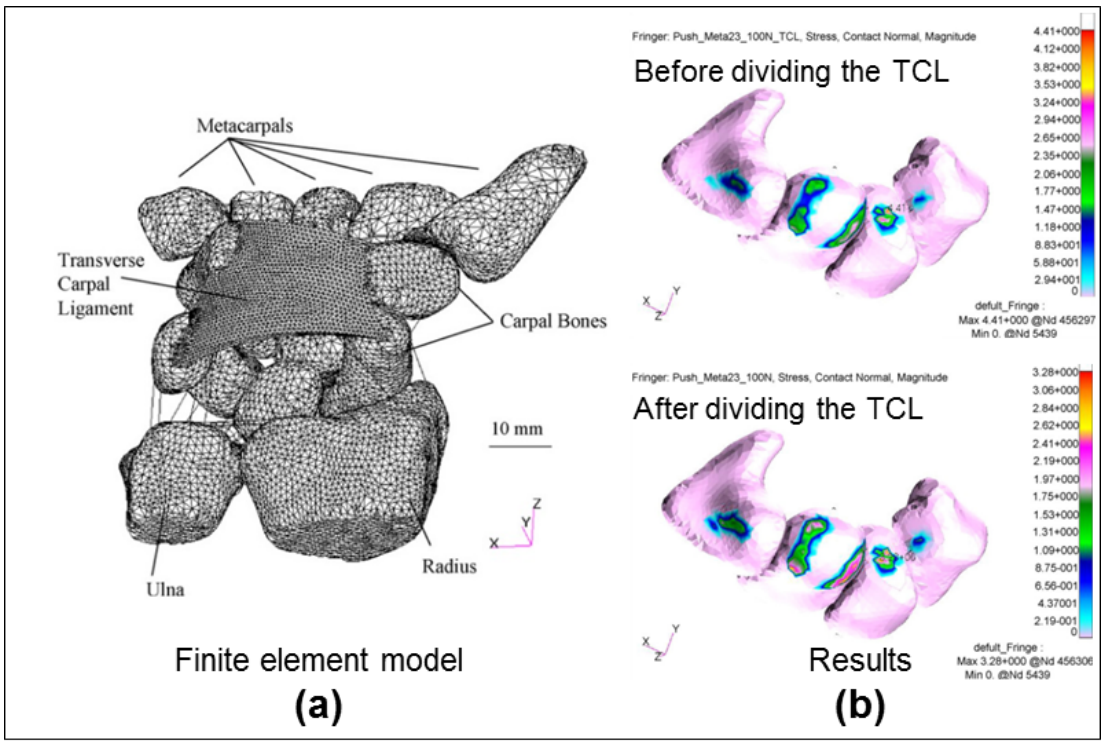

Figure 2.24: Finite element model developed by Guo. (a) FE model, (b) Stress distributions before and after dividing the TCL. Modified from Guo [93].

Gislason *et al* have worked intensively in the finite element modelling of the human wrist. Gislason FE models were constructed from MRI; the bones and the cartilage were segmented from the MRI images directly. The ligaments were modelled as non-linear, tension-only spring elements. In the first work simulating grip loading, a single element with distributed origin and insertion points on the nodes [94]; in the consecutive works the ligaments were modelled as an array of spring elements [95], and even the ligaments were modelled as surfaces but were later dismissed due to over-constraint of the joint [96]. This research group investigated the load distribution through the wrist during the gripping, the effects of partial wrist arthrodesis on carpal bone behaviour, total wrist arthroplasty and the load transmission in an implanted wrist as shown in Figure 2.25. The simulations were done in the neutral position only.

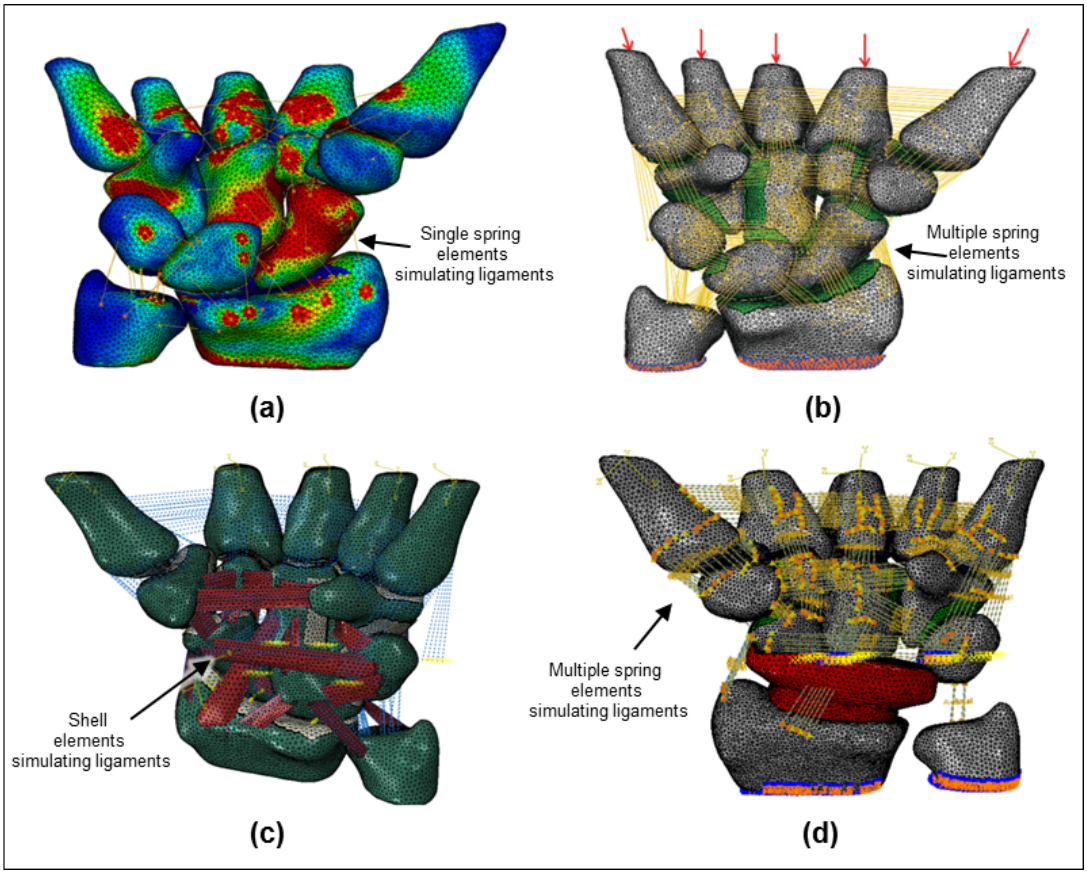

Figure 2.25: Finite element models developed by Gislason. (a) Simulation of grip loading. (b) Simulation of partial arthrodesis. (c) Over-constraint model. (d) Simulation of total wrist arthroplasty. Modified from Gislason [94, 95, 97].

Bajuri *et al* have worked largely in the FE analysis of the wrist. Their work comprises the simulation of wrist rheumatoid arthritis, partial fusions and wrist arthroplasty. The finite element models were created from CT images; the model includes solid cartilage layers and non-linear spring elements working in tension-only to simulate the ligaments. The study cases comprise cartilage destruction, loss of carpal height, dislocation of the carpus, dislocation of the scaphoid, hand scoliosis, bone erosion, wrist arthroplasty and total wrist arthroplasty procedure as shown in Figure 2.26. The pathological conditions were simulated based on assumptions found in clinical reports because of the limited information. All the analysis were done in the neutral position; in cases where the loading changes the position of the bones, the carpal motion is reported despite the simulation was not intended to inspect into other position but the neutral posture.

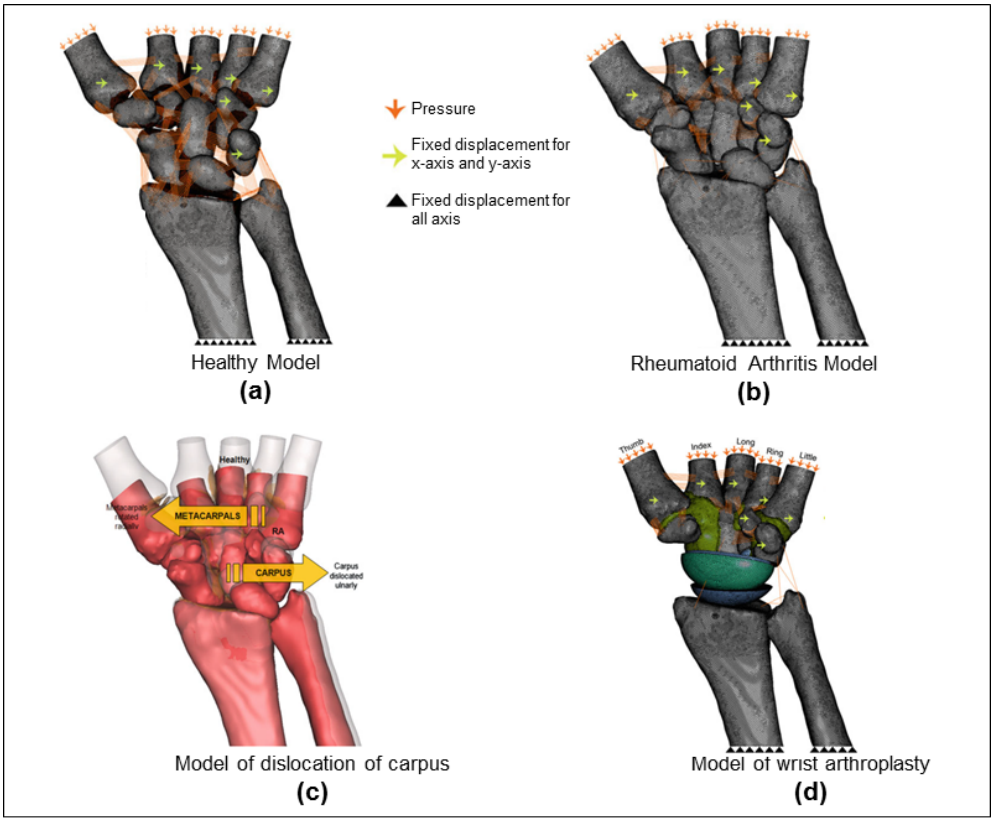

Figure 2.26: Finite element models developed by Bajuri. (a) Healthy wrist model. (b) Rheumatoid arthritis model. (c) Dislocation of carpus model. (d) Total wrist arthroplasty model. Modified from Bajuri [98].

Previous mentioned studies modelling the carpal bones, FE models have been also used to explored the performance of wires, implants and screws used in the carpal bones. Ezquerro *et al* [99] tested the influence of wire positioning upon the initial stability of scaphoid fractures fixation using Kirschner wire (K-wire). The FE constructed for the analysis comprised the scaphoid and a portion of the radius as shown in Figure 2.27-a; five configurations of the k-wires were simulated with the models; the reported results show the contact pressure distribution for each configuration. Grosland *et al* [100] evaluated the design of an ellipsoidal component proposed as a universal prosthesis for the radiocarpal joint in the treatment of total arthroplasty as illustrated in Figure 2.27-b. Varga *et al* [101] analysed the performance of two screws used in the fixation of the scaphoid fractures using a FE model shown in Figure 2.27-c.

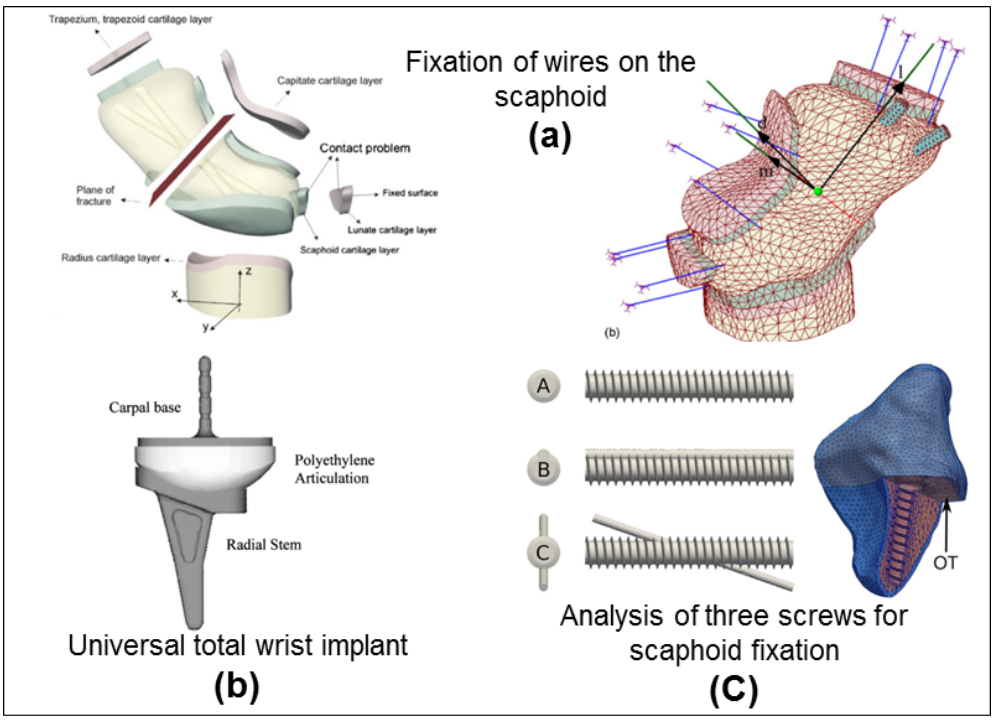

Figure 2.27: Finite element analysis of prostheses and fixation elements. a) Kirshner wires used for the fixation of the scaphoid. Modified from Grosland [100], b) Implant for the wrist joint arthroplasty. Modified from Ezquerro [99], c) Screw fixation for scaphoid fractures Modified from Varga [101].

2.5 Discussion

Several authors categorised the lunate bone into two main groups based on the distal region surface [9, 10, 41, 49]. Type I lunate has a single facet that articulates with the capitate, and type II lunate has and additional facet that articulates with the hamate. The size of the extra facet remains controversial because of the difficult access to measured it externally; however, a lunate can be classified into type II when the distance between the capitate and triquetrum is larger than $4mm$ [9, 10]. No registry of the incidence of lunate type is available but type II lunate has a prevalence of 63% to 73% according to references [49, 55, 57, 102].

The lunate categorisation is rarely considered in clinical studies or during the proposal of new carpal surgeries although the proven association with a variation of intercarpal ligaments and carpal kinematics [9, 27, 102]. The outcomes from the scapholunate ligament reconstruction surgery are diverse not only in comparison among techniques but also different between two patients under the same procedure [5, 6]. This can be related to the lunate categorisation but has not been yet studied.

Findings from cadaveric and in vivo studies using 2D images (x-rays) have related the carpal motion of wrists with a type I lunate to a row mechanics whereas wrist with a type II lunate to a column mechanics. More recently, have been some attempt to corroborate this finding using 3D data from MRI and CT scan images [28–34], the results supported in general the relationship between the type of lunate and the carpal kinematics but also initiated the discussion the complex 3D kinematics of carpal bones during the general wrist motion, which has not been widely studied.

For accurate reproduction of the *in-vivo* kinematics, it is crucial to implement the use of new approaches such as the finite element method. The use of FE models has been successfully used in the field of biomechanics. FE models can represent realistically an *in-vivo* situation if validated correctly. However, the development of a computational model able to reproduce carpal kinematics is challenging, due to its multi-body interactions and restrictions. The latest approach in computational biomechanics of the wrist is restricted to static or semi-static problems. Currently, studies using wrist FE models focuses on the analysis of contact between the carpal bones and force transmission in a static position [91, 94, 97, 98]. As far as the carpal kinematics is a concern, the finite element method has not been significantly applied.

The use of FE models in the evaluation of ligament reconstruction has advantages. The FE approach offers the use of the same computational framework to compare different techniques under the same conditions. In clinical trials and cadaver experiments, there is a biological variability that influences the results and can potentially lead to bias conclusions. The stiffness of the cadavers is the most important variable to consider in kinematics studies. In the next chapter, the construction of the FE model for a type II wrist is presented in detail from CT-scan images to the validation of the model.

Chapter 3

Finite Element Model

This chapter describes in detail the steps to develop a CT-scan based finite element model of the human wrist. The model was constructed from computed tomography data. The construction of the model started with the segmentation of the images to create volumetric surfaces for the eight carpal bones, radius, ulna and five metacarpals. The 3D geometries were imported into Abaqus 6.14 ® (Dassault Systemes, RI) to assemble the joint, to create the cartilage structures and incorporate the ligaments. After that, the material properties for each tissue involved were defined as well as the interactions and constraints. The FE model was employed to investigate the carpal kinematics for an intact ligament scenario; also was used as the base to further investigate the effect of the scapholunate ligament disruption. The FE model was modified accordingly to simulate ligament reconstruction techniques reported in Chapter 4, Chapter 5 and Chapter 6 of this thesis.

3.1 Background

The FEM is a numerical procedure used to obtain approximate solutions to complex engineering systems. The foundation of the FE method consists in the discretisation of a structure into a finite set of elements in order to simplify the solution of the system. The discrete counterparts are formed and connected by nodes that hold the elements together forming a grid known as "mesh" that

represents the physical shape of the structure under analysis. In order to solve the system, fundamental equations are defined at each node, then the equations are solved by a numerical method using polynomial functions for each of the finite elements, the solution for each element is then interpolated over the nodal domain that connects the elements, thus an approximated solution for the entire domains is obtained [103–105].

The power of the FE method is its versatility. Structures with arbitrary shape, arbitrary support and arbitrary loads can be analysed easier using FE methods than by approaching with classical analytical methods [103]. The practical use of this method started in the aircraft industry in the early 1950s to perform airframe and structural analysis. In the biomechanical field, in 1972, the stress caused by physiological loads was investigated on a human femur by Brekelmans [106]. With the introduction of more powerful computational resources more complex models have been developed [107].

The FE method is comprised of the following stages: pre-processing, processing and post-processing. The pre-processing stage covers the definition of the loads, boundary conditions, materials and the generation of the FE mesh by discretising the domain into small elements (finite element). In the processing stage is where all the numerical computing is done. In the post-processing stage, the results obtained for the nodes/element can be analysed as individual values in a point of interest or a set of nodes/elements can be represented graphically by plotting the results.

The basis to solve a finite element analysis is done by the Hookes Law:

$$F = kx \tag{3.1}$$

Where F is the force, k is the constant factor (stiffness) and x is the displacement [108].

The number of equations that the method must resolve depends on the size and type of elements forming the mesh, hence the number of nodes. For example, in a linear formulation, a C3D8R element is defined by 8 nodes; whereas in a quadratic formulation a C3D20R element is defined by 20 nodes. Each node has an associated displacement, the same number of equations as nodes in the model has to be created [108]. The resultant system of linear algebraic equations is expressed as:

$$[F] = [K][u] \tag{3.2}$$

Where $[F]$ is the force matrix, $[K]$ is the stiffness matrix and $[u]$ is the displacement matrix [108].

Once the displacements [u] are known, then the stresses and strains can be determined using Youngs modulus:

$$\sigma = E\varepsilon \tag{3.3}$$

Where E is Youngs modulus, σ is the stress and ε is the strain [108].

The finite element solver used in this research is Abaqus/standard 6.14 ® (Dassault Systems, RI, USA). This approach was selected for having the following characteristics:

1. Solves linear and non-linear problems. Such as non linearities occurring from material with non-linear behaviour, large displacements, and boundary non-linearities including contacts and friction between surfaces.

2. Material properties can be defined as linear or non-linear.

3. Considers the rate-dependent plasticity of the material.

Abaqus/Standard finite element software package determines approximate solutions to the equilibrium equations taking into account the relevant constitutive and geometric relationships[108].

3.2 Model geometry

The computed tomography (CT) scan images from the left wrist of a 59-years-old male with a type II wrist was used to construct the finite element model. A CT scan is an imaging procedure that uses combinations of sequential X-ray images taken from different angles to produce cross-sectional images of specific areas of a patient to see inside the body without cutting. The CT scan used in this thesis comprised from the distal end of the radius and ulna to the metacarpals. The type II lunate was confirmed following the criteria describe by Galley *et al* [9]; by measuring the distance between the capitate and the triquetrum is $6.5mm$ which is greater than $4mm$, characteristic to be considered type II lunate.

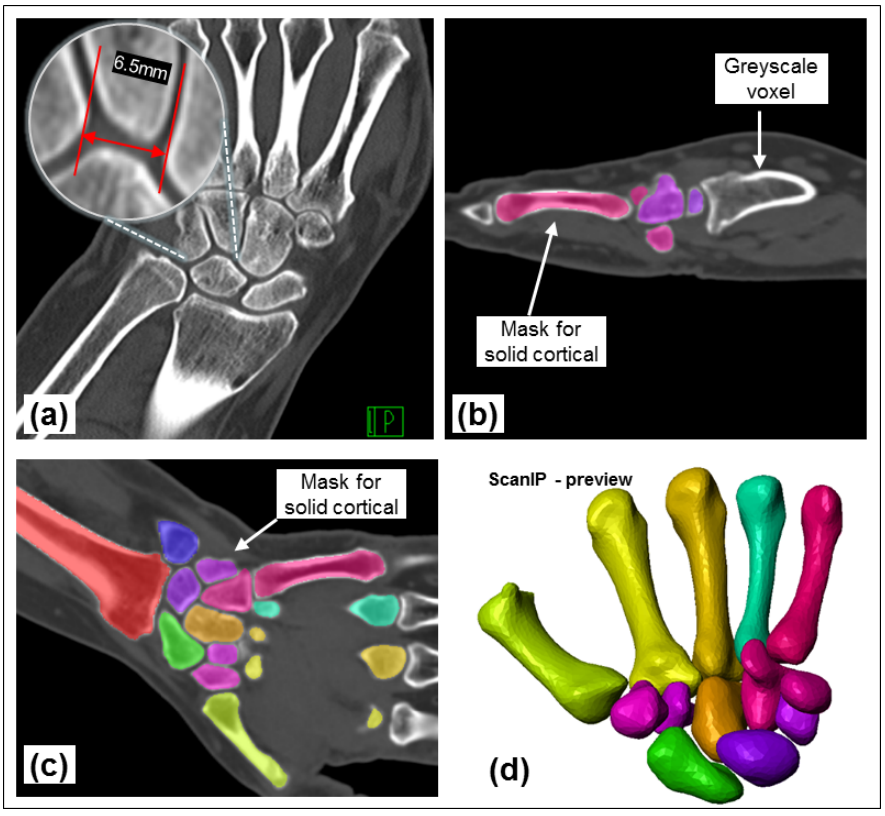

Figure 3.1: Segmentation process. (a) CT slide image showing the lunate facet, (b) Threshold and segmentation of greyscale voxel, (c) Masks for solid cortical bone, (d) ScanIP® 3D rendering surfaces.

The volume of images consisted of 232 slices with a thickness of $1mm$ and a transverse resolution of 512 x 512; the image stack was in the Digital Imaging and Communications in Medicine (DICOM) file format. The images were imported into ScanIP® (Simpleware Ltd., Exeter, UK) to build volume surfaces.

Masks were separately created for the cortical and trabecular sections of each bone using a semi-automatic method. A greyscale threshold was defined with a lower value of 115 and upper value of 255; then, the tool masked automatically the pixels within the range throughout all the slides as shown in Figure 3.1. Due to the short distance between the bones, a thorough visual inspection was done to assure that the borders of the bones were separated to avoid overlapping. The "Paint" tool was used to fill the spaces omitted by the threshold when necessary.

The cortical thickness was determined from the CT images and varied for each bone, being the average $2mm$. ScanIP ® creates a 3D triangular facet surface mesh based on the segmented images; once the masks were completed for each bone, morphological filters were applied to smooth the surfaces. Individual three-dimensional surfaces were exported separately as IGES file format, limiting the number of triangle elements to 5000 per part, to balance the surface quality, file size and computing time.

3.3 Assembly of the bone structures

The three-dimensional geometries (IGES files) were imported individually into Abaqus 6.14 ® as solid parts. An intermediate step in the assembly was necessary to consolidate the cortical and trabecular part of each of the carpal bones. First, the parts representing the cortical and trabecular bone were imported and overlapped in an assembly maintaining their original position and orientation; then, the trabecular bone (solid) was subtracted from the cortical bone (solid) to create a cortical shell. The new cortical shell and the trabecular part were merged into a new single solid part with two sections for the material assignment as shown in Figure 3.2. This intermediate step was done for each bone.

The bones were assembled within the "Assembly module" in Abaqus/CAE®. The full assembly was aligned to the Abaqus coordinate system. The axis formed from the long part of the radius to the third metacarpal was aligned to the Z-axis, the axis formed from the radial styloid to the ulnar styloid was aligned to the X-axis and the Y-axis directed from dorsal to the palmar side of the radius.

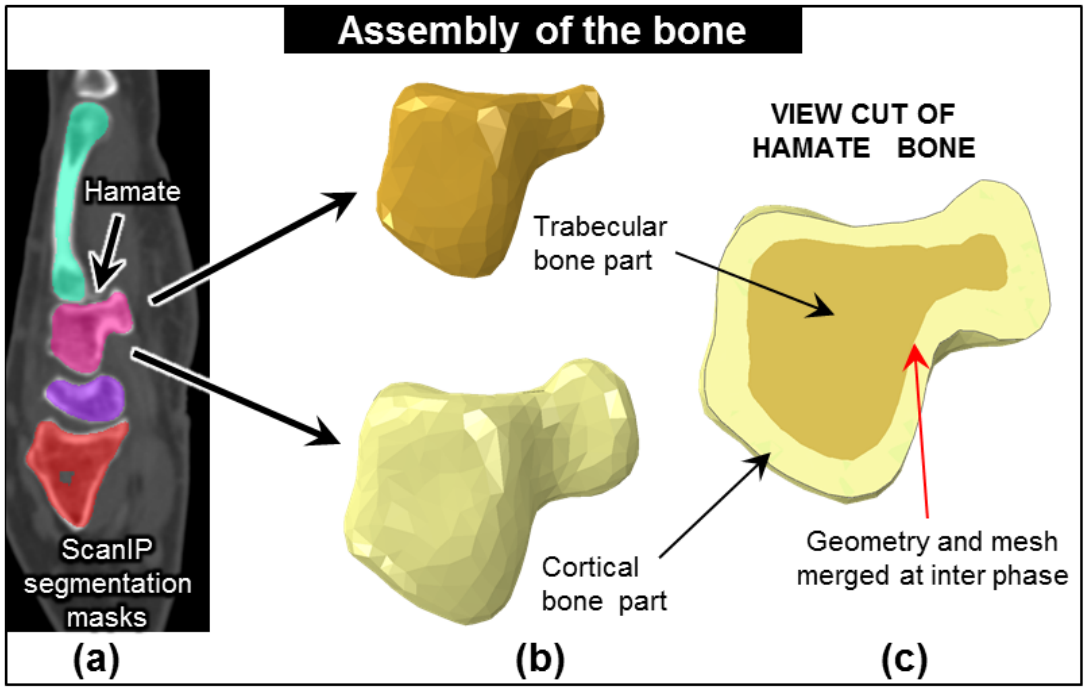

Figure 3.2: Assembly of the bones structures. (a) ScanIP processed segmentation masks,(b) Volume surfaces for the trabecular and cortical bones imported into Abaqus and then merge to form the bone with two sections,(c) View cut showing the two sections of the bones merged to form one solid bone. Shared nodes at the inter phase.

3.3.1 Cartilage structures construction

The geometry of the articular cartilage was not able to be acquired from the CT-scan data due to technical limitations. The process that CT-scan uses to record tissue types is based on the contrast resolution of materials under the beam of X-ray. The x-ray beam intensity needed to record bones is too high to

record also slender cartilages, and vice versa [109]. On the CT-scan images, the cartilage always appears superimposed to the bones structures which make it very difficult to identify. As an alternative to this, the cartilage geometry was constructed based on the geometry of the bones directly in Abaqus ®.

The gap between bones. In order to determine the cartilage thickness of each bone, the gap between the bones was measured using the *COPEN* variable in Abaqus ®. Surfaces over the bones were drawn at the potential articulation areas; a total of 27 pair were identified where the gap was measured as shown in Figure 3.3-(a).

The thickness of the cartilage. A simulation was set in Abaqus/CAE® with no load or motion applied. After running the job, the minimum value of opening (COPEN) was recorded for each interaction as illustrated in Figure 3.3-(b). In general, the thickness of the cartilages is half of the minimum gap value between the two interactive surfaces. However, when two or more articulating areas are very close to each other on the same facet, then only one cartilage is build covering both areas; the thickness value for this consolidated cartilage is the shorter gap of both interactions. To close the gap in the bigger clearance, the remnant of the value was assigned to the thickness of the other paired bone. The advantage of using this method is to give a smooth shape to the cartilage and soften the transition between cartilage and cartilage. Using this technique, the cartilage layers avoid abrupt changes in the sliding of the bones or disruption in the gliding of the surfaces.

Construction of the cartilage. Once the final pairs of articulations were defined and the thickness of cartilage reckoned, new surfaces were drawn over the cortical part of the bones. Cartilage layers were modelled with wedge elements (C3D6) by offsetting outwardly elements contained in the surfaces from the mesh by using the tool "Bottom-up mesh" in the "Mesh module" of Abaqus/CAE® as shown in Figure 3.3-(c). The thickness value for each cartilage was assigned accordingly to the previous calculations.

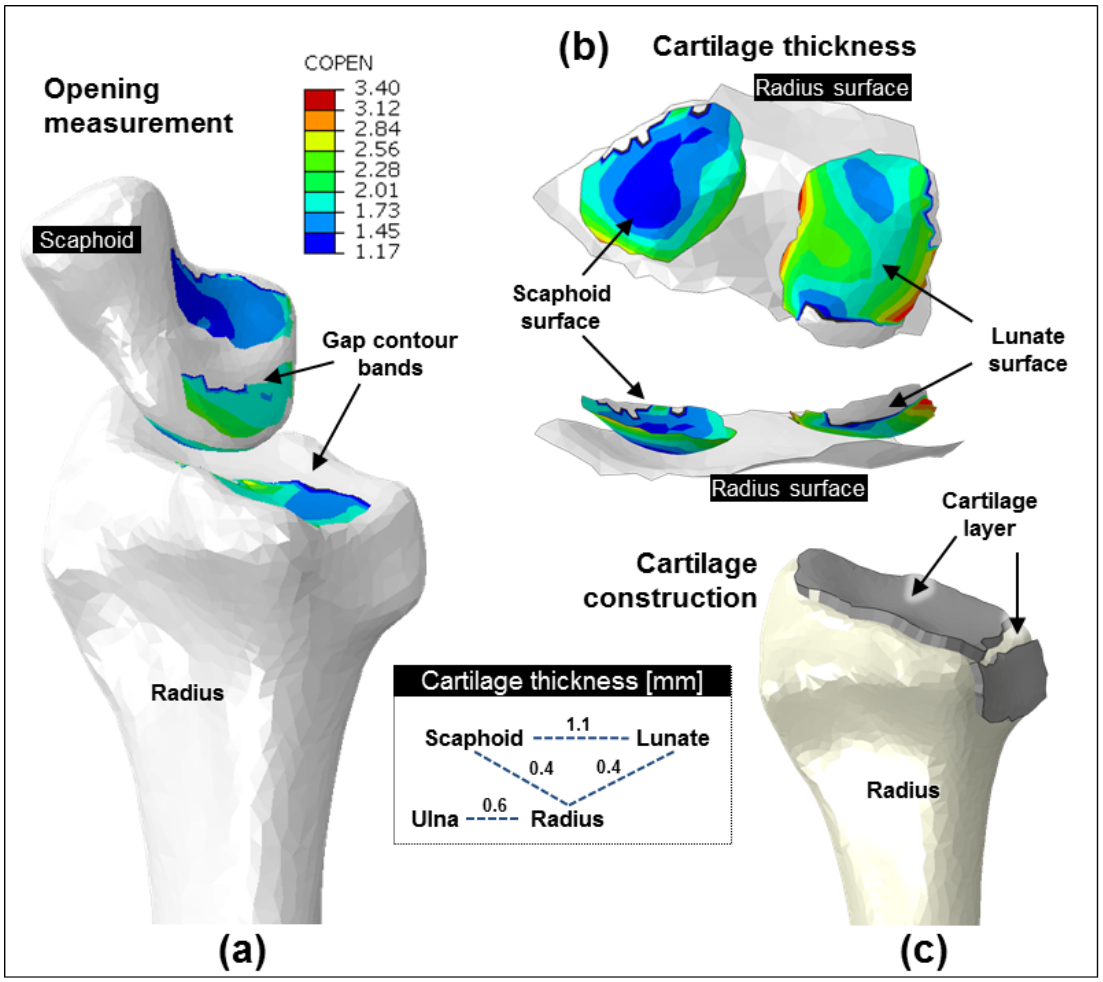

Figure 3.3: (a) Measurement of the gap between bones, (b) Calculation of the cartilage thickness, (c) Build and re-process of the cartilage structures.

Because the cartilage layer was built as mesh-dependant, post-processing steps were needed to generate a mesh-independent solid part. From the offsetting cartilage layer, a shell covering all the facets of the cartilage layer was constructed using a python script. The mesh elements were deleted to hollow out the shell; the solid was created from the shell in the "Part module" of Abaqus/CAE®. This process was necessary because mesh-dependant cartilage becomes invalid as soon as the mesh of the bone changes, being necessary to construct the cartilages every time the mesh changes; contrary to the mesh-independent solid part that can be re-mesh independently from the bone. The solid cartilage layer was merged to

the bone using "Boolean" operation in the "Assembly module" of Abaqus/CAE®. The adding of the articular cartilage makes the bone a three-sections solid part comprising trabecular bone, cortical bone and articular cartilage.

3.3.2 Ligaments

The modelling of ligaments was completed using spring and shell elements. The insertion points of the ligaments to the bones were located based on the anatomic studies, anatomic visualisation software, and then corroborated by medical staff. A type II wrist presents unique ligament connections between triquetrum, capitate and hamate bones [64]. Nakamura *et al* found three configurations of ligaments connecting triquetrum-capitate and triquetrum-hamate at the volar side as shown in Figure 3.4. The configuration is associated with the type of lunate thus the type of wrist. The FE model included this characteristic ligament connection because this influences the kinematics of the bones.

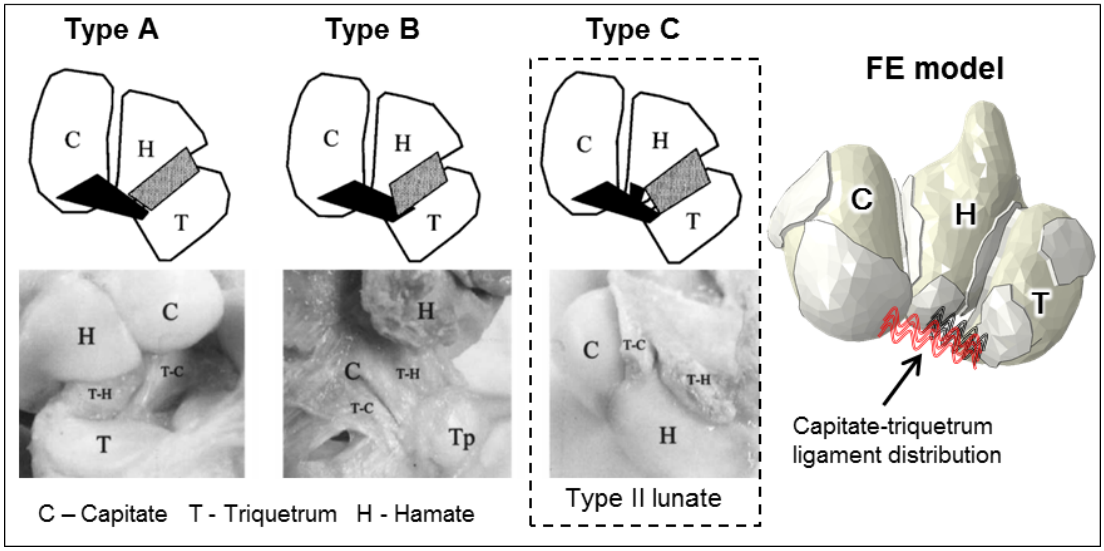

Figure 3.4: Relationship between the capitate and triquetrum ligament for different types of lunate bone morphology. Modified from Nakamura [64]

Thirty-one sets of ligaments were modelled using two-node spring elements. The ligaments were set to work in tension-only with non-linear behaviour. Each set of ligaments was modelled using multiple spring elements to distribute the force over the area to avoid stress concentrations.

Ligament stiffness values range from $10N/mm$ to $325N/mm$. Table 3.1 shows the stiffness values for all the ligaments included in the FE model. As described in Section 2.1.3, the mechanical behaviour of the ligament was modelled as non-linear. The setting of this behaviour in the FE model was achieved defining pairs of force-strain values (f, Δu) as indicated in the Abaqus user's guide.

Three pair of points were calculated to define the force-strain curve shown in Figure 3.5. The pair of values were calculated at 3%ε and 20%ε that are the initial and final part of the linear region, respectively.

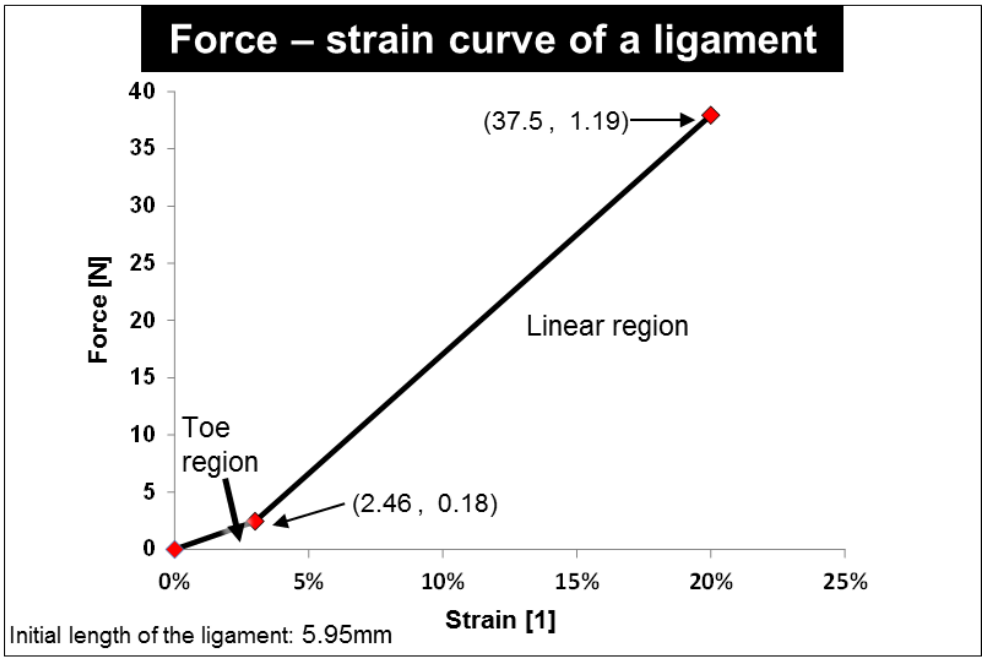

Figure 3.5: Example of a force-strain curve for the dorsal region of the scapholunate ligament. Curve developed from a stiffness value (k) of $37.5N/mm$; showing pair of values calculated for the Abaqus solver.

The strain value was determined based on the initial length of the

spring-ligaments. The strain was calculated as $\varepsilon = \frac{l-l_0}{l_0}$; where l is the momentary length of the ligament during the motion. The initial length l_0 of the spring was measured directly in the FE model in the neutral position, defined by the distance between the two elements connection. Considering that each ligament was modelled as a collection of spring elements, the initial length was assumed as the average length of the collection.

The magnitude of the force at $3\%\varepsilon$ and $20\%\varepsilon$ was calculated using the linear stiffness value of the ligament, shown in Table 3.1. At $3\%\varepsilon$ the stiffness was assumed to be 10% of the linear stiffness value which is similar to studies modelling the "toe region" [21, 90, 92, 97, 110].

The values defining the non-linear mechanical behaviour of the spring-ligaments were calculated at:

1. The $non-tension$ region $F(u_{@l<l_0})$
2. The starting region $F(u_{@l_0})$
3. The *toe region* $F(u_{@3\%\varepsilon})$
4. The yield point $F(u_{@20\%\varepsilon})$

Definition of non-linear behaviour is not supported in the graphical interface of Abaqus/CAE thus the input file (*.inp*) was modified manually for each simulation run.

Three shell-ligaments were included to simulate the wrapping effect of the intercarpal and radiocarpal ligaments. The insertion points and the trajectories of the shell-ligaments were based on the anatomical description and corroborated by the medical staff. The shells were built within Abaqus by defining closed-loop wires that allow the creation of shell surfaces. The mechanical behaviour of the shell elements was defined with the stress-strain relationship and corresponding cross-sectional area based on the stiffness reported in the literature, as shown in

Table 3.1: Ligaments stiffness of ligaments included in the FE model

Ligament	**Stiffness** $[N/mm]$	**Ligament**	**Stiffness** $[N/mm]$
Dorsal radiocarpal	27 [1]	Volar trapeziotrapezoid	110 [1]
Radial collateral	10 [1]	Volar scaphotrapezial	150[1]
Ulnar collateral	100 [1]	Volar scaphotrapezoidal	150
Radioulnar	50 [1]	Volar scaphocapitate	40 [1]
Radioscaphocapitate	50 [1]	Volar capitotrapezoid	80 [2]
Long radiolunate	75 [1]	Volar capitohamate	210 [2]
Short radiolunate	75 [1]	Volar triquetrocapitate	40 [1]
Ulnolunate	40 [1]	Volar triquetrohamate	300 [1]
Ulnotriquetral	40 [1]	Scapholunate Dorsal	60 [3,4]
Radioulnar	50 [1]	Scapholunate Volar	30 [3,4]
Dorsal intercarpal	128 [1]	Scapholunate Proximal	15 [3,4]
Dorsal trapeziotrapezoid	110 [1]	Lunotriquetral Volar	250 [2]
Dorsal capitotrapezoid	300 [1]	Trapeziotrapezoid	110 [2]
Dorsal capitohamate	325 [1]	Capitotrapezoid	300[1]
Dorsal triquetrohamate	300 [1]	Capitohamate	325 [1]
Dorsal lunatecapitate	150 [1]		
Dorsal lunatehamate	150 [1]		
Dorsal scaphocapitate	150 [1]		

[1] Stiffness value from Bajuri *et al* [110]

[2] Stiffness value from Fischli *et al* [92]

[3] Stiffness value from Berger *et al* [111]

[4] Stiffness value from Savelber *et al* [21]

Table 3.1.

The inclusion of the shell-ligaments was important to prevent the collapse of the joint after the removal of the scapholunate ligament. The wrapping effect of the shells generates a passive contact force on the proximal bones that keep the interaction of the bones. However, including shell ligaments increases computing time and leads to converging problems due to the over-constrain of elements.

3.4 Material properties

Material properties were assigned to the different sections of the bone. Properties for cortical and trabecular bone were assumed to have linear and elastic isotropic behaviour, with values taken from the literature [93, 97, 110]. Table 3.2 contains the material properties for the bone sections and cartilage used in the FE model.

Table 3.2: Material properties

Material	**Young's modulus [MPa]**	**Poisson's ratio [ν]**
Cortical bone	$18,000$	0.2
Trabecular bone	100	0.25

The articular cartilage tissue was defined as isotropic, hyperelastic material. From the literature [97, 110], the Poisson's ratio is 0.45. The numerical approach in Abaqus was the use of the Mooney-Rivlin polynomial strain energy function, shown in equation 2.4.

$$U = C_{10}(I_1 - 3) + C_{01}(I^2 - 3)^2 + \frac{1}{D^1}(J_{el} - 1)^2 \tag{3.4}$$

Where C10=4.1MPa, C01=0.41MPa, D1=0.002225 are material constants for the cartilages obtained from literature [97, 110].

The MooneyRivlin formulation was selected because reproduces better the hyperelastic behaviour of the cartilage compared to other numerical formulations [112–114]. The figure shows the characteristic stress-strain graph for the articular cartilage modelled using the Mooney-Rivlin formulation.

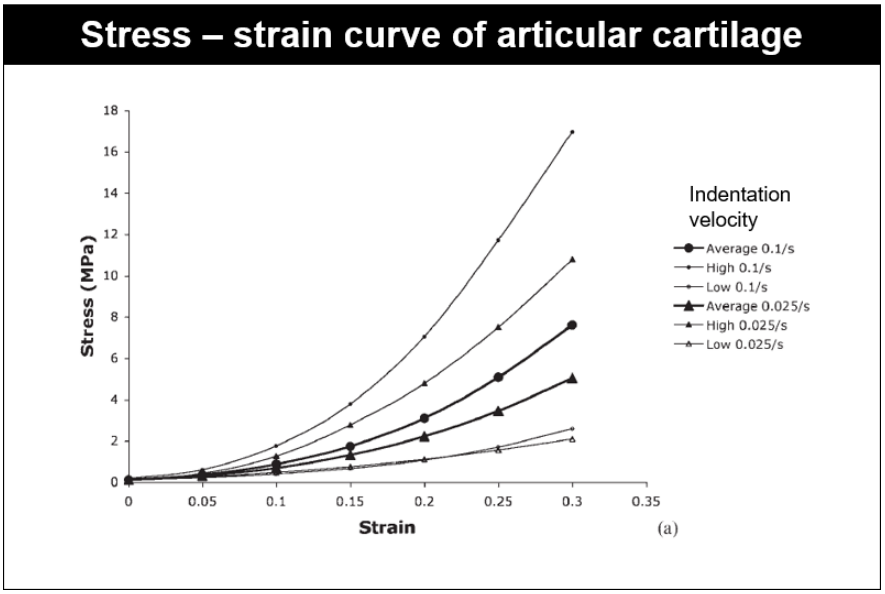

Figure 3.6: The stressstrain characteristics for a healthy cartilage. Taken from [112]

3.5 Interactions

The completion of the assembly was achieved by defining interaction properties between bones. Hard contact between interacting surfaces was defined to avoid penetration of element/nodes. Surface-to-surface contact was defined at the articular cartilage with a friction coefficient of 0.002 to allow free slide. The low friction value was established to avoid the use of a penalty contact with the solving of convergence problems. According to literature, the articulation between distal bones and the metacarpal has a litter or no movement thus the bones were bounded using a contact-tie formulation.

The interaction between shell-ligaments and bones was defined as frictionless. The surface-to-surface contact was defined between the inner surfaces of the shell-ligaments and the outer surface of the bones. Hard contact was defined to avoid penetration of element/nodes. The final assembly is shown in Figure 3.7

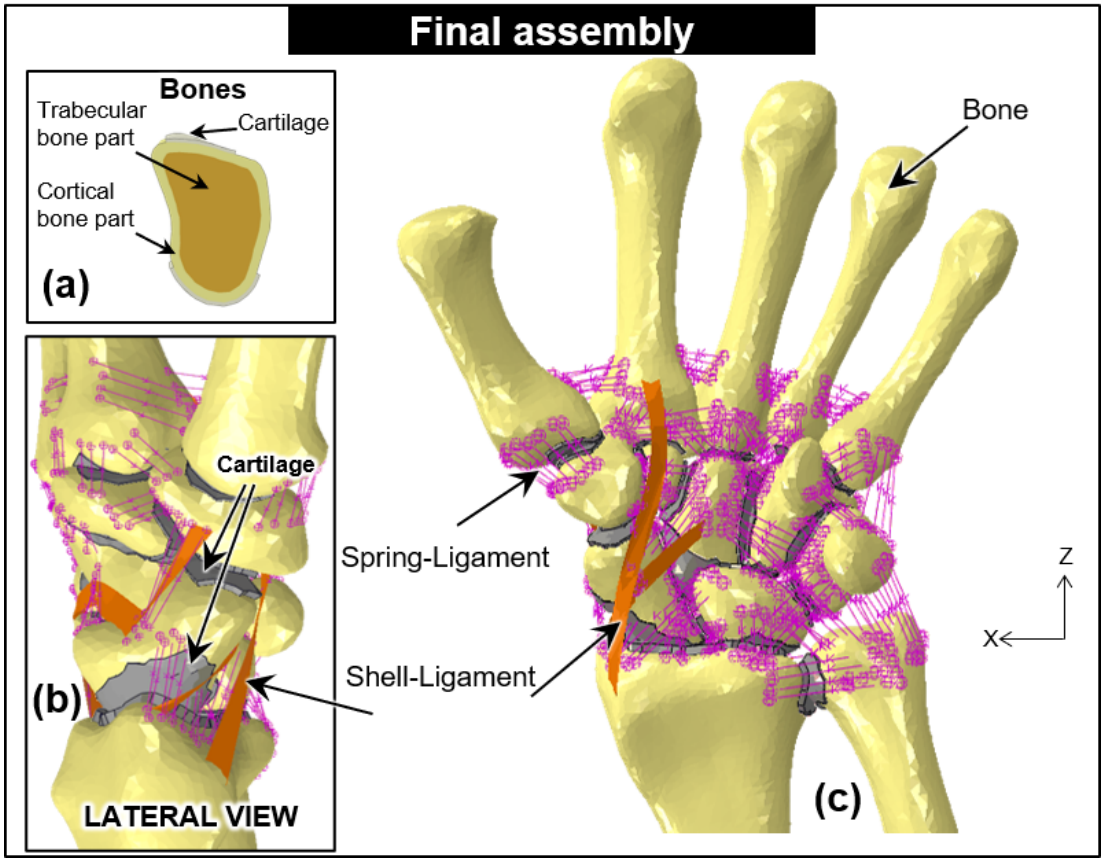

Figure 3.7: Final assembly of the type II wrist. (a) Cut of capitate bone showing the trabecular, cortical and cartilage structures, (b) Lateral view showing the wrapping on the scaphoid of the ligament modelled as shell, (c) Final assembly of type II wrist, including bones, cartilages and ligaments.

3.6 Validation of the model

The FE model was validated by comparing the values obtained from a simulation with the results reported from cadaveric studies [11, 12]. Before proceeding to the validation, a meshed sensitivity analysis was completed to ensure accuracy of the results. The validation comprised the simulation of the clenched fist ulnar deviated position reported by Alonso *et al* [11] shown at the left side in Figure 3.8, and the simulation of the motion of the wrist into four positions reported by Bain *et al* [12] as shown in the right side in Figure 3.8.

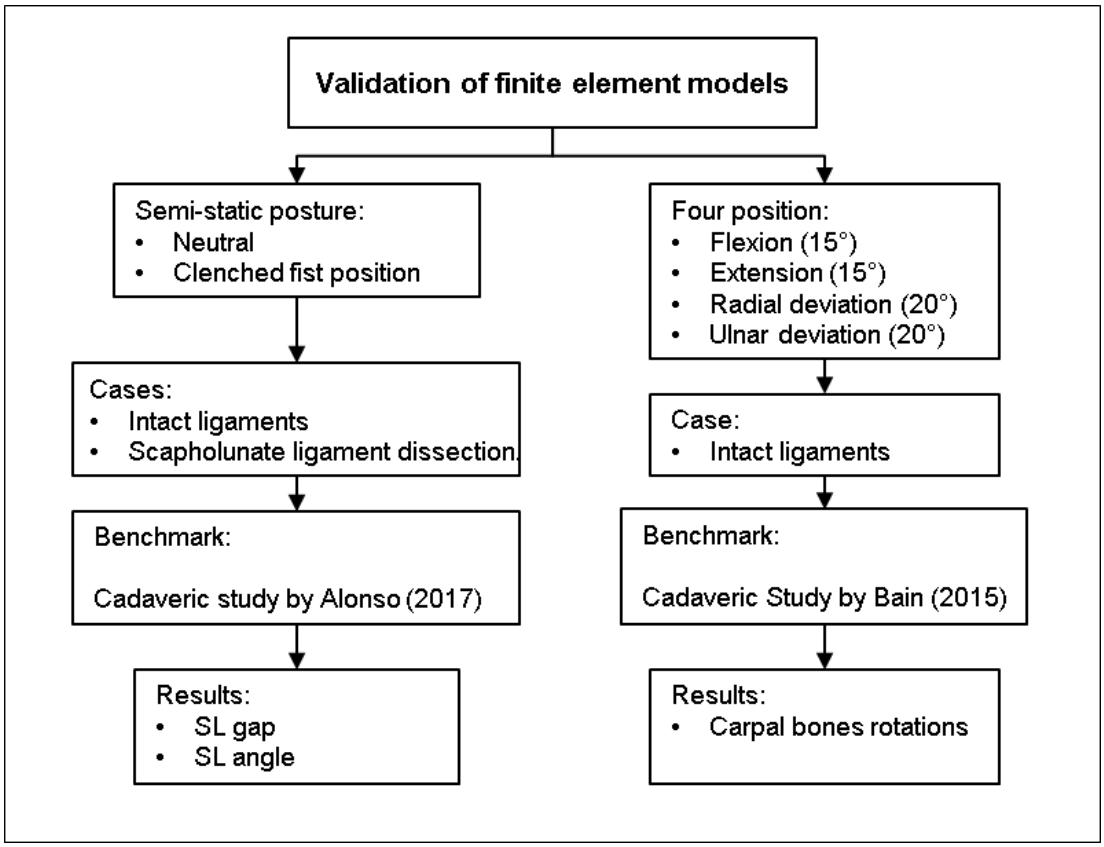

Figure 3.8: Validation flowchart. (a) Validation in a clenched fist position, (b) Validation in four positions of the hand.

3.6.1 Mesh sensitivity

A mesh sensitivity analysis was executed to define the appropriate mesh element size that can calculate accurate results without over excessive computing resources. For this analysis, the model was loaded to simulate fist position in a neutral position using a different density of the element mesh in the bones, cartilages and shell ligaments. The contact area on the lunate bones was measured and compared for six mesh densities as shown in Figure 3.9. The mesh density was selected once the contact area value varied by less than 5% compared to a finer mesh.

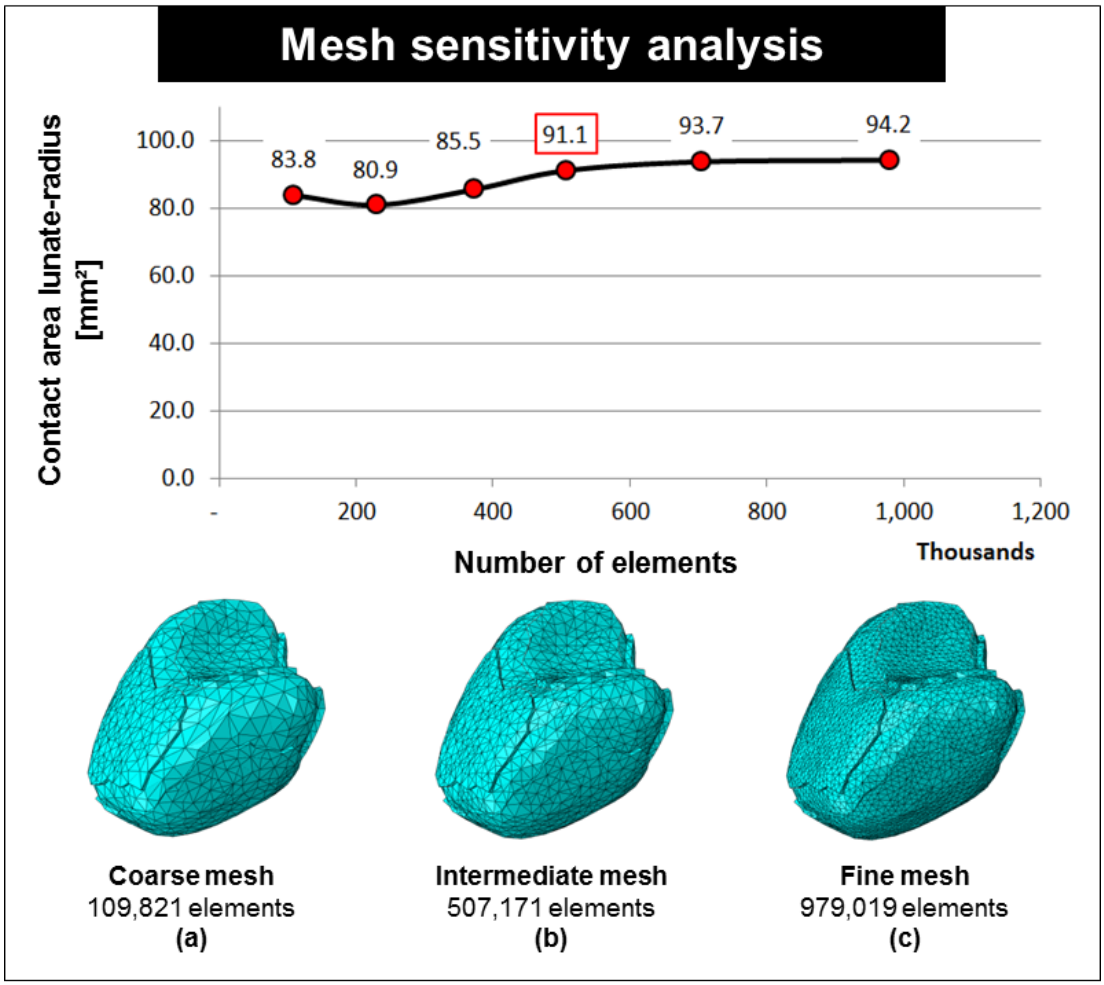

Figure 3.9: Mesh sensitivity analysis.

The model with the coarser mesh consisted of a total of 109, 821 elements with a completion time of thirty-five minutes; while the model with the smaller meshed consisted of a total of 979, 019 elements with a completion time of 200 minutes. The mesh sensitivity analysis demonstrated that for models meshed with seed size smaller than 0.7 (fraction of the global element size), the contact area value no changed significantly as can be seen in Figure 3.9.

The final model consisted of a total of 507, 327 elements. The type of elements is shown in Figure 3.10. 10, 372 are wedge elements of type C3D6 for the cartilage, 496, 491 tetrahedral elements of type C3D4 for the solid bones, 301 quadrilateral elements of type S4R and 7 triangular elements of type S3 for the shell-ligaments and 156 spring element for the spring-ligament. The model had a total of 111, 404 nodes. The computing time for this case was 80 min.

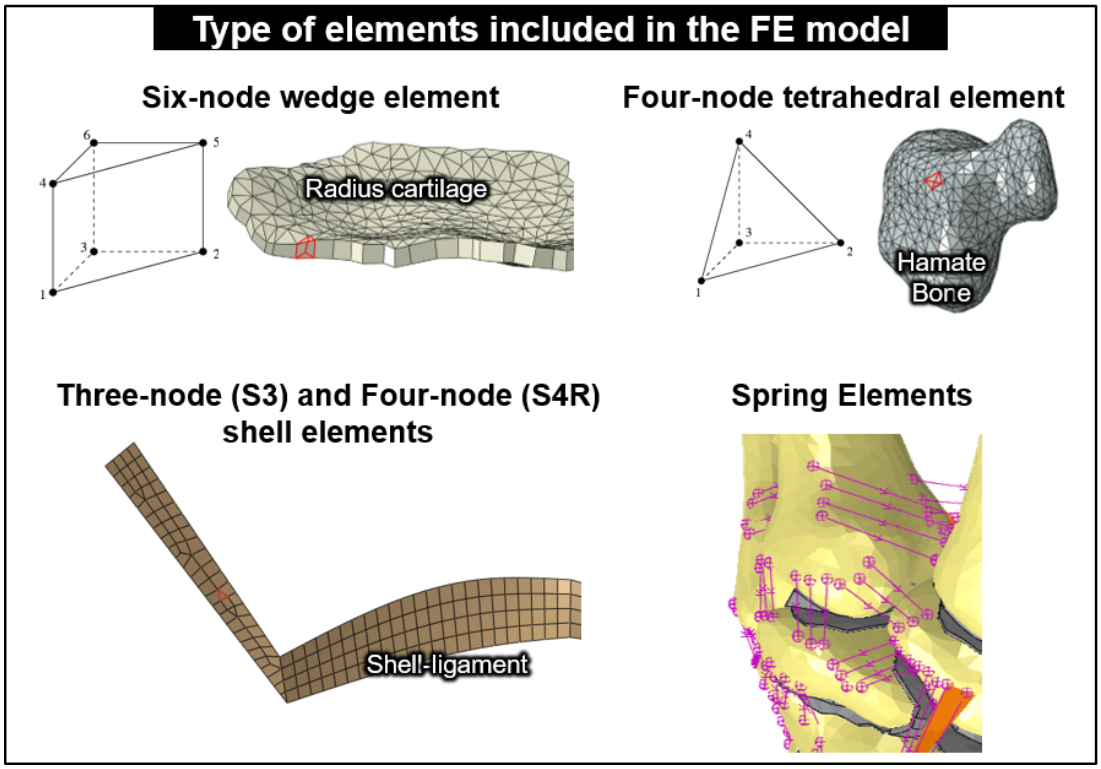

Figure 3.10: Type of elements included in the FE model.

3.6.2 Validation against cadaveric data. Clenched fist ulnar deviation position

The FE model validation was undertaken by replicating a cadaver study reported by Alonso *et al* [11]. The cadaver study comprises two cases, the intact ligaments case and the SLIL sectioning. The two cases were simulated using the FE model by replicated the loading scenario and boundary conditions to produce a clenched fist position the selfsame setting described in the cadaveric study. The computed results obtained from the FE for the SL gap and the SL angle were compared to those from the cadaveric study.

3.6.2.1 Description of the cadaveric case

The experimental setup reported by Alonso *et al* [11] was conducted on fifteen cadaveric specimens sectioned at the mid-forearm. Each specimen was held into a plastic cylinder with cement, then selected tendons were exposed at the dorsal side to apply loads and produce the clenched fist posture. The exposed tendons are flexor digitorum superficialis (FDS), flexor digitorum profundus (FDP), flexor pollicis longus tendon (FPL), flexor carpi ulnaris (FCU), extensor carpi ulnaris (ECU) and extensor digitorum communis (EDC). The FDP and FPL were grouped to create an FDP/FPL bundle. Metal weights of $15N$ were attached to FCU, ECU, FDS, FDP/FPL; plus an extra weight of $20N$ stitch locked to the EDC. Figure 3.11-(a).

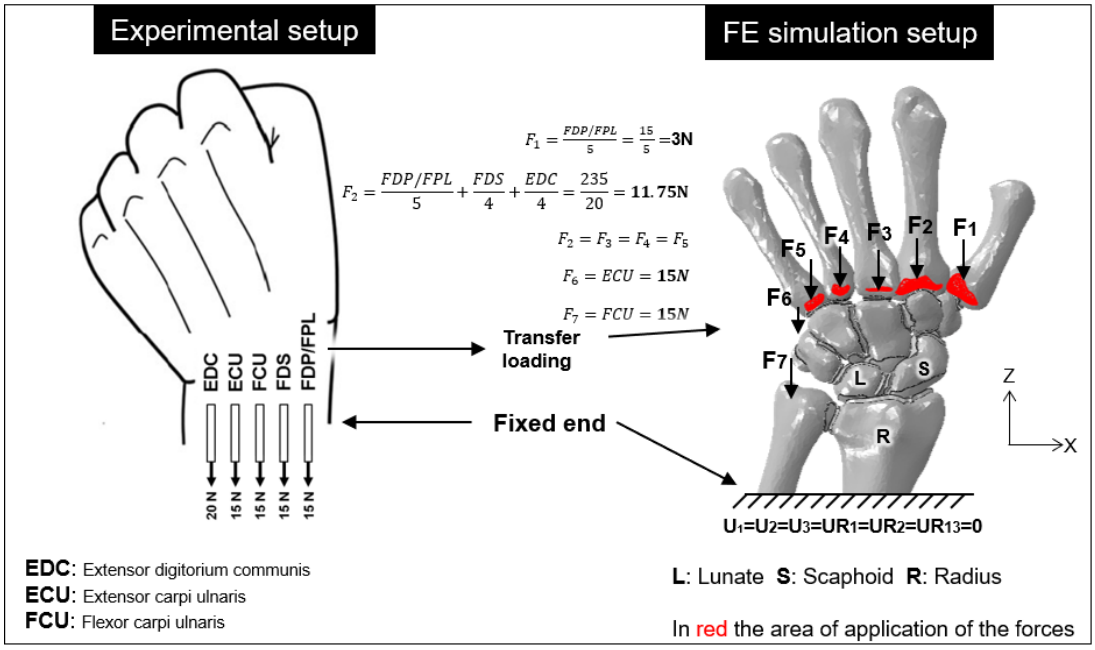

Figure 3.11: Experimental set up by Alonso (2017) and simulation with the FE model. The proximal part of the ulna and radius encastred, i.e. with zero degrees of freedom.

The SL gap and SL angle were measured in both intact and sectioning cases. The SL gap was measured on a posterior-anterior x-ray as the short distance between the border of the scaphoid and lunate bones, following the description by Lee [115] as shown in Figure 3.12. The SL gap was defined by the distance between two points on the edges of lunate and scaphoid at both dorsal and volar side. To locate the points to measure the SL gap, two imaginary arcs known as Gilula lines were used as shown in Figure 3.12. The proximal arc described by outlining the proximal convexities of the scaphoid, lunate and triquetrum; whereas the distal arc traces the distal curvatures of the same bones. An auxiliary arc is drawn at the half distance of the Gilula lines, the intersection between this arc and the border of the bones define the points to measure the SL gap; $S_D - L_D$ for dorsal side and $S_V - L_V$ for the volar side as shown in Figure 3.12.

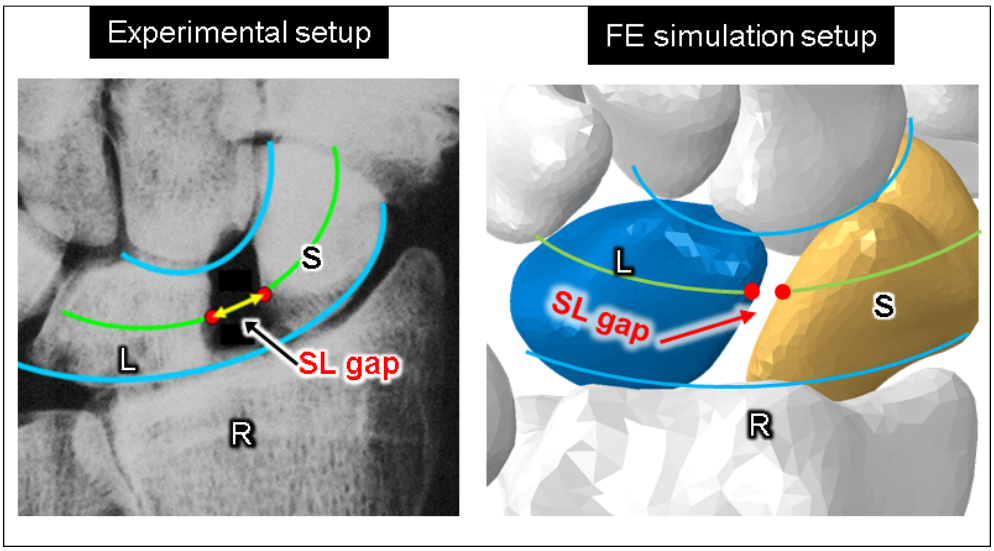

Figure 3.12: Measurement of the SL gap in the experimental and FE model.

The SL angle was measured on a lateral radiograph as explained by Larsen [116]: two axes were drawn, one tangent to margins of the scaphoid at palmar proximal and distal regions; another axis on the lunate being a perpendicular line to the tangent drawn between the two distal poles as shown in Figure 3.13. The angle between the two axes is the SL angle, which value ranges normally between $30° - 60°$.

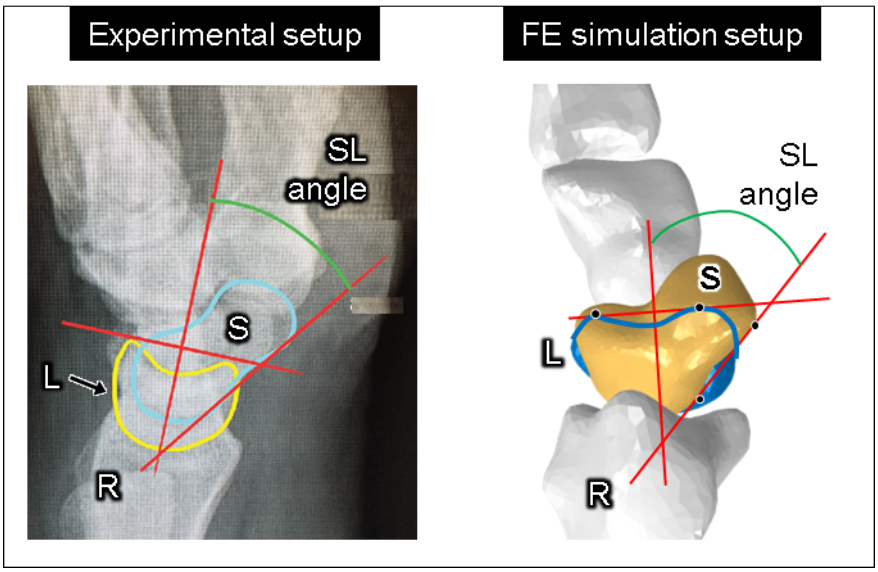

Figure 3.13: Measurement of the SL angle in the experimental and FE model.

3.6.2.2 Simulation of the clenched fist position

The cadaveric loading conditions were replicated in the FE model. The proximal end of the radius and ulna were constrained in all direction. Loading in the FE model was applied to the base of the metacarpal bones. The magnitude of the loads was distributed as follow: $3N$ on metacarpal 1, $11.75N$ on metacarpals 2 to 5. Additionally, two loads of $15N$ were applied to the pisiform and the dorsal base of the fifth metacarpal to produce the ulnar deviated posture as described in Figure 3.11.

In the FE models, the SL gap and SL angle were calculated by tracking nodes. Analogous to the experimental, two nodes were selected in a posterior view to measure the SL gap as described by Lee *et al* [115] as shown in Figure 3.12. Similarly, in the lateral view, four nodes were selected to calculate the SL angle as shown in Figure 3.13. The coordinates of the nodes were tracked to calculate both gap and angle.

3.6.2.3 Results

Figure 3.14 shows the results from the type II wrist FE model for the SL gap and SL angle for the intact ligament and the SLIL sectioning cases, alongside to the values published by Alonso *et al* [11]. In the intact case, the values from the FE models at the dorsal side were $2.4mm$ and $2.8mm$ for the loaded neutral and the loaded ulnar deviated clenched fist position respectively. After completing the simulation for the SLIL sectioning, the value of the SL gap increased to $3.5mm$.

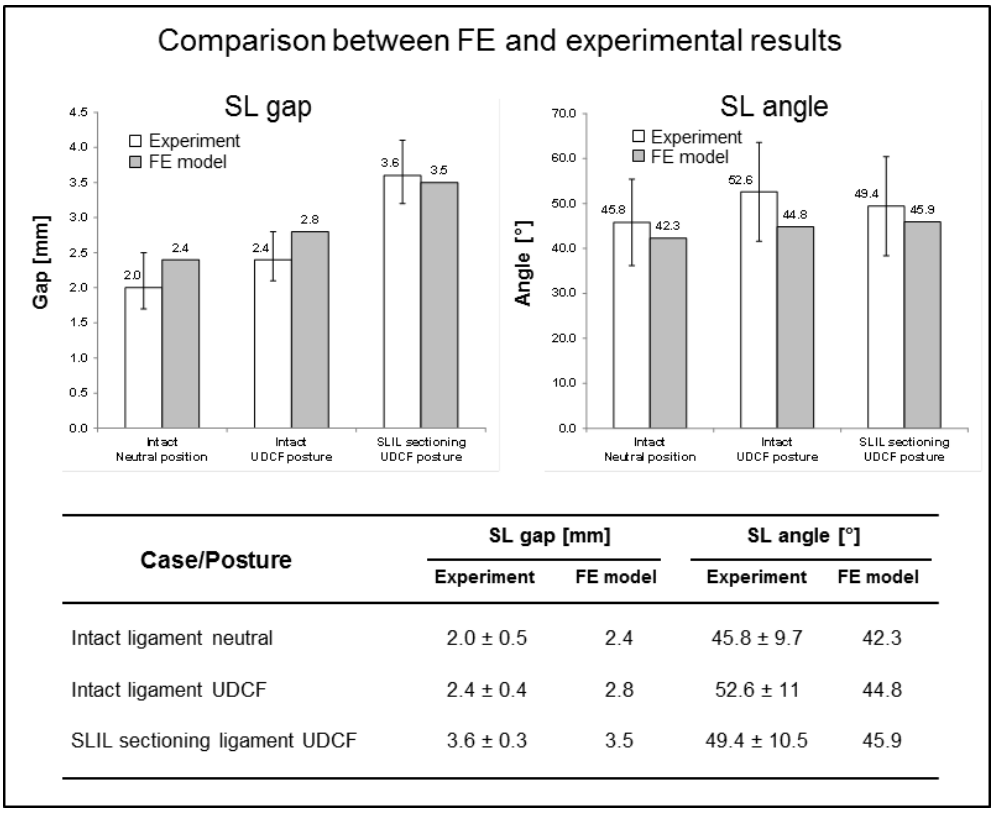

Case/Posture	SL gap [mm]		SL angle [°]	
	Experiment	FE model	Experiment	FE model
Intact ligament neutral	2.0 ± 0.5	2.4	45.8 ± 9.7	42.3
Intact ligament UDCF	2.4 ± 0.4	2.8	52.6 ± 11	44.8
SLIL sectioning ligament UDCF	3.6 ± 0.3	3.5	49.4 ± 10.5	45.9

Figure 3.14: Comparison of predicted SL gap at dorsal side an angle from the intact type II wrist and SLIL sectioned models against the cadaveric study from Alonso *et al* [11]. FE - Finite Element; SLIL - Scapholunate interosseous ligament; UDCF - Ulnar deviated clenched fist posture.

Regarding the SL angle, the values measured were 42.3° and 44.8° for the intact case at the neutral and the loaded ulnar deviated clenched fist position respectively. The value of the angle increased to 45.9° after the SLIL sectioning.

The results obtained from the FE model were consistent with those of Alonso *et al*. When comparing the values obtained for the neutral position, the SL gap ($2.4mm$) and SL angle (42.3°) fell within the standard deviation of the corresponding values reported in the cadaveric study ($2.0 \pm 0.5mm$ for SL gap and $45.8 \pm 9.7°$ for the SL angle. As can be seen in Figure 3.14, the results were consistent in all the cases, it was thus considered the FE models validated and it was reasonable to use them to further analysis.

3.6.3 Validation against cadaveric data. Carpal kinematics

The capacity of the FE model to simulate kinematics of the carpal bones was validated by replicating a cadaver experiment reported by Bain *et al* [12]. The movement of the carpal bones was tracked during the simulation of the passive motion of the wrist in four positions: flexion-extension ($15° - 15°$) and radioulnar deviation ($20° - 20°$). The results obtained numerically were compared to those obtained experimentally.

3.6.3.1 Definition of the experimental set-up

The cadaveric set-up reported by Bain *et al* [12] was done on 4 type II wrists. The specimen preparation started with the fixation into two aluminium pots of the proximal end of the forearm (radius and ulna) and the distal end of the hand (metacarpals). Bone pins were inserted into the ulna, radius, third metacarpal, scaphoid, lunate, triquetrum and capitate. Three markers were attached to each bone pin to motion tracking as shown in Figure 3.15-a.

The passive motion on the specimens was performed by the customised platform. The proximal region was held rigidly, while the distal region of the specimen was mounted in the movable platform as shown in Figure 3.15-a. The motion of the platform was controlled to reproduce flexion ($15°$), extension ($15°$), radial deviation ($20°$) and ulnar deviation ($20°$). Additionally, a load of $10N$ was applied axially across the wrist. The trajectories of the markers were recorded by a motion capture system to compute the rotation angles of the pinned bones.

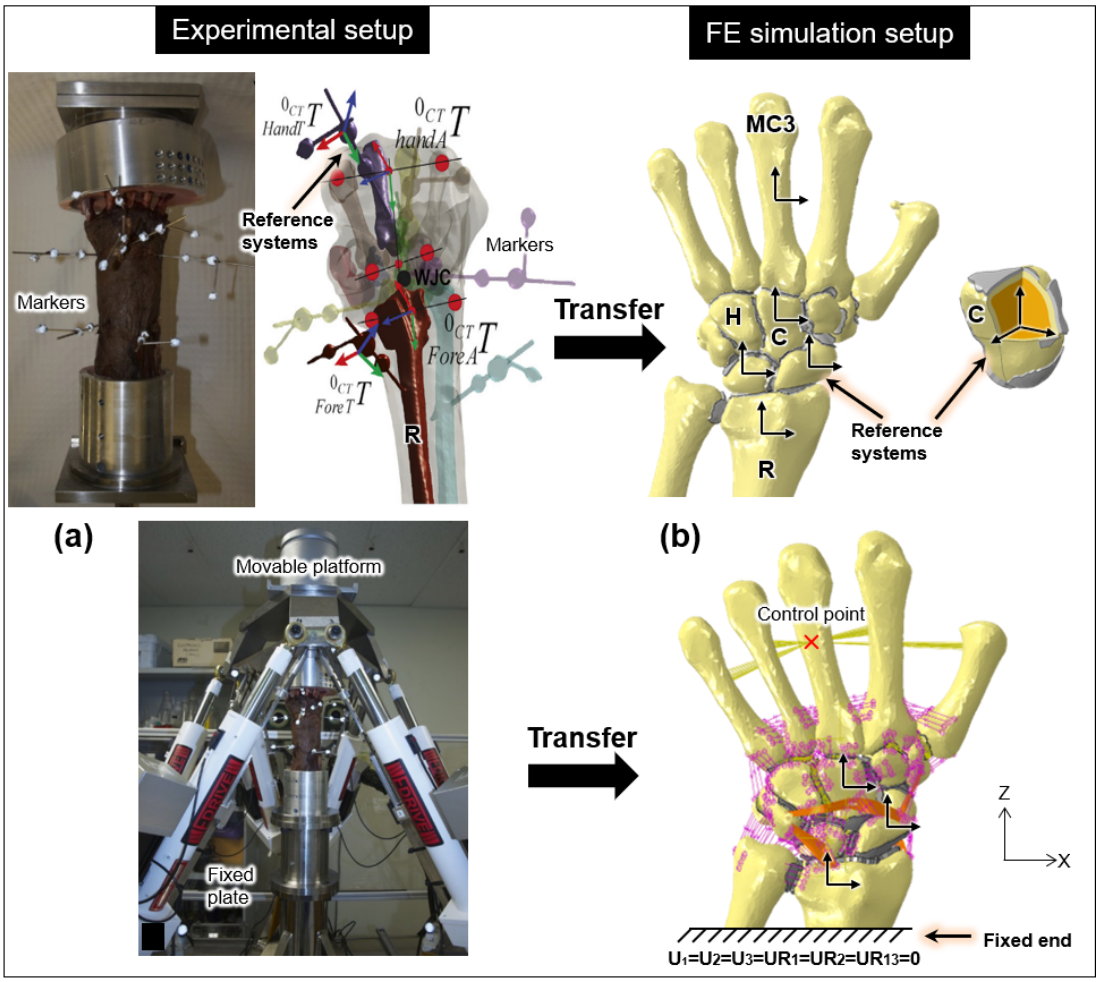

Figure 3.15: Experimental and simulation setup to measure carpal kinematics. (a) Experimental setup showing the markers used to track the carpal kinematic, and the customised rig to produce passive motion of the wrist. Modified from Fraysse [47] (b) FE simulation setup showing the reference system location to measure the carpal kinematics in the models, and the boundary conditions to produce the passive motion in the FE model. The proximal part of the ulna and radius was encastred. Each carpal bones has 6 degrees of freedom.

3.6.3.2 Simulation of carpal kinematics

The cadaveric set-up was replicated in the type II wrist FE model. The proximal end of the ulna and radius was fully constrained to simulate the fixation of the rigid plate, i.e. the end has zero degrees of freedom. The five metacarpals were tied to a control point located in the midway of the second and the fifth

metacarpal as shown in Figure 3.15-b. The passive motion was achieved by moving the control point into the four positions the same magnitude as the experimental set-up. A compression load of $10N$ was applied on the metacarpals to produce a contact between the bones.

Each carpal bone has 6 degrees of freedom. The rotation of the bones was calculated for the carpal bones. To compute the values in the FE model, an orthogonal coordinate system was located at the volume centroid of each bone as shown in Figure 3.15-b. The rotation of the bones was calculated between the orthogonal system at the initial and final position.

3.6.3.3 Results

The obtained values from the FE models fell within the standard deviation of the results published by Bain *et al* [12] as shown in Figure 3.16. The rotation of the bones was reported in two planes. Motion *in-plane* is referred to the motion occurring in the same plane of motion of the joint; for example, the flexion of the scaphoid during wrist flexion. The *out-of-plane* motion is the movement perpendicular to the plane of motion of the joint; for example, the radioulnar deviation of the scaphoid during wrist flexion.

A convention of signs was defined to describe the motions around the axis of the coordinate system. Flexion (+X), Extension (-X) measured around the X-axis; Ulnar deviation (+Y) and radial deviation (-Y) measured around the Y-axis. Note that the sign in the obtained values indicates the direction of the rotation.

Figure 3.16 shows the *in-plane* rotation of the bones calculated by the FE model during wrist flexion alongside the values from Bain *et al.* The rotations of the scaphoid, lunate and triquetrum relative to the radius were 11.7°, 8.3° and 10.1°, respectively. As can be seen, all the values fell within the standard deviation reported in the cadaveric study, except for the lunate which value was shorter by 1.7° compared to the value of cadaveric. The rotation of the capitate relative to the scaphoid, lunate and triquetrum was 2.5°, 5.8° and 3.6°, respectively. Regarding the *out-of-plane* rotations, in all cases the value calculated by the FE model fell within the standard deviation except for the triquetrum relative to the radius which was 3.5° larger to the value reported by Bain *et al*; however, the value in cadaver was 0 ± 0.

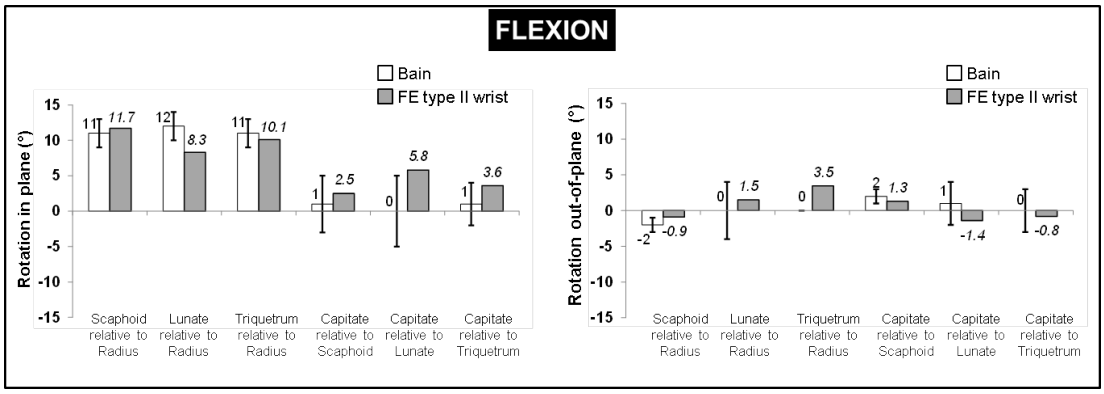

Figure 3.16: Comparison of the carpal kinematics values between the FE model results and cadaveric study during flexion.

Figure 3.16 shows the in-plane rotation of the bones calculated by the FE model during wrist extension alongside to the values from Bain *et al.* The rotations of the scaphoid, lunate and triquetrum relative to the radius were $-11.1°$, $-7.9°$ and $-8.7°$, respectively. The sign indicates the direction of the rotation following the sign convention explained previously. The rotation of the capitate relative to the scaphoid, lunate and triquetrum was $-2.3°$, $-6.4°$ and $-4.9°$, respectively.

As can be seen, all the values fell within the standard deviation reported in the cadaveric study. Regarding the out-of-plane rotations, in all cases the value calculated by the FE model fell within the standard deviation except for the scaphoid relative to the radius which was 1.5° shorter to the value reported by Bain *et al.*

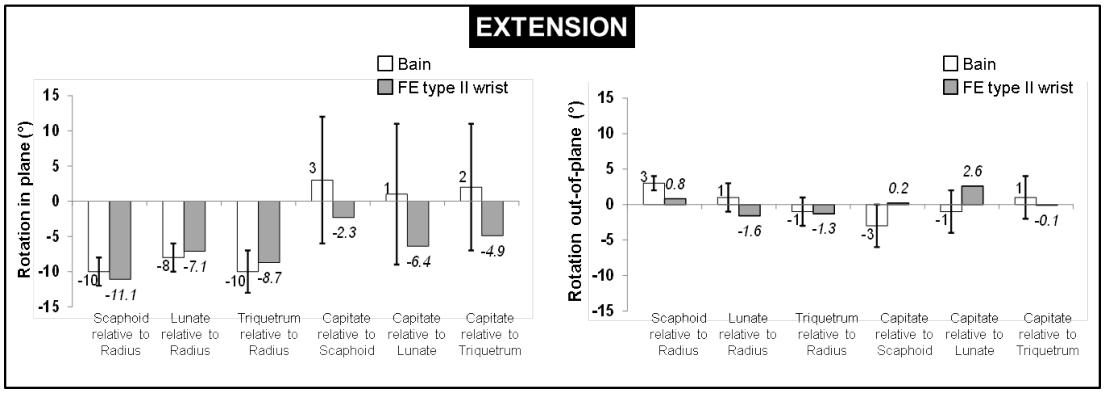

Figure 3.17: Comparison of the carpal kinematics values between the FE model results and cadaveric study during extension.

Figure 3.18 shows the in-plane rotation of the bones calculated by the FE model during wrist radial deviation alongside to the values from Bain *et al.* The rotations of the scaphoid, lunate and triquetrum relative to the radius were $-7.1°$, $-5.6°$ and $-7.1°$, respectively. The rotation of the capitate relative to the scaphoid, lunate and triquetrum was $-7.5°$, $-11.4°$ and $-8.5°$, respectively. Upon inspection, it was noticed that all the values fell within the standard deviation except for the capitate relative to scaphoid which value was shorter by 3.5° compared to the value from cadaveric. Regarding the out-of-plane rotations, the larger rotation was calculated for the lunate relative to radius, triquetrum relative to the radius and capitate relative to triquetrum.

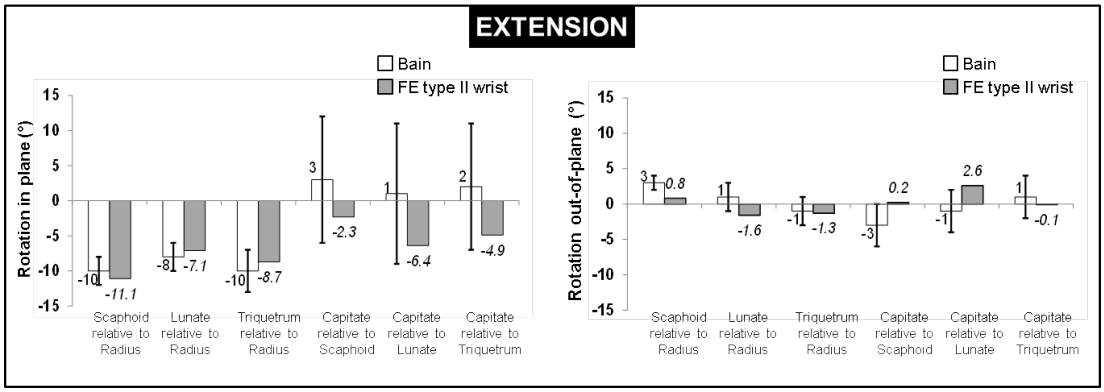

Figure 3.18: Comparison of the carpal kinematics values between the FE model results and cadaveric study during radial deviation.

Figure 3.19 shows the in-plane rotation of the bones calculated by the FE model during wrist extension alongside to the values from Bain *et al.* The rotations of the scaphoid, lunate and triquetrum relative to the radius were 10.1°, 10.3° and 15°, respectively. The rotation of the capitate relative to the scaphoid, lunate and triquetrum was 7.9°, 7.3° and 5.6°, respectively. As can be seen, all the values fell within the standard deviation reported in the cadaveric study. Regarding the out-of-plane rotations, in all cases the value calculated by the FE model fell within the standard deviation except for the scaphoid relative to the radius which was 3.6° shorter to the value reported by Bain *et al.*

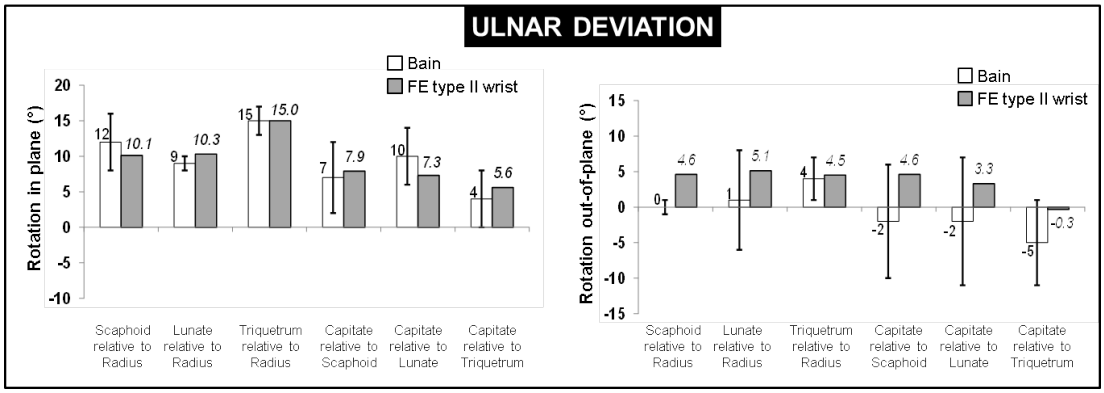

Figure 3.19: Comparison of the carpal kinematics values between the FE model results and cadaveric study during radial deviation.

The rotation of the bones predicted by the FE model was consistent with the rotations reported by Bain *et al* [12] in all the cases, especially for the *in-plane* of motion values. The rotation values in the out-of-plane motion were slightly higher especially during radial deviation; however, the magnitude is smaller and as reported in the cadaveric study the motion capture system was very sensitive to small values measured in the out-of-plane. Upon inspection of the rotation values in both planes and all position, the prediction of the rotation with the FE model was acceptable, it was thus considered the FE models validated to use it to further analysis.

The computed rotation values obtained from the FE values are consistent with the values reported in the cadaveric study. However, some values fell outside of the standard deviation area. The discrepancy in those values was the result of the biological variability. A deterioration of the mechanical properties of cadavers is a well-documented phenomenon and need to be considered. The ligament and muscle stiffness presented in the cadaver was not included in the FE models. The bones in the FE can move more freely compared to the cadaver.

3.6.4 Validation against cadaveric data. Contact area.

The effectiveness of the FE model was tested by simulating further experimental work previously published [84, 117, 118]. The distribution of the contact area between the scaphoid and lunate has been published previously by Tencer [117], Viegas [118] and Blevens [84].

3.6.4.1 Definition of the experimental setup

The contact area at the radiocarpal joint was measured using pressure-sensitive paper manufactured by Fuji Prescale pressure-sensitive paper ® (super low pressure, NY, USA). The transducer is composed of two thin flexible plastic sheets, one containing dye-laden microspheres of various breaking strengths distributed randomly over the surface and the other half containing a developer

to fix the dye. As the pressure increases, more microspheres are broken, increasing the colour density of the print on the paper as shown in Figure 3.20.

The pressure paper was inserted into the joint space through a dorsal capsular incision. To avoid print development due to relative shear motion of the joint, the paper was inserted when the joint was distracted and flexed, then the joint was positioned and load axially to record contact. The measurement of contact area was registered on a light table using a video digitizing system.

The scaphoid and lunate contact areas on the radius were measured and the scapholunate contact area ratio was calculated by dividing the value of the scaphoid/radius area between the lunate/radius area.

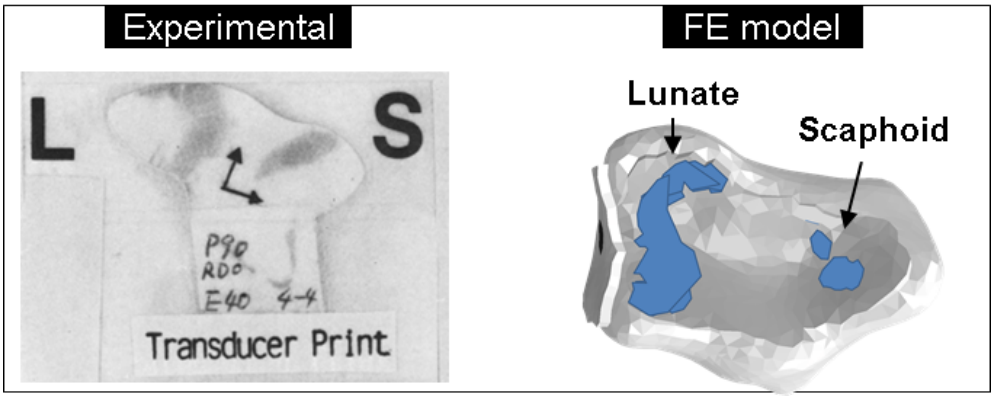

Figure 3.20: Contact area measurement at the radiocarpal joint in the experimental and FE model.

Tencer *et al* [117] measured the contact area and pressure in five hand specimens in 36 positions combining neutral position, flexion (20°), extension (20°, 40°), radial deviation (20°) and ulnar deviation (10°, 20°). Viegas *et al* [118] reported the contact area using five hand specimens; similar to Tencer, Viegas measured the contact area at 36 static positions combining flexion/extension and radial/ulnar deviation. Blevens *et al* [84] reported the contact area in 12 cadaver wrists. The measurement was recorded in each of the following wrist positions: neutral, 20° extension, 20° flexion, 20° radial deviation, and 20° ulnar deviation.

3.6.4.2 Results

The contact areas were measured in the FE models for the intact ligament case at the neutral position, 20° extension, 20° flexion, 20° radial deviation, and 20° ulnar deviation as shown in Figure 3.20. The comparison between the three cadaver studies and the FE model was undertaken including the contact area values only for the same arc of motion. Figure 3.21 shows the contact area ratios recorded in experimental and the values calculated with the FE model. In general, the values predicted by the model compare well with the experimentally determined values.

The accuracy of the contact area values calculated in the FE model was assured because of the mesh sensitivity analysis reported at the subsection 3.6.1 of this thesis.

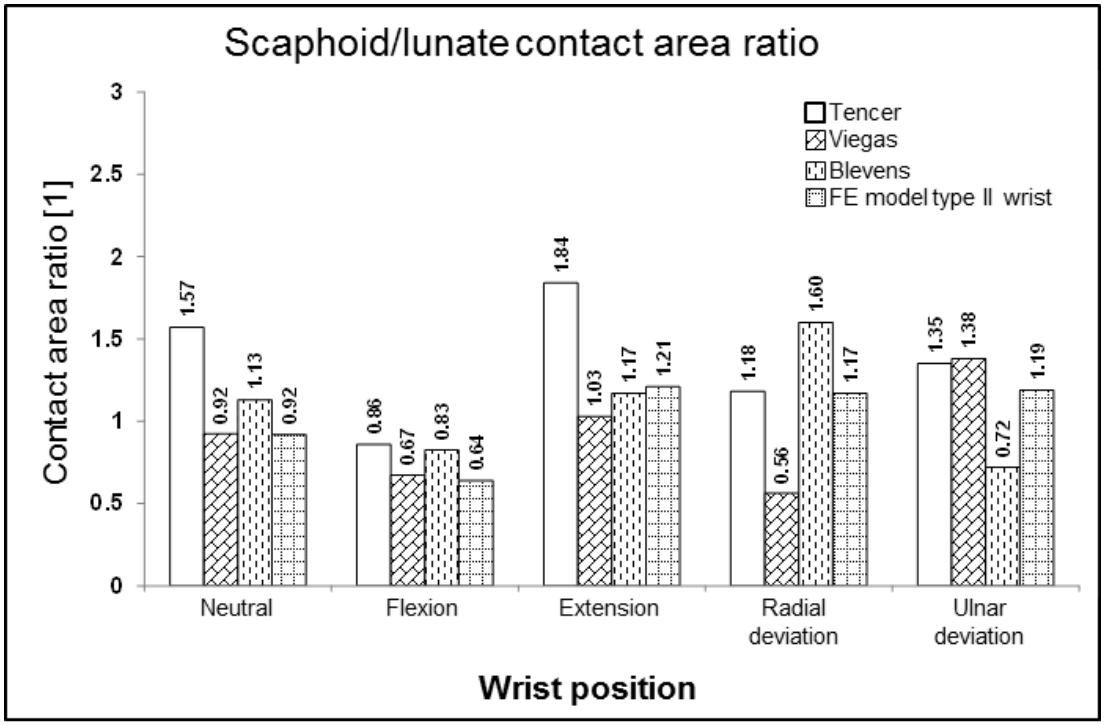

Figure 3.21: Comparison of the contact area between cadaveric studies and FE models at radiocarpal joint.

3.7 Discussion

A FE model of the type II wrist was developed from CT-scan data to examine the carpal bones kinematics. To acquire veracious 3D surfaces to construct the FE model, bone geometry was segmented from the CT-images using a semi-automatic thresholding process. The segmentation was intervened only in cases when the semi-automatic process was unable to register the bone or when the limits of the bones were overlapped which is common in wrist CT images due to the small inter-bone spaces, the irregular shape of closely packed carpal bones and the non-uniformity of the bone tissue, ranging from dense cortical bone to the textured spongy bone [119].

The cartilage layers were constructed by offsetting the articular surfaces over the bones. The thickness corresponds to half of the minimum distance between the two articulating bones. This estimation method is similar to that used in other studies modelling the wrist joint [92, 95, 110]. Moore et al [17] segmented more accurately the cartilage layer of the carpal bones using a micro μCT and MRI; however, the selection of the CT-scan data for this thesis was focused in selecting a subject with a type II wrist from a bank of images where the technical acquisition features could not be changed. A hyperelastic material model was employed to represent soft tissue (cartilage) behaviour, which is considered to be an accurate approach [110]

During the assembly of the model, a few simplifications were done to reduce the number of interactions, for example, each metacarpal bone was rigidly constraint to the underlying carpal bone. Rainbow et al [120] reported that in general the capitate and third metacarpal move as one unit, only in cases of extreme extension the metacarpal can move about 4 degrees farther than the capitate which would justify the above simplification.

In the FE model, the triquetrum and pisiform interaction was also considered as rigidly bounded, preserving all the attached ligaments to the pisiform. Studies on pisiform anatomy [57, 121, 122] reported that the pisiform is over-constraint to the triquetrum by 10 soft-tissues attachments including two portions of the pisotriquetral ligament. In this context, shear forces on the articular surface of the pisiform caused by the force transmission via the ligaments were not considered and their influence on the triquetrum kinematics needs to be further investigated.

Although the FE model was considered validated, its limitation must still be noted. Our model was subject to a number of simplifications, assumptions, and limitations typical of complex numerical problems in the biomechanical field. For example, our model considered cancellous bone as exhibiting elasticplastic, isotropic material behaviour. Also, whilst it is recognized that the elastic modulus of cancellous bone depends primarily on apparent bone density, the exact form of the dependency is contested [123], and this is further complicated by the dependency of the relationship on trabecular orientation, loading direction, and anisotropy. However, it is recognised that within a single anatomical site, density range is limited [123], which suggests that an invariant bone property, as was employed in our study, should provide sufficient accuracy.

The majority of the ligament included in the model were represented using tension-only spring elements, which although a common approach, is known to have its limitations, for example, in cases of complex nonuniform 3D stress/strain [124]. More accurate representation requires 3D FE modelling treatment; however, the required approach is highly involved, extremely time-consuming [124] and can over constraint the model [96].

The stiffness values were obtained from literature on cadaveric studies and wrist joint modelling [21, 90, 92, 97, 110]. The mechanical behaviour of the ligaments was specified with the values of a $force - strain$ curve. The pair of points (strain, force) were calculated based on the stiffness value and the initial average

length (l_0) of the set of spring representing the ligaments at $\varepsilon = 0$, $\varepsilon = 3\%$ and $\varepsilon = 20\%$. These values specified the non-linear ligament behaviour in terms of the stiffness; however, the estimation of these values was a simple approximation for the cases where the data is not available [124]. In practice though, ligaments tend to operate in or close to the linear region, so our modelling assumption should provide reasonable accuracy. It was observed that a pretension of the ligaments in the first step of the simulation helped to the convergence of the FE models.

Ligaments were simulated as a set of spring elements; however, the effect of the ligament acts as a single axial force vector for each spring which is not comparable with the effect that the multiple fibres forming the ligaments have on the force transmission in the wrist. This simplification in the modelling of ligaments have been proved successful in several types of research in the field of biomechanics and the modelling of the wrist joint. The viscoelastic ligament behaviour was not included in the FE model, a large number of parameters are required for accurate nonlinear viscoelastic behaviour representation; therefore, parameter data availability is key, but these data are generally not widely available [124].

The type II wrist models were developed from the CT scan of the left hand of a single subject; therefore, any results and conclusions drawn from the analyses should be viewed in this context and interpreted with care.

Overall, the FE model produced accurate predictions in terms of carpal kinematics, which would be advantageous for the purpose of this thesis. The model including all the ligaments (spring elements) will work as a benchmark in the following comparisons, and it will be referred to as the intact ligament model. The SLIL sectioning case and the three ligament reconstruction technique will be modelled based on the intact model. In the following Chapters, the models will be modified accordingly in order to simulate the virtual surgery and to produce the motion that each case requires.

Chapter 4

Performance evaluation of scapholunate ligament reconstruction techniques at clenched fist position

This chapter presents the performance evaluation of three tenodesis techniques, modified Brunelli technique (MBT), Corella, and scapholunate axis method (SLAM) in repairing scapholunate interosseous ligament (SLIL) disruption for a type II wrist using finite element-based virtual surgery. The techniques were assessed based on FE model predictions of SL gap and angle at both dorsal and volar sides and scaphoidlunate contact area. The carpal mechanic of the wrist was investigated using the FE models in order to determine whether the application of the ligament reconstruction techniques alters wrist kinematics. In addition, a comparison of the carpal mechanics in the context of row/column theory was undertaken to study the kinematics of the two types of the wrist. The values for the type I wrist were obtained from results reported by Alonso *et al* [11] from FE models of type I wrists.

4.1 Background

Scapholunate (SL) dissociation occurs when the scaphoid and lunate move excessively in relation to one another; it is caused by the injuring of the SL interosseous ligament (SLIL) and affects carpal instability [2]. Often, SLIL injuries are not diagnosed or treated during an acute phase of injury because it can take 3 to 12 months after trauma before dynamic instability develops and the SL dissociation can be detected radiologically; additionally, in some cases, people may have a tear of the SLIL but not present clinical symptoms [3]. SL instability has been reported to occur in approximately 5% of cases of wrist sprains [3] and is believed to be as common as scaphoid fractures [125].

Some authors have theorised that the effect on carpal instability after SLIL tear may be moderated by the bone geometry, which may help to explain why some patients go on to progressive instability whilst others do not [65, 66, 126]. In a cadaver study, Werner *et al* determined that bone geometry at the distal radius and proximal scaphoid may have a moderate effect on the carpal instability after sectioning [126]. Rhee et al found from a clinical review that patients possessing an additional articulation between the lunate and hamate have a lower incidence of DISI following a complete SLIL tear [66]. Other researchers, however, have found no link between bone geometry and carpal instability following SL injury [59].

The wrist has been categorised into type I and type II depending on the morphology of the lunate bone. A type I lunate is identified as having the shortest distance between the capitate and triquetrum (CT distance) on a posterior anterior radiograph [9, 10] of $\leq 2mm$ as shown in Figure 4.1. A type II lunate has an extra facet that articulates with the hamate [9, 10, 41, 49], and a CT distance ≥ 4 and $\leq 8.9mm$ (Figure 4.1-b) [9, 10]. A third, intermediate group, laying between type I and type II wrists, has also been identified by some researchers [59].

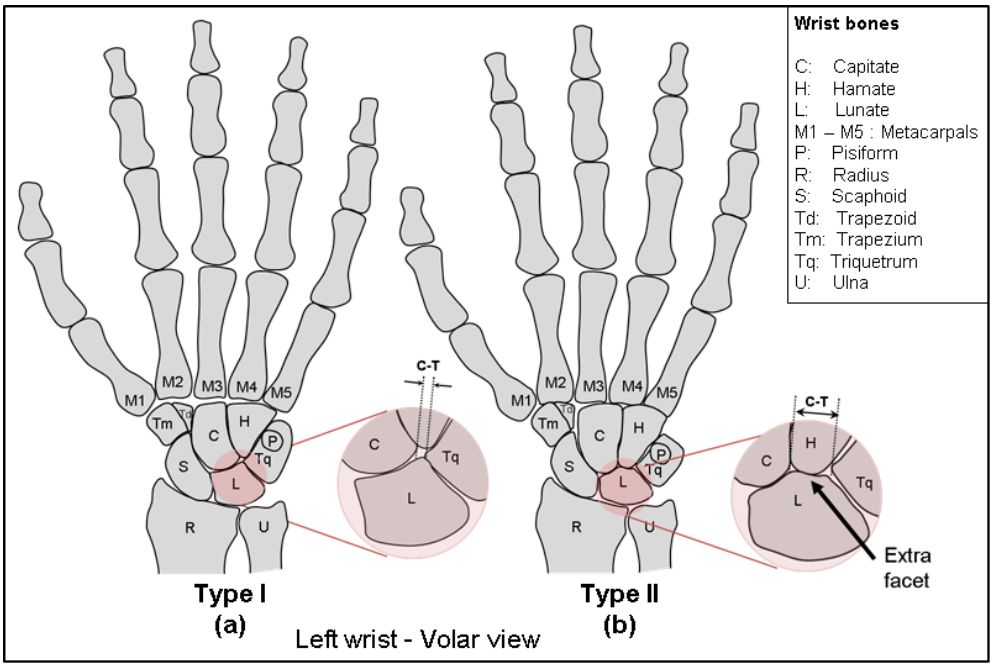

Figure 4.1: (a) Type I lunates do not articulate with hamate. (b) Type II lunates have an extra facet that allows articulation with the hamate, C-T distance ranging $\leq 4mm$ to $8.9mm$.

There is a clear difference between a type I and II wrist in articular cartilage contact as shown in Figure 4.2 [41, 57]. In an inspection of the transversal cuts from CT-scan data, there is no contact between the hamate and the lunate in any plane; contrary, in a type II wrist there is contact between the hamate and lunate in more than one plane as shown in Figure 4.2-b.

No registry of the incidence of type I and type II wrists has been set up, but some previous studies on lunate morphology reported type II wrists to be more common, with the proportion of the frequency of a type II lunate being 63% to 73% [49, 55, 57, 102]. The categorisation is seldom mentioned in the literature, and only recently have some authors discussed the incidence, variation, associated pathologies, and the clinical importance of the extra facet, including some studies that relate lunate morphology to carpal mechanics. Statistically, there is no correlation between lunate type and gender, age, hand dominance, or occupation [9, 27].

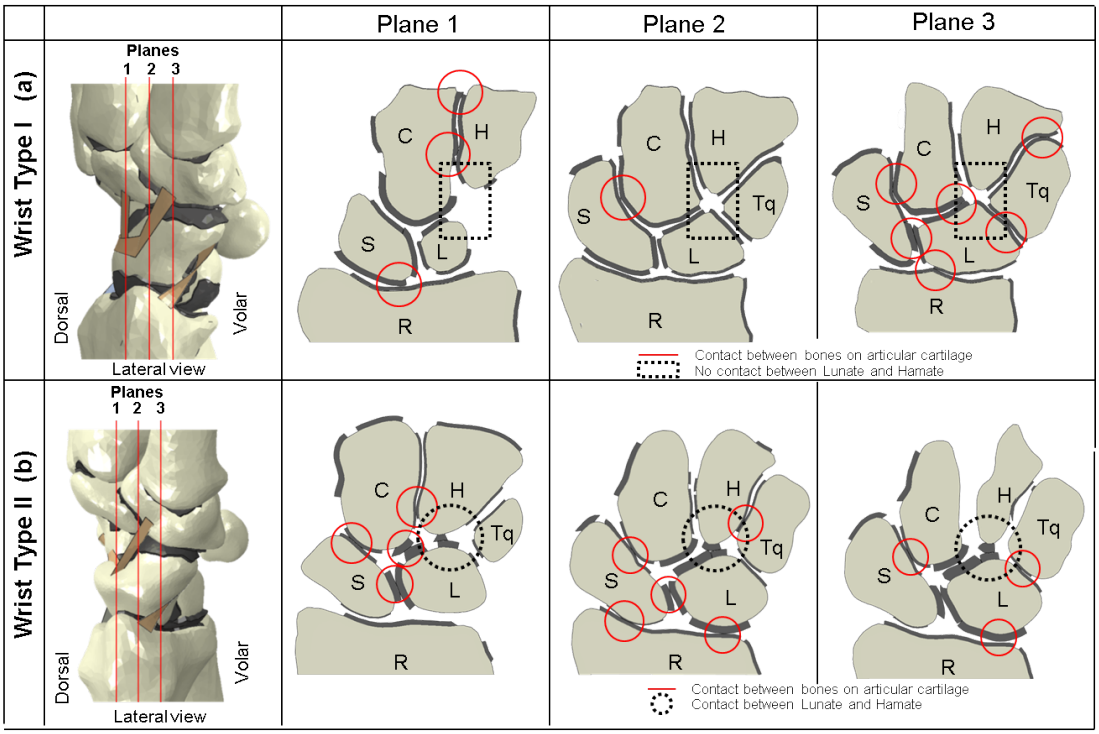

Figure 4.2: Contact between articular cartilages of the bones for different planes in the neutral position. (a) Type I wrist, there is no contact between the hamate and lunate in any plane. (b) Type II wrist, there is contact between the hamate and lunate in more than one plane.

Usually, carpal mechanics may be described using two main motion theories, row theory and column theory, with type I wrists considered to exhibit row mechanics and type II column mechanics [9] as shown in Figure 4.3.

In row theory, the carpal bones are divided into two rows of adjacent bones. The proximal row consists of the scaphoid, the lunate, the triquetrum, and the pisiform; the distal row composes of the hamate, capitate, trapezium, and trapezoid as shown in Figure 4.3-a [9, 27]. During clench fist ulnar deviation (volar view), the proximal row rotates and slides over the concave surface of the radius; meanwhile, the distal row rotates in the same direction sliding over the proximal row allowing the motion (Figure 4.3-b).

In column theory, the carpal bones are distributed into three columns: The lateral column consists of the scaphoid; the central column consists of lunate, capitate, hamate, trapezium, and trapezoid; and the medial column consists of the triquetrum and pisiform (Figure 4.3-c). Column theory suggests that during ulnar deviation (volar view), the central column rotates clockwise (in the ulnar direction); simultaneously, the medial column slides over the hamate to the dorsal side making space for the moving bones; meanwhile, the scaphoid tilts towards the vertical by the pulling of the ligament that joins it with trapezium and trapezoid [9, 27] (Figure 4.3-d). To date, validation of these theories has only been performed using plane Xray and fluoroscopic studies [9, 27, 49].

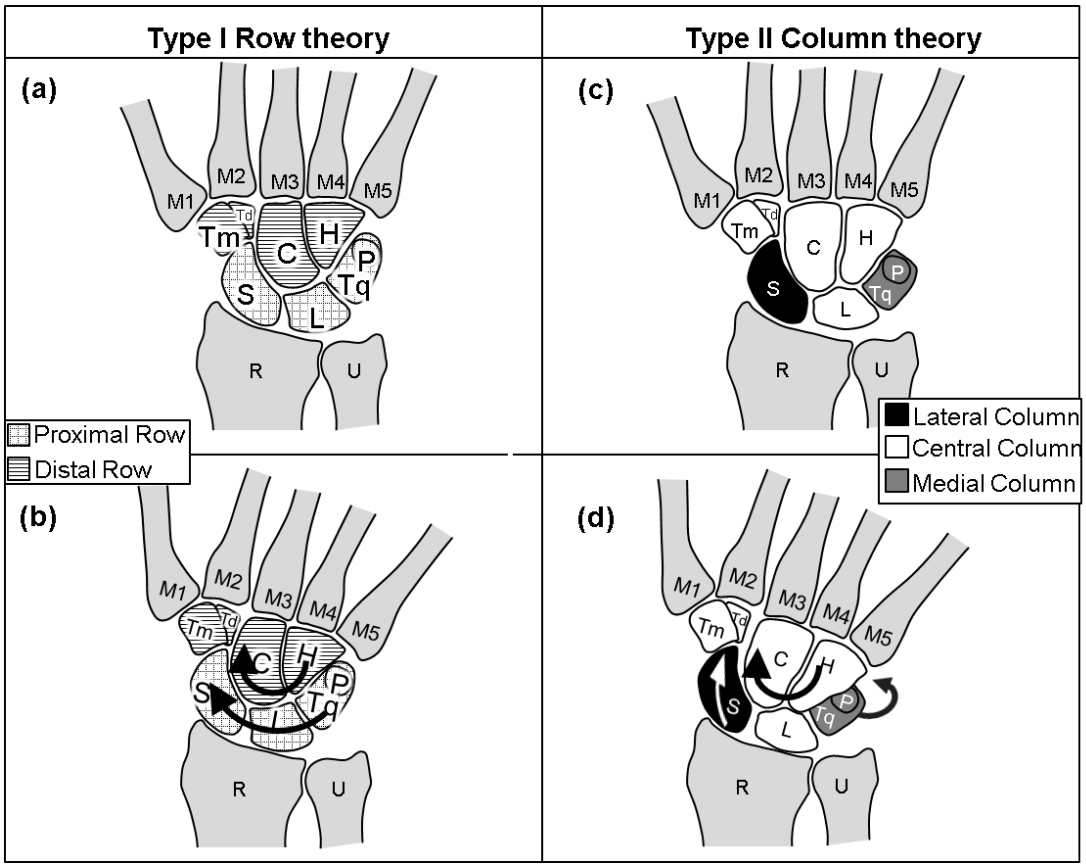

Figure 4.3: Wrist motion theories. Type I Row theory; (a) Type I, Neutral position, (b) Type I, Clenched fist ulnar deviated position. Type II Column theory; (c) Type II, Neutral position, (d) Type II, Clenched fist ulnar deviated position

A number of surgical techniques have been employed to reconstruct the SLIL following injury in cases where the SLIL is nonrepairable but the SL dissociation is reducible; these include the Brunelli tenodesis method and the modified Brunelli technique (MBT) [73, 74, 127] and, more recently, the Corella [5] and the SL axis methods (SLAM) [6]. Existing in vitro studies comparing the performance of the techniques have failed to report whether the specimens considered were type I or type II wrists [6].

4.2 Material and methods

Six FE models were developed to simulate the intact SL ligament type II wrist in neutral posture and five ulnar deviated clenched fist position cases: intact SL ligament, SLIL sectioning, and MBT, Corella, and SLAM tenodesis techniques.

To assess the performance of the reconstruction techniques, dorsal and volar SL gap and SL angle were obtained for the six scenarios from the type II wrist models. Contact areas of lunate and scaphoid bones were also obtained from the models to complement the evaluation. Additionally, the carpal mechanics was investigated to study the kinematics before and following the application of the virtual reconstruction techniques.

4.2.1 FE modelling

The FE models used in the performance evaluation of the tenodesis techniques were constructed based on the intact ligament FE model for the type II wrist which construction is described in detail in chapter 3 of this thesis, shown in Figure 4.4.

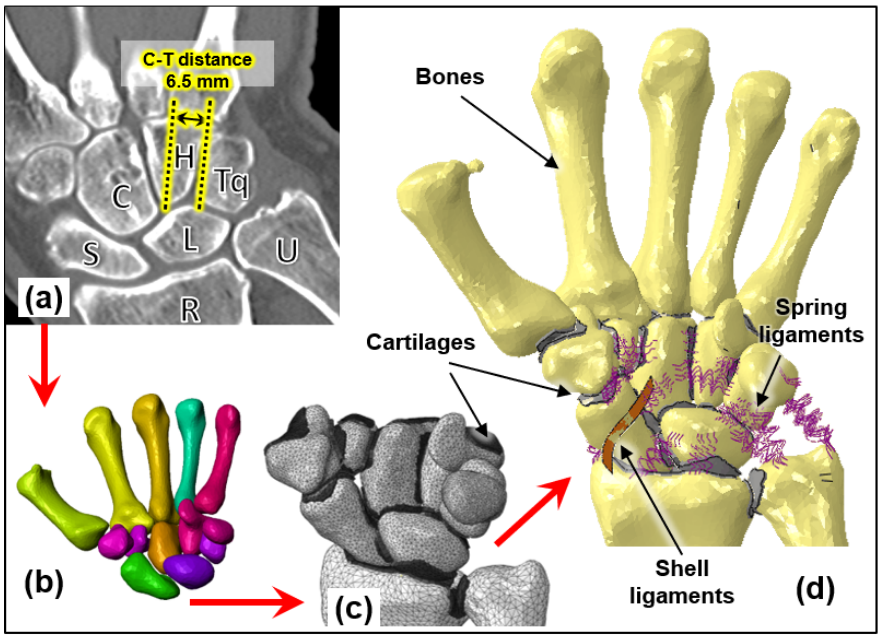

Figure 4.4: (a) CT scan, the distance between the capitate (C) and Triquetrum (Tq) is 6.5*mm*. (b) Solid parts imported into Abaqus to create the assembly of the wrist. (c) Modelling of the cartilage by offsetting of elements at the articulating surfaces between bones. (d) Finite element model of the healthy wrist showing the bones, the articular cartilage, set of ligaments, forces and boundary conditions.

4.2.2 Loading, boundary conditions, and mesh sensitivity analysis

To simulate clenched fist posture, the set up proposed by Alonso *et al* [11] was simulated in the FE model. The cadaveric study was explained in detail at subsection 3.6.2 of this thesis.

A mesh sensitivity analysis was performed using the intact model in the neutral position to ensure the accuracy of the predictions. The lunate bone contact area was considered, and mesh density was increased until the value of the contact area changed by less 5%. Table 4.1 shows the relation between the total elements of the FE model and the time to complete the simulation. Models with seed size smaller than 0.7 do not change the contact area by less of 5%. This mesh density was then employed for the subsequent analysis.

The final model consisted of a total of 507,327 elements. 10,372 are wedge elements of type C3D6 for the cartilage, 496,491 tetrahedral elements of type C3D4 for the solid bones, 301 quadrilateral elements of type S4R and 7 triangular elements of type S3 for the shell-ligaments and 156 spring element for the spring-ligament. The model had a total of 111,404 nodes.

Table 4.1: Mesh density scenarios used in the mesh sensitivity analysis.

Seed size	**Total Element**	**Completion time** $[min]$	**Contact area** mm^2
2	109,821	35	83.8
1	229,791	45	80.9
0.8	372,476	50	85.5
0.7	507,171	80	91.1
0.6	704,957	140	93.7
0.5	979,019	200	94.2

4.2.3 Virtual reconstruction

Six cases were modelled: intact-neutral clenched fist posture, intact-ulna deviated clenched fist position, SLIL sectioning ulna deviated clenched fist position, and three reconstruction techniques (Corella, MBT, and SLAM). For the SLIL sectioning case, the SLIL was fully removed, so there was no association between the scaphoid and lunate via ligament. The virtual reconstruction techniques were modelled following the description detailed in subsection 2.3.2 of this thesis.

For the virtual MBT technique, a 3-mm-diameter hole was drilled from the palmar tuberosity to the dorsal point of insertion of dorsal SLIL in the scaphoid. To produce the hole, an axis linking the insertion points at palmar and dorsal sides was positioned. Then, a 3-mm-diameter cylinder was aligned to the axis overlapping the scaphoid. The cut was done by extracting the cylindrical portion

from the bone. The same procedure to hole the bones was followed to drill the bones in the other techniques. [1]

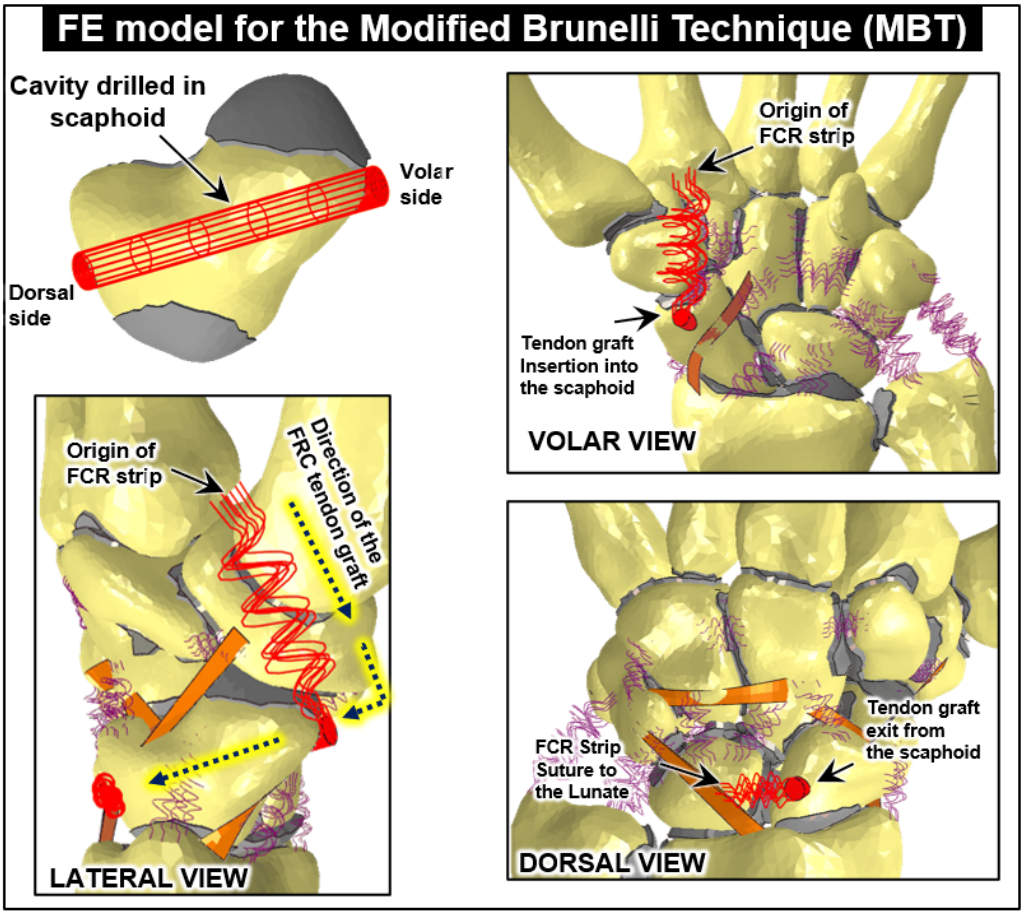

Figure 4.5: FE model for the Modified Brunelli Technique.

To generate the FE model for the MBT technique, the scaphoid in the SLIL sectioning FE model was replaced by the cut-scaphoid. An update of the interactions and contact with the other bones were implemented to set up the model. Additionally, the spring-ligaments adhered to the scaphoid had to be reconnected to the cut-scaphoid. The shell-ligaments contact and interaction were updated as well for the cut-scaphoid.

[1]The calculation of the rotation of the bones was done by setting a local reference system at the centroid of volume of the bone. After the drilling the cavity, this volume centroid changed and the local reference system was moved to the nearest node of the new volume centroid. The effect that the cavity had in the motion was not considered.

The assembly was completed by positioning a solid cylinder representing the portion of the FCR tendon graft. The cylinder passed from volar to the dorsal side of the cut-scaphoid through the hole made and then connected to the lunate bone at the dorsal side as shown in Figure 4.5. The tendon graft was fully bonded to the internal wall of the cut-scaphoid using a tie-constraint formulation. The cylinder was mesh using triangular prism elements (C3D6) and linear brick elements (C3D8).

The final FE model for the MBT technique consisted of a total of $534,481$ elements. The number of elements increased by $27,310$ due to the cut made in the scaphoid. The completion time for this model was 90 min.

In the Corella technique, the scaphoid and the lunate bone were drilled. In the scaphoid, the cavity was done from the palmar tuberosity to the dorsal point of insertion of the scapholunate ligament. In the lunate, the cavity was drilled from the dorsal to the volar side of the bone at the medial region, parallel to the articular surface.

To construct the FE model for Corella, the scaphoid and the lunate were replace in the SLIL sectioning FE model by the cut-scaphoid and the cut-lunate, respectively. The interactions and contact relationships were updated in the new assembly, as well as the ligaments attached to the two bones. Additionally, the spring-ligaments adhered to the scaphoid and lunate had to be reconnected to the cut-scaphoid. The shell-ligaments contact and interaction were updated as well for the cut-scaphoid and the cut-lunate.

The assembly was completed by positioning cylinders representing the portion of the FCR tendon graft within the bones. The cylinders representing the portion of the FCR tendon graft were passed sequentially through the scaphoid and the lunate connecting both bones at dorsal and volar sides as shown in Figure 4.6. The tendon graft was fully bonded to the internal wall of the cut-scaphoid and the cut-lunate using a tie-constraint formulation. The cylinder was mesh using

triangular prism elements (C3D6) and linear brick elements (C3D8).

The final FE model for the Corella technique consisted of a total of 556, 243 elements. The number of elements increased by 49, 072 due to the cut made in the scaphoid and lunate bones. The completion time for this model was 100 min.

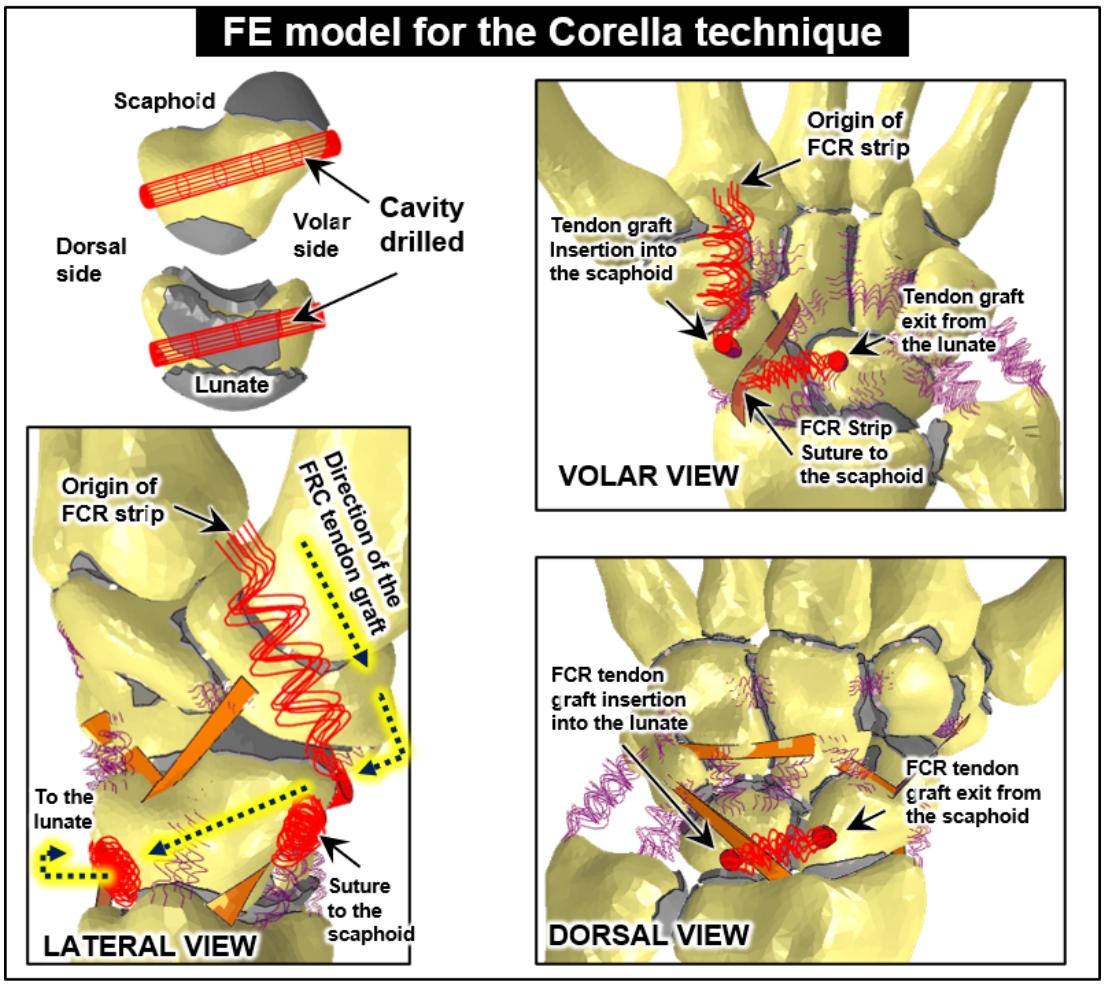

Figure 4.6: FE model for the Corella technique.

SLAM method was simulated by drilling sequentially the scaphoid and lunate on the lateral side along the coronal plane. The position of the tunnel was from mid-lateral side of the scaphoid to the proximal ulnar corner of the lunate.

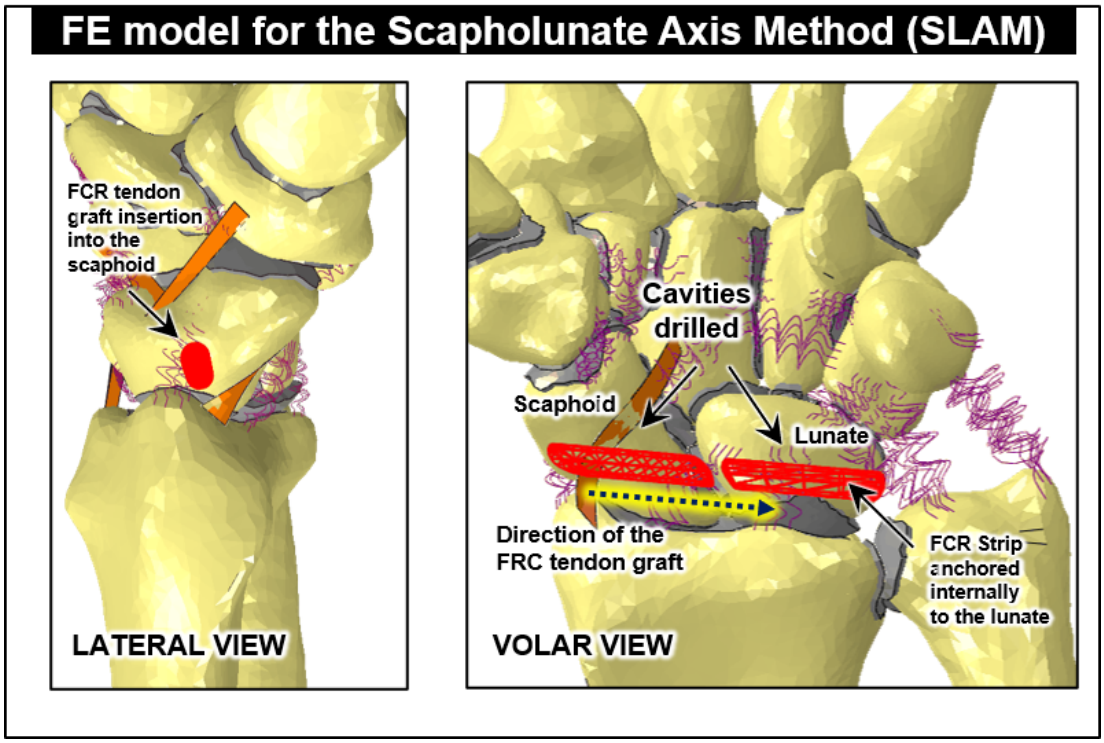

Figure 4.7: FE model for the Scapholunate Axis Method.

The assembly of the FE model for the SLAM technique was completed after replacing the cut-bones in the SLIL sectioning FE model. The interactions and contact relationships were updated in the new assembly, as well as the ligaments attached to the two bones. Additionally, the spring-ligaments adhered to the scaphoid and lunate had to be reconnected to the cut-scaphoid. The shell-ligaments contact and interaction were updated as well for the cut-scaphoid and cut-lunate.

The cylinder representing the portion of the FCR tendon graft passed sequentially through the scaphoid and anchored to the lunate connecting the central regions of both bones as can be seen in Figure 4.7. The tendon graft was fully bonded to the internal wall of the cut-scaphoid and cut-lunate using a

tie-constraint formulation. The cylinder was mesh using triangular prism elements (C3D6) and linear brick elements (C3D8). The stiffness of the tendon grafts in all cases was assumed to be the same as the stiffness of the dorsal SLIL [11].

The final FE model for the SLAM technique consisted of a total of $534,792$ elements. The number of elements increased by $27,621$ due to the cut made in the scaphoid and lunate bones. The completion time for this model was 90 min.

4.2.4 SL gap and angle calculation

The SL gap was calculated at the volar and dorsal side for the type II wrist from the models following the method by Larsen *et al* [116], described in detail in subsection 3.6.2 of this thesis.

The SL gap was calculated as the distance between two points on the edges of lunate and scaphoid at both dorsal and volar side. To locate the points to measure the SL gap, two imaginary arcs, Gilula lines, were used: a proximal arc, running along the proximal convexities of the scaphoid, lunate, and triquetrum, and a distal arc, tracing the distal curvatures of the scaphoid, lunate, and triquetrum. An auxiliary arc was then drawn at the midpoint between the proximal and distal arcs lines, and the intersection between the auxiliary arc and the edges of the scaphoid and lunate were employed to define the points used to measure the SL gap: $S_D - L_D$ for dorsal side and $S_V - L_V$ for the volar side as shown in Figure 4.8.

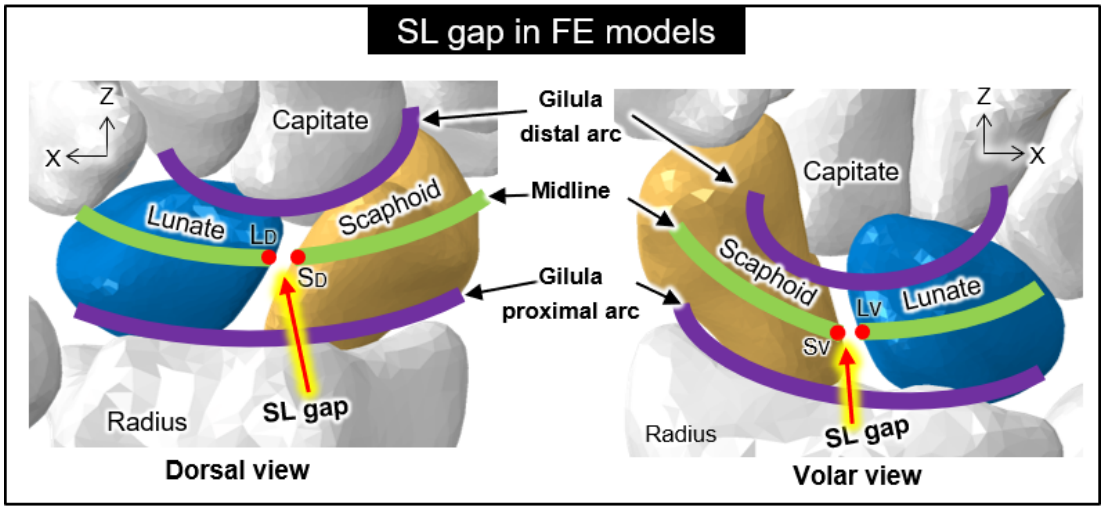

Figure 4.8: SL gap measurement in the FE models. The SL gap from FE model, calculated from the distance between two points defined at the intersection of the midline of the Gilula arcs (proximal and distal) and the border of the lunate and scaphoid.

The SL angle was calculated using two lines projected on a lateral view using the method described by Larsen et al [116]: on the scaphoid, a line tangential to the proximal and distal margins at the volar side, and on the lunate, a line perpendicular to the tangent of the two distal poles as shown in Figure 4.9.

In addition, to facilitate the comparison of the performance of the reconstruction techniques, the area affected by the rupture of SL ligament was analysed by obtaining contact area values and contact patterns for the articular cartilage surface between the scaphoid and lunate for the intact ligament case, SLIL sectioning, and the three virtual reconstructions scenarios.

In order to assess the motion of the carpal bones, the position of each bone was obtained from the numerical models for all the scenarios at neutral and ulnar deviated clenched fist positions. Each bone was represented as a point located at its volume centroid. The coordinates of each bone centroid were plotted for the two positions to visualise the motion in three orthogonal planes.

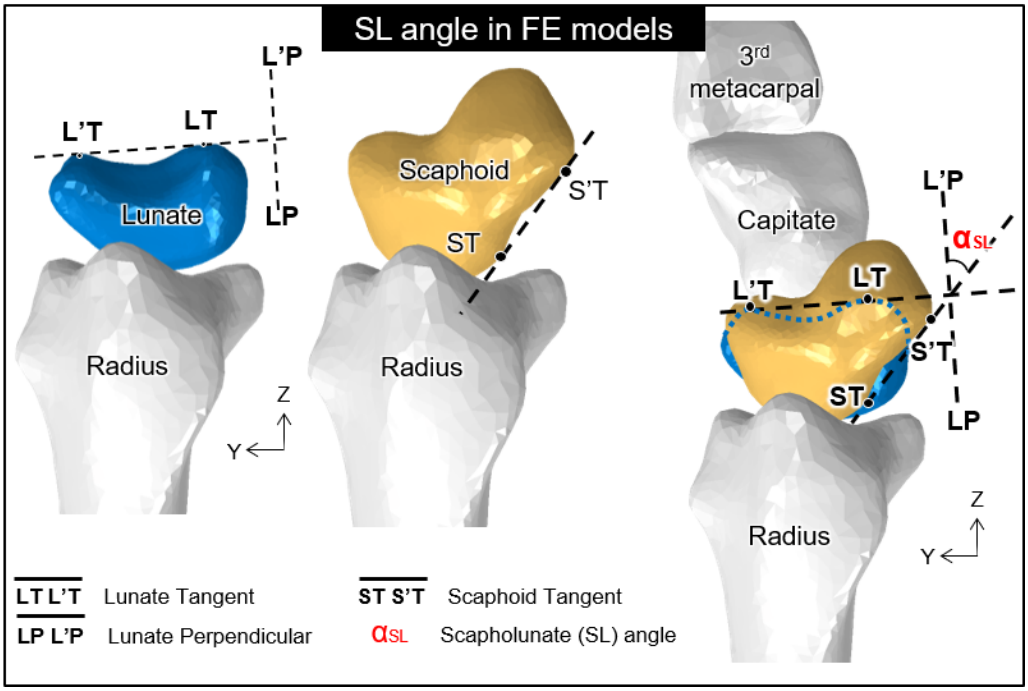

Figure 4.9: SL angle measured between two lines in the lateral view. Line 1 (LP-L'P), perpendicular to the tangent line of the two distal poles of the lunate (LT-L'T). Line 2 (ST-S'T) a tangent line of the proximal and distal margin of the scaphoid at palmar side. The SL angle is the angle between Line 1 and Line 2.

4.3 Results

4.3.1 Reconstruction techniques comparison: Dorsal and volar SL gap and angle

The predicted values for the SL gap for all the scenarios including the reconstruction techniques are presented in Table 4.2 for the type II wrist. For the intact scenario in the neutral position, the SL gaps predicted by the type II wrist model were 2.4 and 2.5mm at the dorsal and volar side, respectively. For the ulnar deviated clenched fist position, the SL increased to 2.8mm at both dorsal and volar side, an increase of 16.6% and 12.0%, respectively, compared with the neutral position.

Table 4.2: Result for the SL gap and SL angle from the FE models.

Scenarios	**SL gap [mm]**		**SL angle [°]**
	Dorsal	**Volar**	
Intact ligaments at neutral position	2.4	2.5	42.3
Intact ligaments	2.8	2.8	44.8
SLIL sectioning	3.5	3.1	45.9
Corella	2.7	2.6	41
Scapholunate Axis Method (SLAM)	2.7	2.4	40.5
Modified Brunelli Technique (MBT)	2.7	3.1	39.8

Following SLIL sectioning, in ulnar deviated clenched fist position, the SL gap increased by $0.7mm$ (25%) and $0.3mm$ (10.7%) at dorsal and volar side compared with the intact scenario. At the dorsal side, all three reconstruction techniques reduced the SL gap by $0.8mm$ (20%) compared with the SLIL sectioning to $0.1mm$ (3.5%) less than that of the intact scenario. At the volar side, the Corella and the SLAM techniques both reduced SL gap compared with SLIL sectioning, by $0.5mm$ (16%) and $0.7mm$ (22.6%), respectively, to $0.2mm$ (7.1%) and $0.4mm$ (14.2%) lower respectively than the intact scenario. The MBT technique failed to reduce the volar SL gap following SLIL sectioning, with the gap remaining $0.3mm$ (10.7%) greater than for the intact scenario [2].

[2]This thesis uses extensively anacronyms of surgical procedures: Modified Brunelli technique (MBT) and Scapholunate axis method (SLAM). Occasionally, the anacronym is followed by a word that causes pleonasm word sequence, for example MBT technique or SLAM method. The author decided to permit the pleonasm in order to preserve the clinical anacronyms and give fluency to the redaction.

Predicted values for SL angle for the type II wrist for the scenarios are presented also in Table 4.2. The SL angle from the intact scenario increased by 5.9% from 42.3° at the neutral position to 44.8° at the ulnar deviated clenched fist position. After SLIL sectioning, SL angle increased by 1.1° (2.5%). The reconstruction techniques all reduced SL angle compared with the SLIL sectioning case to below the intact value: Corella, SLAM, and MBT techniques reduced SL angle to below the intact ulna deviate clenched value by 3.8° (8.4%), 4.3° (9.6%), and 5° (11.2%), respectively.

4.3.2 Contact area: Scaphoid - lunate bones

Figure 4.10 shows the contact area patterns and values between the scaphoid and lunate for the various scenarios. Results are shown next to corresponding values for a type I wrist, obtained from a previous study reported by Alonso *et al* [11] from FE models of type I wrist. The values for the type I wrist were not previously reported but have been calculated to be able to compare between type I and type II wrist.

For the type I wrist, in the intact ulnar deviated clenched fist case, a relatively small region ($1.2mm^2$) of scaphoidlunate contact area can be discerned towards the dorsal side of the lunate as shown in Figure 4.10. Following SLIL sectioning, there is no contact at all between the scaphoid and the lunate. The Corella reconstruction technique restored the connection between the scaphoid and lunate, resulting in a contact region of similar shape, location, and area ($1.7mm^2$) to the intact wrist ulnar deviated clenched fist case. The MBT technique failed to restore any contact between the scaphoid and lunate, whereas SLAM resulted in increased contact between the scaphoid and lunate, resulting in a contact region of greater area ($3.8mm^2$) being produced towards the location of the hole drilled in the scaphoid through which the graft passes.

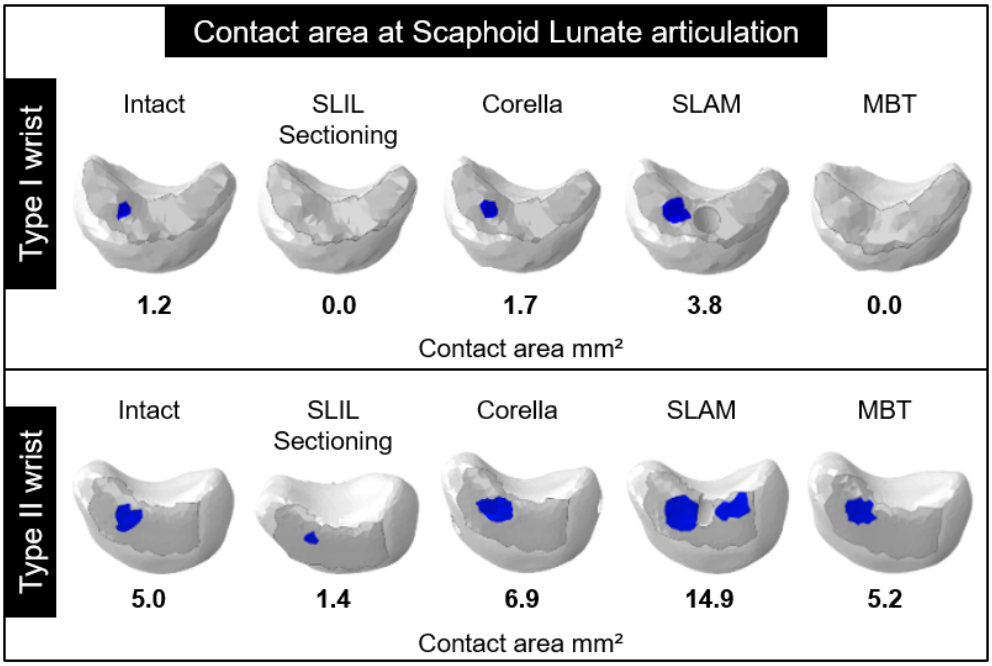

Figure 4.10: Comparison of the contact area patterns at the Scaphoid Lunate interface for the intact, SLIL Sectioning and the three tenodesis techniques.

For the type II wrist, in the intact ulnar deviated clenched fist case, a region ($5.0mm$) of scaphoidlunate contact can be seen towards the dorsal side of the lunate as shown in Figure 4.10. Following SLIL sectioning, a small contact region remains ($1.4mm^2$) between scaphoid and lunate. Corella results in the connection between the scaphoid and lunate being restored, resulting in a contact region of similar shape, location, and area ($6.9mm^2$) to the intact wrist ulnar deviated clenched fist case. As with the type I wrist, SLAM results in increased contact between the scaphoid and lunate, medially ($14.8mm^2$), around the scaphoid graft hole, compared with the intact ($5mm^2$). Of the three techniques, MBT resulted in scaphoidlunate contact area ($5.2mm^2$) closer to the intact case.

4.3.3 Type I and II carpal mechanics: Row/column theory

Figure 4.11 shows the motion pattern of the bones of the carpal joint for both the type I and type II wrist when moving from the neutral to ulnar deviated clench fist position; superior, volar, and lateral views are presented.

For the type I wrist, the plots show that scaphoid and lunate displacement is relatively small during the motion. The scaphoid and lunate exhibit similar displacement in two planes (ZX and ZY); in plane ZX, both bones displaced $1.2mm$, whilst in plane ZY, scaphoid displaced $1.5mm$ and lunate $1.6mm$; scaphoid displacement is greater compared with the lunate in the YX plane, 1.3 and $0.9mm$, respectively. Triquetrum and pisiform displacement are similar in all three planes and of greater magnitude than the scaphoid and lunate. The displacement of the trapezoid, trapezium, capitate, and hamate is appreciably greater than that of the scaphoid and lunate; in addition, these bones exhibit a similar displacement pattern.

For the type II wrist, the plots indicate that as the wrist moves from the neutral to ulnar deviated clench fist position, the triquetrum and pisiform displace dorsally, exhibiting similar displacement in the three planes. In comparison, scaphoid displacement is smaller in the volar and distal directions. The trapezoid, trapezium, capitate, hamate, and lunate all exhibit a similar movement pattern, with displacement less than the triquetrum, pisiform, and scaphoid. Whilst scaphoid and lunate displacement is similar in the YX plane (1.1 and $1.2mm$, respectively), differences can be clearly seen in the ZX where scaphoid moved $0.6mm$ and lunate $1.2mm$, and ZY planes where scaphoid moved $0.9mm$ and lunate $0.7mm$.

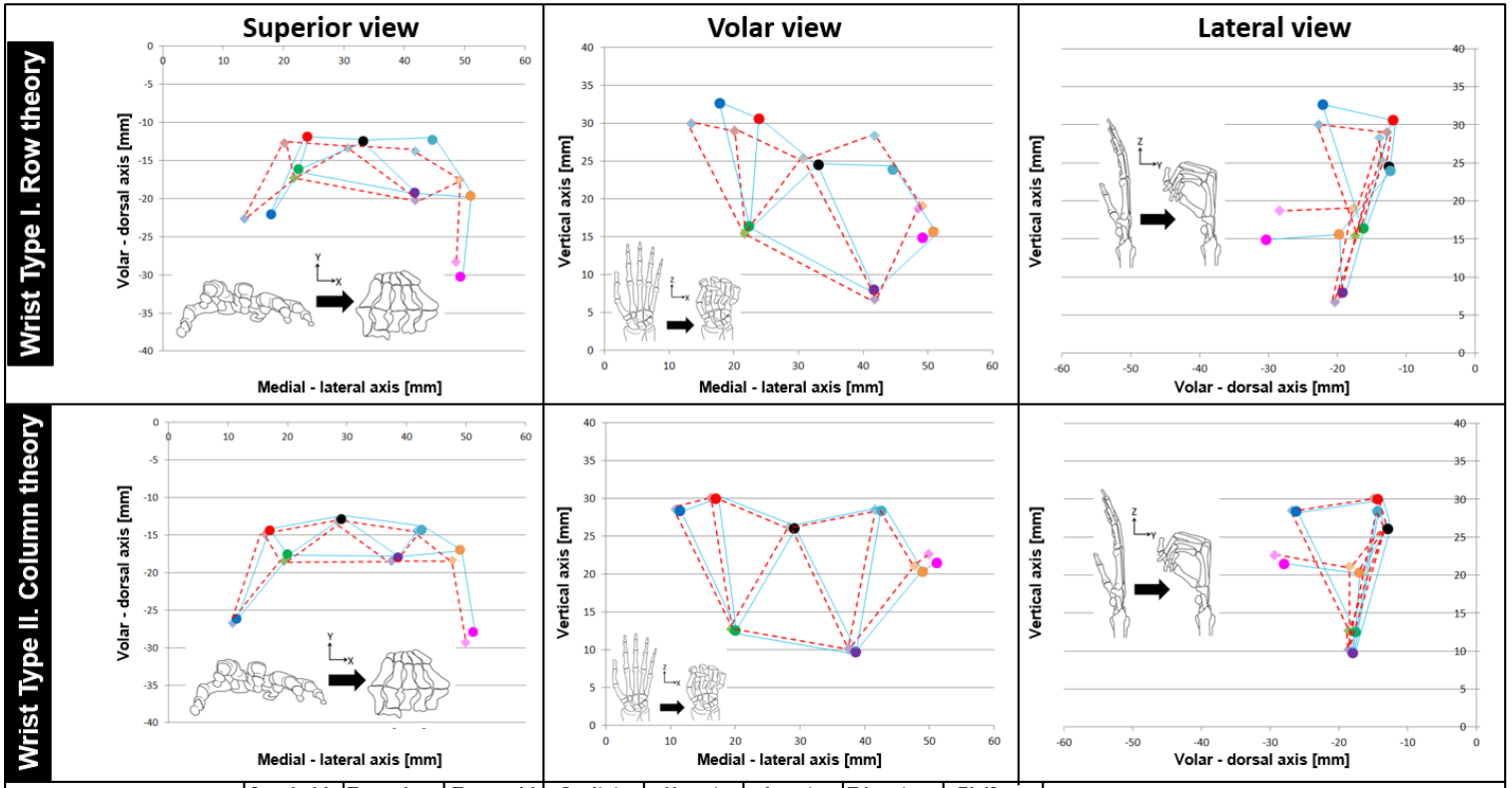

		Scaphoid	Trapezium	Trapezoid	Capitate	Hamate	Lunate	Triquetrum	Pisiform
X-Y PLANE	Type I	1.3	4.5	3.9	2.6	3.2	0.9	2.7	2.0
	Type II	1.1	0.9	0.9	0.8	0.9	1.2	2.2	1.9
Z-X PLANE	Type I	1.2	5.2	4.1	2.6	5.2	1.2	3.8	3.9
	Type II	0.6	0.7	0.7	0.7	0.9	1.2	1.8	1.7
Z-Y PLANE	Type I	1.5	2.7	1.8	1.2	4.6	1.6	4.6	4.3
	Type II	0.9	0.6	0.5	0.3	0.2	0.7	1.6	1.8
3D XYZ	Type I	1.6	5.2	4.2	2.8	5.4	1.6	4.4	4.3
	Type II	1.1	0.9	0.9	0.8	1.0	1.3	2.3	2.2

The distance of the centroid of each bone when moving from neutral to ulnar deviated clench fist position [mm]

Neutral – Neutral position

CF-UD – Clench fist – Ulnar Deviation position

Capitate, Hamate, Scaphoid, Trapezoid, Lunate, Pisiform, Trapezium, Triquetrum

Figure 4.11: Comparison of the motion for type I and type II wrist during ulnar deviation.

4.3.4 Type I and II performance of the reconstruction techniques: Wrist kinematics

The carpal kinematics variation after the sectioning of the scapholunate ligament and the application of the reconstruction techniques was assessed by comparing the position of the carpal bones using as a benchmark their position from the intact ligament scenario.

For the ulnar deviated clench fist position, the location of the carpal bones was reported in three views: superior, volar, and lateral. Also, a tabular comparison of the position of the centroid of each of the carpal joint bones for the SLIL sectioning and Corella, SLAM and MBT techniques compared with the intact wrist.

In comparison of the techniques, Table 4.3 shows the distance calculated between the points representing the centroids of the scaphoid and lunate bones, following SLIL sectioning and Corella, SLAM, and MBT techniques compared with the intact wrist case for both the type I and type II wrist in the ulnar deviated clenched fist position. The FE analysis software, Abaqus, provided the coordinates of the centroids of the bones, facilitating their tracking during the movement.

Table 4.3: Distance between centroids of the scaphoid and lunate bone.

Case	**Type I wrist** $[mm]$	**Type II wrist** $[mm]$
Intact	21.26	18.81
SLIL	22.46	19.05
Corella	21.16	18.60
SLAM	21.96	17.81
MBT	21.63	18.88

4.3.4.1 Type I wrist

It can be seen upon inspection of in Figure 4.12 that after SLIL sectioning of the type I wrist, the scaphoid exhibited greater displacement in the three planes compared with the lunate ($2.05mm$ overall compared with $1.62mm$). Displacement of the lunate was similar to that of the intact case, only 1.9% greater overall, whereas scaphoid displacement was 22.8% greater compared with the intact wrist. The distance between the scaphoid and lunate centroids increased by $1.2mm$ compared with the intact wrist as a result of SLIL sectioning as shown in Table 4.3.

Figure 4.13 shows that following application of the Corella technique, the scaphoid and lunate displacement pattern was similar to that of the intact scenario (lunate displacement 0.63% lower, scaphoid 3.6% greater), with the distance between the centroids of the two bones being slightly smaller compared with the intact case ($0.1mm$ less, Table 4.3). No significant change in the motion of the other carpal bones was discernible.

For the SLAM technique, shown in Figure 4.14, scaphoid and lunate displacement pattern diverged from that of the intact (lunate displacement 6.9% lower, scaphoid 12% greater). The distance between the scaphoid and lunate was greater compared with the intact case (by $0.7mm$, Table 4.3), with the lunate exhibiting displacement more to the volar side than the intact case with the scaphoid displacing towards the proximal pole, at the articulation area with the scaphoid.

After MBT reconstruction, the scaphoid and lunate displacement was similar in nature to the intact case as shown in Figure 4.15, with the distance between the centroids of the two bones being greater compared with the intact case (by $0.37mm$, Table 4.3) but smaller compared with the SLAM technique. No significant change compared with the intact wrist in the displacement pattern of the remaining carpal bones was observed following MBT reconstruction.

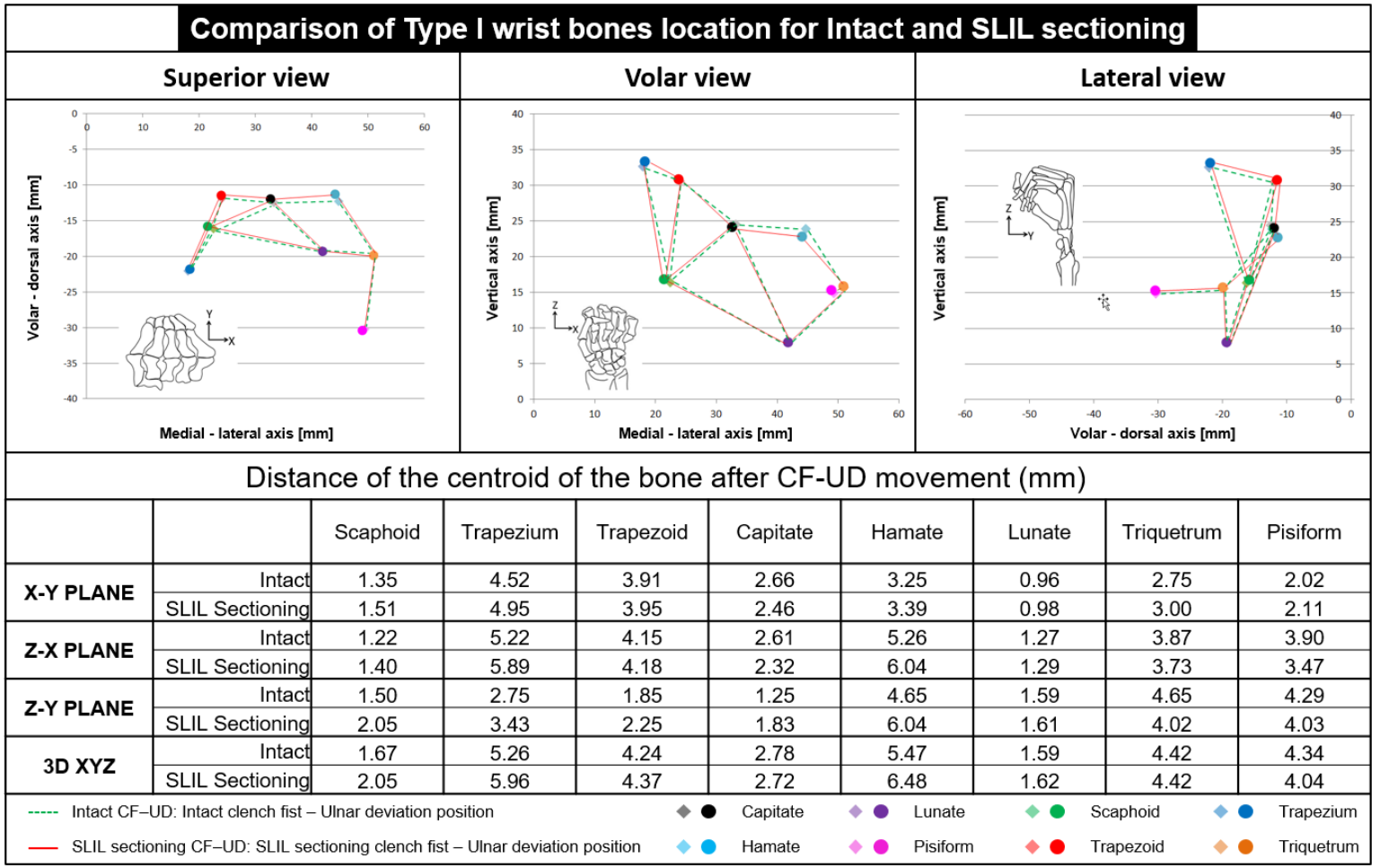

Distance of the centroid of the bone after CF-UD movement (mm)

		Scaphoid	Trapezium	Trapezoid	Capitate	Hamate	Lunate	Triquetrum	Pisiform
X-Y PLANE	Intact	1.35	4.52	3.91	2.66	3.25	0.96	2.75	2.02
	SLIL Sectioning	1.51	4.95	3.95	2.46	3.39	0.98	3.00	2.11
Z-X PLANE	Intact	1.22	5.22	4.15	2.61	5.26	1.27	3.87	3.90
	SLIL Sectioning	1.40	5.89	4.18	2.32	6.04	1.29	3.73	3.47
Z-Y PLANE	Intact	1.50	2.75	1.85	1.25	4.65	1.59	4.65	4.29
	SLIL Sectioning	2.05	3.43	2.25	1.83	6.04	1.61	4.02	4.03
3D XYZ	Intact	1.67	5.26	4.24	2.78	5.47	1.59	4.42	4.34
	SLIL Sectioning	2.05	5.96	4.37	2.72	6.48	1.62	4.42	4.04

Intact CF–UD: Intact clench fist – Ulnar deviation position

SLIL sectioning CF–UD: SLIL sectioning clench fist – Ulnar deviation position

Capitate Lunate Scaphoid Trapezium

Hamate Pisiform Trapezoid Triquetrum

Figure 4.12: Location of the bones after clench fist position comparing the intact scenario to the SLIL sectioning scenario.

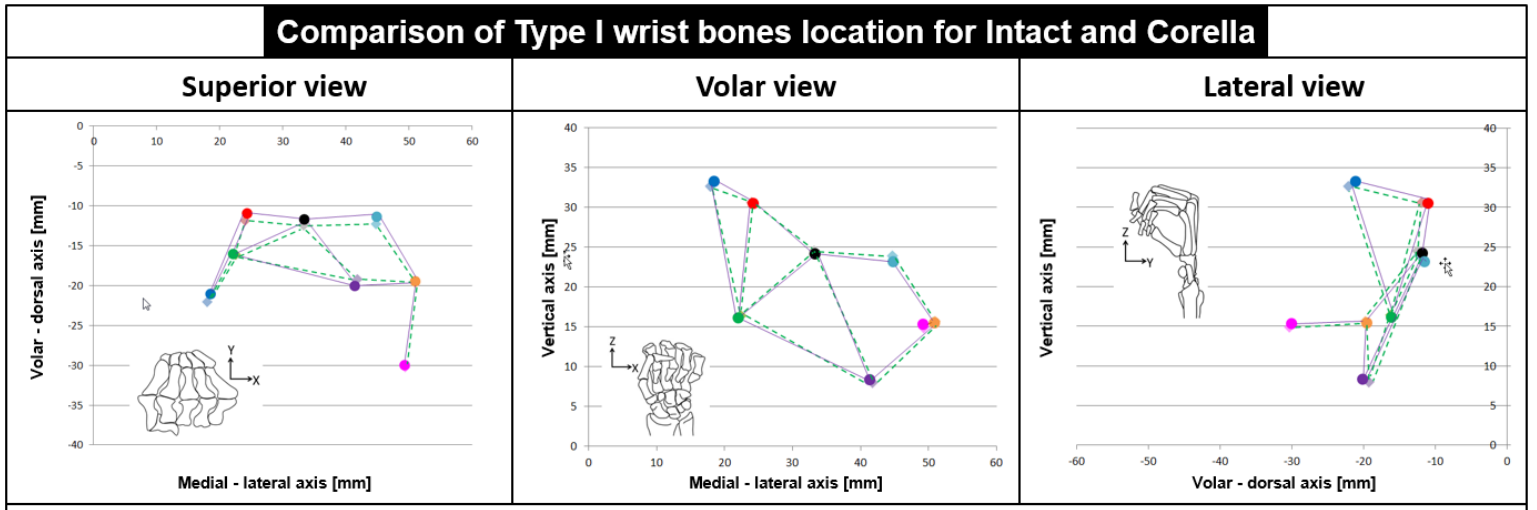

Distance of the centroid of the bone after CF-UD movement (mm)

		Scaphoid	Trapezium	Trapezoid	Capitate	Hamate	Lunate	Triquetrum	Pisiform
X-Y PLANE	Intact	1.35	4.52	3.91	2.66	3.25	0.96	2.75	2.02
	Corella	1.5	5.31	4.53	3.14	3.85	0.9	2.67	1.79
Z-X PLANE	Intact	1.22	5.22	4.15	2.61	5.26	1.27	3.87	3.90
	Corella	1.35	6.03	4.45	2.9	5.99	1.32	4.05	3.49
Z-Y PLANE	Intact	1.50	2.75	1.85	1.25	4.65	1.59	4.65	4.29
	Corella	1.73	3.6	2.35	1.98	5.67	1.58	4.08	3.8
3D XYZ	Intact	1.67	5.26	4.24	2.78	5.47	1.59	4.42	4.34
	Corella	1.73	3.6	2.35	1.98	5.67	1.58	4.08	3.8

Intact CF–UD: Intact clench fist – Ulnar deviation position

Corella CF–UD: Corella clench fist – Ulnar deviation position

Capitate, Lunate, Scaphoid, Trapezium, Hamate, Pisiform, Trapezoid, Triquetrum

Figure 4.13: Location of the bones after clench fist position comparing the intact scenario to the Corella technique.

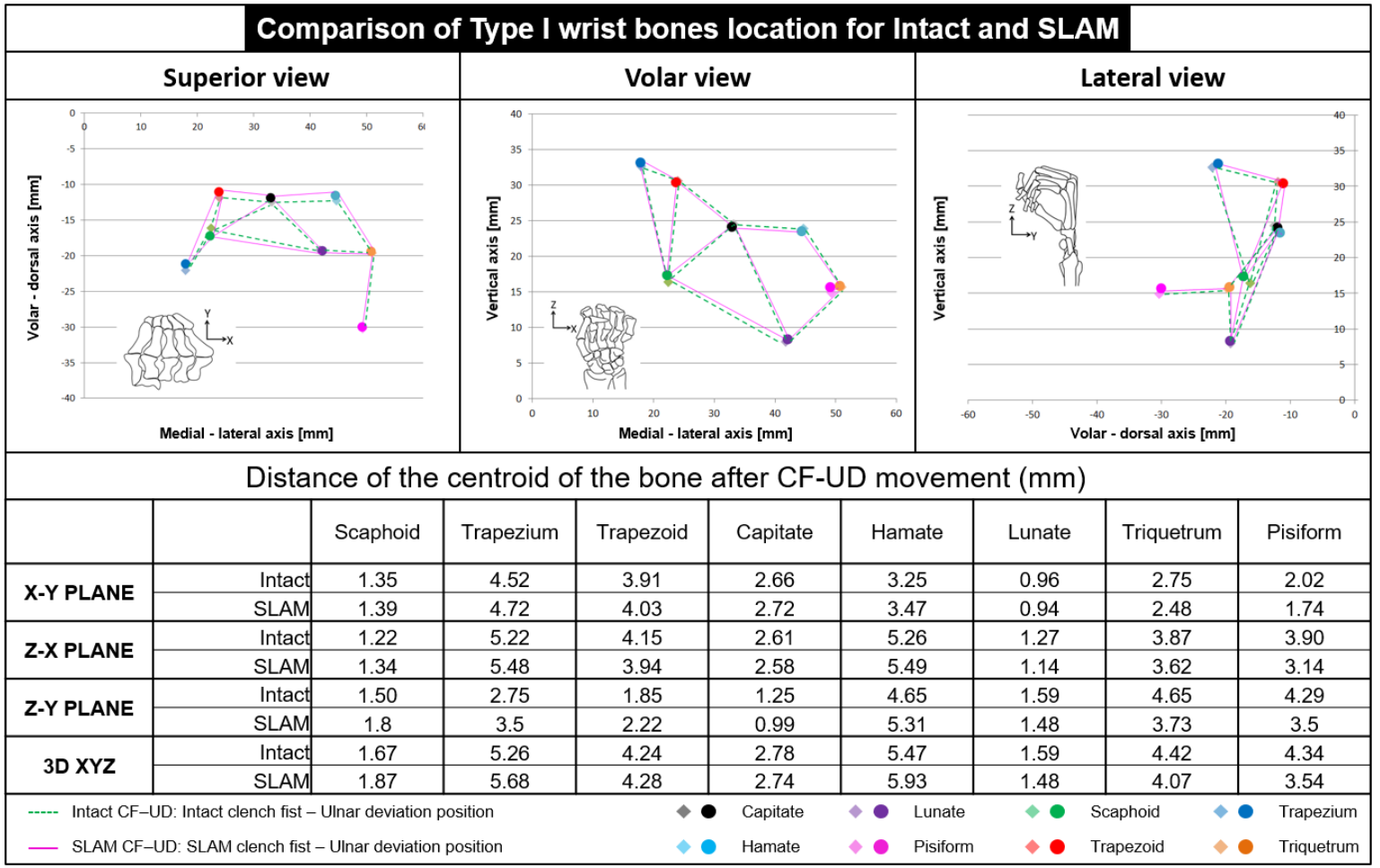

		Scaphoid	Trapezium	Trapezoid	Capitate	Hamate	Lunate	Triquetrum	Pisiform
X-Y PLANE	Intact	1.35	4.52	3.91	2.66	3.25	0.96	2.75	2.02
	SLAM	1.39	4.72	4.03	2.72	3.47	0.94	2.48	1.74
Z-X PLANE	Intact	1.22	5.22	4.15	2.61	5.26	1.27	3.87	3.90
	SLAM	1.34	5.48	3.94	2.58	5.49	1.14	3.62	3.14
Z-Y PLANE	Intact	1.50	2.75	1.85	1.25	4.65	1.59	4.65	4.29
	SLAM	1.8	3.5	2.22	0.99	5.31	1.48	3.73	3.5
3D XYZ	Intact	1.67	5.26	4.24	2.78	5.47	1.59	4.42	4.34
	SLAM	1.87	5.68	4.28	2.74	5.93	1.48	4.07	3.54

Figure 4.14: Location of the bones after clench fist position comparing the intact scenario to the Scapholunate axis method (SLAM).

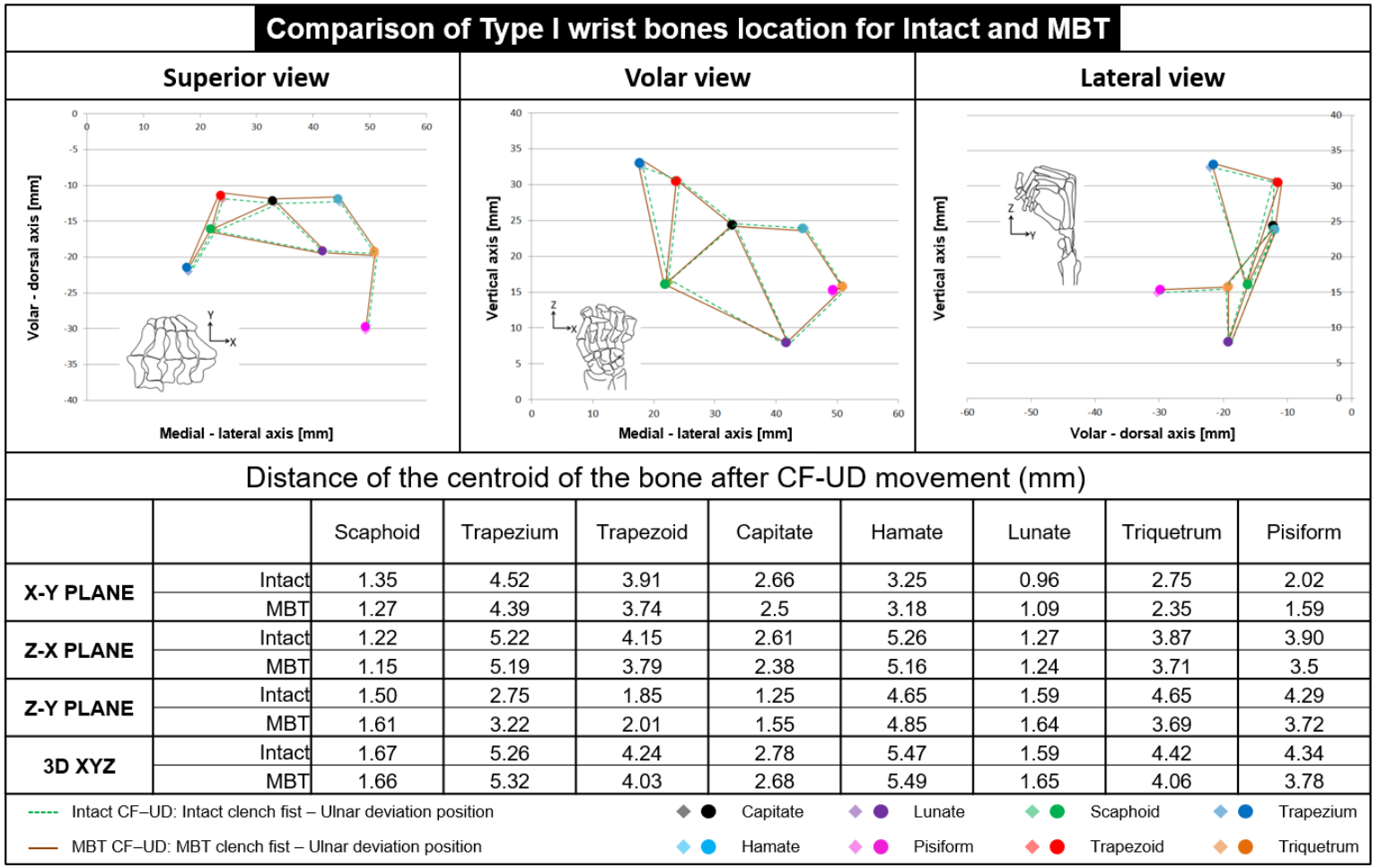

Distance of the centroid of the bone after CF-UD movement (mm)

		Scaphoid	Trapezium	Trapezoid	Capitate	Hamate	Lunate	Triquetrum	Pisiform
X-Y PLANE	Intact	1.35	4.52	3.91	2.66	3.25	0.96	2.75	2.02
	MBT	1.27	4.39	3.74	2.5	3.18	1.09	2.35	1.59
Z-X PLANE	Intact	1.22	5.22	4.15	2.61	5.26	1.27	3.87	3.90
	MBT	1.15	5.19	3.79	2.38	5.16	1.24	3.71	3.5
Z-Y PLANE	Intact	1.50	2.75	1.85	1.25	4.65	1.59	4.65	4.29
	MBT	1.61	3.22	2.01	1.55	4.85	1.64	3.69	3.72
3D XYZ	Intact	1.67	5.26	4.24	2.78	5.47	1.59	4.42	4.34
	MBT	1.66	5.32	4.03	2.68	5.49	1.65	4.06	3.78

Intact CF–UD: Intact clench fist – Ulnar deviation position
MBT CF–UD: MBT clench fist – Ulnar deviation position
Capitate, Lunate, Scaphoid, Trapezium, Hamate, Pisiform, Trapezoid, Triquetrum

Figure 4.15: Location of the bones after clench fist position comparing the intact scenario to the modified Brunelli technique (MBT).

4.3.4.2 Type II wrist

Figure 4.16 shows that following SLIL sectioning of the type II wrist, both scaphoid and lunate movement remains close to that of the intact, displacement of the two bones was slightly greater ($0.1mm$ lunate, $0.4mm$ scaphoid), but the relative position of the two bones remains very similar to the intact ligament case, with scaphoidlunate centroid distance increasing by only $0.24mm$ in comparison as can be seen in Table 4.3.

Following application of the Corella technique, the displacement of the trapezium, trapezoid, capitate, and hamate remained similar to that of the intact case, but lunate displacement was altered as a consequence of gap overclosure after applying the reconstruction technique as can be seen in Figure 4.17. In addition, the scaphoid moved slightly more towards the lunate; however, the direction of the motion for both the scaphoid and lunate was broadly similar to the intact case but with the magnitude being greater for both bones ($0.1mm$ scaphoid, $0.3mm$ lunate). For the Corella technique, scaphoidlunate centroid distance was $0.21mm$ less than the intact case (Table 4.3).

Following application of the SLAM technique, scaphoid displacement was more towards the lunate compared with the intact case, with the scaphoid taking a more vertical position during the movement to the ulnar deviated clench fist position as shown in Figure 4.18. Compared with the intact wrist, both scaphoid and lunate motion was greater ($0.4mm$ scaphoid, $0.2mm$ lunate). The motion of the trapezium, trapezoid, capitate, and hamate and of the triquetrum and pisiform was not significantly altered following application of the technique. Lunate displacement tended to be more in the lateral direction with the distance between the lunate and scaphoid bones being discernibly less (by $1mm$, Table 4.3), following SLAM application compared with the intact scenario.

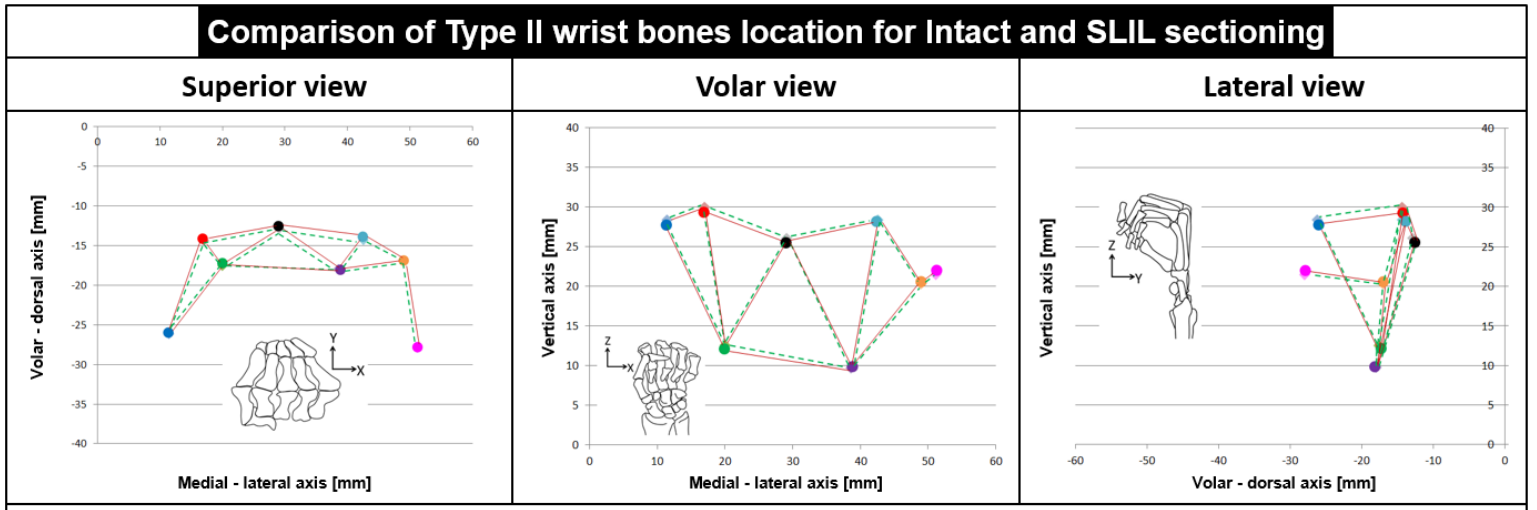

Distance of the centroid of the bone after CF-UD movement (mm)

		Scaphoid	Trapezium	Trapezoid	Capitate	Hamate	Lunate	Triquetrum	Pisiform
X-Y PLANE	Intact	1.1	0.9	0.9	0.8	0.9	1.2	2.2	1.9
	SLIL Sectioning	1.3	0.9	0.9	0.8	1	1.4	2	2
Z-X PLANE	Intact	0.6	0.7	0.7	0.7	0.9	1.2	1.8	1.7
	SLIL Sectioning	0.8	1	0.9	0.9	0.8	1.4	1.4	1.4
Z-Y PLANE	Intact	0.9	0.6	0.5	0.3	0.2	0.7	1.6	1.8
	SLIL Sectioning	1.4	1.1	1	0.9	0.7	0.5	1.5	1.6
3D XYZ	Intact	1.1	0.9	0.9	0.8	1	1.3	2.3	2.2
	SLIL Sectioning	1.5	1.2	1.2	1.1	1	1.4	2	2

Intact CF–UD: Intact clench fist – Ulnar deviation position

SLIL sectioning CF–UD: SLIL sectioning clench fist – Ulnar deviation position

Capitate Lunate Scaphoid Trapezium

Hamate Pisiform Trapezoid Triquetrum

Figure 4.16: Location of the bones after clench fist position comparing the intact scenario to the SLIL sectioning scenario for a type II wrist.

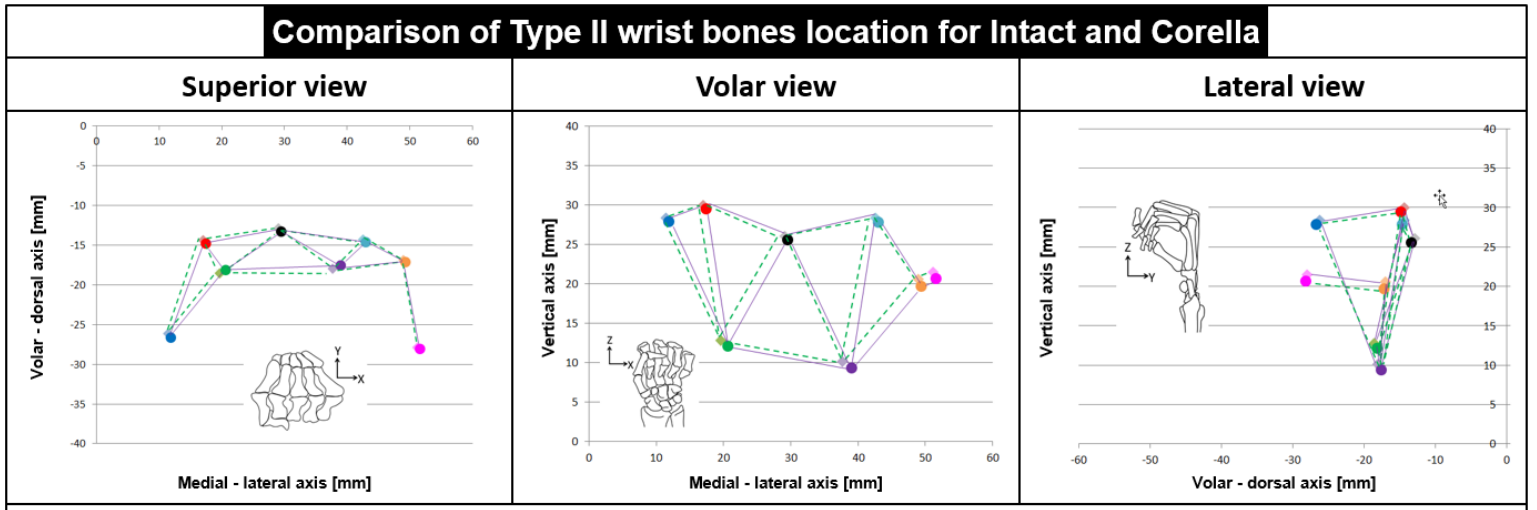

Distance of the centroid of the bone after CF-UD movement (mm)

		Scaphoid	Trapezium	Trapezoid	Capitate	Hamate	Lunate	Triquetrum	Pisiform
X-Y PLANE	Intact	1.1	0.9	0.9	0.8	0.9	1.2	2.2	1.9
	Corella	1	1.1	1.1	1.1	1.3	1.4	2.1	2.1
Z-X PLANE	Intact	0.6	0.7	0.7	0.7	0.9	1.2	1.8	1.7
	Corella	1.2	1.2	1.3	1.3	1.5	1.5	2.2	2.6
Z-Y PLANE	Intact	0.9	0.6	0.5	0.3	0.2	0.7	1.6	1.8
	Corella	0.8	0.6	0.6	0.7	0.7	0.9	1.9	2.3
3D XYZ	Intact	1.1	0.9	0.9	0.8	1	1.3	2.3	2.2
	Corella	1.2	1.2	1.3	1.3	1.5	1.6	2.5	2.8

Intact CF–UD: Intact clench fist – Ulnar deviation position

Corella CF–UD: Corella clench fist – Ulnar deviation position

Capitate, Lunate, Scaphoid, Trapezium, Hamate, Pisiform, Trapezoid, Triquetrum

Figure 4.17: Location of the bones after clench fist position comparing the intact scenario to the Corella technique for a type II wrist.

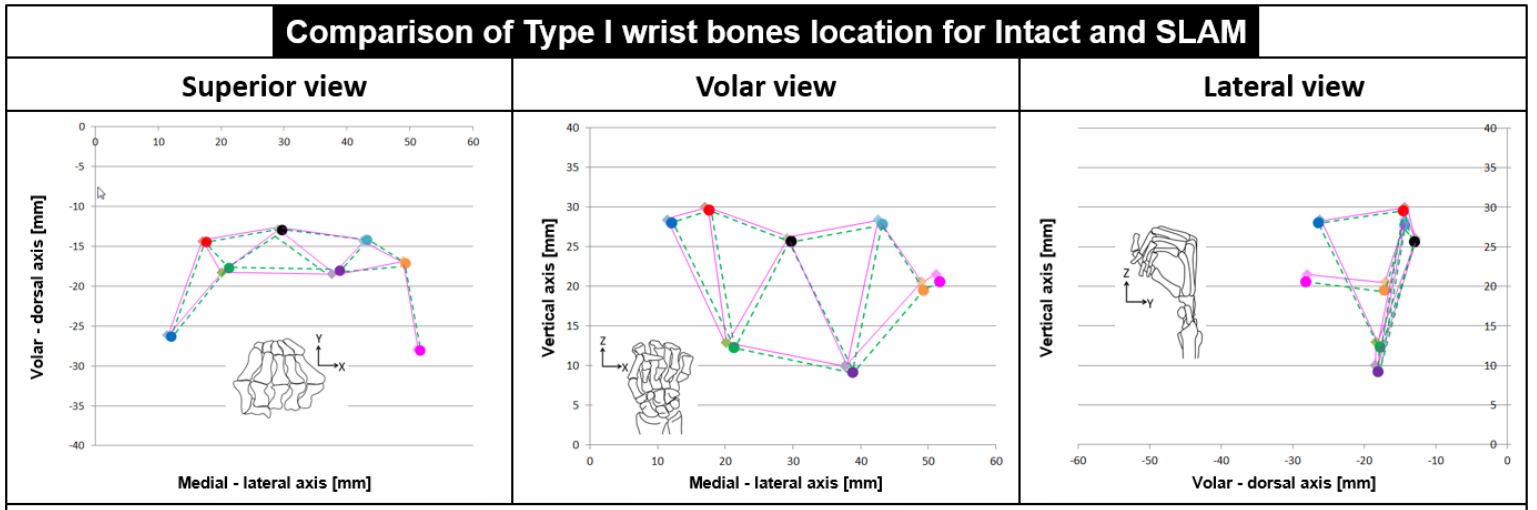

Distance of the centroid of the bone after CF-UD movement (mm)

		Scaphoid	Trapezium	Trapezoid	Capitate	Hamate	Lunate	Triquetrum	Pisiform
X-Y PLANE	Intact	1.1	0.9	0.9	0.8	0.9	1.2	2.2	1.9
	SLAM	1.4	1.4	1.4	4.3	1.5	1.3	2.1	2.1
Z-X PLANE	Intact	0.6	0.7	0.7	0.7	0.9	1.2	1.8	1.7
	SLAM	1.4	1.4	1.4	1.4	1.7	1.4	2.3	2.7
Z-Y PLANE	Intact	0.9	0.6	0.5	0.3	0.2	0.7	1.6	1.8
	SLAM	0.9	0.7	0.6	0.6	0.7	0.9	2.0	2.4
3D XYZ	Intact	1.1	0.9	0.9	0.8	1	1.3	2.3	2.2
	SLAM	1.5	1.5	1.5	1.4	1.7	1.5	2.6	2.9

Intact CF–UD: Intact clench fist – Ulnar deviation position

SLAM CF–UD: SLAM clench fist – Ulnar deviation position

Capitate, Lunate, Scaphoid, Trapezium, Hamate, Pisiform, Trapezoid, Triquetrum

Figure 4.18: Location of the bones after clench fist position comparing the intact scenario to the Scapholunate axis method (SLAM) for a type II wrist.

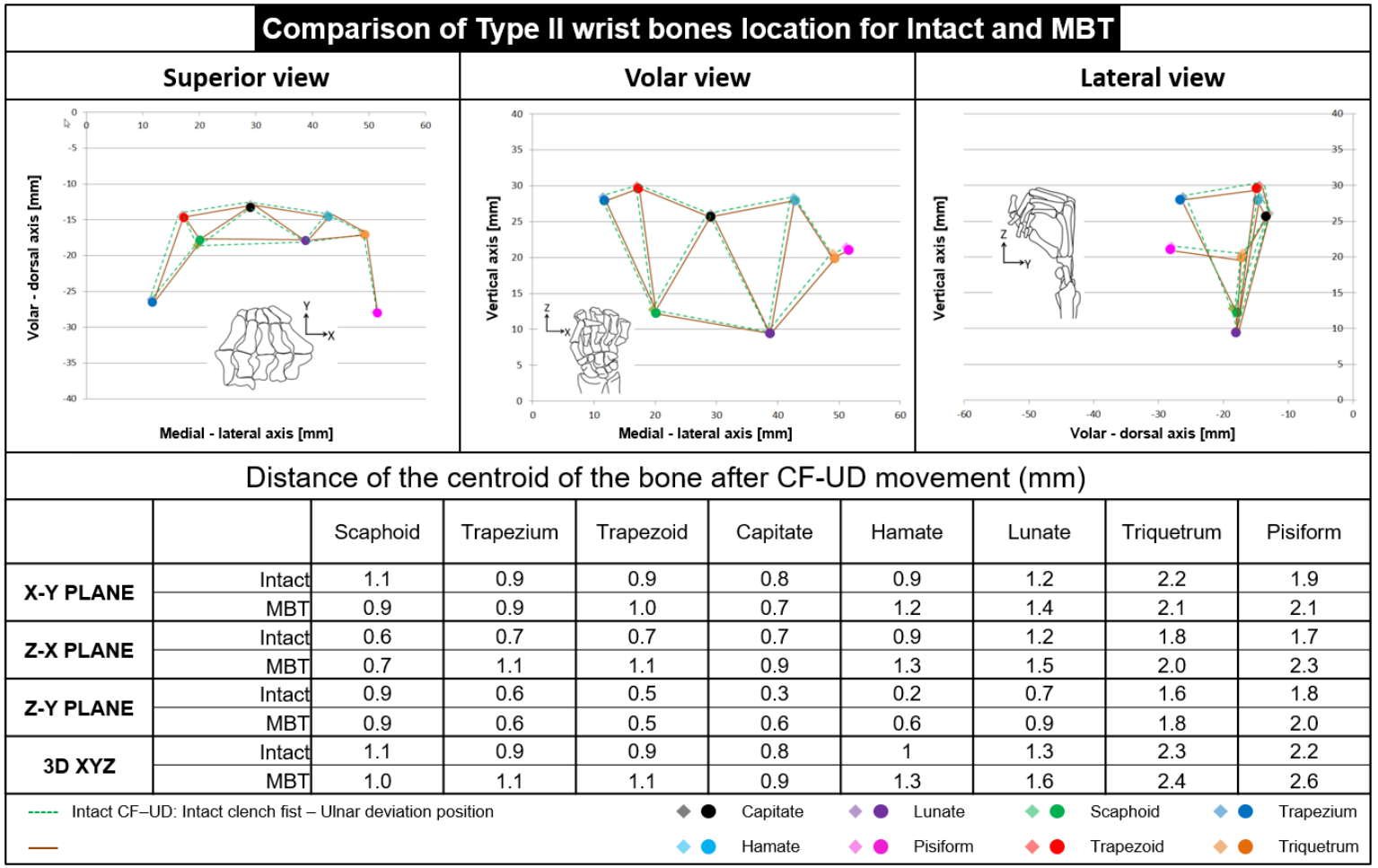

Distance of the centroid of the bone after CF-UD movement (mm)

		Scaphoid	Trapezium	Trapezoid	Capitate	Hamate	Lunate	Triquetrum	Pisiform
X-Y PLANE	Intact	1.1	0.9	0.9	0.8	0.9	1.2	2.2	1.9
	MBT	0.9	0.9	1.0	0.7	1.2	1.4	2.1	2.1
Z-X PLANE	Intact	0.6	0.7	0.7	0.7	0.9	1.2	1.8	1.7
	MBT	0.7	1.1	1.1	0.9	1.3	1.5	2.0	2.3
Z-Y PLANE	Intact	0.9	0.6	0.5	0.3	0.2	0.7	1.6	1.8
	MBT	0.9	0.6	0.5	0.6	0.6	0.9	1.8	2.0
3D XYZ	Intact	1.1	0.9	0.9	0.8	1	1.3	2.3	2.2
	MBT	1.0	1.1	1.1	0.9	1.3	1.6	2.4	2.6

----- Intact CF–UD: Intact clench fist – Ulnar deviation position

——

Capitate, Lunate, Scaphoid, Trapezium, Hamate, Pisiform, Trapezoid, Triquetrum

Figure 4.19: Location of the bones after clench fist position comparing the intact scenario to the modified Brunelli technique (MBT) for a type II wrist.

After MBT reconstruction, lunate motion pattern was altered because of the constraint of the ligament graft at the dorsal side as can be seen in Figure 4.19. The distance between the centroids of the lunate and scaphoid bones is larger compared with the intact scenario (18.88mm compared with 18.81mm, Table 4.3).

Comparing the distances presented in Table 4.3, it can be seen that for the type I wrist, Corella reconstruction resulted in a lunatescaphoid centroid distance closest to the intact wrist (within 0.1mm), followed by MBT then SLAM. For the type II list, MBT reduced lunatescaphoid distance closer to the intact wrist (within 0.07mm), followed by Corella and SLAM.

4.4 Discussion

4.4.1 Reconstruction techniques comparison: Dorsal and volar SL gap and angle and contact area analysis

The results of the reconstruction technique comparison indicated that for the type II wrist, the Corella reconstruction technique was better able to restore dorsal and volar gap and SL angle to that of the intact (ligament) wrist following SLIL sectioning than the SLAM and MBT techniques. Application of the Corella technique following simulated SLIL sectioning resulted in a dorsal gap within 3.5%, a volar gap within 7.1%, and an SL angle within 8.4% of the intact scenario. Of the two other techniques considered, SLAM was better able to restore dorsal, volar gap, and SL angle than MBT. The Corella technique produced scaphoidlunate contact patterns and areas of similar shape and values to those of the intact wrist.

Following SLIL sectioning, there was no contact area between scaphoidlunate cartilage articulation for the type I wrist, whereas for the type II wrist, some contact was maintained. This supports the findings of previous clinical and

cadaveric research that determined that the extra articulation in a type II wrist may help to reduce instability in cases of SL ligament injury [65, 66, 126].

The FE model predicted SL gaps in the range 1.7 to 2.7mm for Corella, 2.1 to 2.7mm for SLAM, and 2.2 to 3.1mm for MBT compared with 1.8 to 2.8 for the intact case. The relatively small differences in the SL gap between the different reconstruction techniques predicted by the FE model concurred with the results from cadaver experimentation and reported clinical outcomes.

Lee *et al* [6] reported the results of the application of three SL reconstruction techniques (SLAM, MBT, and Blatt capsulodesis) in cadaver limbs. Both the MBT and SLAM techniques were found to restore SL gap to within 1mm of the intact case for a clenched fist posture. In a retrospective cohort study, Links *et al* [77] compared clinical and radiographic outcomes in patients with chronic SL dissociation following treatment with MBT versus 4bone tendon weave technique. In the case of MBT, the SL gap following reconstruction was found to be $2.2 \pm 0.4mm$. In another study of 19 patients who had undergone the MBT procedure, Chabas *et al* [76] reported a mean static SL distance of 2.4mm. Yao *et al* [78] report the in outcome for 13 patients who had undergone SLAM, after a followup period of 11 months, the mean postoperative SL gap was 2.1mm. Although relatively small, research indicates that these differences can be clinically significant.

Ideally, the surgical technique should restore a normal relationship between carpal bones, preserve the range of motion, and grip strength whilst achieving a pain free wrist. Further, unsatisfactory results have been reported for techniques that fail to directly correct SL gap [76]. Where clinical outcomes have been compared, greater improvement in mean pain and DASH scores, motion, and grip strength have been reported for techniques able to provide relatively small (eg, $2.2 \pm 0.4mm$ compared with $3.0 \pm 0.8mm$) yet significantly greater improvement of SL gap and angle [78].

4.4.2 Type I and II carpal mechanics: Row/column theory

Several previous studies have attempted to elucidate the row and column theories of carpal mechanics and relate them to type I and II wrists [9, 49, 102]. The comparison undertaken in this chapter supports the assertion that type I wrists exhibit row mechanics and type II column mechanics [9, 49].

The analysis of the motion pattern of the bones of the carpal joint for the type I wrist when moving from the neutral to ulnar deviated clench fist position showed that the lunate rotates clockwise to the ulnar side sliding over the radius as shown in Figure 4.11; at the lateral side of the lunate, the scaphoid follows the motion preserving the distance between the bones and hence their relative position in two planes (ZX and ZY, Figure 4.11) as described by row theory. In the YX plane, the displacement of the scaphoid was greater; as a consequence of the rotation of the scaphoid to a more vertical position.

The remaining bones, which are considered to make up the proximal row, the triquetrum and pisiform exhibited a similar displacement pattern to each other. In addition, the analysis showed that trapezium, trapezoid, capitate, and hamate (distal row) moved together, as a lever unit rotating around a centre, the capitate being the closest bone to the pivot point; during the motion, the trapezium and trapezoid moved upwards following the rotation whilst the capitate and the hamate moved downwards. This unit (the distal row) behaved like a rigid unit, with the distance between the bones being preserved in all three planes during motion.

For the case of the type II wrist, the trapezium, trapezoid, capitate, hamate, and lunate exhibited similar motion pattern, behaving as a unit (central column) rotating around the lunate. The proximal bones of the type II wrist, the scaphoid, lunate, and triquetrum, exhibited displacement patterns, which were

clearly different from each other, which was not the case for the type I wrist, supporting the view that these three bones belong to three distinct columns, the lateral, central, and medial columns, respectively.

Unlike the type I wrist, for type II, the scaphoid displacement was similar to that of the lunate only in the YX plane (Figure 4.11); in planes ZX and ZY, the magnitude of the displacement of the scaphoid was different as a consequence of a rotation along the X-axis to take up a more vertical position and the rotation around its longitudinal axis. The triquetrum and pisiform demonstrated greater displacement compared with other bones, especially in the YX plane. This was in accordance with column theory, whereby during the movement, the medial column (triquetrum and pisiform) tilted dorsally to make space for the bones of the central column; this movement affected the relative position between the lunate and the triquetrum in the ZX and ZY planes.

4.4.3 Type I and II performance of the reconstruction techniques: Wrist kinematics

4.4.3.1 type I wrist

The analysis of wrist kinematics following application of the ligament reconstruction simulations to the type I wrist indicated that none of the techniques significantly altered the motion pattern of the wrist and all continued to exhibit row behaviour.

Following simulation of the Corella reconstruction, motion of the bones in the distal row was effectively unchanged, and the triquetrum behaved as in the intact scenario; the lunate and scaphoid exhibited a similar movement pattern as the intact case but maintaining slightly closer proximity to each other because of the constraints at both volar and dorsal sections.

In the case of SLAM reconstruction, in the proximal row, the triquetrum maintained the motion pattern as in the intact wrist case. Compared with the intact wrist, the lunate moved more volarly in the centre where the bone is attached to the scaphoid by the ligament reconstruction. The scaphoid motion was more towards the proximal pole at the articulation area to the scaphoid, where the two bones are linked by the ligament after the reconstruction. The distance between the two bones was greater compared with the intact case.

For MBT, the motion of the bones in the distal row following reconstruction was akin to that of the intact wrist, as was the triquetrum motion (proximal row). The lunate and scaphoid moved together similar to the intact but sliding slightly more over the radius. Again, the distance between the lunate and scaphoid bones was greater compared with the intact case. Overall, the kinematic analysis confirmed that the Corella technique was best able to restore motion closest to the intact scenario for the type I wrist.

4.4.3.2 Type II wrist

For the type II wrist, the kinematic analysis also determined that the application of the ligament reconstruction techniques do not significantly alter wrist motion pattern (column behaviour).

Following application of Corella reconstruction, the motion of the trapezium, trapezoid, capitate, and hamate (central column) remained essentially unchanged compared with the intact wrist; in addition, the direction of motion of the bones of the medial column (triquetrum and pisiform) was unaltered. The scaphoid (lateral column) motion was slightly more towards the lunate (central column) because of the constraints imposed at dorsal and volar side by the ligament graft.

For the SLAM technique, the only significant difference compared with the intact wrist was that the lateral column (scaphoid) moved more towards the central column (lunate); also, the scaphoid tended to take a more vertical position

during the motion as a result of the insertion point of the ligament graft in the middle of the area that articulates to the lunate, allowing a point of rotation for this bone. In addition, the lunate rotation was greater compared with the intact wrist as it followed the motion of the scaphoid as a result of the ligament graft.

For the MBT reconstruction, the motion of the bones of the central column did not change significantly compared with the intact wrist as was the case with the lateral column (scaphoid). In the central column, the lunate motion pattern was altered; at the dorsal side, the movement was constrained by the ligament graft, but at the volar side, the lack of a constraint enabled a small rotation of the bone opening the gap at the volar side. The medial column (triquetrum and pisiform) was also altered slightly; the motion was greater as the column followed the motion of the lunate. Overall, the kinematic analysis confirmed that the Corella technique was best able to restore motion closest to the intact scenario for the type II wrist.

The wrist kinematic analysis presented in this chapter compared carpal bone motion of type I and type II wrists following SLIL sectioning with the intact ligament scenario. For the type I wrist, following sectioning, the scaphoid exhibited appreciably greater displacement whereas the lunate was less affected. For the type II wrist, the motion of the scaphoid and lunate remained very close to that of the intact. This finding supports those reported by Rhee [66] and Hasse [65] that type II wrists are less prone to instability even following SL ligament injury.

The evaluation undertaken at clenched fist posture was relevant in terms of restoration of the scapholunate interval and corroboration of row/column carpal kinematics; however, the effect that the reconstruction techniques have in the individual carpal motion was still undefined. In order to complete the evaluation, it was necessary to evaluate the performance of the reconstruction techniques in other hands postures; focusing not only in the restoration of the SL gap but also in carpal kinematics of the individual bones.

Chapter 5

Performance evaluation during flexion and extension.

In Chapter 4, the results indicated that the Corella technique was best able to restore the dorsal gap, volar gap and SL angle in repairing the scapholunate ligament disruption for a type II wrist. However, the results were limited to a clenched fist ulnar deviated position. This Chapter presents the performance evaluation of the three tenodesis techniques during 20° flexion and 20° extension.

5.1 Background

Carpal mechanics is explained using two main motion theories linked to the distal morphological variants of the lunate. In Chapter 4 of this thesis, it was corroborated that a type I lunate exhibited row mechanics and type II column mechanics [128]. For a type II wrist, the scaphoid, lunate and triquetrum exhibited different motion patterns endorsing the view that these three bones belong to three distinct columns.

The SLIL is the primary stabiliser of the scapholunate joint [13, 129]. Dissociation of the SLIL is a common injury that affects carpal kinematics which causes pain, reduces grip strength and limit the range of motion; an untreated lesion can progress into carpal instability [130]. Alteration of the carpal kinematics after SLIL sectioning has been investigated in cadaveric experimental studies [46, 131–134]. Crisco *et al* [135] reported that after the SLIL sectioning, the rotation of the lunate decreased in extension and the rotation of the scaphoid increased in flexion. Johnson *et al* [136] reported the carpal kinematics changes during a functional grasp activity in ten subjects with unilateral SLIL dissociation. The contralateral hand was used as normal control (intact wrist). The mean translation and rotation for both lunate and scaphoid were greater for the injured ligament wrist compared to the intact wrist.

The treatment for the SLIL dissociation consists of a surgical procedure aimed to reconnect the bones by tethering a portion of the Flexor Carpi Radialis (FCR) tendon or tendon graft. Various surgical techniques approach differently to repair the disruption; Corella technique tethers the two bones at the volar and dorsal side [5], while SLAM technique does it at the middle region of the bones with a reinforce at volar side [6] but Brunelli and derivations techniques focus on the repairmen only at the dorsal side of the SLIL [4].

Long-term follow-up studies are very limited. In the available reports, the ability of the reconstruction techniques was assessed by measuring the changes in the SL gap and SL angle before and after surgery, and by comparing the range of motion of the operated hand against the contralateral hand. The contralateral hand is taken as a benchmark because the "original" range of motion of the injured wrist is unknown.

In a follow-up of 6 months of the Corella technique in one patient, Corella *et al* [5] reported a reduction in the range of motion by 11% in extension and 22% in flexion after the surgical intervention. Yao *et al* [78] reported the results achieved with the use of the SLAM technique in 13 patients. In average, the mean postoperative wrist flexion and extension was 45 and 56 degrees, respectively.

Regarding the MBT, Talwalkar *et al* [4] reported the outcomes from 55 patients. In average, the range of motion was reduced by 31% in flexion and 20% in extension compared with the contralateral side. Chabas *et al* [76], in a follow-up of 19 patients after MBT operation, reported a reduction of range of motion by 27% in flexion and by 25% in extension. Links *et al* [77], reported that the flexion was reduced by 37% and the flexion was reduced by 35%, in a study conducted in 21 patients.

Although previous studies had evaluated the advantage in the correction of the SL gap and SL angle by attaching the bones at multi-planar levels, the potential alteration in kinematics is unknown.

5.2 Materials and methods

A total of ten FE models of a type II wrist simulated flexion and extension in the cases: the intact SL ligament, SLIL sectioning, MBT, Corella, and SLAM tenodesis techniques.

The SL gap and the SL angle were measured at 20° flexion and 20° extension. Also, the contact areas between the lunate and the scaphoid were obtained from the FE models to identify changes in the interaction as part of the evaluation. Additionally, alteration in the carpal kinematics was inspected by measuring the rotations of the carpal bones before and after the application of the reconstruction techniques.

5.2.1 Finite Element modelling

The FE models used in this evaluation were based on the model for the intact ligament case which construction was described in chapter 3. The geometry of the carpal bones, the ligament set and material properties remained unchanged. The loading scenario and the boundary conditions were modified accordingly to produce 20° flexion and 20° extension.

5.2.1.1 Boundary Conditions

The proximal ends of the ulna and radius were encastred, i.e. with zero degrees of freedom. All the carpal bones and metacarpals have 6 DOF's. The five metacarpals were tied to a control point located in the midway of the second and the fifth metacarpal as shown in Figure 5.1.

A convention of signs was defined to describe the motions around the axis of the coordinate system. Flexion (+X), Extension (-X) measured around the X-axis. The passive motion was achieved by moving the control point, in one case by 20° around the X-axis to produce flexion and, in another case, by $-20°$ around the X-axis to produce extension. Note that the sign in the case of extension indicates the direction of the rotation. A compression load of $10N$ was applied on the metacarpals to produce a contact between the bone.

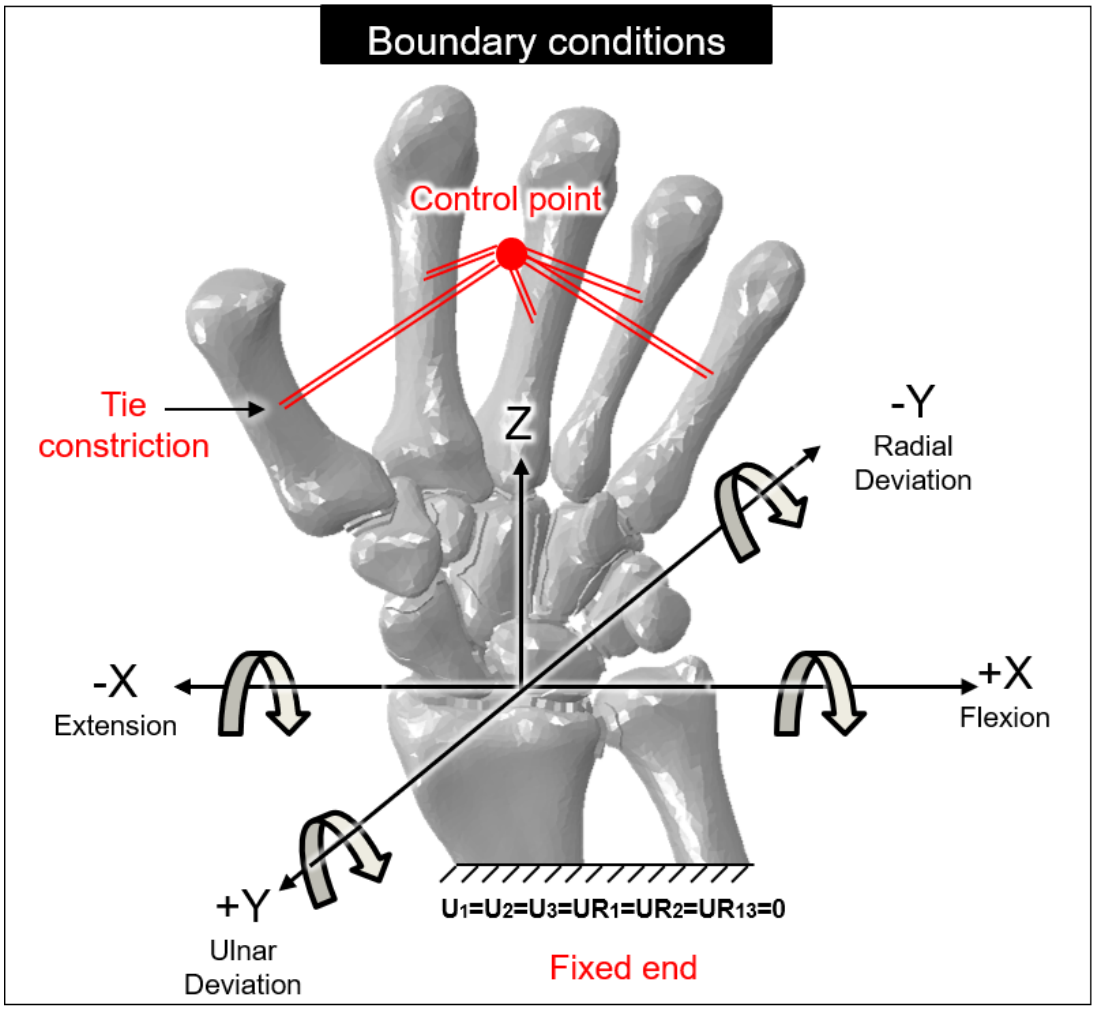

Figure 5.1: FE simulation setup showing the reference system and the boundary conditions to produce the passive motion.

5.2.2 Mesh sensitivity analysis

The methodology for the mesh sensitivity analysis was previously described in Chapter 3 in Section 3.6.1.

5.2.3 Modelling of the scapholunate ligament reconstruction techniques

The methodology for the modelling of the ligament reconstruction techniques was previously described in Chapter 4 in section 4.2.3.

5.2.4 SL gap, SL angle and bone motion calculation

The methodology to measure the SL gap and the SL angle was previously described in Chapter 3 in section 3.6.2. The rotation of the bones was calculated individually for all the carpal bones. To compute the values in the FE model, an orthogonal coordinate system was located at the volume centroid of each bone as shown in Figure 5.2 by labelling nodes at the origin of the system and one node to each of the axes. The computing of the rotation matrix was carried out externally using a Matlab code. The rotation of the bones was calculated between the orthogonal system at the initial and final position.

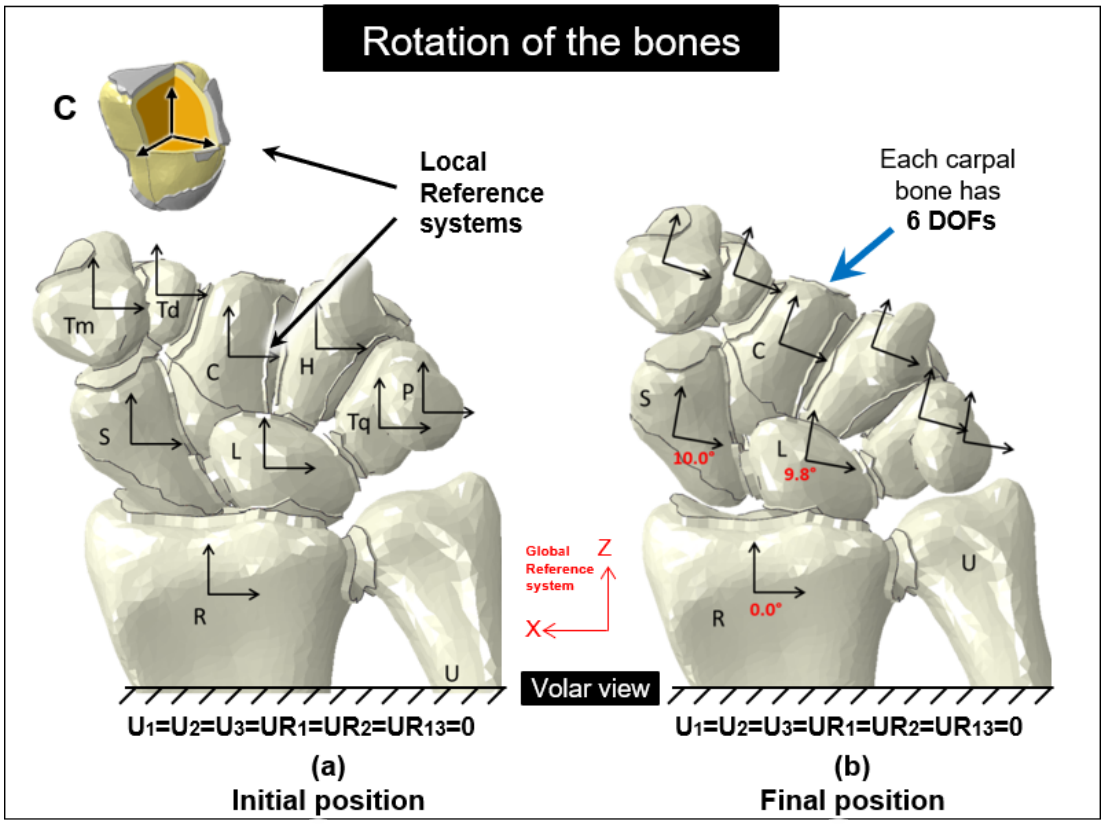

Figure 5.2: Rotation assessment of the carpal bones. (a) Location of the reference system at each carpal bone at the initial posture. (b) Final orientation of the carpal bones at the final position.

5.2.5 FE Model Validation

Validation of the type II wrist FE model was described in detail in Chapter 3 in Section 3.6.2. In the previous Chapter, the FE models were employed to simulate a cadaveric study with the wrist in the neutral and ulnar deviated clenched fist positions [128]. The validation of the FE models was extended into the flexion and extension positions by comparing the carpal bones rotations predicted with the FE models to carpal bones rotations from a cadaveric study conducted by Bain *et al* [12]. The details of this validation are described in detail in Chapter 3 in Section 3.6.3.

5.3 Results

5.3.1 FE Model validation

The results of the validation of the FE models were previously presented in Chapter 3 in Section 3.6.3.

5.3.2 Ligament reconstruction technique performance: SL gap and SL angle

5.3.2.1 Flexion

The predicted values for the SL gap for the FE models of the intact (ligament) wrist, SLIL-sectioned case and the MBT, SLAM and Corella ligament reconstruction methods with the wrist positioned at 20° flexion are presented in Figure 5.3.

The sectioning of the scapholunate ligament resulted in an increased in SL gap, by 6.1% at the dorsal side and 16.7% at the volar side compared to the intact ligament case. Following the reconstruction techniques, at dorsal side the SL gap

was reduced by $0.1mm$ for Corella and SLAM compared to the SLIL sectioned scenario, to within 3% of the intact ligament whereas the MBT reduced the SL gap by $0.2mm$, back to the intact ligament value. At the volar side, the gap was closed by $0.3mm$ (7.1%), $0.1mm$(2.4%) and $0.6mm$(14.3%) for Corella, SLAM and MBT respectively compare to SLIL scenario. At the volar side, MBT technique was the only technique that restored the SL gap to the intact ligament value.

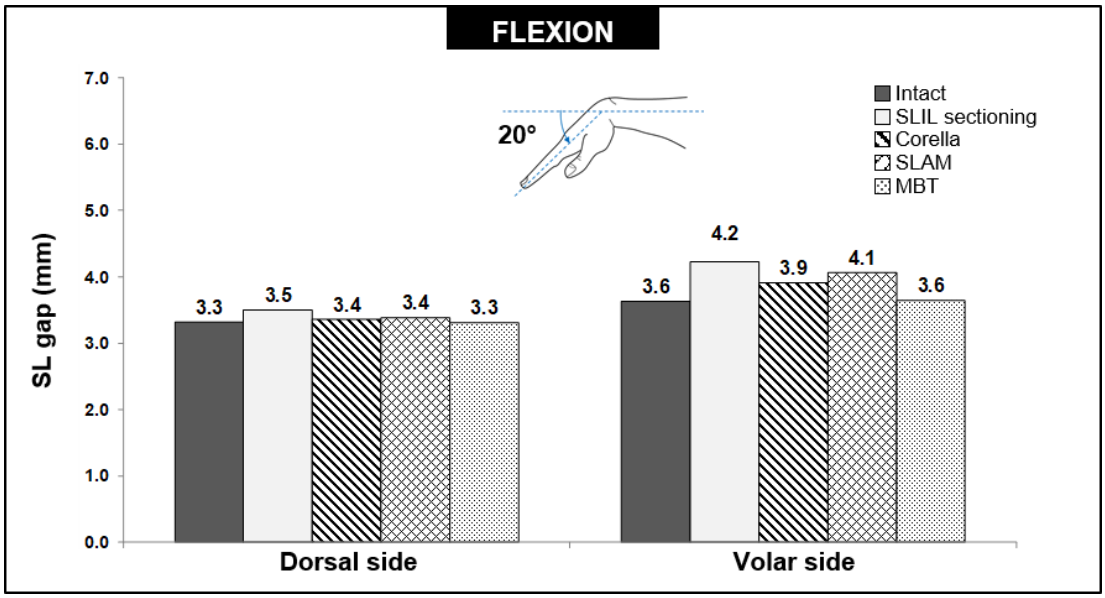

Figure 5.3: Comparison of SL gap during flexion.

Predicted values for SL angle are presented in Figure 5.4. The SL angle from the intact scenario increased by 1.3% (0.6°) after the SLIL sectioning compared to the intact ligament case. Application of the Corella reconstruction technique resulted in a further increase in the angle by 0.2°. SLAM technique reduced SL angle by 0.4° (0.8%) and 1.2° (2.5%) compared to the SLIL sectioning, thus, the SL angle for the MBT was 0.6° (1.3%) smaller to the value measured in the intact ligament scenario.

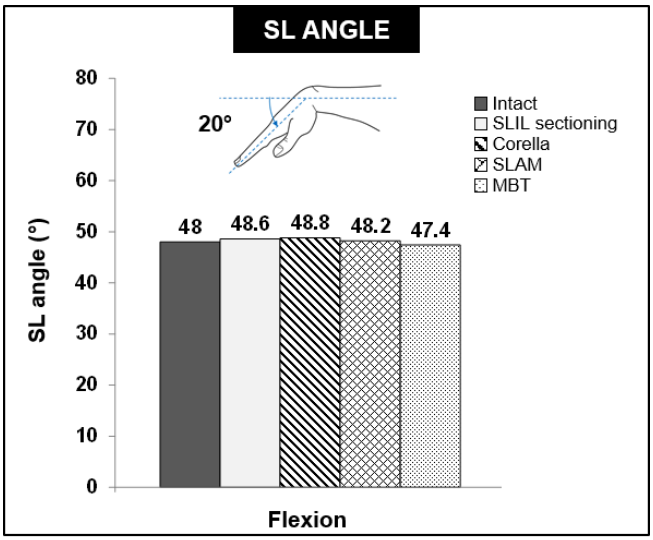

Figure 5.4: Comparison of SL angle during flexion.

5.3.2.2 Extension

Figure 5.5 shows the values for the SL gap predicted with the FE models of the intact ligament case, SLIL sectioned case and the MBT, SLAM and Corella ligament reconstruction methods with the wrist positioned at 20° extension.

After the SLIL sectioning, the SL gap increased by 0.3mm (8.6%) and 0.1mm (3.1%) at the dorsal and volar side respectively compared to the intact ligament wrist scenario. Following the reconstruction techniques, at the dorsal side, the gap closed by 0.2mm (5.3%) for Corella and 0.3mm (7.9%) for SLAM and MBT compared to the SLIL gap, restoring the value of the SL gap to the value for the intact scenario at this side. At the volar side, the SL gap value further increased by 0.2mm (6%) for Corella and was reduced by 0.2mm (6%) and 0.1mm (3%) for SLAM and MBT respectively compare to SLIL scenario. At volar side, MBT technique was the only technique that restores the SL gap to the intact ligament value.

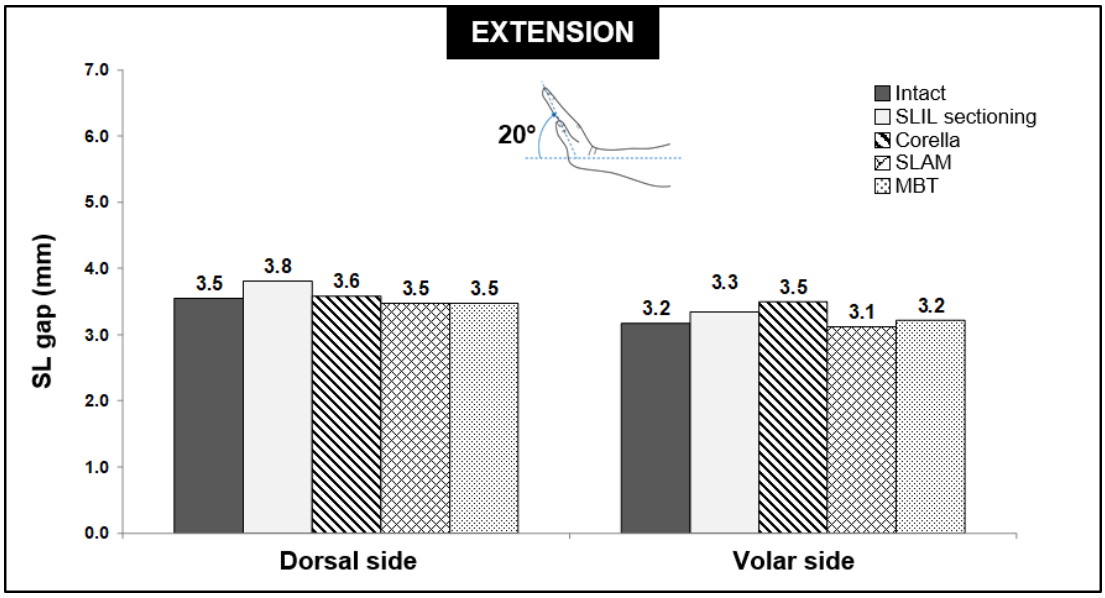

Figure 5.5: Comparison of SL gap during extension.

Predicted values for SL angle are presented in Figure Figure 5.6. The SL angle increased by 0.8° following SLIL sectioning. All the reconstruction techniques reduced SL angle compared to the SLIL sectioned case, and below the value measured at the intact case. The SL angle was restored to within 1.4° (4.3%), 0.3° (0.9%) and 0.4° (1.2%) of the intact wrist for the Corella, SLAM and MBT techniques respectively.

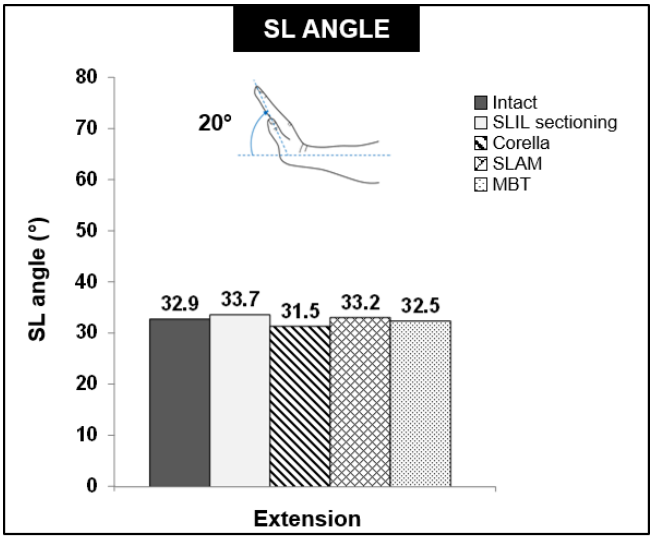

Figure 5.6: Comparison of SL angle during extension.

5.3.3 Contact area comparison at scaphoid lunate articulation

Figure 5.7 shows the contact area patterns on the articular surface of the lunate at the articulation between the scaphoid and lunate for all the reconstruction techniques for the type II wrist as calculate by the FE models.

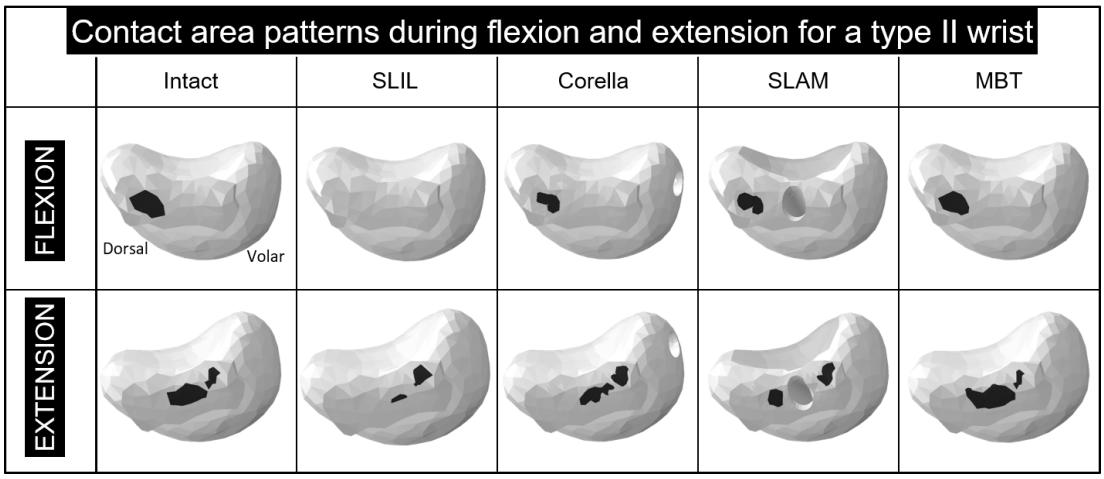

Figure 5.7: Comparison of the contact area patterns between scaphoid and lunate at flexion and extension.

5.3.3.1 Flexion

For the intact scenario during flexion, an area of $10mm^2$ of scaphoid-lunate contact was discernible at the dorsal side of the lunate surface. Following SLIL-sectioning there was no visible contact between the lunate and the scaphoid. Application of the three ligamentous reconstructions techniques restored scaphoid-lunate contact with the MBT technique resulting in a contact area more similar in size ($7.9mm^2$), shape and location to that of the intact case compared to both the Corella ($5.6mm^2$) and SLAM ($5.7mm^2$) methods.

5.3.3.2 Extension

For extension, in the intact ligament scenario, a contact area of $14.2mm^2$ was determined, consisting of two separate but adjacent regions, one towards the centre and the other more towards the volar region of the articular surface on the lunate. SLIL sectioning resulted in a significant reduction in the contact area to $5.4mm^2$. The MBT technique resulted in a contact area more similar in size ($13.6mm^2$), shape and location to the intact case compared to both the Corella ($12.1mm^2$) and SLAM ($9.3mm^2$) methods.

5.3.4 Carpal kinematics

5.3.4.1 Flexion

During wrist flexion of 20° in the intact case, the proximal bones flexed in the plane of motion by 15.4° for scaphoid, 8.8° for lunate and 11.4° for triquetrum while at the same time rotated out-of-plane by −5.3°, 1.1° and 2.7° respectively as shown in Figure 5.8. After SLIL sectioning, in-plane rotation increased by 22.1% for the scaphoid, but was reduced by 9.1% for the lunate and 6.1% for the triquetrum compared to the intact scenario.

Following the reconstruction techniques, the in-plane rotation of the proximal bones recover their rotation course. For the scaphoid, the rotation was restored to within 1.5° (9.7%) for Corella, 0.5° (3.2%) for SLAM and 0.3° (1.9%) for the MBT, to below the same value as the intact case. The rotation of the triquetrum also was restored to within 0.3° (1.9%) for Corella, 0.1° (1.9%) for SLAM, and MBT to the same value compared to the intact scenario. The results for the rotation of the lunate was more contrasting, Corella and MBT restored the rotation to within 0.2° (2.3%) to the same value of the intact case; however, the SLAM reduced further the rotation to below 1.5° (17%) the value of the intact case.

Out-of-plane rotations were smaller in all cases compared to the in-plane rotation at the flexion; however, there were changes after the reconstruction techniques. For the scaphoid, all the techniques increased the rotation by 0.8° , 1.7°, and 0.9° for the Corella, SLAM and MBT, compared to the intact case, respectively. For the lunate, the rotation was also increased to within 1.4° for Corella, 0.6° for SLAM, and 0.1° for MBT, compared to the intact case. For the triquetrum, the rotation increased to within 0.3° for the Corella and MBT, and decreased by 0.1° for the SLAM compared to the intact case.

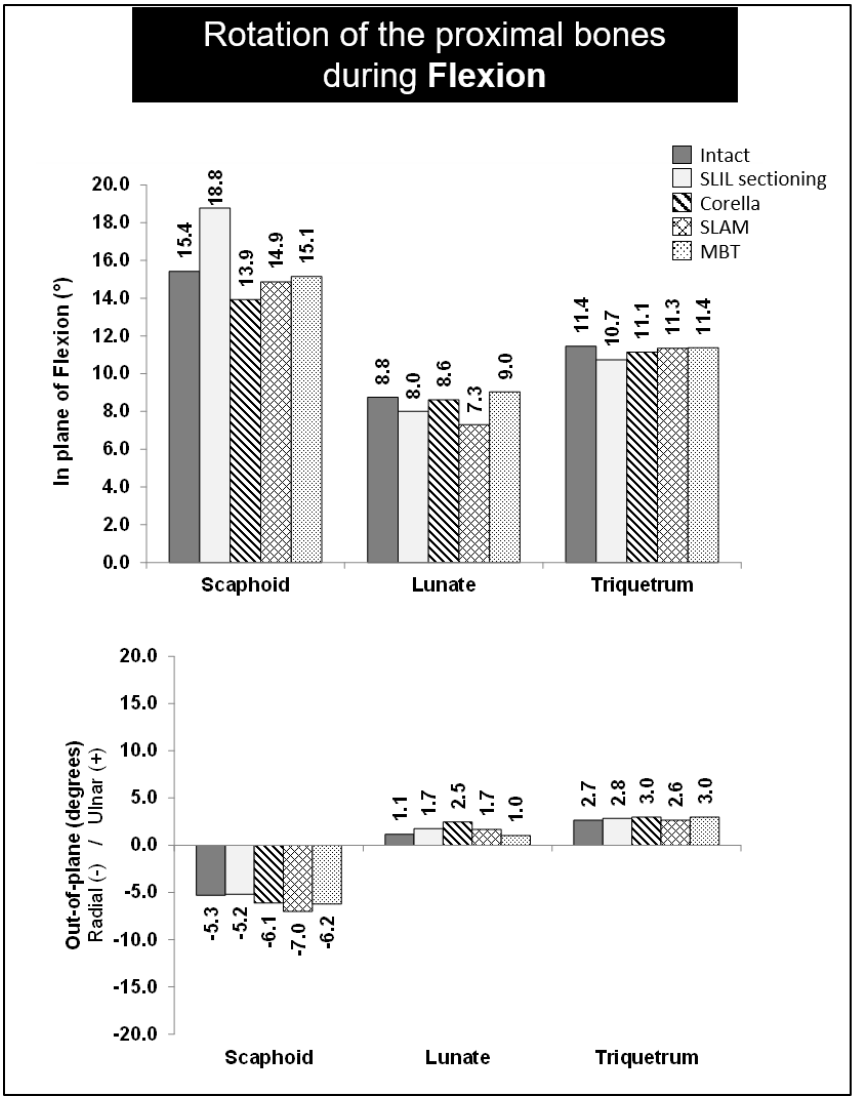

Figure 5.8: Results for the rotation of the proximal bones during flexion.

5.3.4.2 Extension

During wrist extension of $-20°$ for the intact case, the proximal bones extend in-plane of motion by $-16.2°$ for scaphoid, $-10.6°$ for lunate and $-13.2°$ for triquetrum; at the same time the bones rotate out-of-plane by $3.8°$, $0.0°$, $-1.0°$, respectively, figure 5.9. After the SLIL sectioning, in-plane rotation increased by 13% for the scaphoid, 7.5% for the lunate and 3.8% for the triquetrum.

Following the reconstruction techniques, the in-plane rotation of the proximal bones restored the rotation tendency. For the scaphoid, the rotation was restored to within $1.3°$ (8%) for Corella, $0.5°$ (3%) for SLAM and $0.1°$ (0.6%) for the MBT, to the value of the intact case. The results for the rotation of the lunate restored to within $0.3°$ (2.8%), $0.4°$ (3.7%), and $0.6°$ (5.6%) for the Corella, SLAM and MBT, to the value of the intact case, respectively. The rotation of the triquetrum also was restored to within $0.1°$ (0.7%) for Corella, $0.2°$ (1.5%) for SLAM, and MBT to the same value compared to the intact scenario.

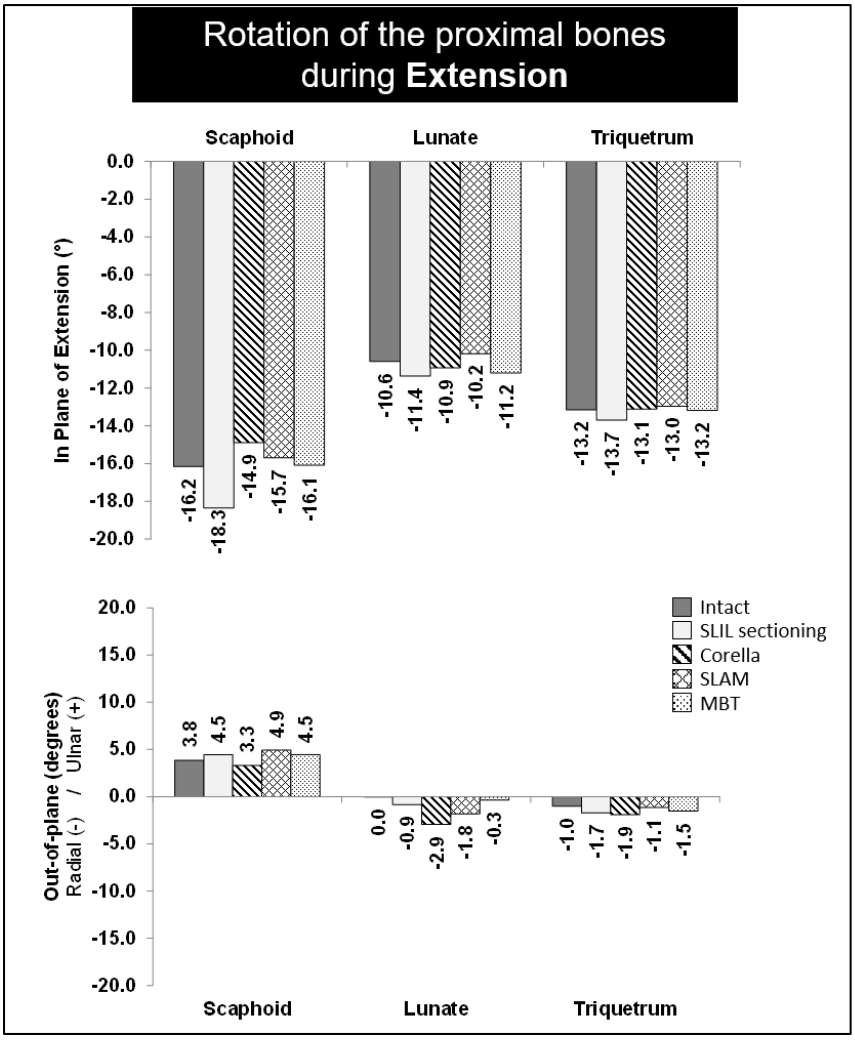

Figure 5.9: Results for the rotation of the proximal bones during extension.

Out-of-plane rotations were smaller in all cases compared to the in-plane rotation at the extension; however, there were changes after the reconstruction techniques. For the scaphoid, the rotation was smaller by 0.5° for the Corella, and bigger by 1.1°, 0.7° compared to the value registered in the intact case. For the lunate, the FE models predicted a radial rotation of 2.9°, 1.8°, and 0.3° for the Corella, SLAM and MBT after the application of the reconstruction, respectively. For the triquetrum, the rotation increased to within 0.9° for the Corella, 0.1° for SLAM, and 0.5° for the MBT compared to the intact case.

5.4 Discussion

Ligament reconstruction techniques focus on restore and maintain the gap between the scaphoid and the lunate. The procedures tether the scaphoid and lunate at multi-planar points in order to restore the connection. However, this tie distorts carpal kinematics and limits wrist motion [5, 6, 137]. Follow-up reports have described a loss of range of motion of the wrist and loss of grip strength. The challenge is to determine which of the techniques have minor alterations to the wrist motion[4, 5, 76–78].

5.4.1 SL gap, SL angle and contact area

The SL gap values predicted with the FE models for the flexion and extension positions were slightly bigger to those obtained in the clenched fist ulnar deviated posture reported in Chapter 4. The magnitude of the SL gap values was consistent with the values obtained in cadaver experimentation and follow-up reports. However, in those studies, the SL gap was measured at neutral posture [4, 5, 76–78]. In this analysis, the SL gap was reported at the flexion and extension to determine if the techniques were able to keep the opening between the scaphoid and lunate through the range of motion.

For flexion and extension, the MBT technique restored and maintained the SL gap to a close value of the intact ligament. Of the three techniques, MBT was better able to restore SL gap and angle.

After simulating the scapholunate ligament sectioning, the FE models predicted an increase of up to $0.3mm$ and an SL volar gap increase of up to $0.6mm$; SL angle increased by up to $0.8°$. MBT restored the SL gap value at both dorsal and volar side to the intact ligament value in flexion and extension and SL angle to within $0.6°$ in flexion and $0.4°$ in extension.

The performance of the Corella and SLAM techniques contrasted depending on

the position. At flexion, Corella was more effective than SLAM in restoring the SL volar gap and the SL angle; contrary, at extension, SLAM was better in restoring the SL volar gap and SL angle than the Corella technique.

The MBT technique produced contact area patterns of similar shape and values to those of the intact wrist at flexion and extension positions. After the SLIL sectioning, no contact area was discerned at flexion but some contact was maintained at extension. Of the two other techniques, Corella reproduced similar patterns but with smaller values. SLAM technique modified the contact pattern because the facet on the lunate was drilled during the application of the technique; however, the pattern was similar to the pattern registered in the intact scenario.

5.4.2 Wrist kinematics

During wrist flexion and extension, most of the carpal motion occurred at the interaction of the radius and the proximal bones (the radiocarpal joint). The percentage of the contribution of the individual carpal bones varied among studies. Wolfe *et al* [38] used CT to calculate the amount of scaphoid and lunate contributions to global wrist flexion and extension. During flexion, the scaphoid contributed 73% and the lunate 46%; whereas, in extension, the scaphoid contributed 99% and lunate 68%. This percentage of contributions generally concurred with those obtained in other cadaveric and in vivo studies [40, 43].

Bain *et at* [12] assessed the 3-Dimensional kinematics of the carpal bones in various ranges of motion with respect to lunate morphology. In eight cadaveric wrist (4 type I lunates, 4 type II lunates) they measured the relative motion of the radius, carpals, and third metacarpal by using optical motion capture methods in a range comprising flexion-extension (15°-15°) and radio-ulnar deviation (20°-20°). Their results show clear different patterns of motion regarding the lunate type; during flexion-extension, the radiocarpal joint has

significantly greater motion in type I (row theory) than a type II (column theory).

From the intact ligament FE model, during flexion, the in-plane rotation of the scaphoid was 77% (15.4) and the lunate 44% (8.8), considering the total of 20 flexion. In the extension position, the in-plane rotation of the scaphoid was 81% (16.2) and the lunate 53% (10.6), considering the total of 20 extension. The rotations values of the proximal bones concurred to those reported in the references; the slightly less proximal carpal bones motion coincided with the results reported by Bain et al [12] for a type II wrist.

The carpal motion was altered after the rupture of the SLIL ligament; a further rotation of the scaphoid during flexion was observed in the FE model, which agree with the scaphoid luxation described in clinical reports after the loss of the SLIL [6].

Ligament reconstructions have been shown different results due to each technique tethers the bones in different configuration and sides (dorsal, medial or volar), which plays a role in the effectiveness of each technique.

In the inspection of the change of motion of the bones in the in-plane of motion during flexion, MBT restored the rotation of the scaphoid to a closer value to that of the intact case, followed by the SLAM technique. Corella reconstruction reduced the rotation of the lunate which lead to a loss of range of motion after the surgical procedure. For the lunate, MBT and Corella restored the rotation of the bones closer to the value measured in the intact case, whereas the SLAM restricted the lunate rotation. In the inspection of the change of motion of the bones in the out-of-plane of motion, during flexion Corella changes significantly the motion of the lunate while the SLAM does it with the scaphoid.

In the analysis of the in-plane of motion during extension, MBT restored the rotation of the bones to closer value to that registered in the intact case. The other two reconstruction techniques reduced the rotation of the scaphoid when comparing to the intact case. The reduction of the rotation of the scaphoid contributes to the loss of range of motion. For the lunate, Corella worked better than MBT in restoring the rotation of the bone. SLAM reduced the lunate rotation to below the value of the intact case. Additionally, analysing the out-of-plane motions, MBT modified the rotation of the scaphoid while the Corella modified the rotation of the lunate.

In general, for the flexion and extension position, MBT was most effective to repair the connection between the scaphoid and lunate, maintain the interval between the two bones and SL angle without modifying the carpal kinematics.

In the following chapter, the same ligament reconstruction techniques will be analysed for the radial and ulnar deviation position in order to evaluate comprehensively the performance of the techniques through the arch of motion.

Chapter 6

Performance evaluation during radial and ulnar deviation.

In previous Chapters, the ability of three ligament reconstruction techniques was assessed in different for a clenched fist ulnar deviated posture (Chapter 4), and at flexion and extension positions (Chapter 5). This Chapter presents the results of the performance evaluation of the modified Brunelli technique (MBT), Corella and Scapholunate method (SLAM) ligament reconstruction techniques for a type II wrist using finite element-based virtual surgery during 15° radial deviation and 15° ulnar deviation.

6.1 Background

The carpal kinematics during radioulnar deviation is complex in a type II wrist. In Chapter 4, the reliability of the column motion theory for a type II wrist was corroborated. During radial deviation, the scaphoid flexes towards the volar side; whereas during ulnar deviation, the triquetrum moves towards the dorsal side sliding over the hamate [128]. In this context, the bones rotations at in-plane and out-of-plane are of similar importance to analyse.

Bain *et at* [12] assessed the 3-dimensional kinematics of the carpal bones in various ranges of motion with respect to lunate morphology. In eight cadaveric wrist (4 type I lunates, 4 type II lunates) they measured the relative motion of the radius, carpals, and third metacarpal by using optical motion capture methods in a range comprising radio-ulnar deviation (20°-20°). Their results showed clear different patterns of motion linked to two types of lunate. During flexion-extension, the radiocarpal joint registered significantly greater motion in type I wrist (row theory) than a type II wrist (column theory).

In a healthy wrist, the scapholunate ligament allows a moderate rotation between the scaphoid and lunate. After the disruption of the scapholunate ligament the carpal mechanics changes. In Chapter 5 was reported that the in-plane rotation increased after the SLIL disruption. Results from the virtual reconstruction techniques demonstrated that the in-plane rotations of the proximal bones were reduced, which can lead to a loss of the range of motion of the wrist. The evaluation of the performance of the reconstruction techniques was extended to the radial and ulnar position.

6.2 Materials and methods

In this Chapter, a total of ten FE models were developed to simulate radial and ulnar deviation in the cases: the intact SL ligament, SLIL sectioning, MBT, Corella, and SLAM tenodesis techniques for a type II wrist.

Similar to the methodology followed in Chapter 4 and Chapter 5, the performance of the reconstruction techniques was assessed by comparing the SL gap and SL angle after simulating the virtual surgery to the values obtained in the intact ligament model. The contact areas between the lunate and scaphoid were also obtained from the models to identify changes in the interaction. Additionally, the alteration of the carpal kinematics was inspected by measuring the rotations of the carpal bones before and after the application of the reconstruction techniques.

6.2.1 Finite Element model modelling

The FE models used in this evaluation were based on the model for the intact ligament case which construction was described in Chapter 3. The geometry of the carpal bones, the ligament set and material properties remained unchanged. The loading scenario and the boundary conditions were modified accordingly to produce 15° radial deviation and 15° ulnar deviation.

6.2.1.1 Boundary Conditions

In order to reproduce the passive radial and ulnar deviation motions, the five metacarpals were tied to a control point located in the midway of the second and the fifth metacarpal, as shown in Figure 5.1. The proximal ends of the ulna and radius were encastred, i.e. with zero degrees of freedom. All the carpal bones and metacarpals have 6 DOF's.

The convention of signs to describe the motions in the coordinate system defined in Chapter 5 in Section 5.2.1.1 was followed identically. Ulnar deviation (+Y) and Radial deviation (-Y) were measured around the Y-axis. The passive motion was achieved by moving the control point, in one case by 15° around the Y-axis to produce ulnar deviation and, in another case, by $-15°$ around the X-axis to produce radial deviation. The sign in the case of radial deviation indicates the direction of the rotation. A compression load of $10N$ was applied on the metacarpals to produce a contact between the bone.

6.2.2 Mesh sensitivity analysis

The methodology for the mesh sensitivity analysis was previously described in Chapter 3 in Section 3.6.1.

6.2.3 Modelling of the scapholunate ligament reconstruction techniques

The methodology for the modelling of the ligament reconstruction techniques was previously described in Chapter 4 in section 4.2.3. Figure 6.1 shows the FE models developed to simulate the reconstructions.

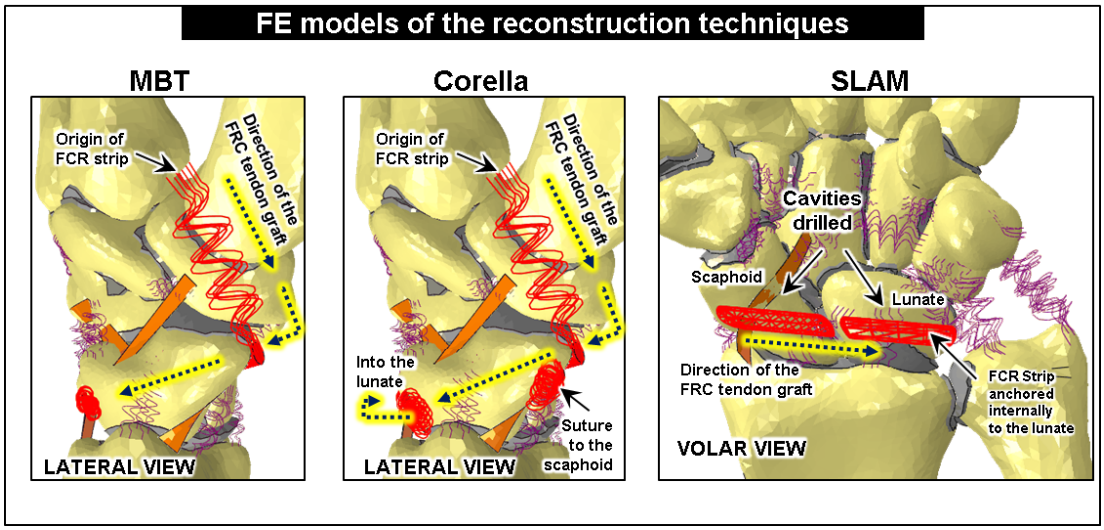

Figure 6.1: FE models of the three reconstruction techniques.

6.2.4 SL gap, SL angle and bone motion calculation

The methodology to measure the SL gap and the SL angle was previously described in Chapter 3 in section 3.6.2. The methodology to measure the rotation of the bones was previously described in Chapter 5 in section 5.2.4. To compute the values in the FE model, an orthogonal coordinate system was located at the volume centroid of each bone as shown in Figure 6.2 by labelling nodes at the origin of the system and one node to each of the axes [1]. The computing of the rotation matrix was carried out externally using a Matlab code.

[1]The calculation of the rotation of the bones was done by setting a local reference system at the centroid of volume of the bone. After the drilling the cavity, this volume centroid changed and the local reference system was moved to the nearest node of the new volume centroid.

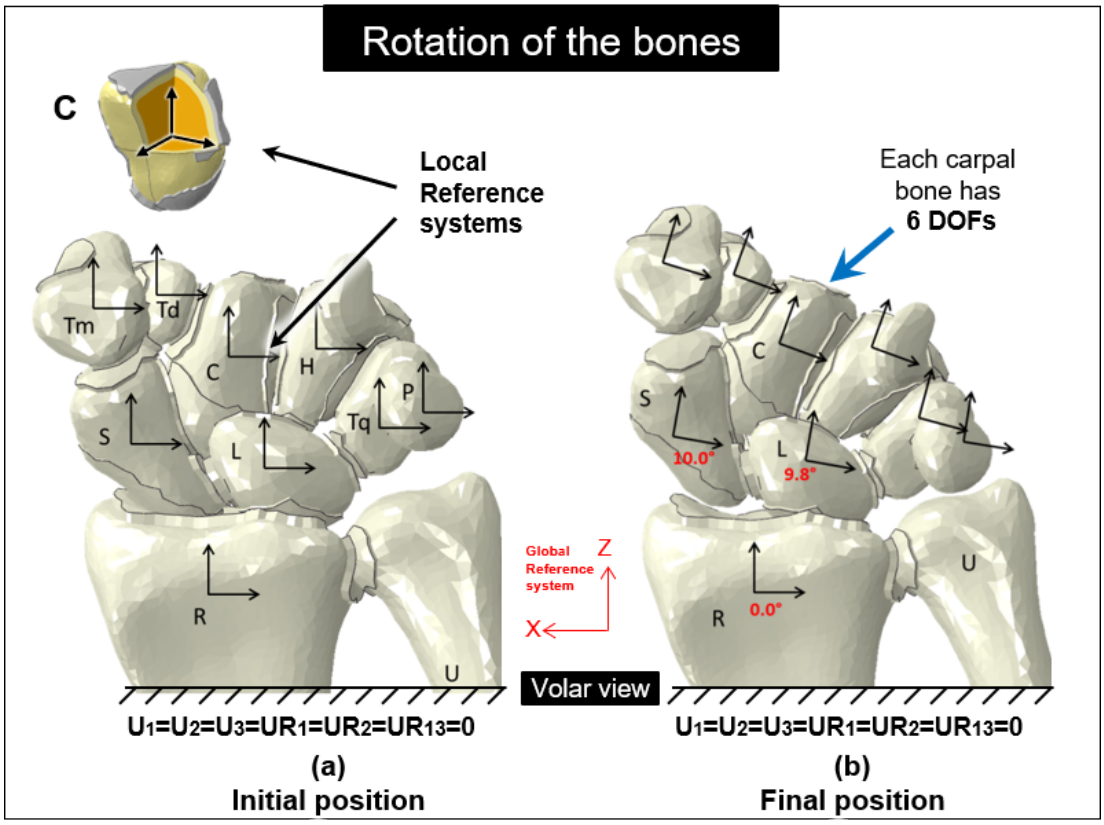

Figure 6.2: Rotation assessment of the carpal bones. (a) Location of the reference system at each carpal bone at the initial posture. (b) Final orientation of the carpal bones at the final position.

6.2.5 FE Model Validation

Validation of the intact ligament FE model of a type II wrist was described in detail in Chapter 3 in Section 3.6.2. The validation was undertaken by comparing the rotations of the lunate, scaphoid and capitate, predicted by the FE models to results from cadaveric studies. The FE models simulated radial and ulnar deviation cases reported in a cadaveric study conducted by Bain *et al* [12].

6.3 Results

6.3.1 FE Model validation

The results of the validation of the FE models were previously presented in Chapter 3 in Section 3.6.3.

6.3.2 Reconstruction techniques comparison: SL gap and SL angle

6.3.2.1 Radial deviation

Figure 6.3 The predicted values for SL gap for the FE models of the intact (ligament) wrist, SLIL-sectioned case and the MBT, SLAM and Corella ligament reconstruction methods with the wrist positioned at 15° of radial deviation.

In the intact ligament case, the SL gap was $3.5mm$ at the dorsal and volar side. After the sectioning of the scapholunate ligament, the SL gap increased by $1.1mm$ (31.4%) at the dorsal side and by $1.2mm$ (34.3%) at the volar side. Following the reconstruction techniques, all reduced the SL gap closer to the value measured at the intact ligament wrist case. At the dorsal gap, MBT restored the gap value to that of the intact case, whereas SLAM and Corella reduced to within $0.1mm$ (2.9%) on the same side. At the volar side, SLAM restored the gap to within $0.3mm$ (8.6%) of the intact ligament case, while both Corella and MBT reduced the gap to within $0.4mm$ (11.4%).

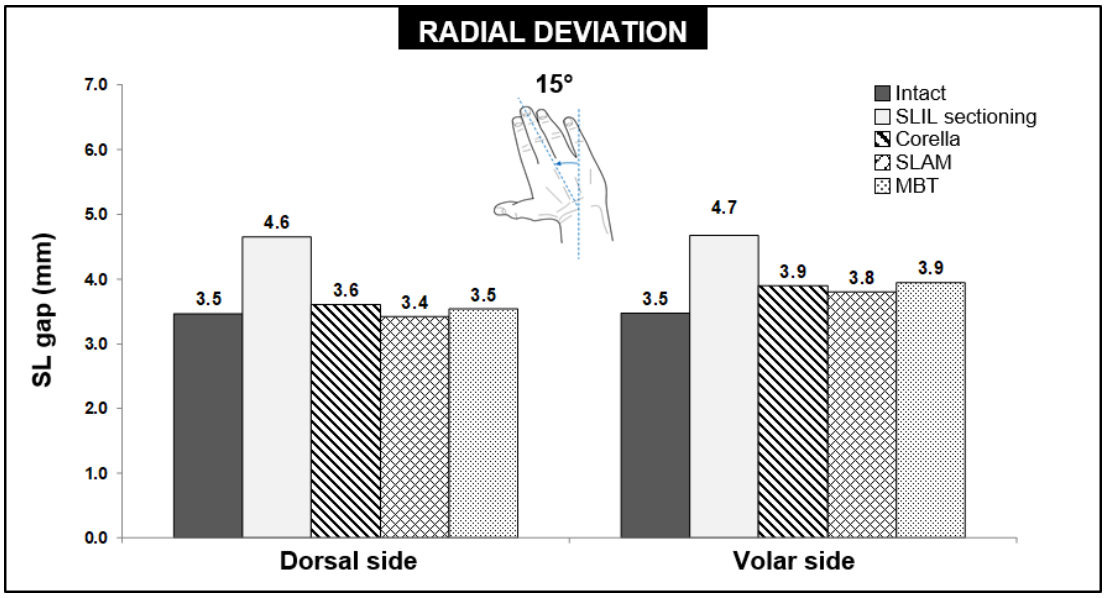

Figure 6.3: Results for the SL gap in four positions.

Comparing to the intact ligament scenario, the SL angle increased by 5.5° following SLIL sectioning as shown in Figure 6.4. Following virtual surgery, Corella was able to restore SL angle to within 0.3° (0.7%) and MBT to within 3.1° (7%) of the intact ligament, however, application of SLAM resulted in an increase in SL angle of 0.7° compared to the SLIL sectioned case.

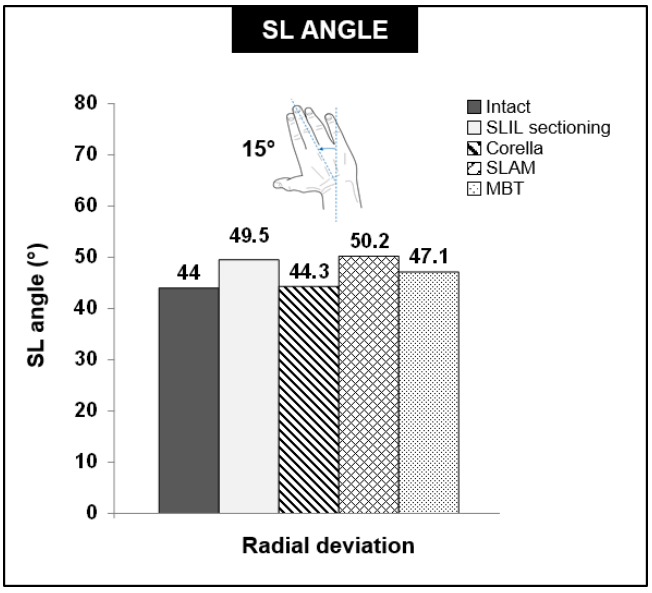

Figure 6.4: Comparison of SL angle during radial deviation.

6.3.2.2 Ulnar deviation

Figure 6.5 shows the predicted values for SL gap for the FE models of the intact (ligament) wrist, SLIL sectioned wrist and Corella, MBT and SLAM reconstruction techniques during ulnar deviation at both dorsal and volar side.

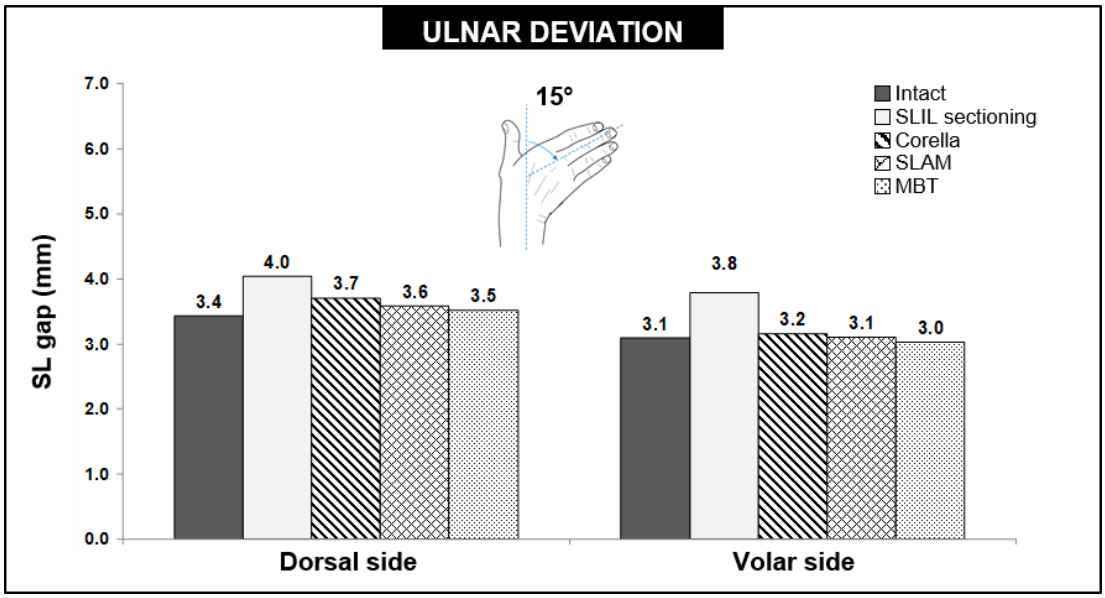

Figure 6.5: Results for the SL gap in four positions.

Following SLIL sectioning, the SL gap increased by 0.6mm (17.6%) at dorsal side and by 0.7mm (22.6%) at volar side compared to the intact ligament case. After the ligament reconstruction, all the techniques reduced the SL gap closer to the intact wrist case. At the dorsal side, MBT restored the gap to within 0.1mm (2.9%), SLAM reduced to within 0.2mm (5.9%) whilst Corella to 0.3mm (8.9%). At the volar side, SLAM restored volar gap to the intact wrist value whilst both Corella and MBT reduced the volar gap to within 0.1mm (3.2%) of the intact scenario.

Regarding the SL angle, in Figure 6.6 can be seen that the application of the reconstruction techniques reduced the SL angle to below the original intact value; SLAM reduced SL angle to 2° lower than the intact wrist and MBT and Corella to 6.5° and 7.8° lower respectively.

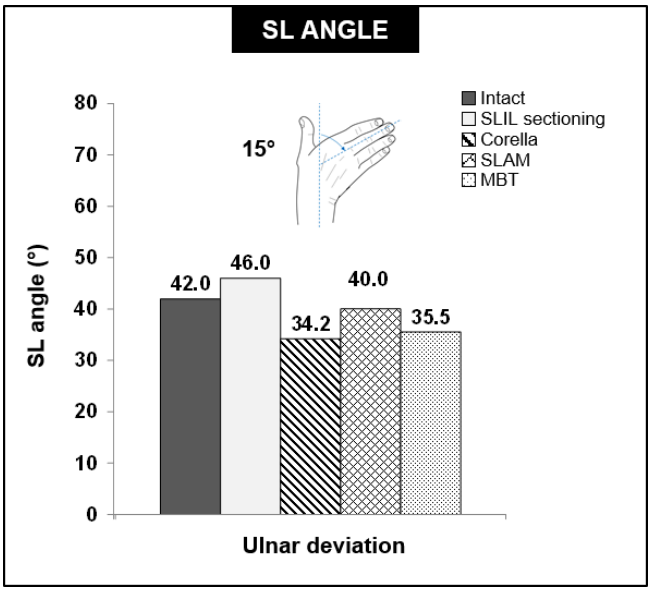

Figure 6.6: Comparison of SL angle during ulnar deviation.

6.3.3 Contact area comparison at scaphoid lunate articulation: Radial and ulnar deviation

Figure 6.7 shows a comparison of the contact area patterns on the articular surface of the lunate to the scaphoid at radial and ulnar deviation positions.

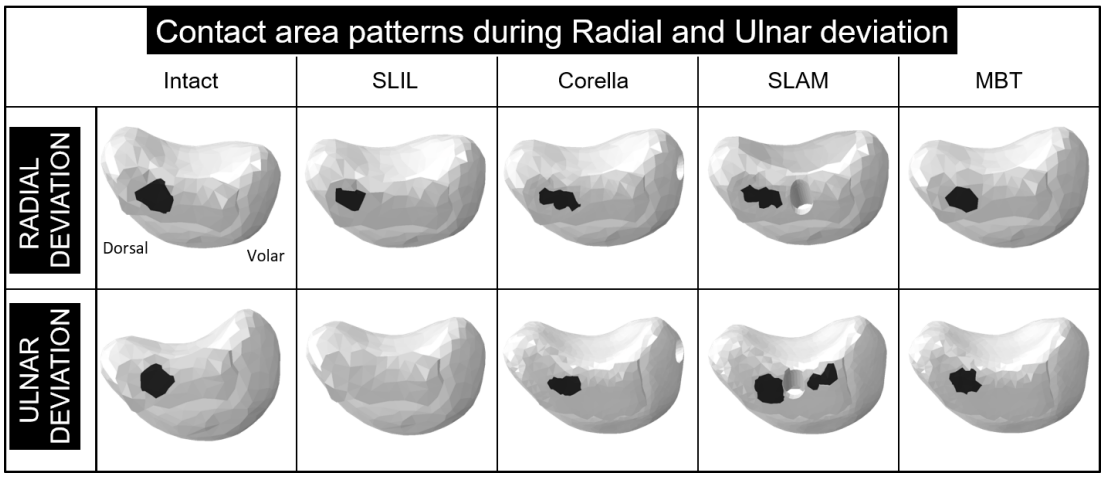

Figure 6.7: Comparison of the contact area patterns between scaphoid and lunate at radial and ulnar deviation.

6.3.3.1 Radial deviation

For the intact scenario during radial deviation, an area of $15.4mm^2$ of scaphoid-lunate contact was predicted at the dorsal side of the articulation. This area was reduced to $9.1mm^2$ following SLIL-sectioning. All three ligamentous reconstruction techniques resulted in increased contact area at scaphoid lunate articulation compared to the SLIL-sectioned case, with MBT ($10.5mm^2$) providing a contact area more similar in shape to the intact wrist scenario, compared to the Corella ($10.7mm^2$) and SLAM ($11mm^2$) method.

6.3.3.2 Ulnar deviation

For ulnar deviation, the intact wrist contact area was $10.7mm^2$. SLIL sectioning resulted in no contact between the lunate and the scaphoid. All three ligamentous reconstruction techniques restored scaphoid-lunate contact, with the MBT technique resulting in a contact area more similar in size ($11.8mm^2$), shape and location to the intact case compared to the Corella ($9.4mm^2$) and SLAM ($15.2mm^2$) methods.

6.3.4 Carpal kinematics

6.3.4.1 Radial deviation

Figure 6.8 shows the in-plane and out-of-plane rotations of the proximal bones at 15° of radial deviation. In the intact case, the proximal bones underwent in plane rotations of $-8.3°$, $-6.0°$ and $-4.2°$ for the scaphoid, lunate and triquetrum respectively, whilst experiencing out-of-plane rotations of 10.3°, 8.3° and 5.1° respectively. After the SLIL sectioning, the rotation of the scaphoid decreased by 12%, and for the triquetrum by 7.7% compared to the intact scenario.

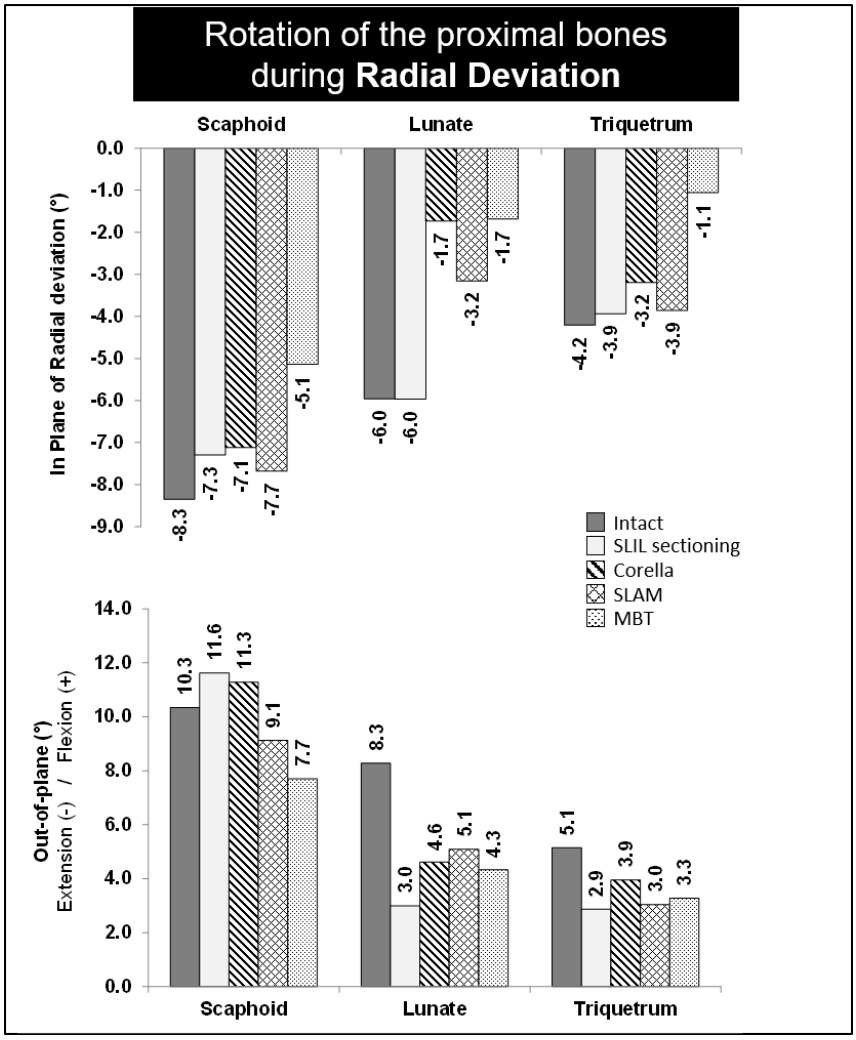

Figure 6.8: Results for the rotation of the proximal bones at radial deviation position.

For the radial deviation position, all the techniques failed to restore the normal rotation especially of the lunate. When compared to the intact case, in the SLAM technique, the rotations were smaller for the scaphoid by 0.6° (7.2%), for the lunate by 2.8° (46%) and for triquetrum by 0.3 (7.1%).

Of the Corella and MBT methods, Corella reduced the rotation of the scaphoid by 1.2° (14.5%), for the lunate 4.3° (71.6%) and for the triquetrum 1.0° (23.8%) compared to the intact case. MBT method reduced the rotation by 3.2° (38.5%) for the scaphoid, 4.3° (71.6%) for the lunate and 3.1° (73.8%) for the triquetrum.

6.3.4.2 Ulnar Deviation

Figure 6.9 shows the in-plane and out-of-plane rotations of the proximal bones at 15° of ulnar deviation. The corresponding values of in-plane and out of plane rotations for the scaphoid, lunate and triquetrum of the intact wrist during ulnar deviation were 9.7°, 8.6°, 10.8° and 0.2°, 0.2°, 0.3°, respectively. After removing the SL ligament, the rotation decreased by 30% for the scaphoid and 2% for the triquetrum but increased by 37% for lunate.

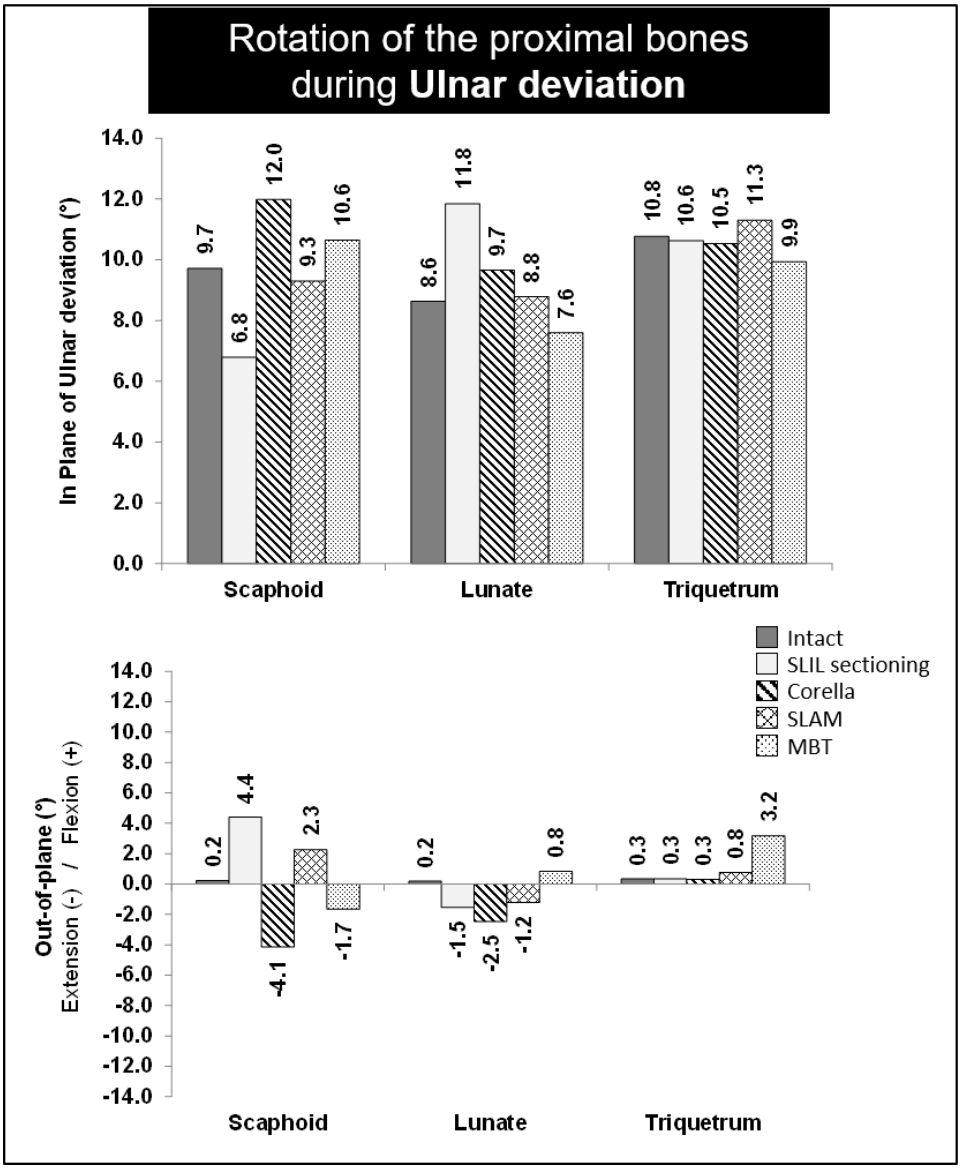

Figure 6.9: Results for the rotation of the proximal bones at ulnar deviation position.

For the ulnar deviation position, after application of the SLAM technique, the rotation was smaller by 0.4° (4.1%) for the scaphoid and by 0.2° (2.3%) for the lunate but was bigger by 0.5° 2.8% for the triquetrum when comparing to the intact case.

Corella technique allowed bigger rotation of the scaphoid by 2.3°(23.7%) and lunate by 1.1° (12.8%) and the rotation of the triquetrum was reduced by 0.3° (4.6%) compared to the intact scenario. MBT also allowed bigger rotation of the scaphoid by 0.9° (9.3%) but reduced the rotation by 1.0° (11.6%) and by 0.9 (8.3%) for the lunate and triquetrum, respectively.

6.4 Discussion

The value of the scapholunate interval post-surgery could imply the success of a ligament reconstruction; however, the reduction of the range of motion of the hand indicates that is not. There is an expectation of some loss of movement following scapholunate ligament reconstruction. This work aimed to identify if any technique allowed significantly greater movement than another.

The reconstruction procedures tether the scaphoid and lunate at multi-planar points in order to restore the connection; however, this tie distorts carpal kinematics and limits wrist motion [5, 6, 137]. The carpal kinematics during radial and ulnar deviation is complex and can be explained using the column theory. At these positions, the scaphoid and triquetrum move in two different planes to allow the motion of the central column. The intricate movements of these bones have not been yet analysed because it is hard to visualise it using the traditional radiographic methods. By reproducing the techniques via virtual surgery, it is easier to understand the effect that the reconstructions have on the carpal mechanics.

6.4.1 SL gap, SL angle and contact area

The SL gap values predicted with the FE models for the radial and ulnar deviation had a similar magnitude to the values obtained for flexion and extension positions reported in Chapter 5; however, SL gap values were slightly bigger to those obtained in the clenched fist ulnar deviated posture reported in Chapter 4.

Following the removal of the SLIL, the FE models predicted an increase of the SL gap up to $0.7mm$ at the dorsal and volar side in ulnar deviation. In the radial deviation, the SL gap value increases up to $1.1mm$ at the dorsal and volar side. Additionally, the SL angle increased by $5.5°$ and $4.0°$ for the radial and ulnar deviation, respectively.

Ligament reconstruction techniques, restored and maintained the dorsal and volar SL gap at ulnar deviation, but all the techniques failed to restored the SL gap at radial deviation position at the volar side. Of the three techniques, MBT was better able to restore SL dorsal gap, restoring it to within $0.1mm$ of the intact wrist for ulnar and radial deviation, whereas SLAM was better able to restore SL volar gap, restoring it to within $0.3mm$ of the intact ligament values. In general, for ulnar and radial deviation, none of the reconstruction techniques could be considered as being superior in restoring SL angle.

The MBT technique produced contact area patterns and areas of similar shape and values to those of the intact wrist at flexion and extension positions. Following SLIL sectioning, some contact between the scaphoid and lunate was maintained at the radial deviation position; but at ulnar deviation, no contact was produced between the same bones. Of the two other techniques considered, Corella reproduced similar patterns but with smaller values. For the SLAM technique, the pattern was modified because the facet on the lunate was drilled to allow the implementation of the technique; however, the pattern was coherent to the pattern registered in the intact scenario.

6.4.2 Wrist kinematics

The results of the ligament reconstructions were contrasting. In the radial deviation, SLAM technique restored better the in-plane and out-of-plane rotations than the Corella and MBT. Inspecting the in-plane of motion, all the techniques restricted the rotation of the lunate. MBT also restricted the rotation of scaphoid and triquetrum. For the out-of-plane rotations, Corella reduced the flexion of the scaphoid but not to the same value of the intact case. SLAM and MBT reduced the rotation of the scaphoid which can progress to a further loss of range of motion after the surgical procedure. None of the techniques restored the out-of-plane rotation of the lunate.

In the ulnar deviation, the in-plane of motion was best restored implementing the SLAM technique, followed by Corella and MBT. Analysing the Corella performance, the results showed that this technique allows bigger rotation of the scaphoid and lunate which can lead to a collapse of the joint. On the other hand, MBT allowed at the same time an increment of the rotation of the scaphoid and a reduction of the rotation fo the lunate, which generated a relative rotation of 3° between the bones, that can restrict the range of motion.

For the radial and ulnar deviation positions, the SLAM leads to improved SL interval and SL angle correction and restore the carpal kinematics compared with other techniques of SL reconstruction. The success of the SLAM technique applied to type II wrist is because is the technique that maintains the natural interaction between the scaphoid and lunate. During the radial and ulnar deviation in a type II wrist, the scaphoid rotates eccentrically with respect to the lunate. The axis of rotation between the bones is inconstant during the wrist motion thus it is difficult to draw an axis functional through all the arc of motion. The incorporation of the dorsal tendon graft in the SLAM reconstruction recreates the biomechanical effect that the dorsal portion of the SL ligament when it is healthy. This dorsal

reinforcement prevents the scaphoid from translating dorsally and resists scaphoid flexion and pronation.

Chapter 7

Conclusions

This thesis evaluated the performance of three reconstruction techniques, modified Brunelli technique (MBT), Corella and Scapholunate method (SLAM), employed in the treatment of the scapholunate ligament injury for a type II wrist using finite element-based virtual surgery.

Three-dimensional finite element (FE) models of the human wrist were constructed from computed tomography data from a hand with a type II lunate. These FE models reproduced carpal kinematics without any restriction in the degrees of freedom of the bone. Each carpal bone has 6 degrees of freedom and its motion is only restricted by its interaction to other bones and a complex set of ligaments.

In the clinic, the reconstruction techniques are evaluated by their ability to restore and maintain the scapholunate (SL) gap and SL angle to a reference value in a static wrist posture. The carpal kinematics is altered after the application of the ligament reconstruction technique; however, the motion pattern is not yet well understood. These variables are intricate to measure experimentally but accessible to measure with the use of FE models.

This thesis evaluated the performance of three ligament reconstruction techniques. The clinical approach of measuring the SL gap and SL angle was

implemented in the assessment. Additionally, the intercortical contact areas between the scaphoid and lunate, as well as the carpal kinematics of the bones were measured in order to explain more clearly the effect of the SLIL disruption and the results of the ligament reconstruction techniques. This thesis aimed to determine which technique allowed a greater range of motion of the hand after a ligament reconstruction.

The evaluation was conducted in five wrist postures: ulnar clenched fist position, 20° flexion, 20° extension, 15° radial and 15° ulnar deviation, in order to assess the effect that the reconstruction techniques have throughout an arc of motion of the hand.

7.1 Conclusions-Performance at ulnar deviated clench fist position

For the ulnar deviated clenched fist position the Corella ligamentous reconstruction technique was the most effective to restore SL gap, angle, and stability following SL ligament injury for a type II wrist and was able to do so without altering the kinematics of the wrist. The Corella reconstruction technique provided a superior outcome restoring dorsal gap, volar gap, and SL angle to within 3.5%, 7.1%, and 8.4%, respectively, of the intact wrist.

A carpal motion analysis was completed using FE models of type I wrist and type II wrist. Using the FE models of the intact ligament case, the individual motion of the carpal bones was registered by tracking the node of the volumetric centroid. The results showed clear differences in the motion pattern when comparing type I and type II wrist. Type I wrist exhibited a row motion pattern with the proximal bones moving equally to same directions as part of the same row. Type II wrist exhibited a column motion pattern with the proximal bones moving to a different direction as expected for elements from different columns.

After the removal of the SL ligament to simulate SL sectioning in a type II wrist, the scaphoid and lunate motion remained very close to that of the intact. Even a small contact area between these two bones was measured at the dorsal region after the removal of the ligament. The kinematic analysis suggested that the extra articulation between the lunate and hamate in a type II wrist may help to improve stability of the wrist following SL ligament injury. After the removal of the SLIL ligament to simulate SLIL disruption, some contact between scaphoid-lunate cartilage articulation was maintained. No previous studies have investigated wrist carpal kinematics after disruption of the SLIL ligament considering the classification of the lunate bone morphology (type I or type II); therefore, it was not possible to compare the results. However, this could explain why some patients with SLIL ligament rupture do not show scapholunate dissociation in x-ray images (visible SL gap).

Following the ligament reconstruction techniques, all the techniques restored the SL gap at the dorsal side closer to the value obtained in the intact case. However, at the volar side, Corella restored the value closer to the intact case to within 7.1%; whereas SLAM technique over closed the gap by 14.2% compared to the intact case. The MBT technique failed to close the interval, with a gap remaining $0.3mm$ (10.7%) greater than for the intact scenario. Inspecting the SL angle, all the techniques reduced the value of the SL angle to below the intact case by 8.4%, 9.6%, and 11.2% for Corella, SLAM and MBT, respectively.

With regard to the carpal kinematics, none of the techniques changed the carpal motion patterns. The results of the simulation showed that the relative distance between the lunate and scaphoid remained similar to the intact ligament case; however, changes in the orientation of the bones were observed. For the Corella technique, the lunate moved closer to the scaphoid due to the effect of the ligament graft bonding at both sides. For the SLAM, the scaphoid took a more vertical position (extend) at the time that was moved more towards the lunate. After the MBT, the lunate bone rotated out-of-plane towards the lunate because

of the constraint of the ligament graft at the dorsal side. Overall, for a type II wrist in the ulnar deviated clenched fist position, the Corella technique restored better the SL gap, SL angle and carpal motion to the values registered in the intact ligament scenario.

7.2 Conclusions-Performance at flexion and extension

For the 20° flexion and the 20° extension positions, the modified Brunelli technique (MBT) was the most effective to maintain the SL gap, SL angle and carpal kinematics for a type II wrist. The MBT reconstruction technique restored the values of the SL dorsal gap, SL volar gap to the same values measured in the intact ligament case and reduced the SL angle to within 1.2% at both positions. The carpal motion at flexion and extension after the MBT application was not altered significantly.

MBT restored the SL gap at the volar and dorsal sides to the same value measured in the intact ligament case and kept the SL angle within 1.2% at both positions. Regarding the carpal kinematics, MBT restored to within 2% the in-plane rotation of the scaphoid and lunate at flexion, and to within 0.6% and 5.6% for the scaphoid and lunate at extension, respectively. At both positions, the in-plane rotation of the triquetrum remained unaltered.

SLAM performed well at the dorsal side in flexion and extension; but at the volar side, the technique failed to close the SL gap. During flexion, SLAM left a gap 8% bigger than the measured in the intact ligament case. The SL angle was restored closer to the value of the intact case (0.9%). The analysis of the carpal kinematic resulted in a reduction of the in-plane rotation of the scaphoid by 3.5% and 3.0% for the flexion and extension position, respectively. The in-plane rotation of the lunate was drastically reduced by 17% in flexion and 3.7% in

extension. The in-plane rotation of the triquetrum was also reduced using this technique.

Corella performance was the worst performance among the three techniques during flexion and extension. The reconstruction restored the SL dorsal gap to the value of the intact ligament case but failed to restore the SL volar gap by leaving a remaining gap 8.3% and 9.3% in flexion and extension, compared to the intact ligament case, respectively. In the kinematic analysis also significant changes were identified, the in-plane rotation of the scaphoid was reduced by 9.7% and 8.0% in flexion. The lunate in-plane rotation was also affected, in flexion was reduced by 2.2%, and in flexion increased by 2.8% compared to the intact scenario. The in-plane rotation of the triquetrum was reduced slightly in both positions.

In conclusion, the MBT technique was superior to other techniques. MBT restored the SL gap and SL angle to similar values registered in the intact ligament model. MBT did not modify significantly the in-plane and out-of-plane rotation of the bones. However, the recorded values were smaller to those obtained in the intact ligament scenario. The reduction in these values can potentially lead to a loss in the range of motion of the hand.

7.3 Conclusions-Performance at radial and ulnar deviation

For the 15° radial deviation and 15° ulnar deviation positions, the scapholunate axis method (SLAM) was the most effective to maintain the SL gap and carpal kinematics for a type II wrist.

The SLAM closed the dorsal SL gap and reduced the SL volar gap to within 8.5% during radial deviation. Also, MBT reduced to within 6.2% of the SL dorsal gap and restored the SL volar gap during ulnar deviation. The SL angle

was bigger by 14.0% in radial deviation and smaller by 5.0% in ulnar deviation, compared to the intact ligament case. In terms of kinematics, the in-plane rotation of the scaphoid was reduced by 7.7% and 4.1% for radial and ulnar deviation, compared to the intact ligament case, respectively. The lunate experienced a considerable in-plane rotation reduction of 46.6% in radial deviation and an increment of 2.3% in ulnar deviation. The triquetrum followed the tendency of the lunate by reducing in 7.1% in radial deviation and increasing by 2.1% in ulnar deviation compared to the intact case.

The Corella technique reduced the SL dorsal gap but failed to restore the SL volar gap during radial deviation. At ulnar deviation, the SL dorsal gap was not restored but the SL volar was reduce to within 3.2% the same value of the intact scenario. The SL angle was 0.6% bigger in the radial deviation but reduced by 18.5% in the ulnar deviation compared to the intact ligament scenario. The carpal kinematic analysis showed that in radial deviation, the in-plane rotation of the scaphoid and lunate was reduced by 14.4% and 71.0% compared to the intact ligament case, respectively. In the ulnar deviation, the in-plane rotation was larger by 23.7% and 12.8% for the scaphoid and lunate, compared to the intact ligament case, respectively.

The MBT had the worst performance from the three techniques analysed. By inspecting the SL gap, MBT restored well the scapholunate gap to the intact ligament case except at the volar side during radial deviation. The SL angle was larger by 7.0% in radial deviation but smaller by 15.4% in ulnar deviation. In terms of kinematics, MBT over restricted the motion in radial deviation by reducing the in-plane rotation by 38.5%,71.0% and 73.8% for the scaphoid, lunate and triquetrum, respectively. In the ulnar deviation, the in-plane rotation of the scaphoid was increased by 9.2%, while the in-plane rotation of the lunate and triquetrum was reduced by 11.6% and 8.3%, respectively.

In conclusion, for the 15° radial deviation and the 15° ulnar deviation positions, the scapholunate axis method (SLAM) was the most effective to maintain the SL gap and carpal kinematics of a type II wrist, followed by Corella and MBT; however, none of the reconstruction techniques could be considered as being superior in restoring SL angle.

7.4 Conclusion-Overall performance summary

Overall, all the techniques restored and preserved the SL dorsal gap in all the positions. At the volar side, at flexion and radial deviation, the results showed a deficiency in maintaining closed the interval. It is suggested to include a volar reinforcement to secure the interaction of the bones and prevent dislocation.

Regarding the carpal kinematics, none of the techniques altered the carpal kinematics in terms of modifying the column motion pattern that is characteristic of the type II wrist. The significant difference in the carpal kinematics between type I and type II wrist was identified to be at the proximal bones, especially for the in-plane and out-of-plane rotation of the scaphoid and triquetrum during radial and ulnar deviation. In this context, the technique that preserves the majority of carpal kinematics at these positions would be advantageous over other techniques.

At clenched fist position, Corella showed good performance followed by SLAM and MBT. At flexion and extension, MBT performed best followed by the SLAM and Corella techniques. At radial and ulnar deviation, SLAM did well followed by the Corella and the MBT. The variation in the results through the arch of motion confirmed the strategy of reviewing the performance of the techniques in the five positions in order to have an all-inclusive evaluation.

In conclusion, SLAM was better able to restore SL gap SL angle and carpal instability following scapholunate injury. SLAM performed well during radial and ulnar deviation because the axis generated to connect the two bones favoured the

relative rotation between the scaphoid and lunate which is characteristic in a type II wrist column kinematics. In general, Corella restricted the in-plane rotations of the bones in several positions, whereas the MBT also restricted the rotation of the bones in the radial deviation posture which could lead to a loss of range of motion of the hand after surgery.

7.5 Research overview

The overall aim of this research project was to evaluate the performance of scapholunate ligament reconstruction techniques on a wrist with a type II lunate.

To achieve this, a FE model was developed from CT scan images of a wrist with a type II lunate. The model comprised 15 bones: radius, ulna, eight carpals and five metacarpals. Layers of articular cartilage were modelled off-setting the bone surfaces at the regions where the bones interact. The wrist joint assembly was completed by adding spring-ligaments and shell-ligaments. The spring-ligament were set to work in tension only showing a non-linear mechanical behaviour. The shell-ligaments were modelled as a hyperelastic material. Tuning of some spring elements was needed to complete validation of the FE model.

The FE model reproduced full carpal kinematics. None of the carpal bones was restricted in its degrees of freedom. Each carpal bone had 6 degrees of freedom and its motion is only restricted by its interaction to other bones and a complex set of ligaments. These numerical models are the first FE models to reproduce accurately full carpal kinematics in a wide range of motion. The use of FE models to evaluate the ligament reconstruction allowed the measurement of variables such as contact area and carpal kinematics that are impossible to measure in the clinic or cadaver studies. Also, the use of FE models provides a fair framework to compare different reconstruction techniques under the same loading and kinematic conditions.

The FE models used to simulate SLIL sectioning and the reconstruction techniques, modified Brunelli technique (MBT), Corella and Scapholunate method (SLAM) were constructed based on the validated model with integral ligaments, also known as the Intact ligament model. With the kinematic results obtained from the intact ligament model, the column motion pattern was confirmed for the type II wrist. The pattern was compared to the outcomes obtained from a type I wrist FE model in order to elucidate the differences between the row (type I wrist) and column (type II wrist) theories of carpal kinematics.

The change of carpal kinematics after the resection of the scapholunate ligament was investigated with the FE model. Based on the intact model of type II wrist, a set of spring elements representing the scapholunate ligament were removed. The gap between the scaphoid and lunate (SL gap) increased after completing the simulation of ulnar deviated clench fist posture; however, some contact between the two bones was maintained, supporting the findings of previous reports that the extra articulation in a type II wrist helps to reduce instability in cases of SL ligament injury.

Regarding the evaluation performance of the ligament reconstruction techniques in a different position, the results were contrasting: one technique was able to close and maintain the SL gap in one position but perform poorly in another. After the analysis of a range of motion comprising clenched fist ulnar deviated, 20° flexion, 20° extension, 15° radial deviation, and 15° ulnar deviation, the SLAM technique was found to perform better in comparison to the other two techniques in a type II wrist. However, these findings do not encourage the use of the SLAM technique. In general, none of the techniques changed significantly the carpal kinematic pattern motion after virtual surgery in the arch of motion studied.

7.6 Clinical relevance

This thesis presented insight into the carpal kinematics at different wrist positions for a type II wrist based on finite element models. The findings indicated that wrist type (type I or type II) is an important factor when considering surgical treatments for wrist instability following a scapholunate ligament injury.

Type II lunate has an incidence of 63% to 73%. From the point of view of carpal mechanics, the column pattern kinematics associated to type II lunate is more complex due to the out-of-plane rotation of the bones, especially during radial and ulnar deviation, compared to the row pattern kinematics of a type I wrist.

No previous studies have assessed the performance of scapholunate ligament reconstruction techniques considering the wrist type classification. Despite the importance that the lunate shape has on the carpal mechanics, its identification and classification before a surgical procedure is not yet a common practice in surgery. The valuable insight offered with the outcomes of this research prompts hand orthopaedic surgeons to assess the type of lunate in order to improve the prediction of the rehabilitation after ligament reconstruction. This work is the first study to include the lunate type as a variable in the performance evaluation of ligament reconstruction.

Using FE models allowed the evaluation of the techniques under the same conditions of ligament stiffness, loading and range of motion, which is not possible to do in *cadaver* or *in-vivo* studies because the conditions change from subject to subject.

7.7 Limitations

The investigation of all the scenarios presented in this thesis was undertaken using finite element modelling, which has a number of limitations. The model was constructed preserving the geometrical integrity of the bones from the CT-scan data. However, the identification of the articular cartilage was inaccessible due to technical restrictions with the contrasting light required to visualise the cartilage in the images. Moore *et al* [17] were able to register the cartilage using micro-computed tomography in disarticulated carpal thus will be convenient to consider this technique in a future FE model.

The majority of the ligaments included in the model were represented using sets of one-dimensional spring elements, which although a common approach, is known to have its limitations, for example, in cases of complex non-uniform 3D stress/strain [124]. More accurate representation requires 3D FE modelling treatment; however, the required approach is highly involved and extremely time-consuming [124]. The approach assuming non-linear behaviour for the spring-ligaments in the model gave accurate results. In practice though, ligaments tend to operate within or close to the linear region, so our modelling assumption should provide reasonable accuracy. A hyperelastic material model was employed to represent soft tissue (cartilage) behaviour, which is considered to be an accurate approach [110].

The type II wrist models were developed from the CT scan of the left hand of a single subject; therefore, any results and conclusions drawn from the analyses should be viewed in this context and interpreted with care. To corroborate the results obtained in this work, more FE models of type II wrist have to be built.

7.8 Future work

The results presented in this work demonstrated the different outcomes that every reconstruction techniques have on the carpal kinematics. The study was limited to the treatment of the scapholunate ligament injury because it is the most injured ligament in the wrist. With the validated models developed in this work, any injury in the carpal bones/ligaments can be investigated, including partial fusion of the bones and its effect in the kinematics.

Regarding the scapholunate ligament reconstruction, in all cases was assumed the use of a portion of the FCR as it is usually in the clinic. The analysis of the use of an artificial graft must be considered in future work. The final tension that the graft ligament has after the surgery was not considered in this thesis as the data is unknown. However, this tension impacts significantly the outcome of the procedure.

Future planned work includes analysis of additional subjects to provide further potential support and verification for the findings of the current investigation. From the results, the SLAM technique was the technique with the best outcome regarding the carpal kinematics. With the inclusion of more subjects, a methodology can be implemented to determine an optimal axis to connect the bones.

References

[1] Ronald. L. Linscheid. Scapholunate ligamentous instabilities (dissociations, subdislocations, dislocations). *Annales de Chirurgie de la Main*, 1984.

[2] Alison Kitay and Scott W. Wolfe. Scapholunate instability: Current concepts in diagnosis and management. *Journal of Hand Surgery*, 37(10):2175–2196, 2012.

[3] Jonny K. Andersson. Treatment of scapholunate ligament injury. *EFORT Open Reviews*, 2(9):382–393, 2017.

[4] Sumedh C. Talwalkar, A. T J Edwards, M. J. Hayton, John H. Stilwell, I. A. Trail, and J. K. Stanley. Results of tri-ligament tenodesis: A modified brunelli procedure in the management of scapholunate instability. *Journal of Hand Surgery*, 31(1):110–117, 2006.

[5] Fernando Corella, Miguel Del Cerro, Montserrat Ocampos, and Ricardo Larrainzar-Garijo. Arthroscopic ligamentoplasty of the dorsal and volar portions of the scapholunate ligament. *Journal of Hand Surgery*, 38(12):2466–2477, 2013.

[6] Steve K. Lee, Dan A. Zlotolow, Anthony Sapienza, Raj Karia, and Jeffrey Yao. Biomechanical comparison of 3 methods of scapholunate ligament reconstruction. *Journal of Hand Surgery*, 39(4):643–650, 2014.

[7] Julio Taleisnik. The ligaments of the wrist. *The Journal of Hand Surgery*, 1(2):110–118, 1976.

[8] J. K. Stanley and I a Trail. Carpal Instability. *J Bone Joint Surg Br*, 76(5):691–700, 1994.

[9] Ian Galley, Gregory I. Bain, and James M. McLean. Influence of lunate type on scaphoid kinematics. *Journal of Hand Surgery*, 32(6):842–847, 2007.

[10] Steven F. Viegas, Kathryn Wagner, Rita Patterson, and Pamela Peterson. Medial (hamate) facet of the lunate. *The Journal of Hand Surgery*, 15(4):564–571, 1990.

[11] Teresa Alonso Rasgado, Qinghang Zhang, David Jimenez Cruz, Colin Bailey, Elizabeth Pinder, Avanthi Mandaleson, and Sumedh Talwalkar. Analysis of tenodesis techniques for treatment of scapholunate instability using the finite element method. *International Journal for Numerical Methods in Biomedical Engineering*, 33(12):1–12, 2017.

[12] Gregory I. Bain, Harry D S Clitherow, Stuart Millar, François Fraysse, John J. Costi, Kevin Eng, Duncan T. McGuire, and Dominic Thewlis. The effect of lunate morphology on the 3-dimensional kinematics of the carpus. *Journal of Hand Surgery*, 40(1):81–89.e1, 2015.

[13] Yasumu Kijima and Steven F. Viegas. Wrist Anatomy and Biomechanics. *Journal of Hand Surgery*, 34(8):1555–1563, 2009.

[14] Robin N. Kamal, Adam Starr, and Edward Akelman. Carpal Kinematics and Kinetics. *Journal of Hand Surgery*, 41(10):1011–1018, 2016.

[15] Nicola Borisch and H. A. Jacob. Wrist kinematics after radiolunate arthrodesis. *Archives of Orthopaedic and Trauma Surgery*, 135(7):1033–1041, 2015.

[16] Laurent Obert, François Loisel, Nicolas Gasse, and Daniel Lepage. Distal radius anatomy applied to the treatment of wrist fractures by plate: a review of recent literature. *Sicot-J*, 1:14, 2015.

[17] Douglas C. Moore, Jane A. Casey, Susannah L. Gilbert, and Joseph J. Crisco. γCT-generated carpal cartilage surfaces: Validation of a technique. *Journal of Biomechanics*, 44(13):2516–2519, 2011.

[18] Jean Vincent Zink, Philippe Souteyrand, Sandrine Guis, Christophe Chagnaud, Yann Le Fur, Daniela Militianu, Jean Pierre Mattei, Michael Rozenbaum, Itzhak Rosner, Maxime Guye, Monique Bernard, and David Bendahan. Standardized quantitative measurements of wrist cartilage in healthy humans using 3T magnetic resonance imaging. *World Journal of Orthopaedics*, 6(8):641–648, 2015.

[19] Richard A Berger. The anatomy and basic biomechanics of the wrist joint. *Journal of Hand Therapy*, 9(2):84–93, 1996.

[20] Richard A Berger. The ligaments of the wrist. A current overview of anatomy with considerations of their potential functions. *Hand Clin*, 13(1):63–82, 1997.

[21] H H C M Savelberg, J G M Kooloos, R Huiskes, and J M G Kauer. Stiffness of the ligaments of the human wrist joint. *Journal of Biomechanics*, 25(4):369–376, 1992.

[22] R Bruce Martin, David B Burr, Neil A Sharkey, and David P Fyhrie. Mechanical Properties of Ligament and Tendon. In *Skeletal Tissue Mechanics*, pages 175–225. Springer New York, New York, NY, 2015.

[23] Eileen Gentleman, Andrea N. Lay, Darryl A. Dickerson, Eric A. Nauman, Glen A. Livesay, and Kay C. Dee. Mechanical characterization of collagen fibers and scaffolds for tissue engineering. *Biomaterials*, 2003.

[24] Victor H (viaf)8672223 Frankel and Margareta. Nordin. *Basic biomechanics of the musculoskeletal system*. Philadelphia : Lippincott Williams & Wilkins, 3rd ed. edition, 2001.

[25] Youngil Youm, R Y McMurthy, Adrian E Flatt, Thomas E Gillespie, Robert Y McMurtry, Adrian E Flatt, and Thomas E Gillespie. Kinematics of the wrist. I. An experimental study of radial-ulnar deviation and flexion-extension. *The Journal of bone and joint surgery. American volume*, 60(4):423–31, 1978.

[26] Masayuki Kobayashi, Richard A Berger, Ladislav Nagy, Ronald L Linscheid, Shigeharu Uchiyama, Macro Ritt, and Kai-Nan An. Normal kinematics of carpal bones: A three-dimensional analysis of carpal bone motion relative to the radius. *Journal of Biomechanics*, 30(8):787–793, 1997.

[27] Barry D. Ferris, Jeremy Stanton, and Javier Zamora. Kinematics of the Wrist. *The Journal of Bone and Joint Surgery*, (82-B):242–245, 2000.

[28] Joseph J. Crisco, Robert D Mcgovern, and Scott W Wolfe. Noninvasive technique for measuring in vivo three-dimensional carpal bone kinematics. *Journal of O*, 19(1):96–100, 1999.

[29] S. W. Wolfe, J. J. Crisco, and L. D. Katz. A non-invasive method for studying in vivo carpal kinematics. *Journal of Hand Surgery (British and European Volume)*, 22(2):147–152, 1997.

[30] Jeroen G. Snel, Henk W. Venema, Thybout M. Moojen, J P Ritt, Cornelis A. Grimbergen, Gerard J. den Heeten, Marco J.P.F. Ritt, Cornelis A. Grimbergen, and Gerard J. den Heeten. Quantitative in vivo analysis of the kinematics of carpal bones from three-dimensional CT images using a deformable surface model and a three-dimensional matching technique. *Medical physics*, 27(9):2037–2047, 2000.

[31] T. M. Moojen, J. G. Snel, M. J.P.F. Ritt, H. W. Venema, G. J. Den Heeten, and K. E. Bos. Pisiform kinematics in vivo. *Journal of Hand Surgery*, 26A:901–907, 2001.

[32] Robert Kaufmann, Jamie Pfaeffle, Brad Blankenhorn, Kathryne Stabile, Doug Robertson, and Robert Goitz. Kinematics of the midcarpal and radiocarpal joints in radioulnar deviation: An in vitro study. *Journal of Hand Surgery*, 30(5):937–942, 2005.

[33] Douglas C. Moore, Joseph J. Crisco, Theodore G. Trafton, and Evan L. Leventhal. A digital database of wrist bone anatomy and carpal kinematics. *Journal of Biomechanics*, 40(11):2537–2542, 2007.

[34] Robin N Kamal, Michael J Rainbow, Edward Akelman, and Joseph J Crisco. In vivo triquetrum-hamate kinematics through a simulated hammering task wrist motion. *The Journal of Bone and Joint Surgery*, 85:1–7, 2012.

[35] Véronique Feipel, Marcel Rooze, S Louryan, and M Lemort. Bi-and three-dimensional CT study of carpal bone motion occuring in lateral deviation. *Surgical and Radiologic Anatomy*, 14:341–348, 1992.

[36] W. T. Jackson, M. S. Hefzy, and Huqing Guo. Determination of wrist kinematics using a magnetic tracking device. *Medical Engineering and Physics*, 16(2):123–133, 1994.

[37] Jun Ichi Ishikawa, Glen L. Niebur, Shigeharu Uchiyama, Ronald L. Linscheid, Akio Minami, Kiyoshi Kaneda, and An Kai-Nan. Feasibility of using a magnetic tracking device for measuring carpal kinematics. *Journal of Biomechanics*, 1997.

[38] Scott W Wolfe, Corey Neu, and Joseph J Crisco. In vivo scaphoid, lunate, and capitate kinematics in flexion and in extension. *The Journal of Hand Surgery*, 25(5):860–869, 2000.

[39] T M Moojen, J G Snel, M J P F Ritt, J M G Kauer, H W Venema, and K E Bos. Three-dimensional carpal kinematics in vivo. *Clinical Biomechanics*, 17(7):506–514, 2002.

[40] Thybout M. Moojen, Jeroen G. Snel, M. J P F Ritt, Henk W. Venema, J. M G Kauer, and Kurt E. Bos. Scaphoid kinematics in vivo. *Journal of Hand Surgery*, 27(6):1003–1010, 2002.

[41] Hisao Moritomo, Akira Goto, Yoshinobu Sato, Kazuomi Sugamoto, Tsuyoshi Murase, and Hideki Yoshikawa. The triquetrum-hamate joint: An anatomic and in vivo three-dimensional kinematic study. *Journal of Hand Surgery*, 28(5):797–805, 2003.

[42] Akira Goto, Hisao Moritomo, Tsuyoshi Murase, Kunihiro Oka, Kazuomi Sugamoto, Takehiro Arimura, Jun Masumoto, Shinichi Tamura, Hideki

Yoshikawa, and Takahiro Ochi. In vivo three-dimensional wrist motion analysis using magnetic resonance imaging and volume-based registration. *Journal of Orthopaedic Research*, 23(4):750–756, 2005.

[43] Robert A Kaufmann, H James Pfaeffle, Brad D Blankenhorn, Kathryne Stabile, Doug Robertson, and Robert Goitz. Kinematics of the Midcarpal and Radiocarpal Joint in Flexion and Extension: An In Vitro Study. *The Journal of Hand Surgery*, 31(7):1142–1148, 2006.

[44] Ravi R. Pillai, Bhaskar Thoomukuntla, Gerard A. Ateshian, and Kenneth J. Fischer. MRI-based modeling for evaluation of in vivo contact mechanics in the human wrist during active light grasp. *Journal of Biomechanics*, 40(12):2781–2787, 2007.

[45] M. Foumani, S. D. Strackee, R. Jonges, L. Blankevoort, A. H. Zwinderman, B. Carelsen, and G. J. Streekstra. In-vivo three-dimensional carpal bone kinematics during flexion-extension and radio-ulnar deviation of the wrist: Dynamic motion versus step-wise static wrist positions. *Journal of Biomechanics*, 42(16):2664–2671, 2009.

[46] Frederick W. Werner, Levi G. Sutton, Mari A. Allison, Louis A. Gilula, Walter H. Short, and Ronit Wollstein. Scaphoid and lunate translation in the intact wrist and following ligament resection: A cadaver study. *Journal of Hand Surgery*, 36(2):291–298, 2011.

[47] François Fraysse, John J. Costi, Richard M. Stanley, Boyin Ding, Duncan McGuire, Kevin Eng, Gregory I. Bain, and Dominic Thewlis. A novel method to replicate the kinematics of the carpus using a six degree-of-freedom robot. *Journal of Biomechanics*, 47(5):1091–1098, 2014.

[48] J??rg Eschweiler, Jan Philipp Stromps, Bj??rn Rath, Norbert Pallua, and Klaus Radermacher. Analysis of wrist bone motion before and after SL-ligament resection. *Biomedizinische Technik*, 61(3):345–357, 2016.

[49] M. A C Craigen and J. K. Stanley. Wrist kinematics. Row, column or both? *Journal of Hand Surgery*, 20(2):165–170, 1995.

[50] Marc Garcia-Elias, M Ribe, J. Rodriguez, M. Cots, and J. Casas. Influence of joint laxity on scaphoid kinematics. *Journal of Hand Surgery*, 20B:379–382, 1995.

[51] John Kauer, Hans Savelberg, Rik Huiskes, and Jan Kooloos. Role of the Wrist Ligaments with Respect to Carpal Kinematics and Carpal Mechanism. *NATO ASI SERIES A LIFE SCIENCES*, 256:271, 1994.

[52] R L Linscheid. Kinematic considerations of the wrist. *Clinical orthopaedics and related research*, 202(202):27–39, 1986.

[53] Heath P. Gould, Richard A. Berger, and Scott W. Wolfe. The origin and meaning of intercalated segment. *Journal of Hand Surgery*, 40(12):2471–2472, 2015.

[54] M J Sandow, T J Fisher, C Q Howard, and S Papas. Unifying model of carpal mechanics based on computationally derived isometric constraints and rules-based motion - the stable central column theory. *The Journal of hand surgery, European volume*, 39(4):353–63, 2014.

[55] J M Mclean, P C Turner, G I Bain, N Rezaian, J Field, and Q Fogg. An association between lunate morphology and scaphoid trapezium trapezoid arthritis. *The Journal of hand surgery, European volume*, 2009(6):778–782, 2009.

[56] S.D. Sagerman, R.M. Hauck, and A.K. Palmer. Lunate morphology: Can it be predicted with routine x-ray films. *Journal of Hand Surgery*, 20(1), 1995.

[57] S.F. Viegas, R.M. Patterson, J.A. Hokanson, and J. Davis. Wrist anatomy: Incidence, distribution, and correlation of anatomic variations, tears, and arthrosis. *Journal of Hand Surgery*, 18(3), 1993.

[58] Byoung Jin Kim, David Kovacevic, Young Min Lee, Jong Hwan Seol, and Myung Sun Kim. The role of lunate morphology on scapholunate instability and fracture location in patients treated for scaphoid nonunion. *CiOS Clinics in Orthopedic Surgery*, 8(2):175–180, 2016.

[59] Eric Quan Pang, Nathan Douglass, and Robin N. Kamal. Association of lunate morphology with carpal instability in scapholunate ligament injury. *HAND*, 13(4):418–422, 2017.

[60] Steven F. Viegas. The lunatohamate articulation of the midcarpal joint. *Arthroscopy: The Journal of Arthroscopic and Related Surgery*, 1990.

[61] Ronald C. Burgess. Anatomic variations of the midcarpal joint. *Journal of Hand Surgery*, 1990.

[62] Amaar M Malik, Mark E Schweitzer, Randall W Cuip, Lee A Osterman, and Goeffery Manton. MR Imaging of the type II lunate bone: Frequency, extent, and associated findings. *American Journal of Roentgenology*, 173(August):335–338, 1999.

[63] B. Aufauvre, G. Herzberg, J. Garret, E. Berthonneaud, and J. Dimnet. A new radiographic method for evaluation of the position of the carpus in the coronal plane: Results in normal subjects. *Surgical and Radiologic Anatomy*, 21(6):383–385, 1999.

[64] K. Nakamura, R. M. Patterson, H. Moritomo, and S. F. Viegas. Type I versus type II lunates: Ligament anatomy and presence of arthrosis. *Journal of Hand Surgery*, 26(3):428–436, 2001.

[65] Steven C Haase, Richard A Berger, and Alexander Y Shin. Association between lunate morphology and carpal collapse patterns in scaphoid nonunions. *The Journal of hand surgery*, 32(7):1009–12, 2007.

[66] Peter C. Rhee, Steven L. Moran, and Alexander Y. Shin. Association between lunate morphology and carpal collapse in cases of scapholunate dissociation. *Journal of Hand Surgery*, 34(9):1633–1639, 2009.

[67] James M. McLean, Gregory I. Bain, Adam C. Watts, Luke T. Mooney, Perry C. Turner, and Mary Moss. Imaging recognition of morphological variants at the midcarpal joint. *Journal of Hand Surgery*, 2009.

[68] D Nuttall, I A Trail, and J K Stanley. Movement of the scaphoid in the normal wrist. *Journal of Hand Surgery (British and European Volume)*, 23B:762–764, 1998.

[69] Richard. A. Berger. The gross and histologic anatomy of the scapholunate interosseous ligament. *Journal of Hand Surgery*, 1996.

[70] S. Sivananthan, L. Sharp, and Y. C. Loh. Management of wrist instability. *Current Orthopaedics*, 21(3):207–214, 2007.

[71] M Morán-Hevia, M D V Lopez, M Vicente Quilez, V Santamaría Pérez, M Molinero Montes, I Noval Tunon, E Guerra del Barrio, and A I Barrio Alonso. Carpal Instability-A Radiological Challenge. *Ecr*, 2017.

[72] Kimia Khalatbari Kani, Hyojeong Mulcahy, and Felix S. Chew. Understanding carpal instability: a radiographic perspective. *Skeletal Radiology*, 45(8):1031–1043, 2016.

[73] Giorgio A. Brunelli and Giovanni R. Brunelli. A new technique to correct carpal instability with scaphoid rotary subluxation: A preliminary report. *Journal of Hand Surgery*, 20(3 PART 2):82–85, 1995.

[74] Marc Garcia-Elias, Alberto L. Lluch, and John K. Stanley. Three-ligament tenodesis for the treatment of scapholunate dissociation: Indications and surgical technique. *Journal of Hand Surgery*, 31(1):125–134, 2006.

[75] Fernando Corella, M. Del Cerro, R. Larrainzar-Garijo, and T. Vázquez. Arthroscopic ligamentoplasty (bone-tendon-tenodesis). A new surgical technique for scapholunate instability: Preliminary cadaver study. *Journal of Hand Surgery: European Volume*, 36(8):682–689, 2011.

[76] Jean François Chabas, André Gay, David Valenti, Didier Guinard, and Régis Legre. Results of the Modified Brunelli Tenodesis for Treatment of Scapholunate Instability: A Retrospective Study of 19 Patients. *Journal of Hand Surgery*, 33(9):1469–1477, 2008.

[77] Annie C. Links, Simon H. Chin, Thanapong Waitayawinyu, and Thomas E. Trumble. Scapholunate Interosseous Ligament Reconstruction: Results With a Modified Brunelli Technique Versus Four-Bone Weave. *Journal of Hand Surgery*, 33(6):850–856, 2008.

[78] Jeffrey Yao, Dan Zlotolow, and Steve Lee. ScaphoLunate Axis Method. *Journal of Wrist Surgery*, 05(01):059–066, 2016.

[79] T. Miyake, H. Hashizume, H. Inoue, Q. Shi, and N. Nagayama. Malunited Colles' fracture Analysis of stress distribution. *Journal of Hand Surgery*, 1994.

[80] F. Schuind, W. P. Cooney, R. L. Linscheid, K. N. An, and E. Y S Chao. Force and pressure transmission through the normal wrist. A theoretical two-dimensional study in the posteroanterior plane. *Journal of Biomechanics*, 28(5), 1995.

[81] D D Anderson and T E Daniel. A contact-coupled finite element analysis of the radiocarpal joint. *Seminars in arthroplasty*, 6(1):30–36, 1995.

[82] Andrew K Palmer and Frederick W. Werner. Biomechanics of the distal radioulnar joint., 1984.

[83] Thomas Trumble, Richard R. Glisson, Anthony V. Seaber, and James R. Urbaniak. Forearm force transmission after surgical treatment of distal radioulnar joint disorders. *Journal of Hand Surgery*, 1987.

[84] Alexander D. Blevens, Terry R. Light, Warren S. Jablonsky, Douglas G. Smith, Avinash G. Patwardhan, Marc E. Guay, and Thomas S. Woo. Radiocarpal articular contact characteristics with scaphoid instability. *Journal of Hand Surgery*, 14(5):781–790, 1989.

[85] M. Oda, H. Hashizume, T. Miyake, H. Inoue, and N. Nagayama. A stress distribution analysis of a ceramic lunate replacement for Kienbock's disease. *Journal of Hand Surgery*, 25 B(5), 2000.

[86] E. Horii, M. Garcia-Elias, K. N. An, A. T. Bishop, W. P. Cooney, R. L. Linscheid, and E. Y.S. Chao. Effect on force transmission across the carpus in procedures used to treat Kienböck's disease. *Journal of Hand Surgery*, 15A:393–400, 1990.

[87] P Ledoux, D Lamblin, and R Targowski. Modifications to the mechanical behavior of the wrist after fracture of the scaphoid. Modeling by finite element analysis. *Acta Orthopaedica Belgica*, 67(3):236–241, 2001.

[88] P Ledoux, D Lamblin, A Wuilbaut, and F Schuind. A finate-element analysis of Kienböck's disease. *Journal of Hand Surgery*, pages 286–291, 2008.

[89] D. Ulrich, B. Van Rietbergen, A. Laib, and P. Rüegsegger. Load transfer analysis of the distal radius from in-vivo high-resolution CT-imaging. *Journal of Biomechanics*, 32:821–828, 1999.

[90] Shawn D Carrigan, Robert A Whiteside, David R Pichora, and Carolyn F Small. Development of a Three-Dimensional Finite Element Model for Carpal Load Transmission in a Static Neutral Posture. *Annals of Biomedical Engineering*, 31(6):718–725, 2003.

[91] Donald D Anderson, Balachandra R Deshpande, Thomas E Daniel, and Mark E Baratz. A three-dimensional finite element model of the radiocarpal joint: distal radius fracture step-off and stress transfer. *The Iowa orthopaedic journal*, 25:108–117, 2005.

[92] S. Fischli, R. W. Sellens, M. Beek, and D. R. Pichora. Simulation of extension, radial and ulnar deviation of the wrist with a rigid body spring model. *Journal of Biomechanics*, 42(9):1363–1366, 2009.

[93] Xin Guo, Yubo Fan, and Zong Ming Li. Effects of dividing the transverse carpal ligament on the mechanical behavior of the carpal bones under axial compressive load: A finite element study. *Medical Engineering and Physics*, 31(2):188–194, 2009.

[94] M. K. Gislason, D. H. Nash, A. Nicol, A. Kanellopoulos, M. Bransby-Zachary, T. Hems, B. Condon, B. Stansfield, and B. Gislason, Magnus K.

and Nash, D.H. and Nicol, A.C. and Kanellopoulos, A. and Bransby-Zachary, M. and Hems, T. and Condon, B. and Stansfield. A three-dimensional finite element model of maximal grip loading in the human wrist. *Proceedings of the Institution of Mechanical Engineers, Part H: Journal of Engineering in Medicine*, 223(7):849–861, 2009.

[95] M K Gíslason, B Stansfield, M Bransby-Zachary, T Hems, and D H Nash. Load transfer through the radiocarpal joint and the effects of partial wrist arthrodesis on carpal bone behaviour: a finite element study. *The Journal of hand surgery, European volume*, 37(9):871–8, 2012.

[96] Magnús Kjartan Gíslason and David H Nash. Finite Element Modelling of a Multi-Bone Joint : The Human Wrist. *Finite Element Analysis New Trends and Developments*, pages 77–98, 2012.

[97] M.K. Gíslason, Benedict Stansfield, and David H. Nash. Finite element model creation and stability considerations of complex biological articulation: The human wrist joint. *Medical Engineering and Physics*, 32(5):523–531, 2010.

[98] Mohd Nazri Bajuri and Mohammed Rafiq Abdul Kadir. Finite element modelling of the healthy wrist joint. In *Computational Biomechanics of the Wrist Joint*, chapter 4, pages 33–40. Springer Berlin Heidelberg, 2013.

[99] F. Ezquerro, S. Jim??nez, A. P??rez, M. Prado, G. de Diego, A. Sim??n, S. Jiménez, A. Pérez, M. Prado, G. de Diego, and A. Simón. The influence of wire positioning upon the initial stability of scaphoid fractures fixed using Kirschner wires. A finite element study. *Medical Engineering and Physics*, 29(6):652–660, 2007.

[100] N Grosland, R Rogge, and B Adams. Influence of Articular Geometry on Prosthetic Wrist Stability, 2004.

[101] Peter Varga, Philippe K. Zysset, Philip Schefzig, Ewald Unger, Winfried Mayr, and Jochen Erhart. A finite element analysis of two novel screw

designs for scaphoid waist fractures. *Medical Engineering & Physics*, 38(2):131–139, 2016.

[102] K. Nakamura, M. Beppu, R.M. Patterson, C.A. Hanson, P.J. Hume, and S.F. Viegas. Motion analysis in two dimensions of radial-ulnar deviation of type I versus type II lunates. *Journal of Hand Surgery*, 25(5), 2000.

[103] Robert Davis Cook. *Finite Element Modeling for Stress Analysis*. John Wiley & Sons, Inc., USA, 1st edition, 1994.

[104] R. Huiskes and E. Y.S. Chao. A survey of finite element analysis in orthopedic biomechanics: The first decade. *Journal of Biomechanics*, 1983.

[105] Young W Kwon and Hyochoong Bang. *The Finite Element Method Using MATLAB*. CRC Press, Inc., USA, 2nd edition, 2000.

[106] W A M Brekelmans, H W Poort, and T J J H Slooff. A New Method to Analyse the Mechanical Behaviour of Skeletal Parts. *Acta Orthopaedica Scandinavica*, 43(5):301–317, 1972.

[107] K J Bathe. *Finite Element Procedures*. Prentice Hall, 2006.

[108] Michael Smith. *ABAQUS/Standard User's Manual, Version 6.9*. Dassault Systèmes Simulia Corp, United States, 2009.

[109] Kira D. Novakofski, Sarah L. Pownder, Matthew F. Koff, Rebecca M. Williams, Hollis G. Potter, and Lisa A. Fortier. High-Resolution Methods for Diagnosing Cartilage Damage In Vivo. *Cartilage*, 7(1):39–51, 2016.

[110] Mohd Nazri Bajuri, Mohammed Rafiq Abdul Kadir, Malliga Raman Murali, and T. Kamarul. Biomechanical analysis of the wrist arthroplasty in rheumatoid arthritis: a finite element analysis. *Medical & Biological Engineering & Computing*, 51(1-2):1–12, 2012.

[111] Richard A. Berger, Toshihiko Imeada, Lawrence Berglund, and Kai Nan An. Constraint and material properties of the subregions of the scapholunate interosseous ligament. *Journal of Hand Surgery*, 24(5):953–962, 1999.

[112] C. P. Brown, T. C. Nguyen, H. R. Moody, R. W. Crawford, and A. Oloyede. Assessment of common hyperelastic constitutive equations for describing normal and osteoarthritic articular cartilage. *Proceedings of the Institution of Mechanical Engineers, Part H: Journal of Engineering in Medicine*, 223(6):643–652, 2009.

[113] Farzaneh Safshekan, Mohammad Tafazzoli-Shadpour, Majid Abdouss, and Mohammad B. Shadmehr. Mechanical characterization and constitutive modeling of human trachea: Age and gender dependency. *Materials*, 9(6), 2016.

[114] Zuoping Li, Jong Eun Kim, James S. Davidson, Brandon S. Etheridge, Jorge E. Alonso, and Alan W. Eberhardt. Biomechanical response of the pubic symphysis in lateral pelvic impacts: A finite element study. *Journal of Biomechanics*, 40(12):2758–2766, 2007.

[115] Steve K. Lee, Healthy Desai, Benjamin Silver, Gurpreet Dhaliwal, and Nader Paksima. Comparison of radiographic stress views for scapholunate dynamic instability in a cadaver model. *Journal of Hand Surgery*, 36(7):1149–1157, 2011.

[116] Claus Falck Larsen, Bjarne Stigsby, Steen Lindequist, Torben Bellstrøm, Finn K. Mathiesen, and Tune Ipsen. Observer variability in measurements of carpal bone angles on lateral wrist radiographs. *The Journal of Hand Surgery*, 16(5):893–898, 1991.

[117] A. F. Tencer, S. F. Viegas, J. Cantrell, M. Chang, P. Clegg, C. Hicks, C. O'Meara, and J. B. Williamson. Pressure distribution in the wrist joint. *Journal of Orthopaedic Research*, 6(4):509–517, 1988.

[118] S F M D Viegas, A F Tencer, J Cantrell, M Chang, P B S Clegg, C M D Hicks, C O'Meara, J B B S Williamson, A F Tencer Ph D, J Cantrell, M Chang Ph D, P B S Clegg, C M D Hicks, C O M D Meara, and J B B S Williamson. Load transfer characteristics of the wrist . Part I . The normal joint. *Journal of Hand Surgery*, 12(6):971–978, 1987.

[119] Thomas B. Sebastian, Hüseyin Tek, Joseph J. Crisco, and Benjamin B. Kimia. Segmentation of carpal bones from CT images using skeletally coupled deformable models. *Medical Image Analysis*, 2003.

[120] Michael J Rainbow, Robin N Kamal, Evan L Leventhal, Edward Akelman, Douglas C Moore, Scott W Wolfe, and Joseph J Crisco. In Vivo Kinematics of the Scaphoid, Lunate, Capitate, and Third Metacarpal in Extreme Wrist Flexion and Extension. *The Journal of Hand Surgery*, 38(2):278–288, 2013.

[121] Tomas Pevny, Ghazi M. Rayan, and Davis Egle. Ligamentous and tendinous support of the pisiform, anatomic and biomechanical study. *Journal of Hand Surgery*, 1995.

[122] Ghazi M. Rayan, Bretton H. Jameson, and Kyung W. Chung. The pisotriquetral joint: Anatomic, biomechanical, and radiographic analysis. *Journal of Hand Surgery*, 2005.

[123] Tony M Keaveny, Elise F Morgan, Glen L Niebur, and Oscar C Yeh. Biomechanics of Trabecular Bone. *Annual Review of Biomedical Engineering*, 3(1):307–333, aug 2001.

[124] Jeffrey A. Weiss, John C. Gardiner, Benjamin J. Ellis, Trevor J. Lujan, and Nikhil S. Phatak. Three-dimensional finite element modeling of ligaments: technical aspects. *Medical Engineering & Physics*, 27(10):845–861, 2005.

[125] W a Jones. Beware the sprained wrist. *British Editorial Society of Bone and Joint Surgery*, 70(2):293 – 297, 1988.

[126] Frederick W. Werner, Walter H. Short, Jason K. Green, Peter J. Evans, and Jacquelyn A. Walker. Severity of scapholunate instability is related to joint anatomy and congruency. *Journal of Hand Surgery*, 32(1):55–60, 2007.

[127] KL Van Den Abbeele, YC Loh, J K Stanley, and IA Trail. Early results of a modified Brunelli procedure for scapholunate instability. *Journal of Hand Surgery (British and European Volume)*, 23B:258–261, 1998.

[128] Roberto Leonardo-Diaz, Teresa Alonso-Rasgado, David Jimenez-Cruz, Colin G. Bailey, and Sumedh Talwalkar. Performance evaluation of surgical techniques for treatment of scapholunate instability in a type II wrist. *International Journal for Numerical Methods in Biomedical Engineering*, (November 2018):1–19, 2019.

[129] Joshua E Johnson, Phil Lee, Terence E. McIff, E Bruce Toby, and Kenneth J Fischer. Effectiveness of surgical reconstruction to restore radiocarpal joint mechanics after scapholunate ligament injury: An in vivo modeling study. *Journal of Biomechanics*, 46(9):1548–1553, may 2013.

[130] R. Schmitt, S. Froehner, G. Coblenz, and G. Christopoulos. Carpal instability. *European Radiology*, 16(10):2161–2178, 2006.

[131] L. K. Ruby, K. N. An, R. L. Linscheid, W. P. Cooney, and E. Y.S. Chao. The effect of scapholunate ligament section on scapholunate motion. *Journal of Hand Surgery*, 12(5):767–771, 1987.

[132] Joshua E. Johnson, Terence E. McIff, Phil Lee, E. Bruce Toby, and Kenneth J. Fischer. Validation of radiocarpal joint contact models based on images from a clinical MRI scanner, 2014.

[133] Frederick W. Werner, Walter H. Short, and Jason K. Green. Changes in patterns of scaphoid and lunate motion during functional arcs of wrist motion induced by ligament division. *Journal of Hand Surgery*, 30A:1156–1160, 2005.

[134] Walter H. Short, Frederick W. Werner, and Levi G. Sutton. Dynamic Biomechanical Evaluation of the Dorsal Intercarpal Ligament Repair for Scapholunate Instability. *Journal of Hand Surgery*, 34(4):652–659, 2009.

[135] Joseph J Crisco, Scott W Wolfe, Corey P Neu, and Sandi Pike. Advances in the in vivo measurement of carpal kinematics. *The orthopedic clinics of North America.*, 32(2), 2001.

[136] Joshua E. Johnson, Phil Lee, Terence E. McIff, E. Bruce Toby, and Kenneth J. Fischer. Scapholunate ligament injury adversely alters in

vivo wrist joint mechanics: An MRI-based modeling study. *Journal of Orthopaedic Research*, 31(9):1455–1460, 2013.

[137] Lawrence Ambrose, Martin A. Posner, Steven M. Green, and Steven Stuchin. The effects of scaphoid intercarpal stabilizations on wrist mechanics: An experimental study. *Journal of Hand Surgery*, 17(3):429–437, 1992.

Annex 1: Journal publication 1

Received: 21 November 2018 | Revised: 18 August 2019 | Accepted: 19 October 2019
DOI: 10.1002/cnm.3278

RESEARCH ARTICLE - APPLICATION

WILEY

Performance evaluation of surgical techniques for treatment of scapholunate instability in a type II wrist

Roberto Leonardo-Diaz[1] | Teresa Alonso-Rasgado[2] | David Jimenez-Cruz[1] | Colin G. Bailey[2] | Sumedh Talwalkar[3]

[1] School of Materials, The University of Manchester, Manchester, UK
[2] School of Engineering and Materials Science, Queen Mary University of London, London, UK
[3] Wrightington Hospital, Wrightington Wigan and Leigh NHS Foundation Trust, Lancashire, UK

Correspondence
Teresa Alonso Rasgado, Professor of Mechanical Engineering, School of Engineering and Materials Science, Queen Mary University of London, London E1 4NS, UK.
Email: t.alonso@qmul.ac.uk

Abstract

We investigated the performance of three tenodesis techniques, modified Brunelli, Corella, and scapholunate axis (SLAM) methods in repairing scapholunate interosseous ligament (SLIL) disruption for a type II wrist using finite element–based virtual surgery and compared the results with those of a previous investigation for a type I wrist. In addition, a comparison of the carpal mechanics of type I and type II wrists was undertaken in order to elucidate the difference between the two types. For the type II wrist, following simulated SLIL disruption, the Corella reconstruction technique provided a superior outcome, restoring dorsal gap, volar gap, and SL angle to within 3.5%, 7.1%, and 8.4%, respectively, of the intact wrist. Moreover, application of the ligament reconstruction techniques did not significantly alter the motion pattern of the type II and type I wrists. For the type I wrist, SLIL disruption resulted in no contact between scaphoid-lunate cartilage articulation, whereas for the type II wrist, some contact was maintained. We conclude that the Corella ligamentous reconstruction technique is best able to restore SL gap, angle, and stability following SL ligament injury for both type II and type I wrists and is able to do so without altering wrist kinematics. Our findings also support the view that type I wrists exhibit row behaviour and type II wrists column behaviour. In addition, our analysis suggests that the extra articulation between the lunate and hamate in a type II wrist may help improve stability following SL ligament injury.

Novelty

- No previous studies have assessed the performance of scapholunate ligament reconstruction techniques considering the two types (I and II) of wrist.
- No previous studies have investigated wrist carpal mechanics both before and after disruption of the SL ligament based on lunate bone morphology.

KEYWORDS

finite element, ligament reconstruction, scapholunate angle, scapholunate gap, row/column theory, type II wrist

1 | INTRODUCTION

Scapholunate (SL) dissociation occurs when the scaphoid and lunate move excessively in relation to one another; it is caused by the injuring of the SL interosseous ligament (SLIL) and affects carpal instability.[1] Often, SLIL injuries are not diagnosed or treated during an acute phase of injury because it can take 3 to 12 months after trauma before dynamic instability develops and the SL dissociation can be detected radiologically; additionally, in some cases, people may have a tear of the SLIL but not present clinical symptoms.[2] SL instability has been reported to occur in approximately 5% of cases of wrist sprains[2] and is believed to be as common as scaphoid fractures.[3] Some authors have theorised that the effect on carpal instability after SLIL tear may be moderated by the bone geometry, which may help to explain why some patients go on to progressive instability whilst others do not.[4-6] In a cadaver study, Werner et al determined that bone geometry at the distal radius and proximal scaphoid may have a moderate effect on the carpal instability after sectioning.[4] Rhee et al found from a clinical review that patients possessing an additional articulation between the lunate and hamate have a lower incidence of DISI following a complete SLIL tear.[5] Other researchers, however, have found no link between bone geometry and carpal instability following SL injury.[7]

The wrist has been categorised into type I and type II depending on the morphology of the lunate bone. A type I lunate is identified as having a shortest distance between the capitate and triquetrum (C-T distance) on a posterior anterior radiograph[8,9] of ≤2 mm (Figure 1A). A type II lunate has an extra facet that articulates with the hamate,[8-11] and a C-T distance ≥4 and ≤8.9 mm (Figure 1B).[8,9] A third, intermediate group, laying between type I and type II wrists, has

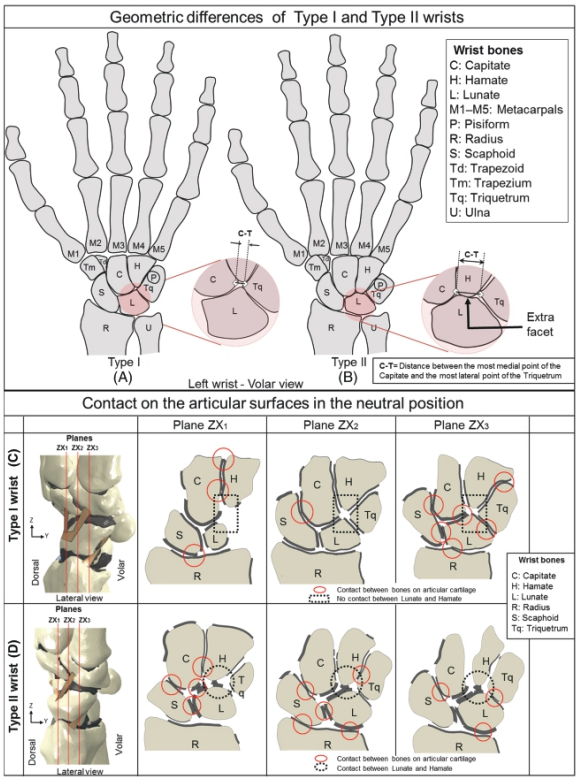

FIGURE 1 A, type I lunates do not articulate with hamate. B, type II lunates have an extra facet that allows articulation with the hamate, C-T distance ranging ≤4 to 8.9 mm. C, contact between articular cartilages of the bones for different planes in the neutral position. Type I wrist, there is no contact between the hamate and lunate in any plane. D, type II wrist, there is contact between the hamate and lunate in more than one plane

also been identified by some researchers.[7] There is a clear difference between a type I and II wrist in articular cartilage contact (Figure 1C,D).[9,10] No registry of the incidence of type I and type II wrists has been set up, but some previous studies on lunate morphology reported type II wrists to be more common, with the proportion of the frequency of a type II lunate[11-14] being 63% to 73%. The categorisation is seldom mentioned in the literature, and only recently have some authors discussed the incidence, variation, associated pathologies, and the clinical importance of the extra facet, including some studies that relate lunate morphology to carpal mechanics. Statistically, there is no correlation between lunate type and gender, age, hand dominance, or occupation.[8,15]

Classically, carpal mechanics may be described using two main motion theories, row theory and column theory, with type I wrists considered to exhibit row mechanics and type II column mechanics.[8] In row theory, the carpal bones are divided into two rows of adjacent bones. The proximal row consists of the scaphoid, the lunate, the triquetrum, and the pisiform; the distal row composes of the hamate, capitate, trapezium, and trapezoid (see Figure 2A).[8,15] During clench fist ulnar deviation (volar view), the proximal row rotates and slides over the concave surface of the radius; meanwhile, the distal row rotates in the same direction sliding over the proximal row allowing the motion (Figure 2). In column theory, the carpal bones are distributed into three columns: The lateral column consists of the scaphoid; the central column consists of lunate, capitate, hamate, trapezium, and trapezoid; and the medial column consists of the triquetrum and pisiform (Figure 2C). Column theory suggests that during ulnar deviation (volar view), the central column rotates clockwise (in the ulnar direction); simultaneously, the medial column slides over the hamate to the dorsal side making space for the moving bones; meanwhile, the scaphoid tilts towards the vertical by the pulling of the ligament that joins it with trapezium and trapezoid[8,15] (Figure 2D). To date, validation of these theories has only been performed using plane X-ray and fluoroscopic studies.[8,11,15]

A number of surgical techniques have been employed to reconstruct the SLIL following injury in cases where the SLIL is nonrepairable but the SL dissociation is reducible; these include the Brunelli tenodesis method and the modified Brunelli technique (MBT)[16-18] and, more recently, the Corella[19] and the SL axis methods (SLAM).[20] Existing in vitro studies comparing the performance of the techniques have failed to report whether the specimens considered were type I or type II wrists.[20]

The aim of the current study is to investigate the performance of three tenodesis techniques, MBT, Corella, and SLAM methods used to repair SL ligament disruption for type I and II wrists. The ability of the techniques to restore wrist stability (SL gap and angle) following SLIL tear is assessed using finite element (FE) models developed to simulate the reconstruction techniques in addition to SL tear and intact wrist scenarios. The techniques are assessed for both type I and II wrists based on FE model predictions of SL gap and angle at both dorsal and volar sides and scaphoid-lunate contact area. In addition, the carpal mechanics of the wrists is investigated using the FE models in order to determine whether application of the ligament reconstruction techniques alters wrist kinematics. Moreover, the current study aims to determine if it is appropriate to employ the same technique for both type I and II wrists or if the choice of ligament reconstruction technique should potentially be made based on wrist type.

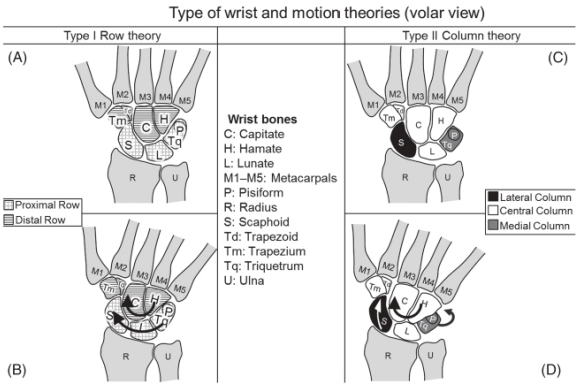

FIGURE 2 Wrist motion theories. Type I—Row theory; A, neutral position; B, ulnar deviated clench fist position. Type II—Column theory; C, neutral position; D, ulnar deviated clench fist position

2 | MATERIALS AND METHODS

Previously, the authors developed a FE model, validated with data from a cadaveric study, which was used to investigate the performance of three surgical SLIL reconstruction techniques used to treat SL instability in type I wrists.[21] The current study is an extension of this investigation but for type II wrists.

Six FE models were developed to simulate the intact SL ligament type II wrist in neutral posture and five ulnar deviated clenched fist position cases: intact SL ligament, SLIL sectioning, and MBT, Corella, and SLAM tenodesis techniques.

Dorsal and volar SL gap and angle were obtained for the six scenarios from the type II wrist models enabling the performance of the reconstruction techniques to be assessed and compared with the results from models of type I wrists, obtained previously by the research group.[21] In addition, contact areas of lunate and scaphoid bones were obtained from the type I and II models enabling the difference between type I and type II wrists to be elucidated and performance of the reconstruction techniques to be further assessed. In addition, the carpal mechanics is investigated in the context of row/column theory for type I and type II wrist in order to study the kinematics of the two types of wrist before and following the application of the virtual reconstruction techniques.

2.1 | FE modelling

The geometry for the 3D FE models was constructed from computed topography (CT) scan images of a type II wrist from the left hand of a subject with no history of injury. The classification of a type wrist II for the subject was based on the criteria described by Galley et al,[8] that being that the minimal distance between capitate-triquetrum (C-T distance) of the subject be ≥4 mm (6.5 mm) (Figure 3A). The CT images comprised 232 slices with a thickness of 1 mm and transverse resolution of 512 × 512, including the distal end of radius and ulna to the metacarpals.

CT scan images were imported into 3D image segmentation and processing software. Semiautomatic segmentation was performed using a thresholding technique to construct the geometries with images resampled with a pixel spacing of 0.4 mm × 0.4 mm × 0.4 mm in order to optimise element size and mesh quality. Two masks were created to produce 3D surface representations of the cortical and cancellous bone for each of the 15 bones, radius, ulna, the eight carpals, and the five metacarpals bones (Figure 3B). The surface representations were imported into Abaqus 6.14 (Dassault Systemes, Rhode Island) and then converted into a solid mesh. Parts representing the bones were assembled in Abaqus to create the wrist model; each part was meshed using solid tetrahedral elements (C3D4) (Figure 3C).

Cartilage layers were modelled with wedge elements (C3D6) by offsetting the articulating surfaces on the external layer of the cortical bone by half the minimum gap between the articulating bones[22] (Figure 3D) to create a solid layer. This solid layer was meshed with wedge elements (C3D6). Surface-to-surface contact was defined between the cartilage surfaces on each articulation for the proximal carpal bones to allow free movement of scaphoid and lunate. A friction coefficient of 0.002 was considered for all the cartilage surface-to-surface interactions.[23] Distal carpal bones were considered tied to simulate the minimal motion between each pair of bones, as reported in previous studies.[24]

Thirty-one sets of ligaments were modelled with two-node springs elements, including 10 extrinsic, 16 intrinsic, and five interosseous ligaments. The origin and insertion points were estimated based on anatomical studies.[25,26] The anatomic relationship of the volar triquetrocapitate (T-C) and the volar triquetrohamate (T-H) was set in accordance with the taxonomy reported by Nakamura.[27] Each set of ligaments was represented by multiple elements to distribute the force over an area to avoid stress concentrations (Figure 3E).

Three ligaments, volar radiocaphocapitate, dorsal radiocarpal, and intercarpal, were modelled using shell elements to simulate the wrapping of these ligaments around scaphoid, lunate and hamate, and capitate and scaphoid, respectively. All 31 sets of ligaments were defined as operating in tension only, with stiffness from 10 to 325 N/mm in accordance with the literature[28-30] (Table S1). For the three ligaments meshed with shell elements, the stress-strain relationships were calculated from their stiffness and the corresponding cross-sectional areas.[26] Contact was defined between the inner surface of the 2D ligaments and the outer surfaces of the bones as a frictionless surface-to-surface interaction.

Linear and elastic isotropic behaviour was assumed for the bone and cartilage; a Young modulus of 18 GPa was employed for cortical bone and 100 MPa for the cancellous bone; a Poisson ratio of 0.2 and 0.25 was used respectively.[23,29,31] Cartilage was defined as a hyperelastic material, for which Mooney-Rivlin parameters C10 and C01 were assigned of 4.1 and 0.41 MPa, respectively.[23,29]

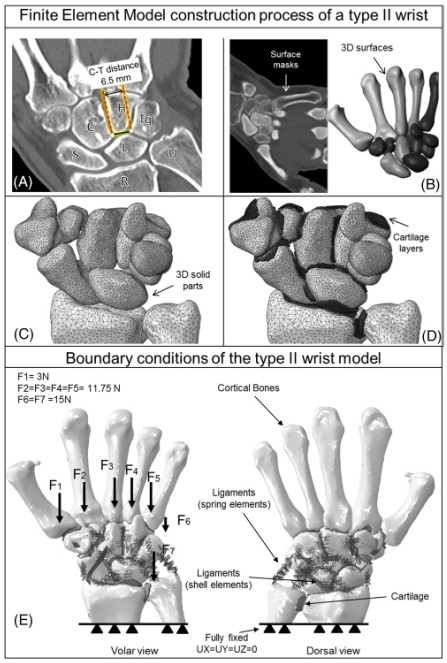

FIGURE 3 A, CT scan, the distance between the capitate (C) and triquetrum (Tq) is 6.5 mm. B, masks drawn on the CT scan images using 3D image segmentation and processing software to generate the 3D surfaces. C, solid parts imported into Abaqus to create the assembly of the wrist. D, modelling of the cartilage by offsetting of elements at the articulating surfaces between bones. E, finite element model of the healthy wrist showing the bones, the articular cartilage, set of ligaments, forces, and boundary conditions

2.2 | Loading, boundary conditions, and mesh sensitivity analysis

The proximal ends of radius and ulna were fully constrained. Loads to simulate clenched fist posture have been proposed in previous studies,[21] and these were used in this study. The forces applied to the numerical model were determined based on those employed in a previous cadaveric study to produce the clenched fist posture.[21] In the cadaveric study, six tendons/tendon groups were exposed to facilitate loading to produce the clenched fist posture. Loading weights of 15 N were attached separately to flexor digitorum superficialis, flexor digitorum profundus/flexor pollicis longus tendon, flexor carpi ulnaris, and extensor carpi ulnaris, whilst a load of 20 N was applied to the extensor digitorum communis. To simulate this loading condition in the numerical model, loads were applied to the proximal region of pisiform and to the dorsal base of the fifth metacarpal; the remaining three loads used to produce the clenched fist posture were applied by equally distributing the forces on the proximal end of the corresponding metacarpal bones. A force of 3 N was applied on the proximal end of metacarpal 1 and, similarly, forces of magnitude 11.75 N on metacarpals 2 to 5. Additionally, vertical loads of 15 N were added; one load applied at the proximal region of pisiform and other to the dorsal base of the fifth metacarpal (Figure 3E). A mesh sensitivity analysis was performed using the intact model in neutral position to ensure the accuracy of the predictions. Lunate bone contact area was considered, and mesh density was increased until the value of the contact area changed by less 5% (Figure 4). This mesh density was then employed for the subsequent analysis. The final model consisted of a total of 507 171 elements (10 372 wedge elements of type C3D6 for the cartilage, 496 491 tetrahedral elements of type C3D4 for the solid bones, 301 quadrilateral elements of type S4R, and seven triangular elements of type S3 for the ligaments represented by shell elements) and 111

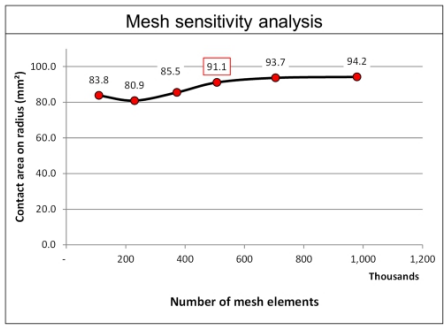

FIGURE 4 Mesh convergence plot. The contact area on radius converged when using a mesh with over 500 000 elements. In a model with 507 171 elements, we were able to achieve accuracy in the results with less computing resource

404 nodes. The lunate-scaphoid cartilage surface was modelled using 164 C3D6 wedge elements (six-noded linear triangular prism), representing a total area of 57.26 mm^2. The average volume of the elements on the lunate-scaphoid surface was 0.22 mm^3, and the average area of the element face (on the cartilage surface) was 0.2 mm^2.

2.3 | Virtual reconstruction

Six cases were modelled: intact-neutral clenched fist posture (Figure 5A), intact-ulna deviate clenched fist position (Figure 5B), SLIL sectioning-ulna deviated clenched fist position (Figure 5C), and three reconstruction techniques (Corella, MBT, and SLAM). For the SLIL sectioning case, the SLIL was fully removed, so there was no association between the scaphoid and lunate via ligament (Figure 5C). The virtual reconstruction techniques were modelled as described in previous studies.[21] For the virtual MBT technique, a 3-mm-diameter hole is drilled from the palmar tuberosity to the dorsal point of insertion of dorsal SLIL in the scaphoid. The graft was positioned, passing from volar to dorsal side of the scaphoid through the hole made and then connected to the lunate bone at the dorsal side (Figure 5D). The tendon graft was simulated using solid cylindrical elements.

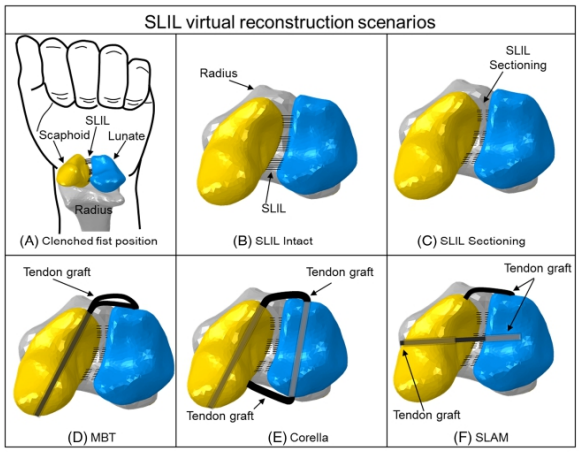

FIGURE 5 SLIL virtual reconstruction scenarios. A, hand showing the scaphoid, lunate, and intact SLIL ligament in neutral clenched fist position. B, SLIL intact ligament. C, SLIL sectioning. D, modified Brunelli tenodesis (MBT). E, Corella. F, SLAM model

In the Corella technique, two holes in the scaphoid and lunate bones are drilled. The tendon graft is then passed sequentially through the scaphoid and the lunate connecting both bones at dorsal and volar sides (Figure 5E). SLAM method was simulated by drilling the scaphoid and lunate on the lateral side along the coronal plane. The position of the tunnel is from midlateral side of the scaphoid to the proximal ulnar corner of the lunate; the tendon graft is passed through the scaphoid and anchored to the lunate connecting the central regions of both bones (Figure 5F). The stiffness of the tendon grafts in all cases was assumed to be the same as the stiffness of the dorsal SLIL.[21]

In the FE models for the virtual reconstruction techniques, the holes in the bones were produced by positioning an axis linking the insertion points at dorsal and volar sides; then a cylinder with the same diameter as the bone graft was aligned to the axis. The cut to extract the cylindrical portion from the bone was achieved using a Boolean operation. The tendon graft representations were assumed to be fully bounded (tie-constraint) to the internal surfaces of the bone. The solver approach used was static/general. Verification was performed by comparing the resultant forces at the bottom surfaces of the radius and ulna with the applied loads.

2.4 | SL gap and angle calculation

The SL gap was calculated at volar and dorsal side for the type II wrist from the models. The SL gap was calculated as the distance between two points on the edges of lunate and scaphoid at both dorsal and volar side. To locate the points to measure the SL gap, two imaginary arcs, Gilula lines, were used (Figure 6A): a proximal arc, running along the proximal convexities of the scaphoid, lunate, and triquetrum, and a distal arc, tracing the distal curvatures of the scaphoid, lunate, and triquetrum. An auxiliary arc was then drawn at the midpoint between the proximal and distal arcs lines, and the intersection between the auxiliary arc and the edges of the scaphoid and lunate was employed to define the points used to measure the SL gap: S_D-L_D for dorsal side and S_V-L_V for volar side (Figure 6A). The SL angle was calculated using two lines projected on a lateral view using the method described by Larsen et al[32]: on the scaphoid, a line tangential to the proximal and distal margins at volar side, and on the lunate, a line perpendicular to the tangent of the two distal poles (Figure 6B).

In addition, to further facilitate comparison of the performance of the reconstruction techniques, the area affected by the rupture of SL ligament was analysed by obtaining contact area values and contact patterns for the articular cartilage surface between the scaphoid and lunate for the intact ligament case, SLIL sectioning, and the three virtual reconstructions scenarios.

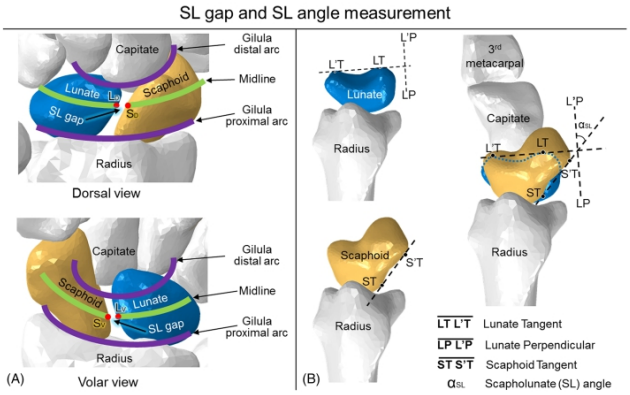

FIGURE 6 A, the SL gap from FE model, calculated from the distance between two points defined at the intersection of the midline of the Gilula arcs (proximal and distal) and the border of the lunate and scaphoid. B, SL angle measured between two lines in the lateral view. Line 1(LP-L'P), perpendicular to the tangent line of the two distal poles of the lunate (LT-L'T). Line 2 (ST-S'T), a tangent line of the proximal and distal margin of the scaphoid at palmar side. The SL angle is the angle between line 1 and line 2

In order to assess the motion of the carpal bones, the position of each bone was obtained from the numerical models for all the scenarios at neutral and ulnar deviated clenched fist positions. Each bone was represented as a point located at its volume centroid. The coordinates of each bone centroid were plotted for the two positions to visualise the motion in three orthogonal planes.

3 | RESULTS

3.1 | Reconstruction techniques comparison: Dorsal and volar SL gap and angle

The predicted values for SL gap for all the scenarios including the reconstruction techniques are presented in Figure 7A for the type II wrist. Results are shown next to corresponding predictions for a type I wrist, obtained from a previous study by the authors.[21] For the intact scenario in neutral position, the SL gaps predicted by the type II wrist model were 2.4 and 2.5 mm at dorsal and volar side, respectively. For the ulnar deviated clenched fist position, the SL increased to 2.8 mm at both dorsal and volar side, an increase of 16.6% and 12.0%, respectively, compared with the neutral position.

Following SLIL sectioning, in ulnar deviated clenched fist position, the SL gap increased by 0.7 mm (25%) and 0.3 mm (10.7%) at dorsal and volar side compared with the intact scenario. At the dorsal side, all three reconstruction techniques reduced the SL gap by 0.8 mm (20%) compared with the SLIL sectioning to 0.1 mm (3.5%) less than that of the intact scenario. At volar side, the Corella and the SLAM techniques both reduced SL gap compared with SLIL sectioning, by 0.5 mm (16%) and 0.7 mm (22.6%), respectively, to 0.2 mm (7.1%) and 0.4 mm (14.2%) lower respectively than the intact scenario. The MBT technique failed to reduce the volar SL gap following SLIL sectioning, with the gap remaining 0.3 mm (10.7 %) greater than for the intact scenario.

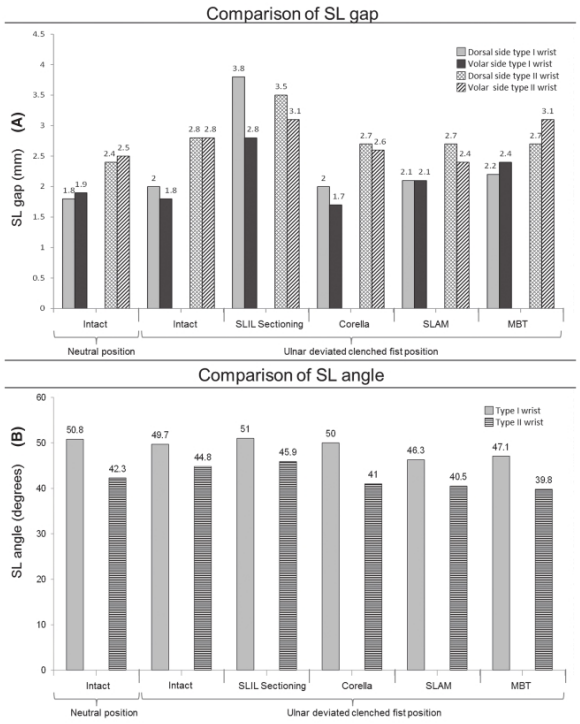

FIGURE 7 A, comparison of the predicted SL gap at dorsal and volar sides in the finite element models for the intact position, SLIL model, and the three reconstruction techniques at the ulnar deviated clench fist position for the both types of human wrist. B, comparison of the predicted SL angle for the intact ligament in neutral position plus intact ligament, SLIL sectioning, and the three reconstruction techniques with the model at the ulnar deviated clench fist position for the both types of wrist

Predicted values for SL angle for the type II wrist for the scenarios are presented in Figure 7B. As with SL gap, results are shown next to corresponding predictions for a type I wrist.[21] The SL angle from the intact scenario increased by 5.9% from 42.3° at neutral position to 44.8° at the ulnar deviated clenched fist position. After SLIL sectioning, SL angle increased by 1.1° (2.5%). The reconstruction techniques all reduced SL angle compared with the SLIL sectioning case to below the intact value: Corella, SLAM, and MBT techniques reduced SL angle to below the intact ulna deviate clenched value by 3.8° (8.4%), 4.3° (9.6%), and 5° (11.2%), respectively.

3.2 | Contact area: Scaphoid-lunate bones

We compared scaphoid/lunate contact area for our type I and II intact wrist models with experimentally determined values available in the literature.[33-35] Figure 8 shows the scaphoid/lunate contact area ratios predicted by our type I and II intact wrist models alongside the values from the cadaveric experimentation undertaken by Tencer et al,[33] Viegas et al,[34] and Blevens et al.[35] Note, the values for the type I wrist were not previously reported[21] but have been calculated as part of the current study. Upon inspection of Figure 8, it can be seen that overall, our model predictions compare well with the experimental determined values.

Figure 9 shows the contact area values between the scaphoid and lunate for the various scenarios for both the type I (Figure 9A) and type II wrist (Figure 9B). For the type I wrist (Figure 9A), in the intact ulnar deviated clenched fist case, a relatively small region (1.2 mm^2) of scaphoid-lunate contact area can be discerned towards the dorsal side of the lunate. Following SLIL sectioning, there is no contact at all between the scaphoid and the lunate. The Corella reconstruction technique restored connection between the scaphoid and lunate, resulting in a contact region of similar shape, location, and area (1.7 mm^2) to the intact wrist ulnar deviated clenched fist case. The MBT technique failed to restore any contact between the scaphoid and lunate, whereas SLAM resulted in increased contact between the scaphoid and lunate, resulting in a contact region of greater area (3.8 mm^2) being produced towards the location of the hole drilled in the scaphoid through which the graft passes.

For the type II wrist (Figure 9B), in the intact ulnar deviated clenched fist case, a region (5.0 mm^2) of scaphoid-lunate contact can be seen towards the dorsal side of the lunate. Following SLIL sectioning, a small contact region remains (1.4 mm^2) between scaphoid and lunate. Corella results in the connection between the scaphoid and lunate being restored, resulting in a contact region of similar shape, location, and area (6.9 mm^2) to the intact wrist ulnar deviated clenched fist case. As with the type I wrist, SLAM results in increased contact between the scaphoid and lunate, medially (14.8 mm^2), around the scaphoid graft hole, compared with the intact (5 mm^2). Of the three techniques, MBT resulted in scaphoid-lunate contact area (5.2 mm^2) closer to the intact case.

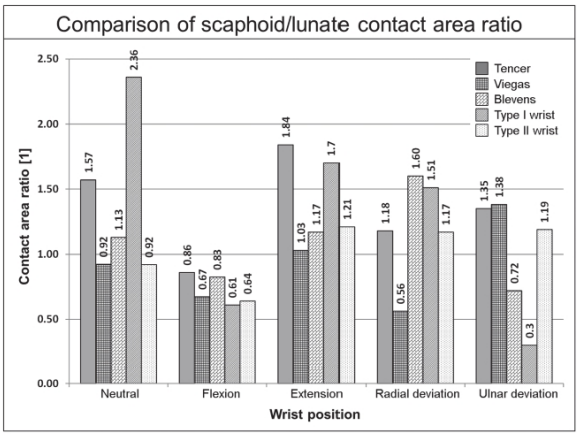

FIGURE 8 Comparison of the scaphoid/lunate contact area ratio between finite element model predictions and experimental values reported in the literature

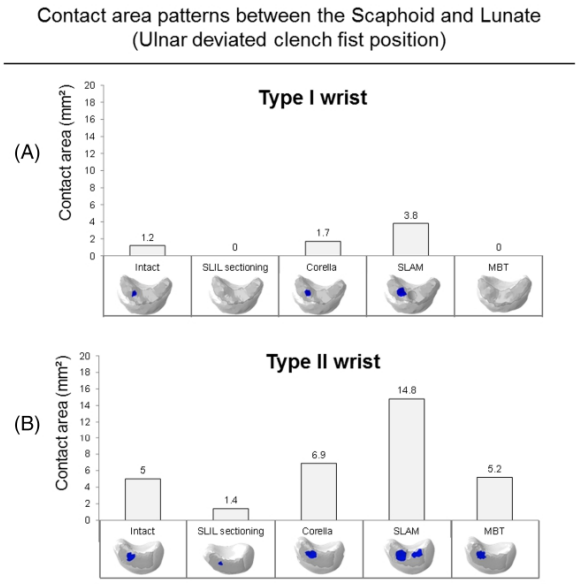

FIGURE 9 Comparison of the contact area patterns at the scaphoid-lunate interface for the intact, SLIL sectioning, and the three tenodesis techniques

3.3 | Type I and II carpal mechanics: Row/column theory

Figure 10 shows the motion pattern of the bones of the carpal joint for both the type I and type II wrist when moving from the neutral to ulnar deviated clench fist position; superior, volar, and lateral views are presented.

For the type I wrist, the plots show that scaphoid and lunate displacement is relatively small during the motion. The scaphoid and lunate exhibit similar displacement in two planes (ZX and ZY); in plane ZX, both bones displaced 1.2 mm, whilst in plane ZY, scaphoid displaced 1.5 mm and lunate 1.6 mm; scaphoid displacement is greater compared with the lunate in the YX plane, 1.3 and 0.9 mm, respectively. Triquetrum and pisiform displacement is similar in all three planes and of greater magnitude than the scaphoid and lunate. The displacement of the trapezoid, trapezium, capitate, and hamate is appreciably greater than that of the scaphoid and lunate; in addition, these bones exhibit a similar displacement pattern.

For the type II wrist, the plots indicate that as the wrist moves from the neutral to ulnar deviated clench fist position, the triquetrum and pisiform displace dorsally, exhibiting similar displacement in the three planes. In comparison, scaphoid displacement is smaller in the volar and distal directions. The trapezoid, trapezium, capitate, hamate, and lunate all exhibit a similar motion pattern, with displacement less than the triquetrum, pisiform, and scaphoid. Whilst scaphoid and lunate displacement is similar in the YX plane (1.1 and 1.2 mm, respectively), differences can be clearly seen in the ZX where scaphoid moved 0.6 mm and lunate 1.2 mm, and ZY planes where scaphoid moved 0.9 mm and lunate 0.7 mm.

3.4 | Type I and II performance of the reconstruction techniques: Wrist kinematics

Figures 11–14 show the position of the carpal joint bones for the intact wrist compared with SLIL sectioning and Corella, SLAM, and MBT technique application, for the type I (Figures 11, 12) and type II wrist (Figures 13, 14) in the ulnar deviated clench fist position; superior, volar, and lateral views are presented. Also shown in Figures 11–14 is a tabular comparison of the position of the centroid of each of the carpal joint bones for SLIL sectioning and Corella, SLAM, and MBT techniques compared with the intact wrist for the ulnar deviated clench fist position.

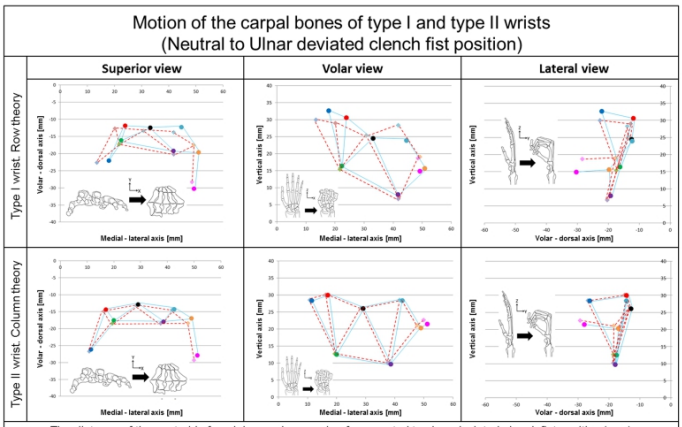

The distance of the centroid of each bone when moving from neutral to ulnar deviated clench fist position (mm)

		Scaphoid	Trapezium	Trapezoid	Capitate	Hamate	Lunate	Triquetrum	Pisiform
X-Y PLANE	Type I wrist	1.3	4.5	3.9	2.6	3.2	0.9	2.7	2.0
	Type II wrist	1.1	0.9	0.9	0.8	0.9	1.2	2.2	1.9
Z-X PLANE	Type I wrist	1.2	5.2	4.1	2.6	5.2	1.2	3.8	3.9
	Type II wrist	0.6	0.7	0.7	0.7	0.9	1.2	1.8	1.7
Z-Y PLANE	Type I wrist	1.5	2.7	1.8	1.2	4.6	1.6	4.6	4.3
	Type II wrist	0.9	0.6	0.5	0.3	0.2	0.7	1.6	1.8
3D XYZ	Type I wrist	1.6	5.2	4.2	2.8	5.4	1.6	4.4	4.3
	Type II wrist	1.1	0.9	0.9	0.8	1	1.3	2.3	2.2

FIGURE 10 Comparison of the motion for type I and type II wrist during ulnar deviation

In comparison of the techniques, Table 1 shows the distance calculated between the points representing the centroids of the scaphoid and lunate bones, following SLIL sectioning and Corella, SLAM, and MBT techniques compared with the intact wrist case for both the type I and type II wrist in the ulnar deviated clenched fist position. The FE analysis software, Abaqus, provided the coordinates of the centroids of the bones, facilitating their tracking during the movement.

3.4.1 | Type I wrist

It can be seen upon inspection of Figure 11A that after SLIL sectioning of the type I wrist, the scaphoid exhibits greater displacement in the three planes compared with the lunate (2.05 mm overall compared with 1.62 mm). Displacement of the lunate is similar to that of the intact case, only 1.9% greater overall, whereas scaphoid displacement is 22.8% greater compared with the intact wrist. The distance between the scaphoid and lunate centroids increased by 1.2 mm compared with the intact wrist as a result of SLIL sectioning (Table 1). Following application of the Corella technique (Figure 11 B), the scaphoid and lunate displacement pattern was similar to that of the intact scenario (lunate displacement 0.63% lower, scaphoid 3.6% greater), with the distance between the centroids of the two bones being slightly smaller compared with the intact case (0.1 mm less, Table 1). No significant change in the motion of the other carpal bones was discernible. For the SLAM technique (Figure 12A), scaphoid and lunate displacement pattern diverged from that of the intact (lunate displacement 6.9% lower, scaphoid 12% greater). The distance between the scaphoid and lunate was greater compared with the intact case (by 0.7 mm, Table 1), with the lunate exhibiting displacement more to the volar side than the intact case with the scaphoid displacing towards the proximal pole, at the articulation area with the scaphoid. After MBT reconstruction (Figure 12B), the scaphoid and lunate displacement is similar in nature to the intact case, with the distance between the centroids of the two bones being greater compared with the intact case (by 0.37 mm, Table 1) but

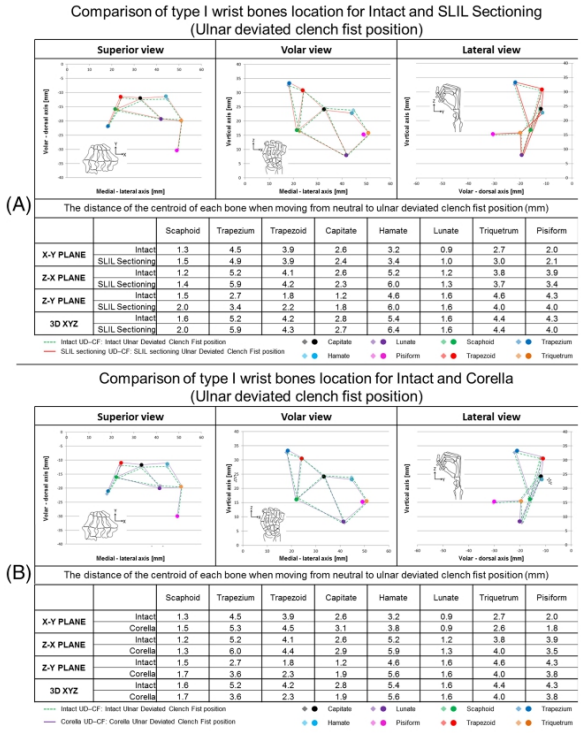

FIGURE 11 A, location of the bones after clench fist position comparing the intact scenario to the SLIL sectioning scenario for a type I wrist. B, location of the bones after clench fist position comparing the intact scenario to the Corella for a type I wrist

smaller compared with the SLAM technique. No significant change compared with the intact wrist in the displacement pattern of the remaining carpal bones was observed following MBT reconstruction simulation.

3.4.2 | Type II wrist

Following SLIL sectioning of the type II wrist (Figure 13A), both scaphoid and lunate movement remains close to that of the intact, displacement of the two bones is slightly greater (0.1-mm lunate, 0.4-mm scaphoid), but the relative position of the two bones remains very similar to the intact ligament case, with scaphoid-lunate centroid distance increasing by only 0.24 mm in comparison (Table 1).

Following application of the Corella technique (Figure 13B), the displacement of the trapezium, trapezoid, capitate, and hamate remained similar to that of the intact case, but lunate displacement was altered as a consequence of gap overclosure after applying the reconstruction technique. In addition, the scaphoid moves slightly more towards the lunate; however, the direction of the motion for both the scaphoid and lunate is broadly similar to the intact case but with the magnitude being greater for both bones (0.1-mm scaphoid, 0.3-mm lunate). For the Corella technique, scaphoid-lunate centroid distance was 0.21 mm less than the intact case (Table 1). Following application of the SLAM technique (Figure 14A), scaphoid displacement was more towards the lunate compared with the intact case, with the scaphoid taking a more vertical position during the movement to the ulnar deviated clench fist position. Compared with the intact wrist, both scaphoid and lunate motion was greater (0.4-mm scaphoid, 0.2-mm lunate). The motion of the trapezium, trapezoid, capitate, and hamate and of the triquetrum and pisiform was not significantly altered following application of the technique. Lunate displacement tended to be more in the lateral direction with the distance between

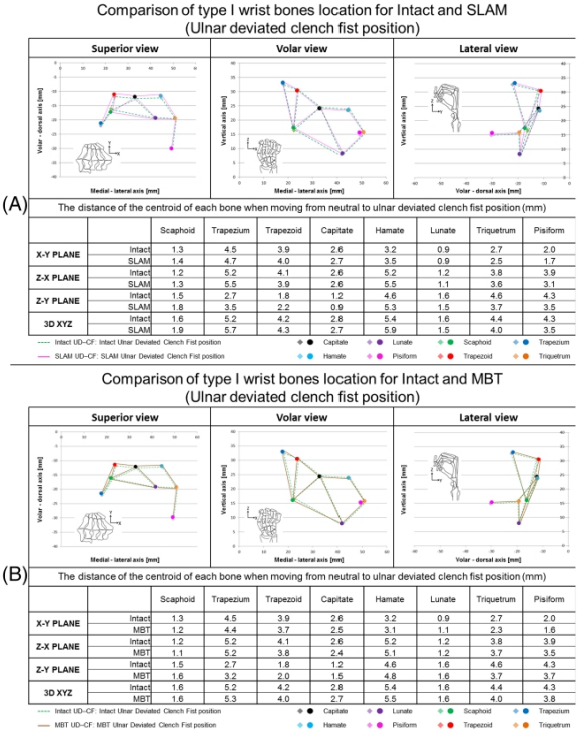

		Scaphoid	Trapezium	Trapezoid	Capitate	Hamate	Lunate	Triquetrum	Pisiform
X-Y PLANE	Intact	1.3	4.5	3.9	2.6	3.2	0.9	2.7	2.0
	SLAM	1.4	4.7	4.0	2.7	3.5	0.9	2.5	1.7
Z-X PLANE	Intact	1.2	5.2	4.1	2.6	5.2	1.2	3.8	3.9
	SLAM	1.3	5.5	3.9	2.6	5.5	1.1	3.6	3.1
Z-Y PLANE	Intact	1.5	2.7	1.8	1.2	4.6	1.6	4.6	4.3
	SLAM	1.8	3.5	2.2	0.9	5.3	1.5	3.7	3.5
3D XYZ	Intact	1.6	5.2	4.2	2.8	5.4	1.6	4.4	4.3
	SLAM	1.9	5.7	4.3	2.7	5.9	1.5	4.0	3.5

		Scaphoid	Trapezium	Trapezoid	Capitate	Hamate	Lunate	Triquetrum	Pisiform
X-Y PLANE	Intact	1.3	4.5	3.9	2.6	3.2	0.9	2.7	2.0
	MBT	1.2	4.4	3.7	2.5	3.1	1.1	2.3	1.6
Z-X PLANE	Intact	1.2	5.2	4.1	2.6	5.2	1.2	3.8	3.9
	MBT	1.1	5.2	3.8	2.4	5.1	1.2	3.7	3.5
Z-Y PLANE	Intact	1.5	2.7	1.8	1.2	4.6	1.6	4.6	4.3
	MBT	1.6	3.2	2.0	1.5	4.8	1.6	3.7	3.7
3D XYZ	Intact	1.6	5.2	4.2	2.8	5.4	1.6	4.4	4.3
	MBT	1.6	5.3	4.0	2.7	5.5	1.6	4.0	3.8

FIGURE 12 A, location of the bones after clench fist position comparing the intact scenario to the SLAM technique for a type I wrist. B, location of the bones after clench fist position comparing the intact scenario to the MBT for a type I wrist

the lunate and scaphoid bones being discernibly less (by 1 mm, Table 1), following SLAM application compared with the intact scenario. After MBT reconstruction (Figure 14B), lunate motion pattern is altered because of the constraint of the ligament graft at the dorsal side. The distance between the centroids of the lunate and scaphoid bones is larger compared with the intact scenario (18.88 mm compared with 18.81 mm, Table 1).

Comparing the distances presented in Table 1, it can be seen that for the type I wrist, Corella reconstruction resulted in a lunate-scaphoid centroid distance closest to the intact wrist (within 0.1 mm), followed by MBT then SLAM. For the type II list, MBT reduced lunate-scaphoid distance closer to the intact wrist (within 0.07 mm), followed by Corella and SLAM.

4 | DISCUSSION

4.1 | Reconstruction techniques comparison: Dorsal and volar SL gap and angle and contact area analysis

The results of the reconstruction technique comparison indicate that for the type II wrist, the Corella reconstruction technique is better able to restore dorsal and volar gap and SL angle to that of the intact (ligament) wrist following SLIL sectioning than the SLAM and MBT techniques. Application of the Corella technique following simulated SLIL sectioning resulted in a dorsal gap within 3.5%, a volar gap within 7.1%, and an SL angle within 8.4% of the intact scenario. Of the two other techniques considered, SLAM was better able to restore dorsal, volar gap, and SL angle than MBT. The authors' previous investigation also found that the Corella technique was the most effective reconstruction method, better able to restore SL gap and angle closer to that of the intact ligament for type I wrists, followed by SLAM. The results

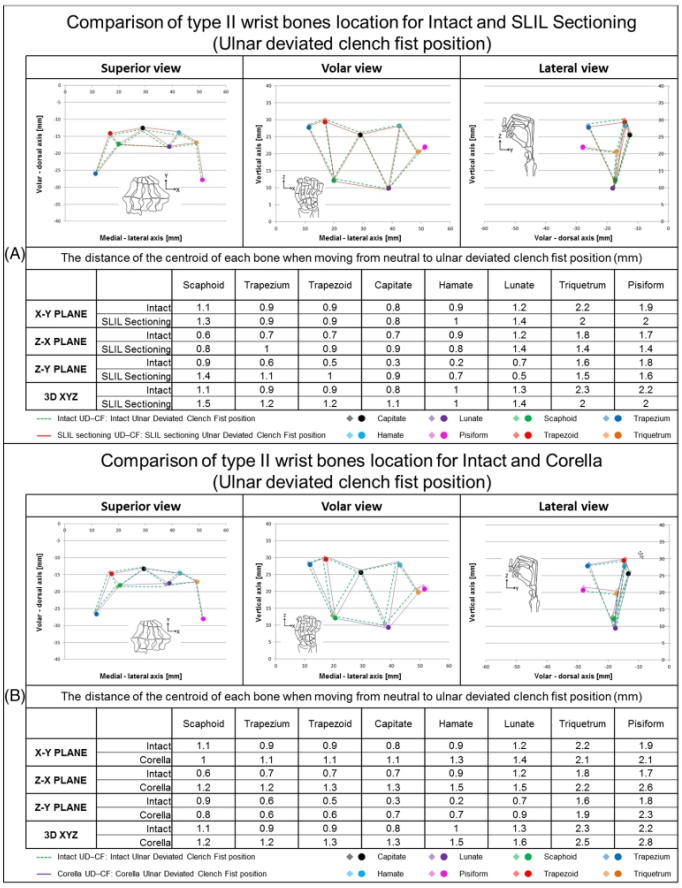

(A) The distance of the centroid of each bone when moving from neutral to ulnar deviated clench fist position (mm)

		Scaphoid	Trapezium	Trapezoid	Capitate	Hamate	Lunate	Triquetrum	Pisiform
X-Y PLANE	Intact	1.1	0.9	0.9	0.8	0.9	1.2	2.2	1.9
	SLIL Sectioning	1.3	0.9	0.9	0.8	1	1.4	2	2
Z-X PLANE	Intact	0.6	0.7	0.7	0.7	0.9	1.2	1.8	1.7
	SLIL Sectioning	0.8	1	0.9	0.9	0.8	1.4	1.4	1.4
Z-Y PLANE	Intact	0.9	0.6	0.5	0.3	0.2	0.7	1.6	1.8
	SLIL Sectioning	1.4	1.1	1	0.9	0.7	0.5	1.5	1.6
3D XYZ	Intact	1.1	0.9	0.9	0.8	1	1.3	2.3	2.2
	SLIL Sectioning	1.5	1.2	1.2	1.1	1	1.4	2	2

(B) The distance of the centroid of each bone when moving from neutral to ulnar deviated clench fist position (mm)

		Scaphoid	Trapezium	Trapezoid	Capitate	Hamate	Lunate	Triquetrum	Pisiform
X-Y PLANE	Intact	1.1	0.9	0.9	0.8	0.9	1.2	2.2	1.9
	Corella	1	1.1	1.1	1.1	1.3	1.4	2.1	2.1
Z-X PLANE	Intact	0.6	0.7	0.7	0.7	0.9	1.2	1.8	1.7
	Corella	1.2	1.2	1.3	1.3	1.5	1.5	2.2	2.6
Z-Y PLANE	Intact	0.9	0.6	0.5	0.3	0.2	0.7	1.6	1.8
	Corella	0.8	0.6	0.6	0.7	0.7	0.9	1.9	2.3
3D XYZ	Intact	1.1	0.9	0.9	0.8	1	1.3	2.3	2.2
	Corella	1.2	1.2	1.3	1.3	1.5	1.6	2.5	2.8

FIGURE 13 A, location of the bones after clench fist position comparing the intact scenario to the SLIL sectioning scenario for a type II wrist. B, location of the bones after clench fist position comparing the intact scenario to the Corella technique for a type II wrist

from the contact area analysis for the type II and I wrists presented support the SL gap and angle findings. The Corella technique produced scaphoid-lunate contact patterns and areas of similar shape and values to those of the intact wrist.

Following SLIL sectioning, our study determined that there was no contact area between scaphoid-lunate cartilage articulation for the type I wrist, whereas for the type II wrist, some contact was maintained. This supports the findings of previous clinical and cadaveric research that determined that the extra articulation in a type II wrist may help to reduce instability in cases of SL ligament injury.[4-6]

Our model predicted SL gaps in the range 1.7 to 2.7 mm for Corella, 2.1 to 2.7 for SLAM, and 2.2 to 3.1 for MBT compared with 1.8 to 2.8 for the intact case. The relatively small differences in the SL gap between the different reconstruction techniques predicted by our model concur with the results from cadaver experimentation and reported clinical outcomes. Lee et al[20] report the results of the application of three SL reconstruction techniques (SLAM, MBT, and Blatt capsulodesis) in cadaver limbs. Both the MBT and SLAM techniques were found to restore SL gap to within 1 mm of the intact case for a clenched fist posture. In a retrospective cohort study, Links et al[36] compared clinical and radiographic

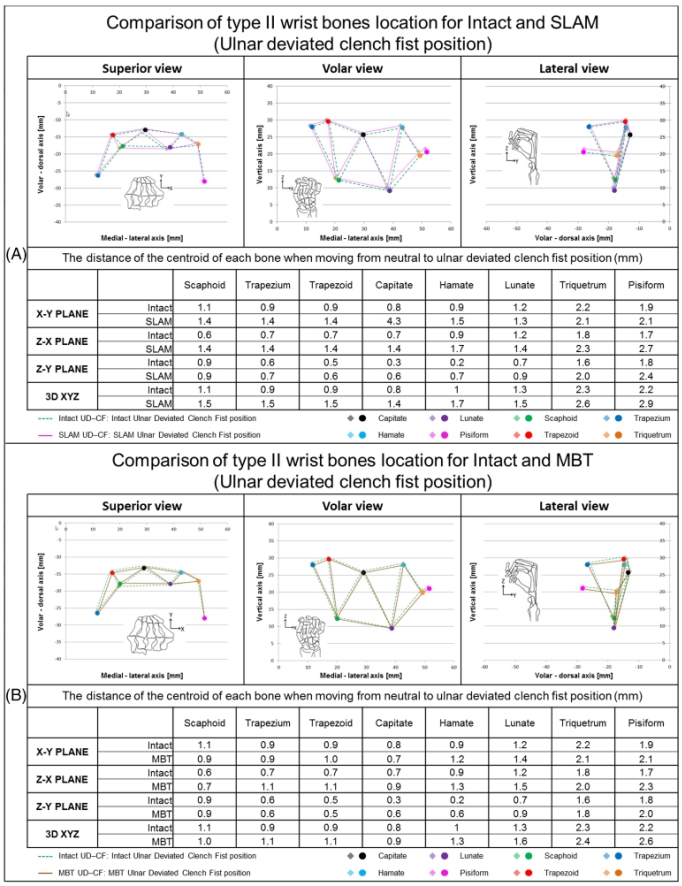

FIGURE 14 A, location of the bones after clench fist position comparing the intact scenario to the SLAM technique for a type II wrist. B, location of the bones after clench fist position comparing the intact scenario to the MBT for a type II wrist

TABLE 1 Distance between centroids of the scaphoid and lunate bone

	Distance, mm	
Case	**Type I wrist**	**Type II wrist**
Intact	21.26	18.81
SLIL	22.46	19.05
Corella	21.16	18.60
SLAM	21.96	17.81
MBT	21.63	18.88

outcomes in patients with chronic SL dissociation following treatment with MBT versus 4-bone tendon weave technique. In the case of MBT, the SL gap following reconstruction was found to be 2.2 ± 0.4 mm. In another study of 19 patients who had undergone the MBT procedure, Chabas et al[37] reported a mean static SL distance of 2.4 mm. Yao et al[38] report the in outcome for 13 patients who had undergone SLAM, after a follow-up period of 11 months, the mean postoperative SL gap was 2.1 mm. Although relatively small, research indicates that these differences can be clinically significant. Ideally, the surgical technique should restore a normal relationship between carpal bones, preserve range of motion, and grip strength whilst achieving a pain free wrist. Further, unsatisfactory results have been reported for techniques that fail to directly correct SL gap.[37] Where clinical outcomes have been compared, greater improvement in mean pain and DASH scores, motion, and grip strength have been reported for techniques that were able to provide relatively small (eg, 2.2 ± 0.4 mm compared with 3.0 ± 0.8 mm) yet significantly greater improvement of SL gap and angle.[38]

4.2 | Type I and II carpal mechanics: Row/column theory

Several previous studies have attempted to elucidate the row and column theories of carpal mechanics and relate them to type I and II wrists.[8,11,13] The results from our study support the assertion that type I wrists exhibit row mechanics and type II column mechanics.[8,11] The analysis of the motion pattern of the bones of the carpal joint for the type I wrist when moving from the neutral to ulnar deviated clench fist position (Figure 2B) shows that the lunate rotates clockwise to the ulnar side sliding over the radius; at the lateral side of the lunate, the scaphoid follows the motion preserving the distance between the bones and hence their relative position in two planes (ZX and ZY, Figure 10) as described by row theory. In the YX plane, the displacement of the scaphoid is greater; as a consequence of the rotation of the scaphoid to a more vertical position. The remaining bones, which are considered to make up the proximal row, the triquetrum and pisiform, exhibit a similar displacement pattern to each other. In addition, the analysis shows that trapezium, trapezoid, capitate, and hamate (distal row) move together, as a lever unit rotating around a centre, the capitate being the closest bone to the pivot point; during the motion, the trapezium and trapezoid move upwards following the rotation whilst the capitate and the hamate move downwards. This unit (the distal row) behaves like a rigid unit, with the distance between the bones being preserved in all three planes during motion.

For the case of the type II wrist, the trapezium, trapezoid, capitate, hamate, and lunate exhibited similar motion pattern, behaving as a unit (central column) rotating around the lunate. The proximal bones of the type II wrist, the scaphoid, lunate, and triquetrum, exhibited displacement patterns, which were clearly different from each other, which was not the case for the type I wrist, supporting the view that these three bones belong to three distinct columns, the lateral, central, and medial columns, respectively. Unlike the type I wrist, for type II, the scaphoid displacement is similar to that of the lunate only in the YX plane (Figure 10); in planes ZX and ZY, the magnitude of the displacement of the scaphoid is different as a consequence of a rotation along the X-axis to take up a more vertical position and the rotation around its longitudinal axis. The triquetrum and pisiform demonstrated greater displacement compared with other bones especially in the YX plane. This is in accordance with column theory, whereby during the movement, the medial column (triquetrum and pisiform) tilts dorsally to make space for the bones of the central column; this movement affects the relative position between the lunate and the triquetrum in the ZX and ZY planes.

4.3 | Type I and II performance of the reconstruction techniques: Wrist kinematics

Our analysis of wrist kinematics following application of the ligament reconstruction simulations to the type I wrist indicated that none of the techniques significantly altered the motion pattern of the wrist, and all continued to exhibit row behaviour. Following simulation of the Corella reconstruction, motion of the bones in the distal row was effectively unchanged, and the triquetrum behaved as in the intact scenario; the lunate and scaphoid exhibited similar motion pattern as the intact case but maintaining slightly closer proximity to each other because of the constraints at both volar and dorsal sections. In the case of SLAM reconstruction, in the proximal row, the triquetrum maintained the motion pattern as in the intact wrist case. Compared with the intact wrist, the lunate moved more volarly in the centre where the bone is attached to the scaphoid by the ligament reconstruction. Scaphoid motion was more towards the proximal pole at the articulation area to the scaphoid, where the two bones are linked by the ligament after the reconstruction. The distance between the two bones was greater compared with the intact case. For MBT, the motion of the bones in the distal row following reconstruction was akin to that of the intact wrist, as was the triquetrum motion (proximal row).

The lunate and scaphoid moved together similar to the intact but sliding slightly more over the radius. Again, the distance between the lunate and scaphoid bones was greater compared with the intact case. Overall, the kinematic analysis confirmed that the Corella technique is best able to restore motion closest to the intact scenario for the type I wrist.

For the type II wrist, the kinematic analysis also determined that application of the ligament reconstruction techniques does not significantly alter wrist motion pattern (column behaviour). Following application of Corella reconstruction, motion of the trapezium, trapezoid, capitate, and hamate (central column) remained essentially unchanged compared with the intact wrist; in addition, the direction of motion of the bones of the medial column (triquetrum and pisiform) was unaltered. The scaphoid (lateral column) motion was slightly more towards the lunate (central column) because of the constraints imposed at dorsal and volar side by the ligament graft. For the SLAM technique, the only significant difference compared with the intact wrist was that the lateral column (scaphoid) moved more towards the central column (lunate); also, the scaphoid tended to take a more vertical position during the motion as a result of the insertion point of the ligament graft in the middle of the area that articulates to the lunate, allowing a point of rotation for this bone. In addition, the lunate rotation was greater compared with the intact wrist as it followed the motion of the scaphoid as a result of the ligament graft. For the MBT reconstruction, the motion of the bones of the central column did not change significantly compared with the intact wrist as was the case with the lateral column (scaphoid). In the central column, the lunate motion pattern was altered; at dorsal side, the movement was constrained by the ligament graft, but at volar side, the lack of a constraint enabled a small rotation of the bone opening the gap at volar side. The medial column (triquetrum and pisiform) was also altered slightly; motion was greater as the column followed the motion of the lunate. Overall, the kinematic analysis confirmed that the Corella technique is best able to restore motion closest to the intact scenario for the type II wrist.

The wrist kinematic analysis presented in the current study compared carpal bone motion of both type I and type II wrists following SLIL sectioning with the intact ligament scenario. For the type I wrist, following sectioning, the scaphoid exhibited appreciably greater displacement whereas the lunate was less affected. For the type II wrist, however, both scaphoid and lunate motion remained very close to that of the intact. This finding supports those reported by Rhee[5] and Hasse[6] that type II wrists are less prone to instability even following SL ligament injury.

Our model is subject to a number of simplifications, assumptions, and limitations typical of complex numerical problems in this research field. For example, our model considered cancellous bone as exhibiting elastic-plastic, isotropic material behaviour. The intact wrist model developed using these properties has been successfully validated previously against the results from cadaveric experimentation,[21] so the material properties employed can be considered sufficiently accurate for this investigation. Also, whilst it is recognized that the elastic modulus of cancellous bone depends primarily on apparent bone density, the exact form of the dependency is contested,[39] and this is further complicated by the dependency of the relationship on trabecular orientation, loading direction, and anisotropy. However, it is recognised that within a single anatomical site, density range is limited,[39] which suggests that an invariant bone property, as was employed in our study, should provide sufficient accuracy.

The majority of the ligaments included in the model were represented using one-dimensional spring elements, which although a common approach, is known to have its limitations, for example, in cases of complex nonuniform 3D stress/strain.[40] More accurate representation requires 3D FE modelling treatment; however, the required approach is highly involved and extremely time consuming.[40] We assumed linear elastic material properties for the ligaments in the model where, in practice, ligaments tend to exhibit non-linear viscoelastic behaviour. However, a large number of parameters are required for accurate non-linear viscoelastic behaviour representation; therefore, parameter data availability is key, but these data are generally not widely available.[40] In practice though, ligaments tend to operate in or close to the linear region, so our modelling assumption should provide reasonable accuracy.[41] A hyperelastic material model was employed to represent soft tissue (cartilage) behaviour, which is considered to be an accurate approach.[29]

Finally, the type II wrist models were developed from the CT scan of the left hand of a single subject; therefore, any results and conclusions drawn from the analyses should be viewed in this context and interpreted with care. Future planned work includes analysis of additional subjects to provide further potential support and verification for the findings of the current investigation. In conclusion, our study has determined that the Corella ligamentous reconstruction technique is best able to restore SL gap, angle, and stability following SL ligament injury for both type II and type I wrists and is able to do so without altering the kinematics of the wrist. Our findings also support the view that in terms of wrist mechanics, type I wrists exhibit row behaviour and type II wrists column behaviour. In addition, our analysis suggests that the extra articulation between the lunate and hamate in a type II wrist may help improve stability of the wrist following SL ligament injury.

REFERENCES

1. Kitay A, Wolfe SW. Scapholunate instability: current concepts in diagnosis and management. *J Hand Surg am*. 2012;37(10):2175-2196.
2. Andersson JK. Treatment of scapholunate ligament injury. *EFORT Open Rev*. 2017;2(9):382-393.
3. Jones WA. Beware the sprained wrist. The incidence and diagnosis of scapholunate instability. *J Bone Joint Surg Br*. 1988;70:293-297.
4. Werner FW, Short WH, Green JK, Evans PJ, Walker JA. Severity of scapholunate instability is related to joint anatomy and congruency. *J Hand Surg am*. 2007;32(1):55-60.
5. Rhee PC, Moran SL, Shin AY. Association between lunate morphology and carpal collapse in cases of scapholunate dissociation. *J Hand Surg am*. 2009;34(9):1633-1639.
6. Haase SC, Berger RA, Shin AY. Association between lunate morphology and carpal collapse patterns in scaphoid nonunions. *J Hand Surg am*. 2007;32(7):1009-1012.
7. Pang EQ, Douglass N, Kamal RN. Association of lunate morphology with carpal instability in scapholunate ligament injury. *Hand*. 2017;1-5.
8. Galley I, Bain GI, McLean JM. Influence of lunate type on scaphoid kinematics. *J Hand Surg am*. 2007;32(6):842-847.
9. Viegas SF, Wagner K, Patterson R, Peterson P. Medial (hamate) facet of the lunate. *J Hand Surg am*. 1990;15(4):564-571.
10. Morimoto H, Goto A, Sato Y, et al. The triquetrum-hamate joint: an anatomic and in vivo three-dimensional kinematic study. *J Hand Surg am*. 2003;28(5):797-805.
11. Craigen MAC, Stanley JK. Wrist kinematics. Row, column or both? *J Hand Surg am*. 1995;20(2):165-170.
12. Viegas SF, Patterson RM, Hokanson JA, Davis J. Wrist anatomy: incidence, distribution, and correlation of anatomic variations, tears, and arthrosis. *J Hand Surg am*. 1993;18(3):463-475.
13. Nakamura K, Beppu M, Patterson RM, Hanson CA, Hume PJ, Viegas SF. Motion analysis in two dimensions of radial-ulnar deviation of type I versus type II lunates. *J Hand Surg am*. 2000;25(5):877-888.
14. McLean JM, Turner PC, Bain GI, Rezaian N, Field J, Fogg Q. An association between lunate morphology and scaphoid-trapezium-trapezoid arthritis. *J Hand Surg Eur Vol*. 2009;34(6):778-782.
15. Ferris BD, Stanton J, Zamora J. Kinematics of the wrist. *J Bone Jt Surg*. 2000;(82–B):242-245.
16. Brunelli GA, Brunelli GR. A new technique to correct carpal instability with scaphoid rotary subluxation: a preliminary report. *J Hand Surg*. 1995;20(3):S82-S85.
17. Garcia-Elias M, Lluch AL, Stanley JK. Three-ligament tenodesis for the treatment of scapholunate dissociation: indications and surgical technique. *J Hand Surg*. 2006;31(1):125-134.
18. Van Den Abbeele KL, Loh YC, Stanley JK, Trail IA. Early results of a modified Brunelli procedure for scapholunate instability. *J Hand Surg*. 1998;23(2):258-261.
19. Corella F, Del Cerro M, Ocampos M, Larrainzar-Garijo R. Arthroscopy ligamentoplasty of the dorsal and volar portions of the scapholunate ligament. *J Hand Surg*. 2014;39:643-650.
20. Lee SK, Zlotolow DA, Sapienza A, Karia R, Yao J. Biomechanical comparison of 3 methods of scapholunate ligament reconstruction. *J Hnd Surg*. 2014;39:643-650.
21. Alonso Rasgado T, Zhang Q, Jimenez Cruz D, et al. Analysis of tenodesis techniques for treatment of scapholunate instability using the finite element method. *Int J Numer Method Biomed Eng*. 2017;33(12):1-12.
22. Fischli S, Sellens RW, Beek M, Pichora DR. Simulation of extension, radial and ulnar deviation of the wrist with a rigid body spring model. *J Biomech*. 2009;42(9):1363-1366.
23. Gíslason MK, Stansfield B, Nash DH. Finite element model creation and stability considerations of complex biological articulation: the human wrist joint. *Med Eng Phys*. 2010;32(5):523-531.
24. Kijima Y, Viegas SF. Wrist anatomy and biomechanics. *J Hand Surg am*. 2009;34(8):1555-1563.
25. Berger RA. The anatomy and basic biomechanics of the wrist joint. *J Hand Ther*. 1996;9(2):84-93.
26. Nagao S, Patterson RM, Buford WL, Andersen CR, Shah MA, Viegas SF. Three-dimensional description of ligamentous attachments around the lunate. *J Hand Surg am*. 2005;30(4):685-692.
27. Nakamura K, Patterson RM, Moritomo H, Viegas SF. Type I versus type II lunates: ligament anatomy and presence of arthrosis. *J Hand Surg am*. 2001;26(3):428-436.
28. Berger RA, Imeada T, Berglund L, An KN. Constraint and material properties of the subregions of the scapholunate interosseous ligament. *J Hand Surg am*. 1999;24(5):953-962.
29. Bajuri MN, Abdul Kadir MR, Murali MR, Kamarul T. Biomechanical analysis of the wrist arthroplasty in rheumatoid arthritis: a finite element analysis. *Med Biol Eng Comput*. 2012;1-12.
30. Savelberg HH, Kooloos JG, Huiskes R, Kauer JM. Stiffness of the ligaments of the human wrist joint. *J Biomech*. 1992;25(4):369-376.
31. Guo X, Fan Y, Li ZM. Effects of dividing the transverse carpal ligament on the mechanical behavior of the carpal bones under axial compressive load: a finite element study. *Med Eng Phys*. 2009;31(2):188-194.

32. Larsen CF, Stigsby B, Lindequist S, Bellstrøm T, Mathiesen FK, Ipsen T. Observer variability in measurements of carpal bone angles on lateral wrist radiographs. *J Hand Surg am*. 1991;16(5):893-898.
33. Tencer AF, Viegas SF, Cantrell J, et al. Pressure distribution in the wrist joint. *J Orthop Res*. 1988;6(4):509-517.
34. Viegas SF, Tencer AF, Cantrell J, et al. Load transfer characteristics of the wrist. Part I. the normal joint. *J Hand Surg am*. 1987 Nov;12 (6):971-978.
35. Blevens AD, Light TR, Jablonsky WS, et al. Radiocarpal articular contact characteristics with scaphoid instability. *J Hand Surg am*. 1989 Sep;14(5):781-790.
36. Links AC, Chin SH, Waitayawinyu T, Trumble TE. Scapholunate interosseous ligament reconstruction: results with a modified Brunelli technique versus four-bone weave. *J Hand Surg am*. 2008 Jul-Aug;33(6):850-856. https://doi.org/10.1016/j.jhsa.2008.02.010
37. Chabas JF, Gay A, Valenti D, Guinard D, Legre R. Results of the modified Brunelli tenodesis for treatment of scapholunate instability: a retrospective study of 19 patients. *J Hand Surg am*. 2008 Nov;33(9):1469-1477. https://doi.org/10.1016/j.jhsa.2008.05.031
38. Yao J, Zlotolow DA, Lee SK. ScaphoLunate axis method. *J Wrist Surg*. 2016 Mar;5(1):59-66. https://doi.org/10.1055/s-0035-1570744 Epub 2016 Jan 6
39. Keaveny TM, Morgan EF, Niebur GL, Yeh OC. Biomechanics of trabecular bone. *Annu Rev Biomed Eng*. 2001;3:307-333.
40. Weiss JA, Gardiner JC, Ellis BJ, Lujan TJ, Phatak NS. Three-dimensional finite element modeling of ligaments: technical aspects. *Med Eng Phys*. 2005;27(10):845-861.
41. Spratley EM, Wayne JS. Computational model of the human elbow and forearm: application to complex varus instability. *Ann Biomed Eng*. 2011;39(3):1084-1091.

SUPPORTING INFORMATION

Additional supporting information may be found online in the Supporting Information section at the end of the article.

How to cite this article: Leonardo-Diaz R, Alonso-Rasgado MT, Jimenez-Cruz D, Bailey CG, Talwalkar S. Performance evaluation of surgical techniques for treatment of scapholunate instability in a type II wrist. *Int J Numer Meth Biomed Engng*. 2019;e3278. https://doi.org/10.1002/cnm.3278